1-1-2022

AMPHIPHILIC JANUS POLYMER NANOPARTICLES FOR PHARMACEUTICAL AND BIOMEDICAL APPLICATIONS

Mahesh Loku Yaddehige

AMPHIPHILIC JANUS POLYMER NANOPARTICLES FOR PHARMACEUTICAL AND BIOMEDICAL APPLICATIONS

A Dissertation

presented in partial fulfillment of requirements

for the degree of Doctor of Philosophy

in the Department of Chemistry and Biochemistry

The University of Mississippi

by

MAHESH LOKU YADDEHIGE

May 2022

ABSTRACT

Amphiphilic hybrid polymers have attracted significant interest as biomaterials for both fundamental research and practical clinical applications due to their unique polymer structure and properties relative to the conventional symmetric polymers. Often referred to as “Janus” polymers combine two different polymer segments (hydrophilic and hydrophobic) of varying degrees, sizes, and functionalities to obtain a single amphiphilic or hetero-functional macromolecule with characteristic features. In particular, amphiphilic “Janus” polymers and their self-assemblies have shown apparent success in nanomedicine owing to their ability to provide highly ordered nanoscale multimolecular aggregates, including micelles and vesicles. However, engineering these polymeric materials on a large scale with nanoaggregates of desirable size and morphology remains challenging. Herein novel synthetic routes and characterization for amphiphilic Janus polymer libraries and their nanoaggregates are presented. The first library discusses the design, synthesis, and characterization of self-assembling amphiphilic Janus dendrimers, which consisted of NH_3^+ (cationic), COO^- (anionic), and OH (neutral) polyamidoamine (PAMAM) as hydrophilic segments and fatty acid branches as the hydrophobic segment. The results of this study afford opportunities to evaluate in-vivo efficacy as well as stability and interactions with bloodstream components. The second system involves in-situ self-assembly, known as polymerization-induced self-assembly (PISA). Using the PISA approach, we designed the first cationic dendritic macro chain transfer agent to synthesize a Janus-type hybrid polymer called a linear dendritic block copolymer (LDBCs). These studies offer a one-pot polymerization method for a new class of

fluorinated Janus-type LDBC for a ^{19}F magnetic resonance imaging (MRI) agent. These results showcase novel yet efficient pathways toward building next-generation biomaterials with unique morphologies and tunable properties.

DEDICATION

This dissertation work dedicates to my mother and father, who always believed me, encouraged me to reach the highest level of education.

ACKNOWLEDGMENTS

I would like to thank my research supervisor, Dr. Davita Watkins, who advised and drove me to achieve my scientific endeavors. She always encouraged and supported me to grow as an independent scientist. She is the supervisor who guided me to become a better scientist and become a better person. I would also like to thank Drs. Cizdziel, Delcamp, Chakraborty, Werfel, and Chougule for taking time out of their busy schedules, being a part of my committee, and providing valuable advice. I would also like to thank all of the grad students, postdocs, undergrads, and research group members who worked with me over these years. In addition, I thank the numerous collaborators who have worked with me and helped me on different projects. Their work and support have been invaluable. Last and certainly not least, I would like to thank my parents, my loving wife, and friends for keeping my spirits high throughout my Ph.D. work.

TABLE OF CONTENTS

LIST OF TABLES

LIST OF FIGURES

LIST OF ABBREVIATIONS AND SYMBOLS

ACN – Acetonitrile

Boc - tert-butyl Carbonate

CAC - Critical Aggregation Concentration

CuAAC - Copper-Catalyzed Azide-Alkyne Cycloaddition

DLS - Dynamic Light Scattering

dRI - Differential Refractive Index

DCM – Dichloromethane

DMF - N-N-Dimethylformamide

DMSO – Dimethyl sulfoxide

DP - Degree of Polymerization

EDA – Ethylenediamine

EPR - Enhanced Permeability and Retention

δ - Chemical Shift Relative to Tetramethylsilane

GPC - Gel Permeation Chromatography

HEK – Human Embryonic Kidney

LDBC - Linear-Dendritic Block Copolymer

MALS - Multi-Angle Light Scattering

MeOH – Methanol

NMR - Nuclear Magnetic Resonance

MA - Methyl Acrylate

M_n - Number-Averaged Molecular Weight

M_w - Weight-Averaged Molecular Weight

PAMAM - Polyamidoamine

PISA – Polymerization induced self-assembly

PCL - Poly(ϵ-caprolactone)

PDI - Polydispersity Index

Ph - Phenyl

RAFT - Reversible Addition-Fragmentation Transfer

R_h - Hydrodynamic Radius

TBE - Tertbutyl ether

TEM - Transmission Electron Microscopy

TFA - Trifluoroacetic Acid

THF – Tetrahydrofuran

CHAPTER I: INTRODUCTION

1.1 AMPHIPHILIC JANUS POLYMERS

Over the past few decades, amphiphilic Janus polymers have attracted interest in biomaterials for both fundamental and practical clinical applications. This growing interest is due to their different structure combinations and unique properties relative to conventional symmetric polymer systems.[1] Amphiphilic Janus polymers combine two different polymer segments (hydrophilic and hydrophobic) of varying degrees, sizes, and functionalities to obtain a single amphiphilic or hetero-functional macromolecule with characteristic features (Fig. 1).[2]

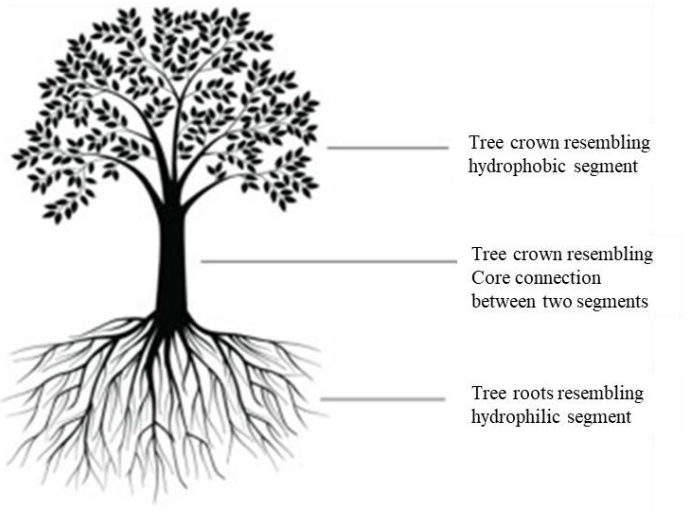

Figure 1. Structural homology of Janus dendrimers to a tree [1]

The first idea about Janus polymers was given in 1992 by the Nobel laureate Pierre-Gilles de Gennes. He described particles where one half of the surface is hydrophobic while the other

part is hydrophilic, being called Janus grain.[3] The first example of Janus polymers was reported in 1993 by Jean M.J. Fréchet, using the convergent approach to synthesize poly(benzyl ether) dendrons.[4] The literature reports several types of Janus polymers: Janus dendrimers, Janus type block copolymers, Janus type linear dendritic block copolymers are the most common and well-studied systems. [5-8]

The broken symmetry of Janus polymers offers the opportunity to form complex self-assembled polymer materials and presents a new class of properties that are presently inconceivable for homogeneous or symmetrical polymers. Due to their unique features, Janus polymers have a promising future in pharmaceutical and biomedical fields, as seen from their recent interest in forming supramolecular hydrogels, enabling polymer nanoparticle delivery systems such as micelles and vesicles for drug encapsulation.[9-10]

1.2 POLYMERIC NANOPARTICLES IN NANOMEDICINE

Nanotechnology accommodates many parts of human life, including agriculture, transportation, electronics, communication, and medicine. Nanotechnology involves understanding and controlling matter at the nanoscale dimension (1 to 100 nm) to create new particles and devices.[11-13] Nanomedicine is the application of nanotechnology in medicine and health care research, which aims to engineer materials at the nanoscale to develop new drugs and delivery systems that mimic or aid understand the cellular processes at the molecular level.[14]

Polymeric nanoparticles are one of the most well-studied organic strategies for nanomedicine. To determine the ideal nanoparticle system for more effective targeted delivery of therapeutic applications, particle size, morphologies, surface charge, polymer material choice, and formulation techniques are all research areas of interest. In addition, attention is given to the

polymer backbone's geometry, resulting nanostructure, and toxicity of the material. Some relevant advanced applications in nanomedicine involve efficient drug delivery, disease diagnosis, molecular imagine, tissue engineering, theranostics, etc. (Fig. 2).[15-17]

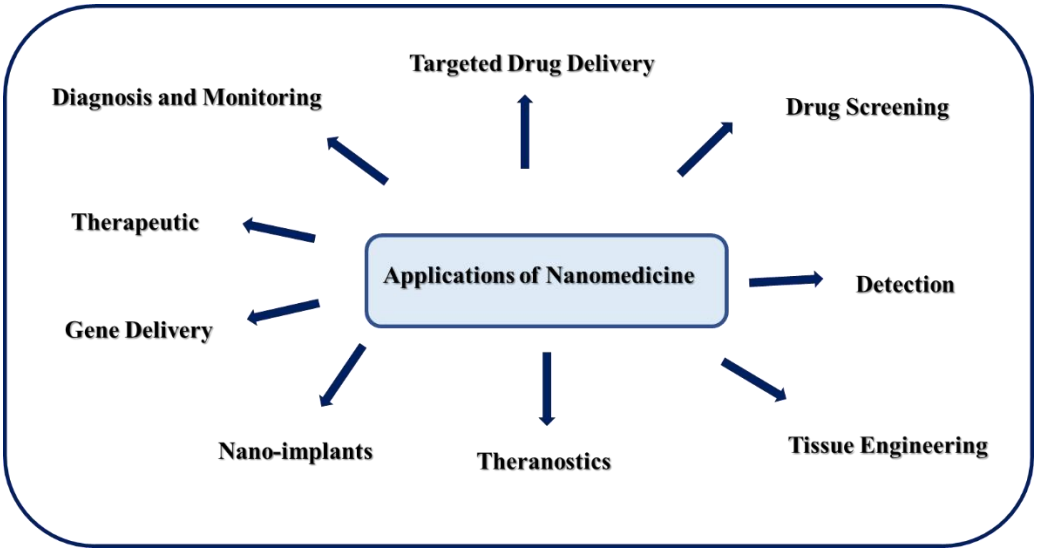

Figure 2. Applications in nanomedicine

In early nano-based applications, initial uses of polymeric nanoparticles were built on non-biodegradable polymers, such as poly(methyl methacrylate) (PMMA), polyacrylamide, and polyacrylates. Polymeric nanoparticles were designed such that the particles exhibit rapid and efficient clearance through the body via urine or feces. However, inflammatory reactions and chronic toxicity were observed using non-biodegradable materials, and thus an adjustment in focus to biodegradable polymers occurred. Biodegradable polymeric nanoparticles became of interest due to reduced toxicity concerns and the ability to influence specific drug release kinetic patterns.[18]

1.3 THE TUMOR MICROENVIRONMENT

During that time, discoveries were made regarding nanoparticle entry, circulation, and cellular uptake. It was found that nanoparticles in the 20–400 nm particle size range can

accumulate at tumor cells via the passive targeting mechanism or enhanced permeability and retention (EPR) effect (Fig. 3).[19] The vascular endothelial lining of the tumor-tissue blood vessels shows significant gaps between adjacent cells, and cancer tissues lack adequate lymphatic drainage simultaneously.[20] Therefore, the drug-loaded nanoparticles are leaked from the blood circulation through these gaps into the tumor tissue, where they are retained for a prolonged period due to the defective lymphatic system, resulting in passive targeting of cancer tissues.[21]

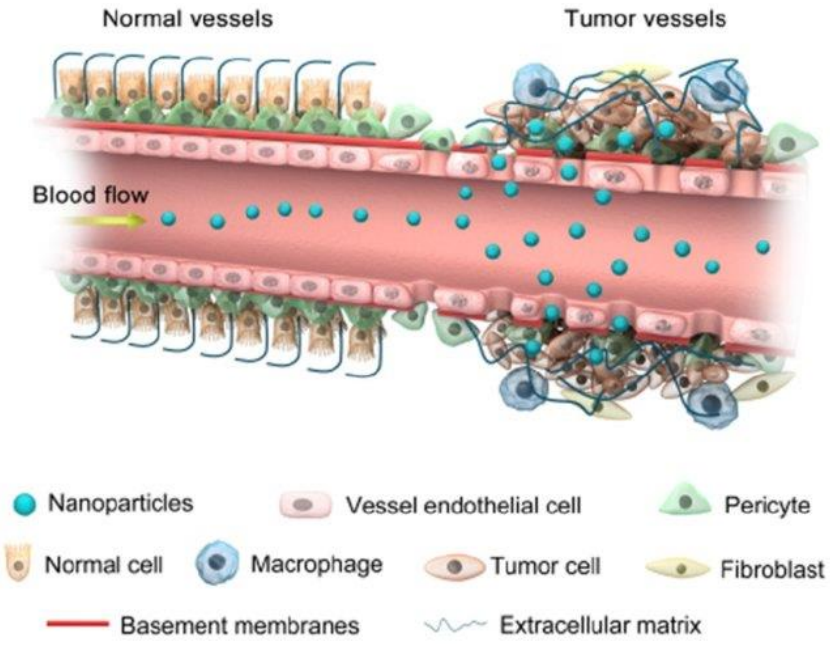

Figure 3. Enhanced permeability and retention (EPR) effect [20]

As the field began to grow, two crucial modes for using and applying polymeric nanoparticles in nanomedicine arose. The first method involved encapsulating therapeutic agents in polymer aggregates.[22-25] The second method included conjugating or coupling the therapeutic agent onto the polymer backbone. Today, the most clinically relevant formulations obtained via the conjugation method are polymer-drug conjugates, polymer-protein conjugates, and dendrimer drugs.[26-30] This approach increases the molar mass of the therapeutic agent, assures prolonged circulation times, and enhances the solubility of hydrophobic therapeutics.[31,32] But, the lack of

versatility limits the applications of this strategy because only a handful of therapeutic/imaging agents could preserve their original properties after a covalent conjugation.[33-35] On the other hand, encapsulation offers accessibility for a vast range of guest molecules. This method utilizes noncovalent interactions such as hydrophobic interactions, hydrogen bonding, and electrostatic interactions to load the guest molecule into a polymeric nanoparticle.[36,37] This approach is effective in synthetic and therapeutic efficacy because the therapeutic/imaging agent does not involve a direct chemical reaction to load or release. The properties of the polymeric nanoparticles directly affect the success of the method. The selected polymeric system can form stable nanoparticles with biocompatible morphologies and sizes while encapsulating the therapeutic agent. Additionally, it can be equipped with targeting and releasing strategies. [38-40]

1.4 POLYMERIC NANOPARTICLES CHARACTERIZATION

Particle size is one of the main determinants of biodistribution and retention of the nanoparticles in target tissues. For size determination, dynamic light scattering (DLS) is commonly used.[41,42] DLS measures the Brownian motion of nanoparticles in suspension and relates its velocity, known as translational diffusion coefficient (D_t) to the size of nanoparticles according to the Stokes−Einstein Equation 1.

$$D_h = \frac{K_B\, T}{3\, \pi\, \eta\, D_t} \qquad (1)$$

Where D_h represent the hydrodynamic diameter (particle size), K_B is Boltzmann's constant, T is thermodynamic temperature, and η is dynamic viscosity.[43] The polydispersity index (PDI) is used to evaluate the average uniformity of a particle solution, and larger PDI values correspond to a larger size distribution in the system. PDI can also indicate nanoparticle aggregation along with the consistency and efficiency of particle surface modifications throughout the particle sample.[44]

A PDI value from 0.1 to 0.25 indicates a narrow size distribution, and a PDI value greater than 0.5 indicates a broad distribution.[45] DLS assumes a spherical shape for nanoparticles; therefore, it is important to validate this assumption via microscopic examination. Transmission electron microscopy (TEM) is a microscopy technique in which an electron beam is transmitted through a suspension on a grid to procedure an image of nanoparticles. TEM provides high-resolution images of nanoparticles with sample preparation that is unlikely to disturb the morphology.

The surface charge of the nanoparticles is usually expressed as zeta potential, which is commonly measured by laser Doppler electrophoresis. This technique evaluates the electrophoretic mobility of suspended nanoparticles in a media and measures the potential at the boundary of the outer layer. Generally, particles with zeta potential more positive than +30 mV or more negative than −30 mV have colloidal stability maintained by electrostatic repulsion.[46] There have been reported studies that explain cationic nanoparticles are better internalized into the cells due to the negative charge cell surface, while neutrally or negatively charged nanoparticles are less efficiently internalized by the different cells.[47]

The critical association or aggregation concentration (CAC) or critical micelle concentration (CMC) can be used to evaluate the stability of self-assembled nanoparticles. The CAC, or CMC, is the concentration at which a self-assembled particle or micelle associates/dissociates.[48] This value provides a quantitative measure of the physical stability of nanoparticles. A relatively low CAC/CMC indicates a more stable micelle system than a high CAC/CMC. In other words, nanoparticles with a low CAC/CMC can resist dissociation upon dilution in the blood.

CAC/CMC can be measured using various detection methods, such as chromatography, conductivity, surface tension, light scattering, and fluorescent probes.[49-53] The most commonly

used method to measure CAC/CMC is to utilize fluorescence probes, such as pyrene, to indicate micelle dissociation. Pyrene is a polycyclic hydrophobic aromatic hydrocarbon that partitions in self-assembled nanoparticles' hydrophobic domain during assembly.[54] When a nanoparticle dissociates, pyrene is exposed to water, showing a different fluorescence profile than when in the hydrophobic environment of the nanoparticles. Therefore, the CAC/CMC can be determined by monitoring the change in the fluorescence profile of pyrene, defined as the concentration at which a drastic band shift is observed. In addition, light scattering is used to determine CAC/CMC. This technique measures the count rate (the intensity of scattered light in DLS), proportional to the number of nanoparticles in solution when nanoparticles size is constant. The count rate is plotted against nanoparticles concentration. The CAC/CMC is defined as the concentration above which the count rate shows a linear increase with the concentration of the components of nanoparticles.[55] The CAC/CMC measurement is a relatively simple and sensitive method of evaluating nanoparticles stability. Still, a disadvantage is that the application is limited to micelles and self-assembled nanoparticles, whose formation is influenced by concentrations of the components.

Confocal microscopy and flow cytometry are generally used to study the cellular uptake of nanoparticles. These methods require nanoparticles to be labeled with a fluorescent marker, which is done by encapsulation or conjugation. When the aim is to track nanoparticles, it is desirable to label the nanoparticles with a fluorescent marker and confirm the stability of the dye-loaded nanoparticles in a solution similar to physiological fluid. Preferably, a drug and a nanoparticle should be separately labeled so that the drug delivery capability of the nanoparticles may be accurately evaluated.

1.5 POLYMER SELF-ASSEMBLY

Morphologies resulting from polymer self-assemblies are directly associated with the physical properties of each polymer segment and mainly depend upon the hydrophobic and hydrophilic ratio of the polymer. Based on the theories of self-assembly established by Israelachvelli et al.,[56] the effect of inherent molecular curvature on the packing of polymer chains leads to these morphological outcomes. The packing parameter (p) defined in Equation 2 combines polymer properties to predict the curvature and the prepared morphologies.[57]

$$p = \frac{v}{a_e L_c} \qquad (2)$$

Here, v is the volume of the hydrophobic chain, a_e is the equilibrium area per molecule at the aggregate interface, and L_c is the length of the hydrophobic chains.

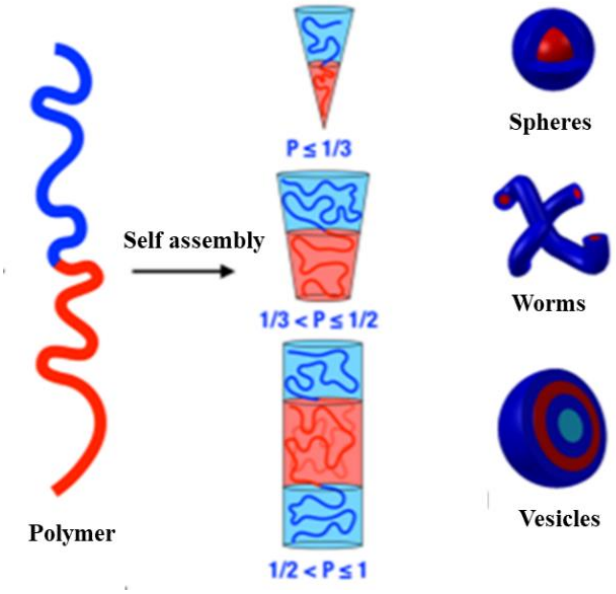

Figure 4. The different morphologies obtained by targeting different packing parameters [57]

Lower hydrophobic content results in a high curvature of the hydrophilic portion, resulting in micelles where p ≤ 1/3. On the other hand, a low-curvature system, resulting from many

favorable Van der Waals interactions, results in a vesicle morphology where p > 1/2. When the p-value is between 1/3 and 1/2, resulting in the formation of worms (Fig. 4). By taking advantage of this phenomenon, Janus polymers can be engineered to achieve the desired morphologies by simply changing the hydrophobic to hydrophilic weight ratio. However, p does not account for the kinetics of particle formation, which results in several experimental considerations. Several research groups [58,61] have determined that self-assembling amphiphilic polymers undergo a kinetic pathway where micelles are formed, elongate into tubes/worms, and eventually pinch off into vesicles. This corresponds to either additional material incorporated into the nanoparticle or fusion of micelles. Worms are the least mechanically stable morphology, especially as they lengthen. This free energy penalty can be removed by the polymer spontaneously folding into vesicles. It requires sufficient material with a large enough hydrophobic core to aggregate into a bilayer vesicle.

Micelles and bilayer vesicles are biologically mimic morphologies, so they have a higher potential as nanocarriers inside the body. Both are spherically shaped nanoparticles that comprise a hydrophobic core (assembly of hydrophobic blocks) and a hydrophilic corona (outer shell). These morphologies offer an optimal drug delivery system for therapeutic agents. The hydrophilic shell enhances the stability of the nanocarrier in the blood by providing steric protection, and the hydrophobic core can carry hydrophobic molecules with high loading capacity. [62-66]

1.6 BIOIMAGING

Bioimaging is one of the powerful techniques to gain insights into biological processes and detect malfunctions inside the body. Over the last few decades, several bioimaging techniques were established to create images of organs, veins, and cells, such as magnetic resonance imaging (MRI), positron emission tomography (PET), ultrasound imaging, and computerized tomography

(CT). However, the search for time-dependent, cost-effective, and safe bioimaging techniques with an excellent resolution continues. Fluorescence imaging allows a pathway to visualize the biological processes from the cellular down to the molecular level in a non-destructive way. Fluorescence-based diagnosis of diseases and fluorescence image-guided surgery has been shown to be successful applications.[67-68] There are several types of bioimaging probes that have been reported in the literature. Fluorescent organic dyes can exhibit high photoluminescence quantum yields (PLQYs), and a large diversity of dyes with adjustable optical characteristics are easily available. However, those small organic molecules usually exhibit poor (photo)stability, and photobleaching frequently creates problems.[69-73] The stability of the fluorescent probes can be improved by the use of inorganic quantum dots containing heavy metals like cadmium, lead, or indium, but the company of those heavy metals increases the cytotoxicity.[74]

1.7 MAGNETIC RESONANCE IMAGING (MRI)

MRI is an *in vivo* imaging technique that uses magnetic fields to visualize soft tissues within the body using a non-destructive way. MRI affords excellent resolution of soft tissues than CT and x-ray imaging, which makes it particularly useful in neurological, cardiovascular, and oncological imaging. MRI is presumed safer than PET, CT, and x-ray imaging because it does not utilize ionizing radiation. MRI uses strong magnetic fields (typically between 0.15 T and 3 T) to align the nuclear magnetic moments of magnetically active nuclei in the body with an external magnetic field.[75-77] Typical anatomical imaging focuses on ^{1}H hydrogen nuclei, the most abundant element in the body. When in the existence of an external magnetic field, the magnetic moment of the hydrogen nuclei precess around the external magnetic field at a frequency (known as the Larmor frequency) that is reliant on the gyromagnetic ratio of the nucleus and the strength of the external magnetic field, given by equation 3:

$$v = \gamma . B \qquad (3)$$

where v is the Larmor frequency (MHz), γ is the gyromagnetic ratio (MHz/T), and B is the magnitude of the external magnetic field.[78] The precession of nuclear magnetic moments is described as a quantum mechanical process. The individual nuclear magnetic moments will align themselves with the external magnetic field in two degenerate quantum states: either parallel or anti-parallel, because of the two possible spin states of the nucleus (±½). The ratio of nuclei in each state is roughly 1:1. However, the anti-parallel state is slightly more energetic than the parallel state. For this reason, there are generally more nuclei in the parallel state than the anti-parallel state; hence there is a net magnetic moment generated within the tissue parallel to the external magnetic field.[79] This vector is denoted as M_o and precesses at the same frequency as the nuclear magnetic moments. The energy difference between the two degenerate states is proportional to the external magnetic field strength; hence the magnitude of M_o increases as B increases.[80]

In addition to a strong external magnetic field, a transverse magnetic field perpendicular to the external field is applied to change the direction of the magnetic moment. This transverse magnetic field oscillates at the Larmor frequency of M_o, which enables it to interfere constructively with precession. The net effect is a change in the direction of M_o, with vector components M_L in the longitudinal (parallel to the external field) direction and M_T in the transverse (perpendicular) direction, as shown in Figure 5. Equilibrium magnetization (M_o) occurs as magnetic dipoles align with the external magnetic field (B_o) (Fig. 5a). Next, a transverse, oscillating magnetic field (B_T) is applied that causes a change in the direction of the equilibrium magnetization (Fig. 5b). This can be further fragmented down into a longitudinal (M_L) and a transverse (M_T) vector component (Fig. 5c). M_T decays and $M_L \rightarrow M_o$ in time as functions of the relaxation parameters, T_1 and T_2 (Fig. 5d).[86, 93] In time, M_L will approach the value of M_o due to random thermal motions of the

molecule. This is called spin-lattice relaxation, and the time required for this to occur is called the T_1 relaxation time. Additionally, M_T will decay as M_o is regenerated via entropic interactions with other magnetic dipoles. This process is called spin-spin relaxation and is quantified by the T_2 relaxation time. In cooperation, the T_1 and T_2 relaxation times are important parameters used to generate a magnetic resonance image.[81,82]

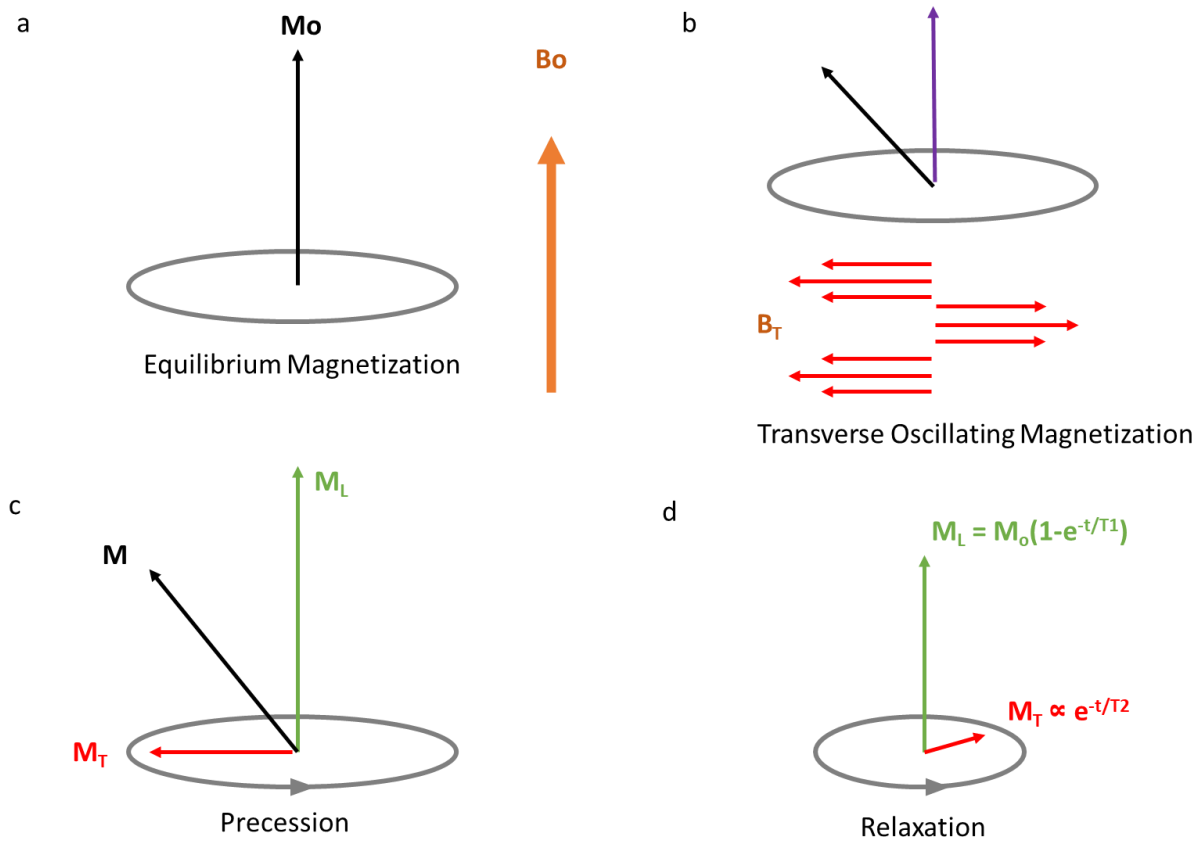

Figure 5. MRI excitation and relaxation phenomena

1.8 THESIS OUTLINE

The main goals of the research outlined in this thesis are to create libraries of novel amphiphilic Janus hybrid polymers, investigate their self-assembly, and evaluate their potential in biomedical applications. The project outlined in Chapter 2 summarizes the design, synthesis,

characterization, and evaluation of a library of biocompatible self-assembling Janus dendrimers (JDs) and their resulting nanostructures possessing either a cationic (NH_3^+), anionic (COO^-), or neutral (OH) surface. The project outlined in Chapter 3 summarizes the synthesis and application of dendritic macro chain-transfer agents (mCTAs) for in-situ self-assembly, known as polymerization-induced self-assembly (PISA). This study shows that our newly designed dendritic chain-transfer agents, mCTA-16OH and mCTA-8ala, were capable of performing PISA and producing amphiphilic linear dendritic block copolymers (LDBCs) in ethanol and water. The project outlined in Chapter 4 is an extended work from Chapter 3. Chapter 4 summarizes the one-pot polymerization synthesis of novel fluorinated Janus-type LDBC for a ^{19}F magnetic resonance imaging (MRI) agent. The results of this research outline have created robust and versatile synthetic strategies to engineer new libraries of Janus polymers, new knowledge in the self-assembly of amphiphilic LDBCs, and an approach to develop next-generation biocompatible nanocarriers.

CHAPTER II: STRUCTURAL AND SURFACE PROPERTIES OF POLYAMINIAMINE (PAMAM) -FATTY ACID-BASED NANOAGGREGATES DERIVED FROM SELF-ASSEMBLING JANUS DENDRIMERS

This chapter adapted from Loku Yaddehige, M.; Chandrasiri, I.; Barker, A.; Kotha, A. K.; Dal Williams, J. S.; Simms, B.; Kucheryavy, P.; Abebe, D. G.; Chougule, M. B.; Watkins, D. L. Structural and Surface Properties of PAMAM – Fatty Acid-based Nanoaggregates Derived from Self-assembling Janus Dendrimers. ChemNanoMat, 2020, 6 (12), 1833–1842. https://doi.org/10.1002/cnma.202000498. (See appendix D for permission license)

This project is a collaborative work between Dr. Chougule and Dr. Kucheryavy. The synthesis and characterization of dendrimers and nanoparticle characterization were performed by Loku Yaddehige, M. Synthesis and characterization of PAMAM hydrophilic dendron were done by Chandrasiri, I.; Barker, A. 2D NMR spectroscopy was done by Kucheryavy, P. The CAC analysis were performed by Williams, J. S. Cytotoxicity assay was performed by Kotha, A. K.

2.1 ABSTRACT

This study summarizes the synthesis, characterization, and evaluation of a library of biocompatible self-assembling Janus dendrimers (JDs) and their resulting nanostructure possessing cationic (NH_3^+), anionic (COO^-), and neutral (OH) surfaces, and their potential as biomaterials. Comprised of a PAMAM dendron as the hydrophilic portion and fatty acid (FA)

functionalized dendrons as the hydrophobic portion, the physicochemical characterization and in vitro cell viability of amphiphilic JDs were performed. Microscopy (TEM) and dynamic light scattering (DLS) analysis indicate the size (i.e., diameters) of spherical JD nanoaggregates ranging from 40 to 100 nm with zeta-potential values ranging from -17.9 to +58.7 mV corresponding to cationic, anionic, and neutral functionalized JDs. Furthermore, these systems exhibited spherical nanoaggregates with critical aggregate concentrations (CAC) ranging from 2.8 to 7.0 mg/L. At low concentrations (<200 μg/mL), JD's nanoaggregates showed minimal cell growth inhibitory properties in the in vitro testing, demonstrating their safety. The results of this study prove that a simple yet strategic combination of chemically distinctive dendritic segments can afford a versatile library of unique JDs nanoplatforms with excellent potential for biomedical applications

2.2 INTRODUCTION

In recent years, amphiphilic Janus dendrimers (JDs) have become a primary topic of supramolecular chemistry due to their flexible functionality and promising bio-organic capabilities.[83] Amphiphilic JDs are synthesized by combining hydrophilic and hydrophobic dendrons of varying generations, sizes, and functionalities to obtain a single amphiphilic or hetero-functional macromolecule with characteristic features. [84-88]

Employing the properties of JDs for the design and development of engineered nanoaggregates is particularly beneficial. When focusing on their applications in nanomedicine, [89] specific properties of the JDs can be utilized to develop biocompatible nanocarriers for drug therapy. Among such properties are the self-assembly and formation of various types of supramolecular nanoaggregates in water (i.e., tubes, micelles, and bilayer vesicles) and the specific tunability achieved through end-group modification of the dendron. [90-94] There have been

numerous reports on the biomedical applications of these unique polymeric structures and their nanoaggregates in the fields of drug conjugation, drug and gene delivery, solubility enhancement of hydrophobic drugs, and bioimaging.[95-101]

Interestingly, the position to utilize JDs as engineered nanoaggregates has been limited. These limitations are often due to surface properties that can affect particle size, surface charge, biodistribution, and cellular interaction.[92] For example, positively charged nanoaggregates have been reported to have higher cellular uptake in human cells due to a charge associated with the negative surface of cell membranes.[102] However, nanoaggregates possessing larger cationic charge densities have been reported to induce cell lysis and, as a result, are toxic to healthy human cells.[103] Alternatively, negatively charged nanoaggregates have been reported for higher circulation times in the bloodstream. [104] Recently, nanoaggregates with a neutral surface have become known as a delivery platform for therapeutics in in-vivo cancer models with minimal toxicity. [105-106]

In regards to size and morphology, it is well noted that nanoaggregates with diameters over 200 nm are inefficient in penetrating tumor tissue as such particle sizes exceed the penetration barrier of the enacted enhanced permeability retention (EPR) effect. [107-108] By a strategic approach toward developing nanoaggregates with controlled surface charge and particle sizes of 10 – 200 nm, these drawbacks can be minimized; thus, achieving safe and efficient engineered nanocarriers for biomedical application. [109]

Herein, we present the design, synthesis, characterization, and evaluation of cationic, anionic, and neutral functionalized polyamidoamine (PAMAM) – fatty acid (FA) amphiphilic JDs and their self-assembled nanoaggregates in aqueous media. In this study, we use biocompatible dendritic segments for the synthesis of novel JDs to minimize the common challenges of stability

and toxicity that traditional nanoaggregates often face. [110] In addition, we summarize the structural and surface properties of the nanoaggregates as well as an evaluation of biomedical efficacy. The dendrimers of this investigation, FA-PAMAM-NH_3^+, FA-PAMAM-OH, and FA-PAMAM-COO^- are presented in Figure 6.

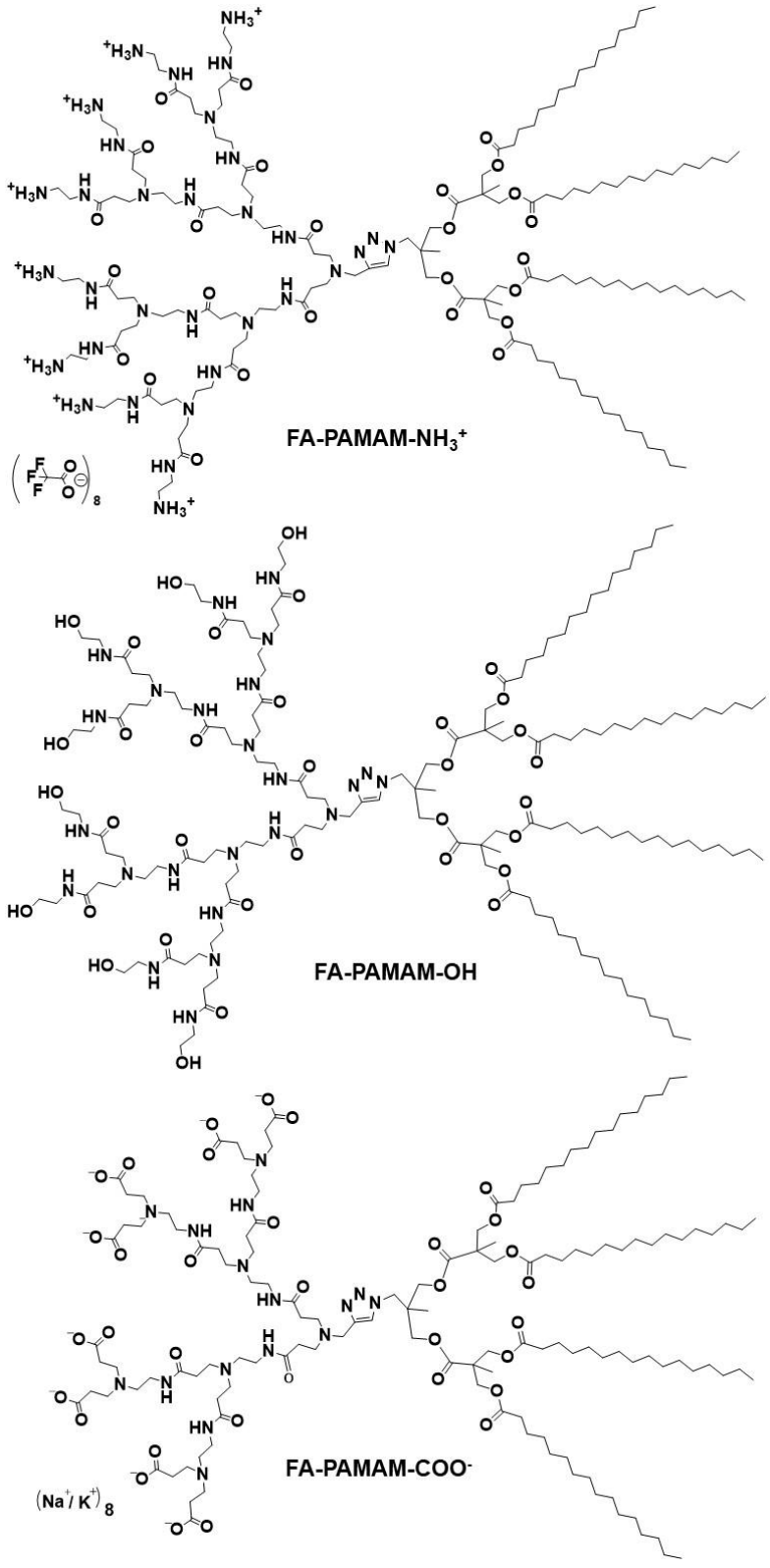

Figure 6. Structures of the FA-PAMAM-NH_3^+, FA-PAMAM-OH, and FAPAMAM-COO^- amphiphilic Janus dendrimers

In this report, we hypothesize that nanoaggregates formed from cationic (NH_3^+), anionic (COO^-), and neutral (OH) charge PAMAM– FA JDs will impart distinct properties and enable them for use in biomedical applications. As depicted in Figure 6, the hydrophilic block consists of a PAMAM dendron. PAMAM is a well-documented hyperbranched polymer and was chosen based on its synthetic accessibility allowing for a variety of functional groups to be readily incorporated. On the opposite segment of the dendrimer structure is the hydrophobic FA branch, which promotes self-assembly into nanostructures via the hydrophobic effect. These were systematically chosen because of their extended pedigree as biocompatible and biodegradable materials. In addition, their presence within the dendrimer is vital to the size, stability, and safety of the resulting nanoaggregate. [111-112]

The synthesis of our macromolecular library was confirmed via nuclear magnetic resonance (NMR) and gel permeation chromatography (GPC). Nanoaggregates were then formed in aqueous media, and the resulting structures were studied by dynamic light scattering (DLS) and transmission electron microscopy (TEM). The effects of surface variation were studied via in vitro cell viability using A549 luciferase expressing non-small cell lung cancer cells. The findings within this study show that a simple combination of unique dendritic segments can afford an exceptional self-assembling polymer platform whose supramolecular nanostructures can be utilized to maximize therapeutic accessibility.

2.3 RESULTS AND DISCUSSION

2.3.1 DESIGN AND SYNTHESIS

This study aims to synthesize and evaluate PAMAM– FA JDs with distinct surface properties for biomedical applications. The PAMAM portion was a logical choice for the

hydrophilic segment due to its extensive use in drug delivery and biomaterials. [113] The PAMAM structure consists of repeating amide segments, which increases biocompatibility and provides structural gaps to store smaller species via hydrogen bond interactions. [114] As the hydrophilic portion, various modifications can be made to the amine terminal groups to yield surface-functionalized nanoaggregates in aqueous media. For this investigation, we selected generation-3 (G3) PAMAM. Studies have shown that larger generations of PAMAM exhibit steric hindrance and crowding. [115-117] Smaller generations are too flexible, causing possible leakage of the drug payload. [118] Due to its amine surface, at specific pH levels (pH < 7.5), PAMAM-based nanoaggregates formed in aqueous media will possess positive/cationic surfaces. Although the design strategy presented here utilizes only a fourth of the typical PAMAM dendrimer, it is intuitive to expect that the cationic density of an amphiphilic JDs comprised of PAMAM will increase upon aggregation.

In turn, we introduce a neutral hydroxyl group to the surface of PAMAM G3 (FA-PAMAM-OH), which will afford nanoaggregates with a neutral surface in aqueous media. For additional comparison, we include a PAMAM G3 surface with carboxylic acid groups (FA-PAMAM-COO-), which can provide a negatively charged surface in PBS buffer at pH 7.4. The variation in surface properties described herein provides numerous advantages regarding the preparation of amphiphilic JDs, their surface-functionalized aggregates, and the potential biomedical application of these materials.

For the hydrophobic segment, we have employed lipophilic FA chains attached to 2,2-bis(hydroxymethyl) propionic acid (bMPA). FAs have been widely studied for their role in cell membranes and energy storage. [119] Because of their high availability in the human body, FAs are well known for their biocompatibility and biodegradability, making them suitable candidates for

developing nanocarriers for biomedical applications. [89-90] The terminal alcohol groups of bMPA allow for esterification under mild reaction conditions while providing an additional level of biodegradability and biocompatibility to the JDs and its resulting nanoaggregate. [120]

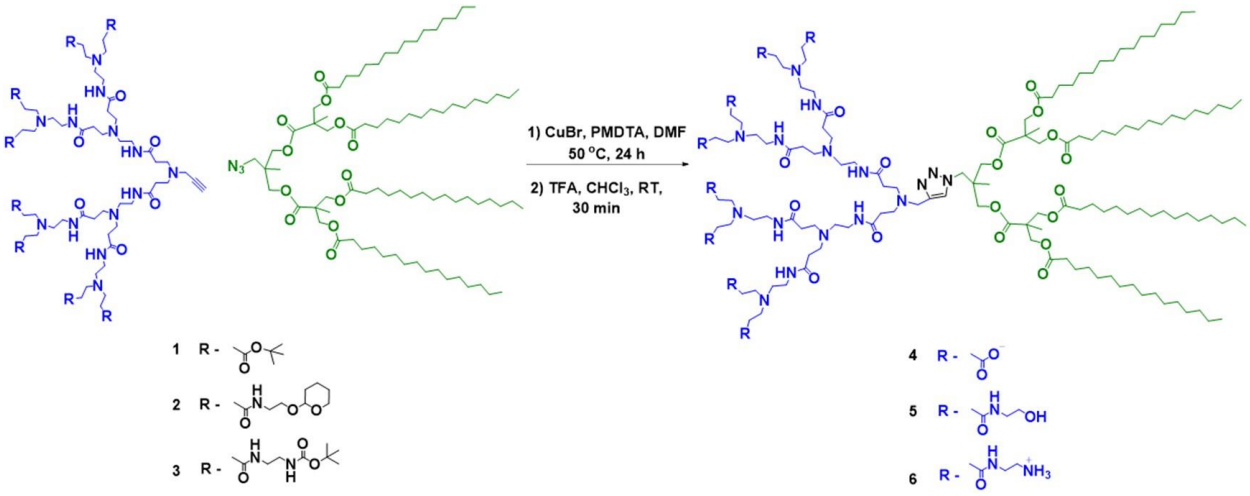

Figure 7. A general synthetic route for the preparation of amphiphilic JDs

A general synthetic scheme for the PAMAM-FA amphiphilic JDs, FA-PAMAM-NH_3^+, FA-PAMAM-COO^-, FA-PAMAM-OH, and their precursors, FA-PAMAM-BOC, FA-PAMAM-TBE, FAPAMAM-THP, is shown in figure 7. In our previous work, [113] we observed that amphiphilic block copolymers with 70:30 hydrophobic to hydrophilic ratio self-assemble into bilayer vesicles in water. Based on our observations as well as those of polymer physics,[114] the molar mass of JDs was designed to keep a 70:30 hydrophobic to hydrophilic weight ratio between the dendrons to yield more biologically relevant nanoaggregates. [121-123]

PAMAM dendrons were synthesized by a divergent method in which the growth of the dendron originated from a core functional group. Using propargyl amine as the focal point, Michael addition with methyl acrylate formed a half-generation dendron yielding G0.5. The reaction was followed by nucleophilic amidation with ethylenediamine to afford full-generation

dendrimers (Scheme 1-2, Appendix A). PAMAM G2 was treated with tertbutyl acrylate in methanol to obtain P-PAMAM-G3-TBE (1) with a 90% yield. PAMAM G2.5 was treated with ((tetrahydro-2H-pyran-2-yl)oxy) methanamine in methanol to obtain P-PAMAM-G3-THP (2) with 81% yield. PAMAM G3 dendron was treated with di-tertbutyl dicarbonate in methanol to obtain P-PAMAM-G3-BOC (3) with a 92% yield.

The hydrophobic dendron is synthesized by Malkoch esterification, [117] 1,1'-carbonyldiimidazole (CDI) is used to activate the carbonyl group of the bMPA and cesium fluoride (CsF) as a catalyst with azide focal point and bMPA as the monomer. The final step of the hydrophobic dendron involves FA attachment using palmitoyl chloride via esterification to obtain hydrophobic dendron A-MPA-4-FA with a 91% yield (Scheme 3-4, Appendix A). The presence of the azide group was confirmed by FTIR using stretching vibrations at 2102 cm^{-1} (Fig. 47, Appendix A).

The hydrophobic and hydrophilic dendrons were linked by copper(I)-catalyzed azide-alkyne cycloaddition (CuAAC) [119] to obtain the three JD precursors. The hydrophobic dendron was used in excess to increase the reaction yields and simplify the purification of the final JD. Indeed, as the final JD and hydrophilic dendron have large molar mass differences, it can be easily separated from the final JD by size exclusion chromatography. This method, which is a variation of previously published methods, [124] allowed the three JDs to be synthesized with yields between 79 - 86%. The JDs precursors were thoroughly characterized (*vide infra*) to confirm structure and purity as sequential and final reactions would yield target JDs not requiring additional purification. Accordingly, removal of the protecting groups BOC, TBA, and THP using trifluoroacetic acid (TFA) afforded the final amphiphilic JDs: FA-PAMAM-NH_3^+, FAPAMAM-COO^-, and FA-PAMAM-OH.

2.3.2 POLYMERIC MATERIALS CHARACTERIZATION

The final products were characterized by ^{1}H and ^{13}C NMR spectroscopy (Fig. 48-53, Appendix A), HSQC, HMBC, and GPC. Precursor FA-PAMAM-TBE is considered here as a representative example to discuss the characterization results (Fig. 8). An overlay of NMR spectra shows characteristic peaks of PAMAM (1.4, 2.19–3.69 ppm) and bMPA-FA (1.27, 5.15 ppm) (Fig. 48, Appendix A). Both segments are present in the spectrum of the coupled product for the precursors. With respect to the hydrophilic block, the peaks corresponding to the protons in the α positions of the triazole are shifted downfield in comparison with those in the starting propargyl-PAMAM dendron (from 3.62 to 4.39 ppm). Concerning the hydrophobic block, the peak corresponding to the protons in the α position of the triazole is also shifted downfield (from 3.32 to 4.29 ppm) in comparison to the starting azide FA dendron. All other resonance signals remain unchanged, and a perfect correlation is observed for the signal integrations corresponding to the hydrophilic and hydrophobic dendrons. In regards to the connection point, ^{1}H NMR signal peak at 7.82 ppm corresponds to the hydrogen attached to the triazole ring (H-4) (Fig. 49, Appendix A). In the ^{13}C NMR spectrum (Fig. 50, Appendix A), signals at 125 ppm and 142 ppm corresponding to the carbon atoms of the triazole C-4 and C-5. The HSQC spectrum confirms the presence of triazole ring by exhibiting a signal at 7.82 ppm in ^{1}H NMR spectrum corresponding to H-4 and 125 ppm in ^{13}C NMR corresponding to C-4. The same ^{1}H NMR signal in the HMBC spectrum further confirms the formation of the triazole ring by showing a cross peak at 142 ppm in 13C NMR corresponding to C-5 and H-4 (Figure 8). A similar analysis was done for the other two JDs, and further information is given in appendix A (Fig 54-65).

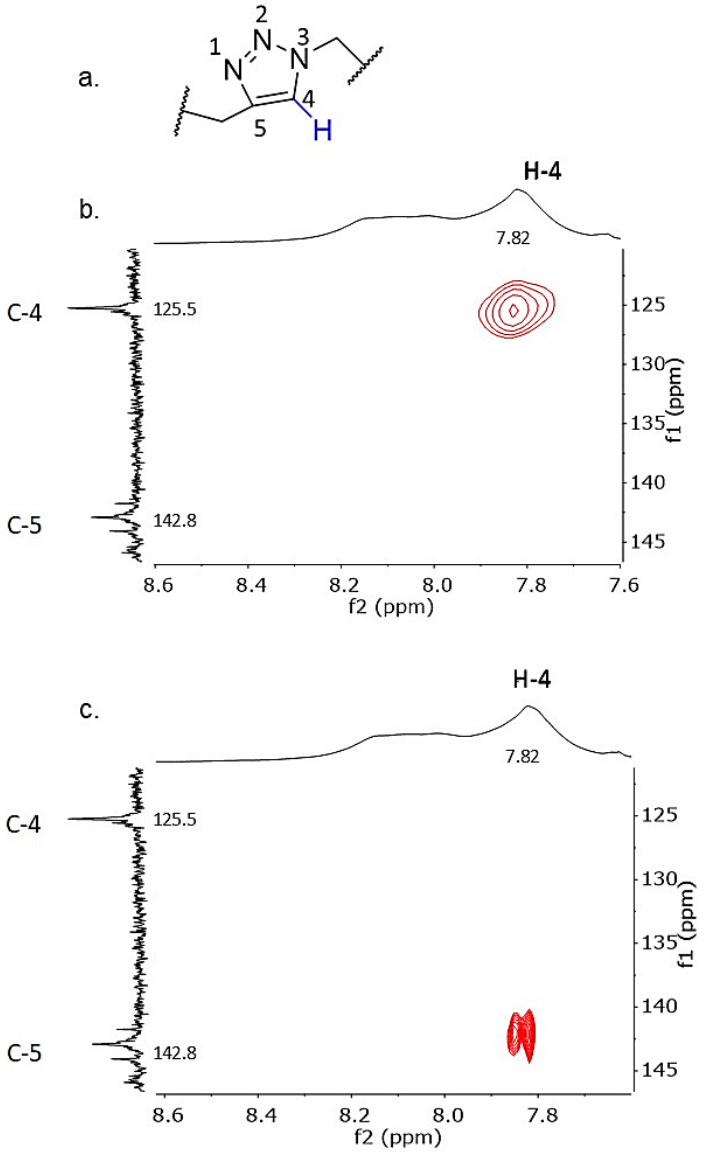

Figure 8. (a) Structure of the triazole ring (b) HSQC NMR spectra of FAPAMAM-TBE (c) HMBC NMR spectra of FA-PAMAM-TBE

Due to the reduced solubility of amphiphilic JDs in THF, protected JD precursors were used for the molecular weight characterization. Molecular weight characterization for the JD precursors is given in Table 1. GPC of protected JDs confirmed the absence of free dendrons that had not reacted during the CuAAC process by having a single peak in the chromatographs. Shoulders appearing adjacent to the main peak in the GPC trace are due to the branching nature of

the dendrimer affecting its elution in the column. [126] (Fig. 66-68, Appendix A). The dispersity values range from 1.02 – 1.06, which indicates the presence of monodisperse polymers. With the precursors confirmed, acid deprotection affords cationic, anionic, and neutral amphiphilic JDs FA-PAMAM-NH_3^+, FA-PAMAM-COOH, and FA-PAMAM-OH.

Table 1. Molecular weight characterization of the JDs by GPC with THF as the elution solvent

Sample	M_{th} g mol^{-1}	M_n g mol^{-1}	M_w g mol^{-1}	Đ
FA-PAMAM-G3-BOC	3785	3625	3801	1.05
FA-PAMAM-G3-TBE	3096	3118	3289	1.06
FA-PAMAM-G3-THP	3665	3716	3781	1.02

M_{th}, M_n, M_w, Đ denote theoretical molar mass, number average molar mass, weight-average molar mass, and dispersity, respectively.

2.3.3 SELF-ASSEMBLY AND MORPHOLOGY

The aggregates of FA-PAMAM-NH_3^+ (cationic JD) were formed in water, and FA-PAMAM-COO^- (anionic JD), FA-PAMAM-OH (neutral JD) were formed in PBS buffer using the nanoprecipitation method.[127-129] Tabulation of nanoaggregate characteristics is provided in Table 2. The critical aggregation concentration (CAC) of the JD nanoaggregates was evaluated by the pyrene probe method.[130] The CAC denotes the concentration at which self-assembled particles are associated or dissociated. In the methodology we used, pyrene was employed as a solvatochromic fluorophore. Pyrene is a lipophilic polycyclic aromatic hydrocarbon, which moves into the compartments in the lipophilic portion of the nanoaggregate during self-assembly. [131] Pyrene shows different fluorescent profiles when they are in the lipophilic portion and water, which leads to the determination of the CAC. This value affords the physical stability of nanoaggregates.

Table 2. CAC values, the average hydrodynamic diameter of the nanoaggregates by TEM and DLS (in number and intensity), and surface charge

Sample	CAC / (mg/L)	R_{TEM} (nm)	R_{hDLS}(nm)	PDI	ζ-potential (mV)
			Number		
FA-PAMAM-G3-NH_3^+	7.0 ± 0.9	55.6 ± 4.1	57.8 ± 16.7	0.19	56.1 ± 6.5
FA-PAMAM-G3-OH	3.3 ± 0.8	47.5 ± 9.2	41.0 ± 9.0	0.47	8.5 ± 1.6
FA-PAMAM-G3-COO^-	2.8 ± 0.5	104.8 ± 4.8	93.1 ± 15.9	0.88	-17.9 ± 2.6

For each of the nanoaggregate sets formed, the CAC values were less than 10 mg/L. The CAC for the amphiphilic JDs ranged from 2.8 to 7.0 mg/L providing relatively low CAC values, and they are comparable to those found in the literature and correlate to the candidacy of these amphiphilic JDs as potential biomaterials.[132] Although the CAC values for each of the amphiphilic JDs are low; there is a significant difference in the CAC based upon the cationic, anionic, and neutral surfaces. Cationic JD has the highest CAC value (7.0 mg/L), and anionic JD has the lowest CAC (2.8 mg/L), with the neutral JD having a value of 3.3 mg/L. A low CAC value illustrates a more stable nanoaggregate system and a resistance to dissociation upon dilution in the blood.[43] Based on CAC values, the results indicate that anionic and neutral JDs form more stable nanoaggregates compared to cationic JD.

The particle size of the amphiphilic JD nanoaggregates in aqueous media was studied by dynamic light scattering (DLS). Anionic JDs have a larger particle size with the number average diameter of 93.1 ± 15.9 nm, an intensity average diameter of 102.2 ± 14.1 nm with 0.882 PDI (Fig. 71-72, Appendix A). For the neutral JD, the number average diameter 41.0 ± 9.0 nm, intensity average DLS data gave two distributions, small hydrodynamic diameters (53.3 ± 12.4 nm), and

larger hydrodynamic diameter (308.2 ± 85.1 nm) with 0.469 PDI (Fig. 73-74, Appendix A). Cationic JD shows a similar particle size to neutral JD with a number average diameter of 57.8 ± 16.7 nm, an intensity average diameter of 103.7 ± 40.3 nm with 0.191 PDI (Fig. 69-70, Appendix A). Based on the PDI value, cationic JDs and neutral JDs shows a narrow size distribution where PDI values range from 0.1 to 0.5, and anionic JDs show a broad distribution with a PDI value greater than 0.5. All particle sizes are below 200 nm, which indicates that they have the potential to escape physiological barriers, take advantage of the EPR effect, possess high potential for prolonged circulation and reduced filtration by the liver and spleen. Overall particle size analysis indicates that all three JDs produce nanoaggregates within a favorable range for cellular uptake. [133]

To examine the morphology of the aggregates and to support the particle size data obtained from DLS, TEM analysis was carried out. Cryo-TEM allowed us to observe the dendrimer aggregates as they are in aqueous solutions and to understand the morphology of the self-assembled aggregates. Based on the cryo-TEM data (Fig. 9), all amphiphilic JDs show spherically shaped nanoaggregates that validate our DLS data.

Cationic JDs show a spherical aggregate (Fig. 9a) with an average particle size of 55.6 nm, which is ideally correlated with the average diameter (57.8 nm) obtained by DLS. The neutral JDs show spherical aggregates with an average particle size of 47.5 nm, and clusters of nanoaggregate aggregates (Fig. 9b) are observed, which explains the bimodal distributions of particle size (53.2 nm, 308.2 nm) that were obtained by DLS. For the average diameter of 53.2 nm, we observed a lower intensity peak when compared to the average diameter of 308.2 nm (Fig. 74, Appendix A). This is due to the bimodal particle size distribution.

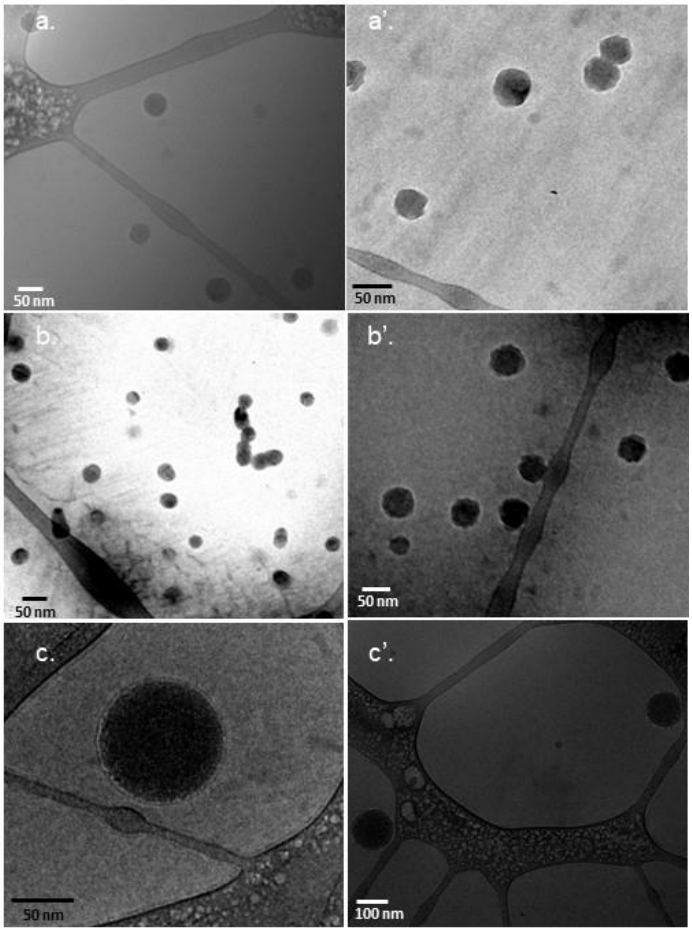

Figure 9. Cryo-TEM images with utilizing uranyl formate as a contrast agent for (a) FA-PAMAM-NH_3^+, (b) FA-PAMAM-OH, and (c) FA-PAMAM-COO^-

DLS is relatively weaker at analysing bimodal or multimodal particle size distribution because the signal of the smaller particle is lost due to the signal intensity of a spherical particle with a radius r is proportional to r^6; as a result, the intensity of smaller particles tends to be weakened by the larger particles.[43] Anionic JDs show similar spherical aggregates (Fig. 9c) with an average particle size of 104.8 nm, which correlates with the average hydrodynamic diameter (93.1 nm) obtained by DLS. As expected, we observe more aggregations in the FA-PAMAM-OH due to their neutral surface. Unlike the cationic and anionic JDs, there is no charge separation

between nanoaggregates, which leads to having more aggregates with the support of hydrogen bonding between nanoaggregates.

A critical aspect of the study is to assess the surface charge of aggregates formed from the amphiphilic JDs. Generally, particles with positive surface charges below 15 mV display the ideal properties such as decreased macrophage uptake,[133] higher tumor retention, and longer circulation time.[45] In addition, the ideal surface charge depends on factors such as cell type, cellular uptake mechanism, and intracellular localization of nanoaggregates.[134] There have been reported studies that explain the ability of cationic nanoaggregates to stay in a tumor for a prolonged time compared to anionic and neutral charged nanoaggregates. Because favorable electrostatic interactions can be made between cationic nanoaggregates and the negatively charged cell membrane at the stage of cellular uptake.[47] The surface charge is commonly expressed as a zeta potential, which is measured by the laser Doppler electrophoresis technique. The cationic JD has a zeta potential of 56.1 ± 6.5 mV in the MilliQ water at pH 7.0. The anionic JD and the neutral JD have zeta potentials of, -17.9 ± 2.6 mV, 8.5 ± 1.6 mV, respectively, in PBS solution at pH 7.4. The zeta potential values confirm the cationic, anionic, and neutral nature of nanoaggregates. Among cationic, anionic, and neutral nanoaggregates, neutral nanoaggregates have the lowest CAC, a particle size of about 50 nm, and a zeta potential below 15 mV.

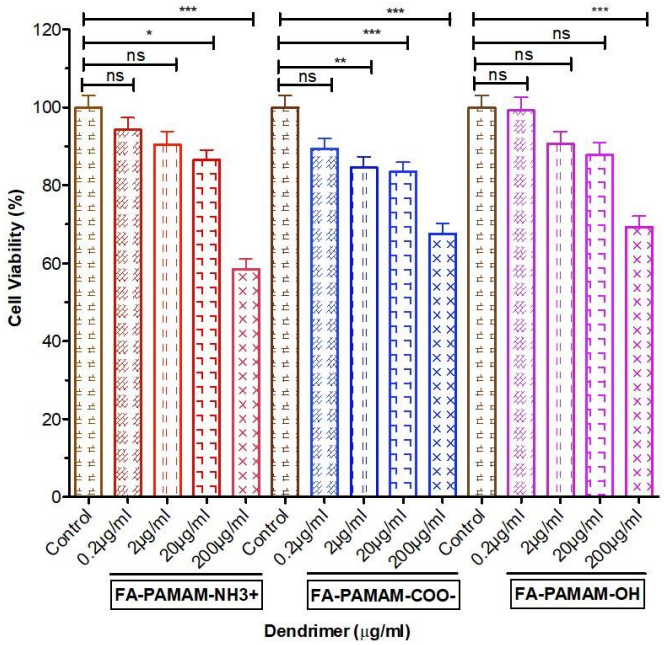

Figure 10. In vitro cell viability profile of A549 luciferase expressing non-small cell lung cancer cells after treating with FA-PAMAM-COO^-, FA-PAMAM-NH_3^+, FA-PAMAM-OH dendrimers (0.2 μg/mL – 200 μg/mL) for 72 h. Cell viability assay was performed by MTT assay as described in Materials and methods. Values presented as mean ± standard deviation of two independent experiments (n = 24).

2.3.4 BIOCOMPATIBILITY AND CELL VIABILITY

After physiochemical characterization, we evaluated the effects of JD nanoaggregates on cell viability against non-small cell lung cancer cells using the MTT assay. The composition, size, and charge of the nanoaggregates play a critical role in cell interactions. The development of nanoaggregates with particle sizes of less than 100 nm is challenging. But our design and synthetic strategy assisted in controlling the size of less than 100 nm and shape and relatively low CAC values of these nanoaggregates. Such satisfactory properties demonstrate their potential to overcome common physiological barriers.[135]

For in vitro cell viability studies, we used A549 Luciferase expressing non-small-cell lung cancer cells. This cell line was chosen considering the potential future uses of the nanoaggregates

for drug and gene delivery in the treatment of lung cancer. In addition, luciferase expressing cells are useful tools for evaluating siRNA loaded nanomedicine for gene silencing capability.[136]

Based on surface charge values, we expected lower cell viability for cationic nanoaggregates, which have higher surface charges. While for neutral and anionic nanoaggregates, we expected much higher cell viabilities relative to the cationic nanoaggregate. The three JD nanoaggregates showed more than 80% cell viability at 0.2 – 20 μg/mL concentration range, which indicates that they are biocompatible (Fig. 10). We noted that the inhibition of cell viability was concentration-dependent. At 20 μg/mL, the cell viability of FA-PAMAM-OH was 87.92 ± 15.1%, FA-PAMAM-COO^- showed 83.53 ± 11.68% and FA-PAMAM-NH_3^+ showed 86.55 ± 12.69% cell viability (all concentrations tested were above the CAC of these nanoaggregates).

When the nanoaggregate concentration is increased further, cell viability starts decreasing. At 200 μg/mL, FA-PAMAM-OH showed the highest cell viability (69.25 ± 14.26%) when compared to FA-PAMAM-COO^- (67.55 ± 13.2%) and FA-PAMAM-NH_3^+ (58.49 ± 12.46%), which indicates that these positively charged dendrimers show higher inhibition of cell viability. Unquestionably, comparatively lower cell viability was expected for the cationic JD nanoaggregates. This is due to their cationic charge density compared to negatively or neutrally charged JDs and potentially higher uptake.[134] The positively charged dendrimer interacts with negatively charged cell membranes, thus inducing cell viability. However, particle sizes and secondary aggregates can also contribute to such observations. The neutral and anionic polymers show a minimal charge to charge interaction with cells.

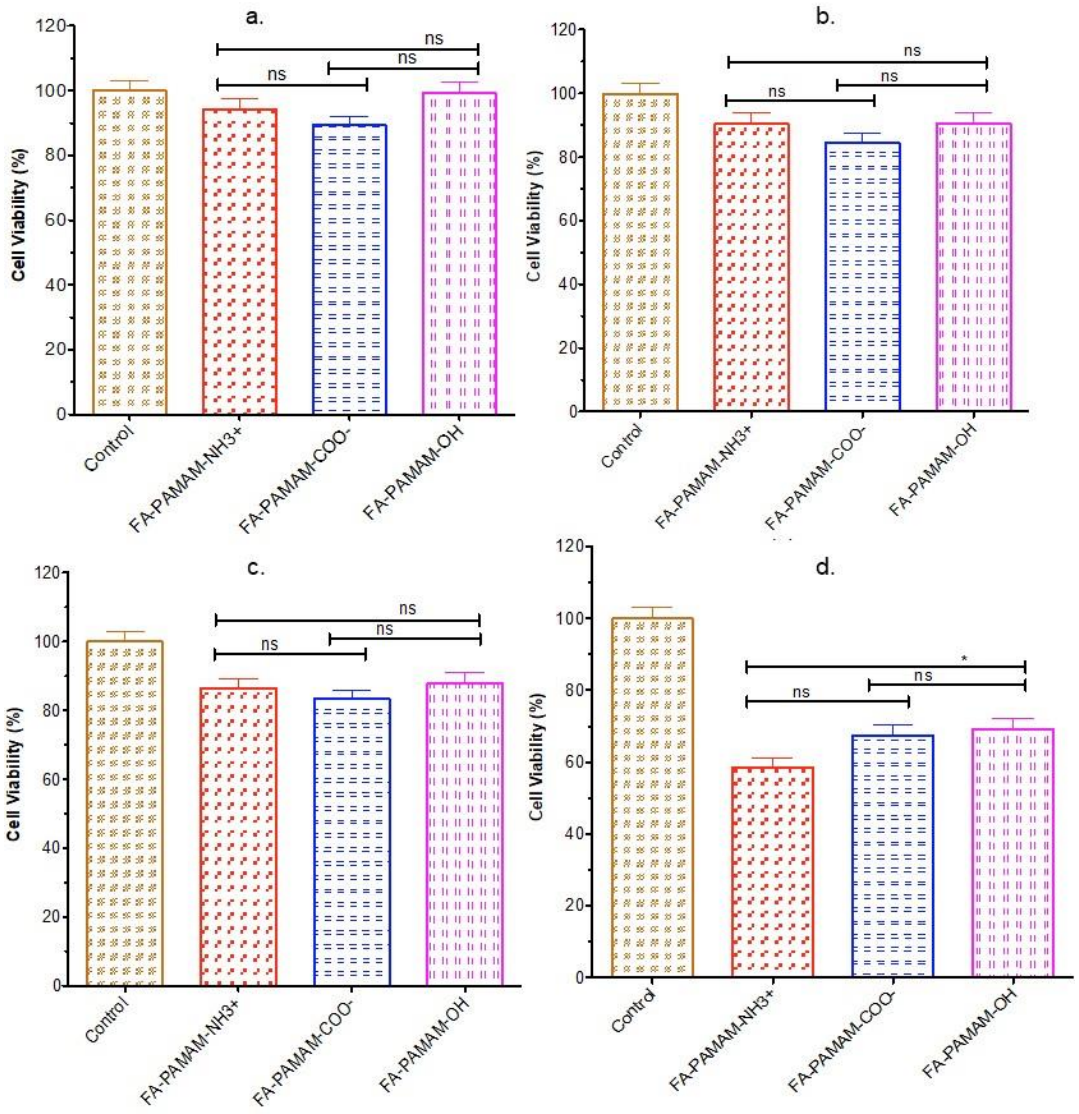

Figure 11. Statistical comparison of FA-PAMAM-COO^-, FA-PAMAM-NH_3^+, FA-PAMAM-OH dendrimers a) 0.2 μg/mL, b) 2 μg/mL, c) 20 μg/mL, d) 200 μg/mL) after 72 hrs treatment against A549 luciferase expressing non-small-cell lung cancer cells. The in vitro viability of dendrimers was performed as mentioned in materials and methods. Values presented as mean ± standard deviation of two independent experiments (n = 24)

In statistical analysis, when compared with a cell line without polymer treatment (control), FA-PAMAM-NH_3^+ showed no statistically significant difference in cell viability at 0.2 μg/mL and 2 μg/mL. However, at concentration of 20μg/mL and 200 μg/mL, it showed significant difference (*P<0.05, ***P<0.001 respectively). For FA-PAMAM-COO^-, at 0.2 μg/mL, there was no

statistically substantial differences but the three additional concentrations (2 μg/mL, 20 μg/mL and 200 μg/mL) showed noteworthy difference in cell viability, **P<0.01, ***P<0.001, ***P<0.001 respectively. FA-PAMAM-OH also did not show statistical difference at low concentrations but at 200 μg/mL it showed considerable differences ***P < 0.001 relative to un-treated control cells (Fig. 11).

Comparatively, FA-PAMAM-COO^-, FA-PAMAM-NH_3^+, and FA-PAMAM-OH JD nanoaggregates at concentrations less than 20 μg/mL showed a non-significant difference in the viability (P > 0.05, Fig. 11a-d). However, at higher concentrations, there was a major difference between FA-PAMAM-NH_3^+ and FA- PAMAM-OH (P < 0.05). Similar to our findings, Navath et al., 2010 and Kannan et al. 2004 found that concentrations of 1 to 100 μg/mL of PAMAM dendrimer showed minimal effect on cell viability in A549 human lung epithelial carcinoma cells [50-52] despite utilizing a full dendrimer relative to the partial structure use herein. It is essential to note that the increase in JDs concentration enhances the formation of secondary aggregations in the media due to an increased chance of collision between nanoaggregates.[136] This presumably causes FA-PAMAM-NH_3^+ to have a significant difference in cell viability with the support of the higher surface charge. Similarly, cell viability depends on the concentration of JDs along with other factors, i.e. time of exposure, end functionality groups, and cell type.[51] The JDs nanoaggregates warrant further studies to elucidate the interaction with cells and mechanism of inhibition of viability.

2.3.5 CONCLUSIONS

A library of PAMAM – FA JDs with distinct physicochemical properties (cationic, anionic, and neutral charge) were successfully synthesized and characterized. The nanoaggregates

comprised of JDs were spherical with sizes of less than 200 nm and surface charge values ranging from -17.9 to +58.7 mV. The CAC for the amphiphilic JDs ranged from 2.8 to 7.0 mg/L, providing relatively low CAC values indicating stable nanoaggregates. In the A549 luciferase expressing non-small-cell lung cancer cell viability assay, the JD nanoaggregates up to 20 μg/mL concentration showed an insignificant effect on cell viability, highlighting the biocompatibility of the resulting nanoaggregates. When the concentration of JDs is increased, cell viability decreases depending on the charge on Janus dendrimers, showing the highest inhibition of cell viability by the positively charged FA-PAMAM-NH_3^+. Overall results indicate that these JDs and their resulting nanoaggregates have high potential as vectors for drug and gene delivery in treating various diseases. Surprisingly due to low surface charge, ideal particle size and low CAC value, neutral nanoaggregates show the best morphological properties for biomedical application. Further experiments are needed to analyze the extent of drug and gene delivery, intracellular uptake and trafficking, and mechanism of cell growth inhibition.

2.4 EXPERIMENTAL

2.4.1 MATERIALS AND METHODS

Reagents and solvents were purchased from Sigma-Aldrich® or Acros® and used without further purification unless otherwise specified. Additional synthetic details, general procedures, and tabulations of materials characterization are given in appendix A. A549 luciferase expressing non-small-cell lung cancer cells were obtained as a gift from Dr. Mandip Singh, Division of Basic and Pharmaceutical Sciences, College of Pharmacy and Pharmaceutical Sciences, Florida A & M University, Tallahassee, FL, USA. HyClone DMEM (Dulbecco's Modified Eagle Medium)/low glucose with 1000 mg/L Glucose, 4.0 mM L-glutamine, and 110 mg/L sodium pyruvate, HyClone penicillin (10,000 units/mL)-streptomycin (10,000 μg/mL) solution were purchased from GE

Healthcare (Utah, USA). Fetal bovine serum (FBS) was obtained from R&D Systems (Minneapolis, USA). 2.5% trypsin (10X), without phenol red, was purchased from Corning (Virginia, USA). Thiazolyl blue tetrazolium bromide reagent was purchased from Sigma (Missouri, USA). Dimethyl sulfoxide (DMSO) was procured from Fischer Chemicals (NJ, USA).

2.4.2 CHARACTERIZATION OF INTERMEDIATES, PROTECTED DENDRONS AND AMPHIPHILIC JANUS DENDRIMERS

^{1}H NMR and ^{13}C NMR spectra of dendrons were collected on a Bruker Avance NEO spectrometer (Bruker, Germany), operating at 500 MHz, 400 MHz, or 300 MHz with $CDCl_3$ or MeOD as the solvent and TMS as an internal standard. HSQC and HSBC spectra were collected on a 400 MHz Bruker Avance NEO spectrometer with the following parameters: HSQC (TD/F1 = 256, TD/F2 = 2048) and HMBC (TD/F1 = 256, TD/F2 = 2048). Infrared spectra were obtained on a Bruker ALPHA-P spectrophotometer in ATR mode and recorded between 4000 and 600 cm^{-1}.

The molecular weight and PDI of the copolymers were determined by gel permeation chromatography (GPC). All the measurements were done using THF, and measurements were done at a flow rate of 1 mL/min at 35 ^{o}C. A Shimadzu 20A GPC system equipped with two PSS SDV analytical 1000 Å columns and a differential refractive index detector were used. Polystyrene standards (900–100,000 g/mol) were used for the calibrations curve, and the data was processed using Astra 7.0 software.

2.4.3 PREPARATION AND CHARACTERIZATION OF SELF-ASSEMBLED AGGREGATES

The amphiphilic JDs with the amine surface FA-PAMAM-NH_3^+(cationic), carboxylate surface FA-PAMAM-COO^- (anionic), and hydroxyl surface FA-PAMAM-OH (neutral) were formed into aggregates employing a nanoprecipitation method.[26,27] For the nanoprecipitation method, 100 μL THF was used as the organic solvent to dissolve 1 mg of JDs in a vial. The solution was added dropwise to a separate vial of MilliQ water at pH 7.0 (2 mL) for the NH_3^+ and 10 mM PBS buffer at pH 7.4 (2 mL) for COOH and OH while gently stirring. THF was evaporate under a stream of nitrogen. Nanoaggregate solutions were allowed to equilibrate for 12 h before further study. Nanoaggregate sizes and ζ-potentials measurements were carried out on a Malvern Instrument Zetasizer Nano ZS using a He–Ne laser with a 633 nm wavelength, a detector angle of 173º at 25 ºC. The size measurements were performed in triplicate for each sample at 0.5 mg/mL concentration to ensure consistency. The morphological study of the nanoaggregates formed from the JDs was carried out by cryogenic-TEM using a JEOL 1250 TEM operated at 100 kV to collect the TEM images using a Gatan Orius 831 bottom mounted CCD camera.

For the measurement of the critical aggregation concentration (CAC), pyrene (1.7 mg, 8.41 μmol) was dissolved in 3 mL of acetone, and 40 μL of the solution was added to 40 mL of deionized water. A series of concentrations of the nanoaggregate suspension ranging from 10^{-8} mg L^{-1} to 10^2 mg L^{-1} was prepared by dilutions of 2 mL per sample. Pyrene solution (2 mL) was added to each vial, and these solutions were equilibrated for 48 h in a dark area. The fluorescence spectra were obtained on a Varian Cary fluorometer from Agilent Technologies. An emission wavelength of 390 nm was used for pyrene, and the excitation spectra were recorded from 300 to 380 nm. The ratio of emission intensities at 338 and 333 nm was graphed as a function of the log of the

concentration. The CAC was calculated as the concentration at the intercept of the lines for the two linear regions of the obtained graphs.

2.4.4 CELL VIABILITY ASSAY

Cell viability assay of the nanoaggregates was performed using an established protocol.[28] Briefly, A549 luciferase expressing non-small-cell lung cancer cells were seeded at a density of 10^4 cells/well in a 96-well microtiter plate in complete DMEM medium (supplemented with 10% FBS, 100 units/mL penicillin, 100 μg/mL streptomycin). After 24 h incubation in a CO_2 incubator (humidified atmosphere of 5% CO_2) at 37 ± 0.5 ^oC, complete DMEM media was removed from wells and varying concentrations (0.2 μg/mL – 200 μg/mL) of the JDs nanoaggregates and the medium was added to the wells. Cells were incubated for 72 h at 37 ± 0.5 ^oC in the CO_2 incubator. MTT reagent was prepared in PBS (pH 7.4) at 5 mg/mL concentration. In each well, 20 μL of MTT reagent was applied and incubated at 37 ± 0.5 ^oC for 4 h. Viable cells convert MTT reagent into purple-colored formazan crystals, and these formazan crystals were dissolved by adding 100 μL of DMSO. The absorbance was measured using a microplate reader (Bio-Tek, VT, USA) at 570 nm.

2.4.5 STATISTICAL ANALYSIS

Multiple independent experiments were performed, and results were expressed as mean ± standard deviation. Significance of differences among groups determined by one-way analysis of variance followed by Tukey's multiple comparison test using GraphPad PRISM Version 5a (San Diego, CA, USA). Differences were considered statistically significant at $P < 0.05$ in all experiments. *P<0.05, **P<0.01, ***P<0.001[29].

CHAPTER III: POLYMERIZATION-INDUCED SELF-ASSEMBLY USING A DENDRITIC CHAIN TRANSFER AGENT FOR THE FORMATION OF LINEAR-DENDRITIC BLOCK COPOLYMERS AND THEIR AGGREGATES

This project is a collaborative work with Williams, J. S. The design, synthesis, and characterization of macro chain transfer agents was performed by Williams, J. S. The kinetic experiments, nanoparticle characterization, and reproducibility were performed by Loku Yaddehige, M.

3.1 INTRODUCTION

Over the past few decades, nanoparticles created from amphiphilic linear-dendritic block copolymers (LDBCs) have been hailed as promising candidates for a variety of applications, including controlled release of drugs, bioimaging, catalysis, mineralization, and photochemistry.[137-140] There is considerable attention has been given to optimizing, developing, and finding efficient routes to formulate block copolymer nanoparticles to fulfill the demands of biological applications. The most commonly used method to create nanoparticles involves polymerization, characterization, purification, and reconstitution in a water-miscible non-selective solvent before adding to water, usually at very low concentrations (<1 wt%).[5] The final step in this process is known as nanoprecipitation.[141] Prud'homme and co-workers developed a high yield production of nanoparticles using the flash-nanoprecipitation (FNP) process. FNP promotes nanoprecipitation of organic actives and blocks copolymers dissolved in a water-miscible solvent

by rapid mixing with water. FNP is a kinetically driven method in which nanoparticle size and monodispersity depend on the degree of mixing. Under the optimized conditions, FNP can produce high-quality, monodisperse nanoparticles in high quantity.[142-144] Winter and co-workers demonstrated an electrospray-assisted interfacial instability process (Aero-IS) as a scalable method for producing block copolymer nanoparticles. Aero-IS involve using a coaxial electrospray arrangement with an inner flow of water-immiscible, organic solvent media containing the block copolymer and an outer flow of surfactant-rich aqueous solution media. Compound spray droplets ejected by the electrospray are taken in an aqueous media, forming a fine emulsion from which micellar nanoparticles are prepared via the IS method. [143- 145] These methods are still mostly practiced at the bench scale. The challenge remains to produce robust and efficient ways to prepare monodispersed block copolymer nanoparticles with controlled size, morphologies, and surface chemistry to fulfill the demands of biological applications.

Polymerization induced self-assembly (PISA) is a promising technology involving in-situ nanoparticle formation during the reaction.[146-148] PISA allows the production of copolymer-based nanoparticles of various shapes compared to other multistep assembly techniques mentioned above.[149] PISA consists of the chain extension of a solvophilic polymer, which is commonly done using reversible addition-fragmentation-transfer polymerization (RAFT), in which the solvophilic polymer acts as a macro chain-transfer agent (mCTA) (Fig. 12).[150] This chain extension is done with a monomer whose corresponding homopolymer is solvophobic. Thus, the hydrophobic effect drives in-situ self-assembly into traditional nanoparticle morphologies (micelles, worms, vesicles, lamellae, etc.).[151] The PISA method can be used to formulate libraries of nanoparticles varying in morphology using a simple one-pot reaction.

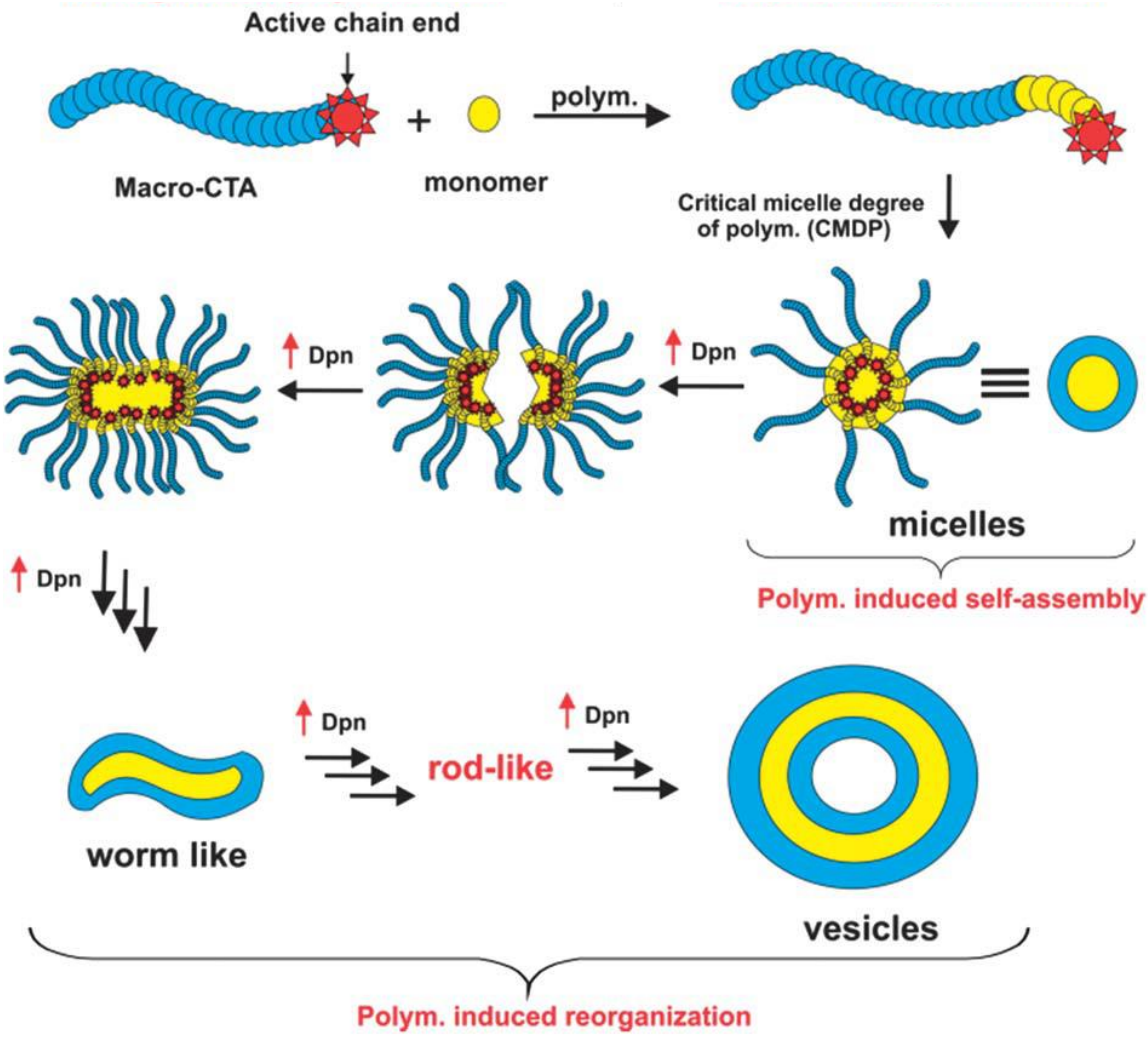

Figure 12. Schematic representation of the general mechanism for making various types of morphologies by RAFT mediated polymerization [151]

As the degree of polymerization (DPn) of the block copolymer increased (monomer conversion), the block copolymers assembled, forming into spherical micelles, worm-like micelles, vesicles, as determined by transmission electron microscopy (TEM) and dynamic light scattering (DLS) measurements. PISA is commonly performed using either a dispersion or emulsion mechanism. Dispersion is the most common, with a monomer soluble in the reaction solvent, which grows into an insoluble polymer in said solvent.[152] In the case of emulsion, neither the polymer nor monomer are soluble in the reaction media, and the reaction forms swollen

micelles encapsulating the monomer as the reaction proceeds. Emulsion polymerization has a strong industrial precedent, being the primary method of synthesizing latexes.[153]

The key difference between traditional latex synthesis and emulsion PISA is that the surfactant participates in the polymerization (often referred to as "surfactant-free" emulsion polymerization), and the controlled mechanism results in monodisperse particles as opposed to the polydisperse particles created in latexes.[154] This accelerates the reaction rate as the degree of polymerization increases, allowing many PISA reactions to reach completion within a few hours.[147] These reactions can be performed at concentrations of up to 50% by weight, decreasing solvent and heating energy requirements.[155] As a critical theoretical consideration, this also facilitates the real-time study of morphology as a function of lipophilic: hydrophilic mass ratio (LHR) with a much greater degree of granularity.

As we look to expand the advantages of PISA and aqueous RAFT, into the development of liner dendritic block copolymers (LDBCs) hybrid architectures. LDBCs combine the accessibility, and processability of linear polymeric chains with the regular and well-defined structure of dendritic segment, which have a precise number of peripheral groups that can be modified for the introduction of functionality in a controlled manner. Fréchet et al. introduced the LDBCs concept in the early 1990s, where a linear polymer is conjugated to a dendritic unit in a range of different configurations.[156] These systems can combine the expedient properties of linear and dendritic (i.e., branched) macromolecules, resulting in a composition of segments with different molecular architectures and chemical properties. Compared to traditional copolymers, the nanoaggregates formed from LDBCs possess enhanced mechanical properties and high monodispersity. [157]

3.2 RESULTS AND DISCUSSION

3.2.1 DESIGN AND SYNTHESIS

The work reported herein demonstrates the use of dendritic mCTAs for PISA and the formation of amphiphilic LDBCs (Fig. 13). Bis(hydroxymethyl) propanoic acid (bMPA) dendrons were chosen as the solvophilic mCTA.[158] Benzyl methacrylate (BzMA) was selected as the monomer and hydrophobic segment due to its literature precedent in PISA and favorable properties, including a glass transition temperature (T_g) that prevents assemblies from becoming kinetically trapped. [159] For PISA, the latter is vitally significant as several factors have been discovered which contribute to kinetic trapping. Specifically, the length of the solvophilic chain has been shown to affect access to complex morphologies. Additionally, a long solvophilic chain has been shown to limit morphologies to the formation of small spheres.[160] Therefore, the use of dendrons and their compact nature relative to traditional linear analogs commonly used in PISA are expected to lead to new nanoparticle morphologies, specifically, large nanostructures (e.g., giant vesicles) that have been inaccessible with the linear mCTAs.

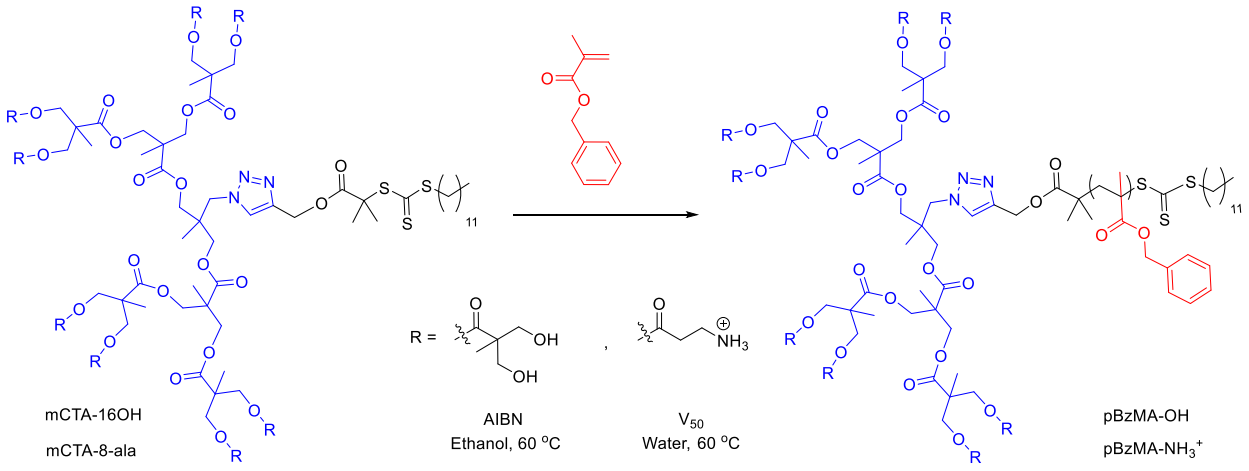

Figure 13. Structures and synthesis outline of the macro chain-transfer agents (mCTAs) and resulting polymers, pBzMA

The mCTA (mCTA-16OH) for our initial studies was synthesized divergently, using Malkoch's method to yield an azide-cored bMPA dendron, [149] followed by copper-catalyzed alkyne-azide cycloaddition (CuAAC) between the dendron and chain-transfer agent (Scheme 1-3, Appendix B). Leveraging previous work,[161-164] ethanol (EtOH) was chosen as a polymerization solvent as the mCTA and monomers are both soluble, but the resulting polymer (pBzMA-OH) and its aggregates are not. The mCTA: initiator ratio was fixed at 5:1 for this work due to a significant literature precedent of this ratio producing well-controlled PISA.[165] Following our previous work on LDBC self-assembly,[166] a monomer: mCTA feed ratio of 63:1 was chosen to obtain targeted degree of polymerization of 63 and expect hydrophobic to hydrophilic weight ratio is 83:17. Of the concentrations examined (10, 20, and 30% reactants by mass), 10 wt% showed no reaction, whereas 30 wt% showed significant flocculation before the reaction began. Therefore, 20 wt% was selected to form pBzMA-OH, and the reaction was monitored from 0 mins to 6 h. ^{1}H NMR signals corresponding to the monomer (a – 6.05 ppm, b- 5.68 ppm, c - 5.25 ppm) and product (c*, 4.87 ppm) were monitored as the reaction progressed (Fig. 14). Peak a and b decrease with time and peak c* increases, showing the polymerization progress. Transmission electron microscopy (TEM), and dynamic light scattering (DLS) afforded additional evidence to support polymerization and self-assembly of pBzMA-OH.

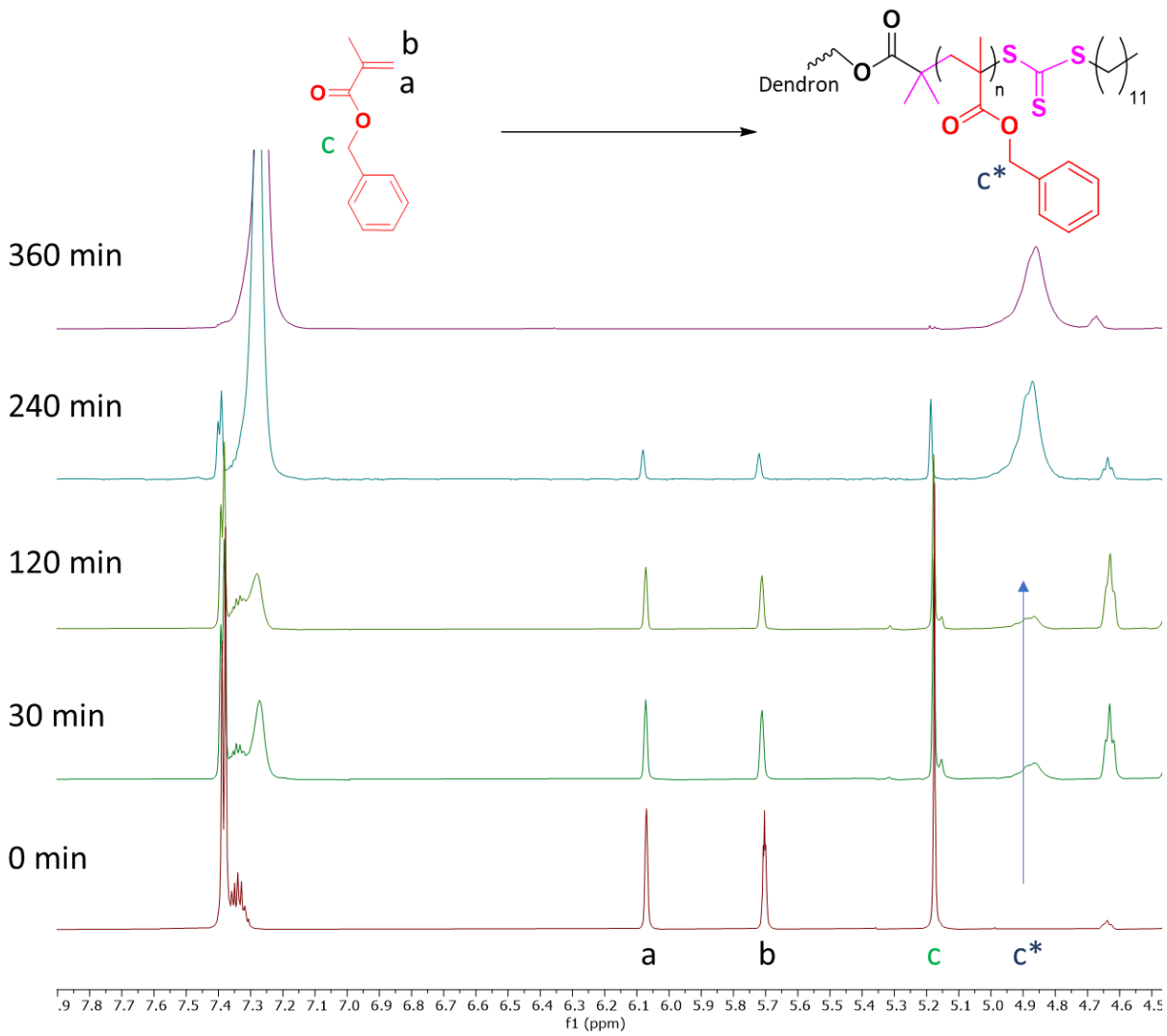

Figure 14. ^{1}H NMR spectra of the reaction of mCTA-16OH with BzMA to form pBzMA

BzMA polymerization using mCTA-16OH in EtOH showed a drastic increase in monomer conversion up to 30 min. This, of course, is due to the formation of large micellular structures that provide a core for solubilizing BzMA, increase the local concentration of the monomer, and increase polymerization kinetics.[159] After 360 min, the reaction goes to full conversion. (Fig 82, Appendix B). After 3 h, a DP of 53 was determined by NMR and GPC (Figs. 83-85, Appendix B), along with spherical particles believed to be micelles averaging a diameter of 51.8 nm according

to DLS (Fig. 15) and TEM (Fig. 16). At 4h, a DP of 60 was observed, with TEM showing micelles fusing into worms.

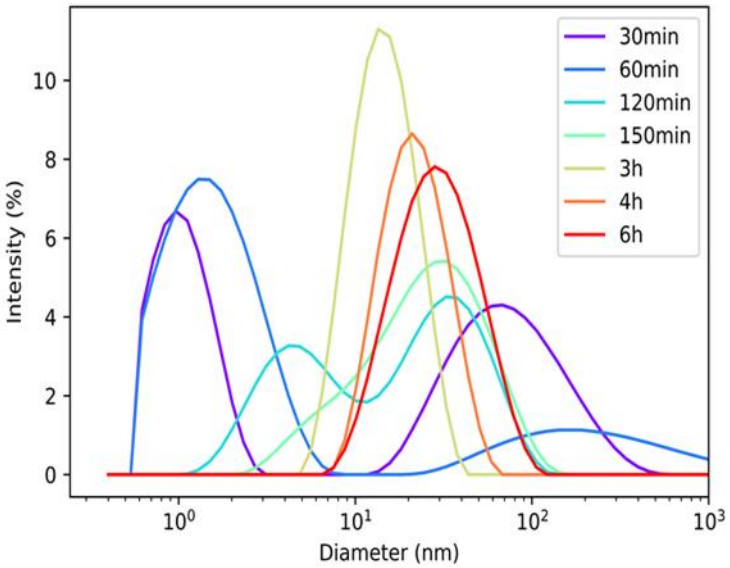

Figure 15. DLS of pBzMA-16OH at various reaction timepoints

Full polymerization (DP = 63) was observed after 6 h, with DLS and TEM suggesting morphological transitions from micelles to worms and finally to vesicles, as outlined in Figs. 15 and 16. These results follow the generally accepted polymer self-assembly mechanism: fluid-like structures followed by micelle formation, worms, then vesicles.[167-169]

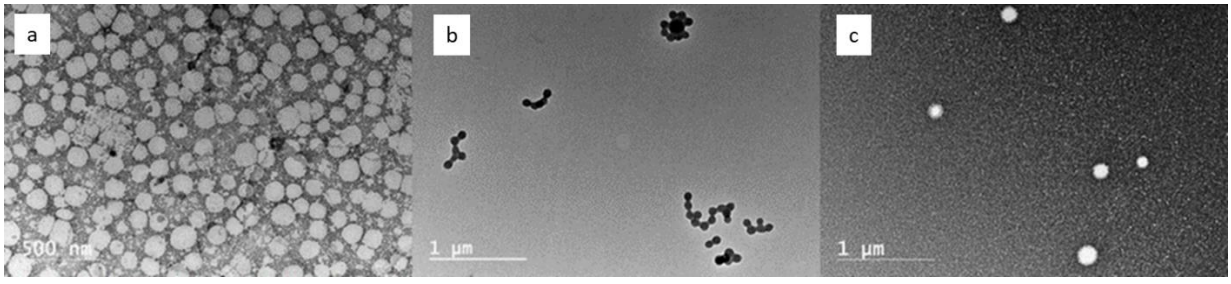

Figure 16. TEM of nanostructures formed at (a) 3 h, (b) 4 h, and (c) 6 h

Next, aqueous RAFT was attempted, as the resulting structures may find applications in nanomedicine, such as drug delivery and bioimaging applications. However, mCTA-16OH, as well as its dendritic precursor, were nearly insoluble in water. Therefore, an additional dendritic mCTA (mCTA-8ala) was synthesized, with alanine end-groups providing a positively charged dendron surface and enhanced water solubility. For the alanine pathway, the Boc groups were removed with trifluoroacetic acid (TFA), resulting in the trifluoroacetate salt of the cationic dendron (Scheme 4, Appendix B). Additionally, the water-soluble 2,2'-azobis(2-methyl-propionamidine) dihydrochloride (V50) was used as the initiator.[170]

Initial addition of BzMA monomer to a solution of mCTA-8ala in DI water resulted in phase separation, but upon degassing, the solution turned turbid, suggesting that mCTA-8ala may also act as an emulsion stabilizer. For this study, we found it imperative to maintain a low pH as alanine-functionalized bMPA has been shown to be relatively unstable at neutral/basic pH at elevated temperatures.[171] Given the pH sensitivity of this initiator, the pH of mCTA-8ala in water at a concentration of 0.37 M was maintained at about 1.7. ^{1}H NMR signals corresponding to the monomer (a - 6.10 ppm, b - 5.65 ppm, c - 5.28 ppm) and product (d* - 4.86 ppm) were monitored as the reaction progressed (Fig. 17). Peak a and b decrease with time and peak d* increases, showing the polymerization progress. Interestingly, the reaction of mCTA-8ala with BzMA exhibited a shorter incubation period of approximately 50 min possibly owing to a more reactive initiator compared to the dispersion PISA conducted with mCTA-16OH; however, it also suggests that this is not a seeded polymerization but a traditional emulsion polymerization.[39]

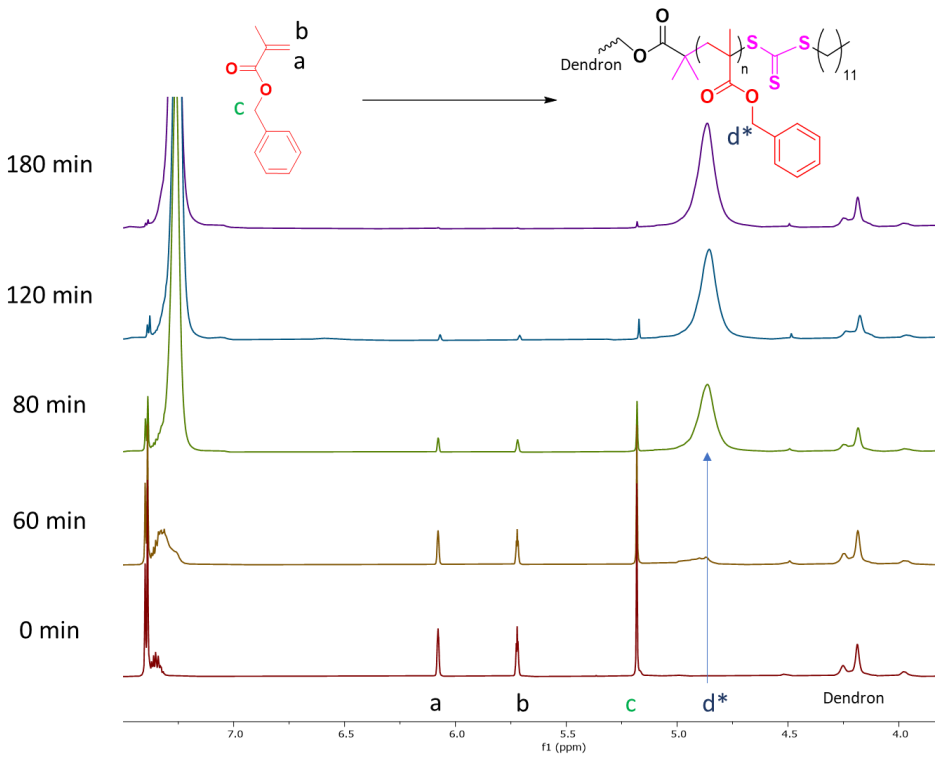

Figure 17. ^{1}H NMR spectra of the reaction of mCTA-8ala with BzMA to form pBzMA-NH_3^+

Monomer conversion was determined by ^{1}H NMR spectroscopy. Sampling involved diluting each extracted aliquot of reaction mixture into DMSO-d_6, a suitable solvent for both BzMA and pBzMA-NH_3^+. Figure 18 provides the monomer conversion vs. time profile of BzMA with mCTA-8ala. However, GPC was not attainable due to the solubility of the resulting polymer. We observed the formation of pBzMA-NH_3^+ with mCTA-8ala turning a milky white upon reaction progression, analogous to previous results with similar systems.[172]

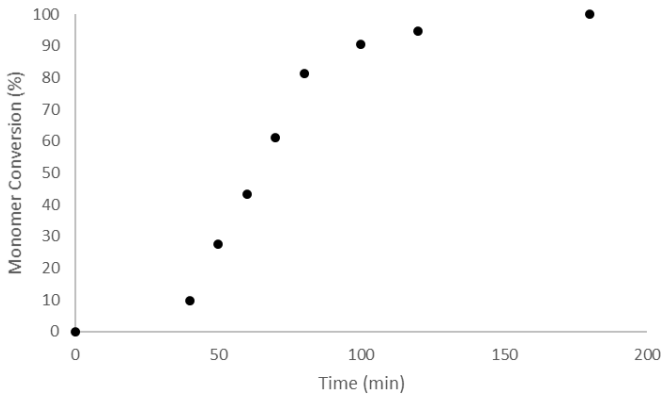

Figure 18. Monomer conversion versus time profile of pBzMA-NH_3^+ polymerization

The first 50 min show an incubation period with monomer conversion up to 10%. There is drastically increase in monomer conversion from 50 min to 120 min up to 90%. Then polymerization goes to >99% conversion within 3 h. We observed that the polymerization solution became cloudy-milky during the polymerization, indicating the formation of nanoparticles. The size of the nanoparticles was determined by DLS. The diameters of the nanoparticles obtained from the block copolymerization/self-organization were measured at different polymerization times using DLS.

DLS confirmed 28.2 nm micelles formed at the 60 min mark (Fig. 19). Particle sizes slowly increased to 58 nm and 66 nm at 70 min and 80 min, respectively, until 120 min, where the reaction rate again increases, likely due to micelles fusing into worm-like structures, which were further confirmed by TEM (Fig. 20). Then worm-like structures extended to vesicles at 180 min with a particle size of 169 nm.

Time / min	Size / nm
60	28
70	58
80	66
120	23 -41 257 – 746
180	169

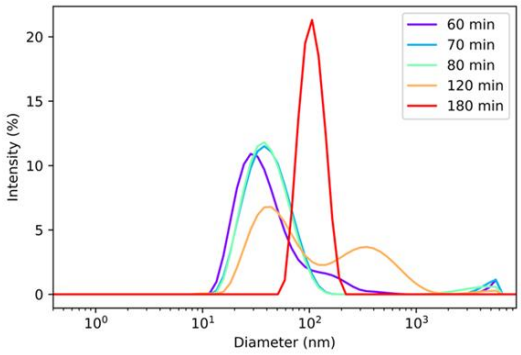

Figure 19. Kinetics of pBzMA-NH_3^+ polymerization, DLS taken over the course of the reaction

TEM of mCTA-8ala as an unreacted crude mixture showed self-assembly (Fig. 87, Appendix B), but revealed a large variety of morphologies with a high PDI, suggesting low stability of the resulting nanoaggregates. Such an observation is supporting evidence for mCTA-8ala as an emulsion stabilizer. Figure 20 shows the evolution of this polymerization of pBzMA-NH_3^+ from well-defined spherical aggregates, which are believed to be micelles (a) to micelle fusion followed by worm-like structure formation (b), and finally vesicle formation (c). These worms ranged in length from 257 to 746 nm, and from 23 to 41 nm in width. Given the relatively low stability of worms,[175] very few were observed, with the predominant morphology still being spherical aggregates. Figure 20c appears to be vesicles ranging from 169 nm in average diameter. Additionally, at 83:17 LHR would be expected to form vesicles exclusively. To the authors' knowledge, this is the first reported example of vesicle formation from emulsion PISA with a cationic mCTA.

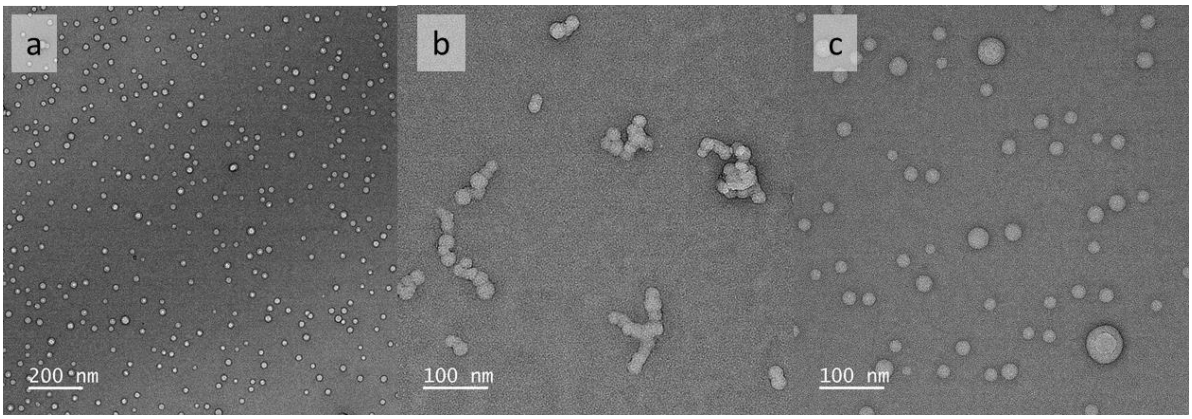

Figure 20. TEM images with utilizing uranyl format as a contrast agent for pBzMA-NH_3^+ over time a) 70 min b) 120 min c) 180 min time points

3.2.2 CYTOTOXICITY

It is crucial to evaluate the cytotoxicity of the nanoparticles to see their potential as therapeutic nanocarriers. We assessed the cytotoxicity of the pBzMA-NH_3^+ vesicles using the CellTiter-Glo luminescent assay, a homogeneous method to determine the number of live cells using ATP quantitation.[176] The viability experiment was done after exposing the HEK cells to six different nanoparticle concentrations for 24 h in a 96 well-plate at 37 ^{0}C. The results are expressed as percent viability and present as mean ± standard deviation of 4 independent experiments (Fig. 21).

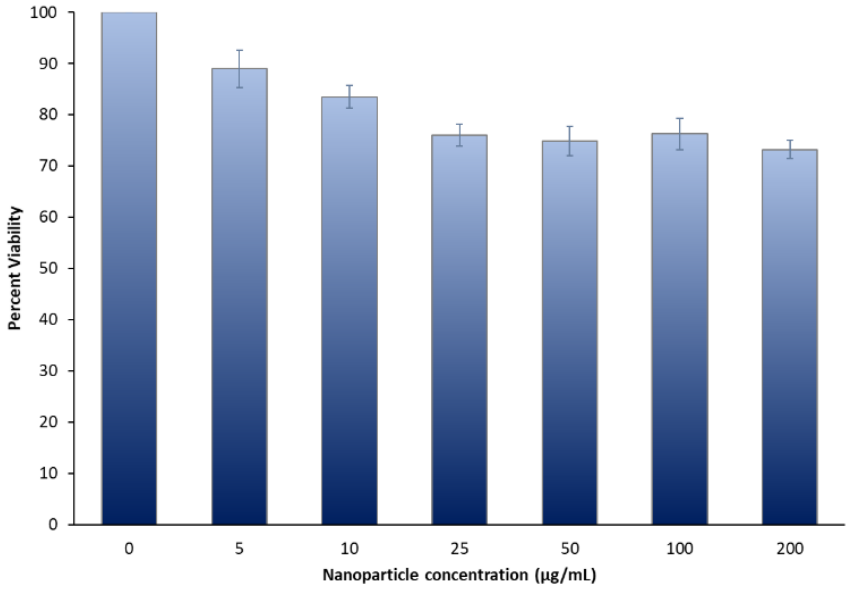

Figure 21. CellTiter-Glo luminescent assay HEK cells to six different nanoparticle concentrations for 24 h in a 96 well-plate at 37 ^{0}C.

The observed cell viability for nanoparticles was > 75 %, even at the highest concentration tested (200 µg/mL). The critical aggregation concentration (CAC) value for the pBzMA-NH_3^+ is 27 µg/mL. From 5 to 25 µg/mL, where polymer concentration below the CAC value showing precent cell viability above 75% confirming the nontoxic behavior of polymer below CAC. From 50 to 200 µg/mL, nanoparticles showing cell viability above 75% which indicates pBzMA-NH_3^+ vesicles are generally non-toxic to living human cells.

3.2.3 HEMOLYSIS

Hemolysis is the destruction of red blood cells (RBCs), which cause the discharge of the iron-containing protein hemoglobin (Hgb) into the blood plasma. A hemolysis assay is a high-throughput screen of nanoparticle hemocompatibility. In hemolysis assay, pBzMA-NH_3^+ vesicles are incubated in blood, and Hgb is discharged by damaged cells and transformed to red-colored cyanmethemoglobin by reagents.[177] Then, the undamaged RBCs and nanoparticles are separated by centrifugation, and the quantity of cyanmethemoglobin in the supernatant is measured by

spectrophotometry.[178] This measured absorbance is related to a standard curve to calculate the Hgb concentration in the supernatant. This Hgb concentration is then related to that in the supernatant of a blood sample treated with negative control (Triton-X) to obtain the percentage of hemolysis caused by nanoparticles.

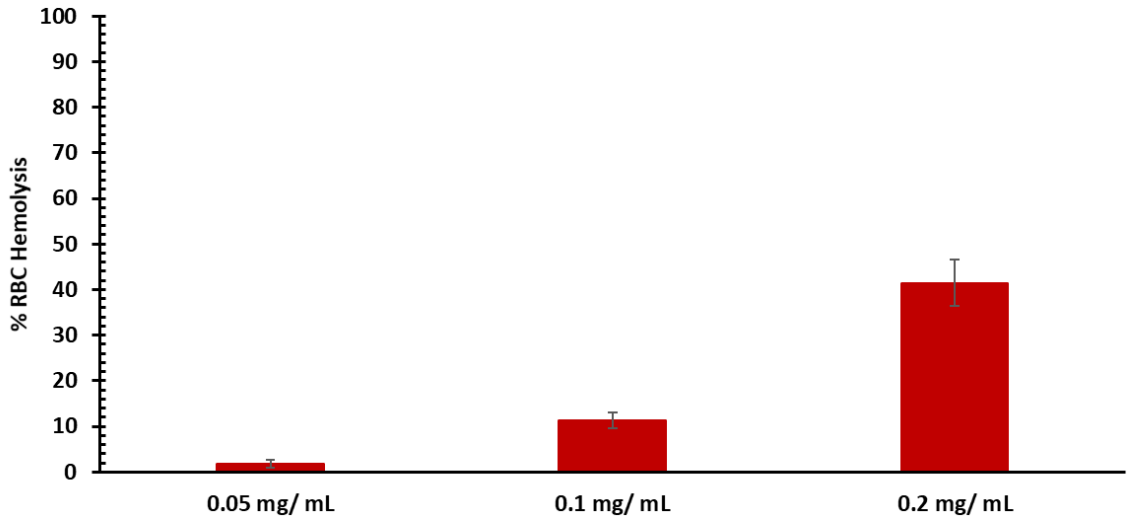

Figure 22. Hemolysis assay on mouse red blood cells

As we consider the application of our polymers for biomedical research, intravenous (IV) methods are the most reasonable to approach. IV injection is a dose of medicine into a vein and straight into the bloodstream. It is one of the promptest ways to deliver a drug into the body.[179] In order to be an ideal nanoparticle carrier inside the body, nanoparticles should not cause any significant hemolysis. Hemolysis data of a nanoparticle sample is essential as the results allow us to gauge the affinity and interaction of nanoparticles with red blood cells. At 0.1 mg/mL, we found that there was 11% hemolysis (Fig. 22). Increasing the concentration via 50% was highly hemolytic. However, at half that concentration, we found only 2% hemolysis. Overall hemolysis test results of the pBzMA-NH_3^+ nanoparticles show no significant hemolysis below 0.05 mg/mL

nanoparticle concentration. This confirms the potential usage of pBzMA-NH_3^+ nanoparticles through IV injection for biomedical applications.

3.3 EXPERIMENTAL

3.3.1 MATERIALS AND METHODS

All chemicals were purchased from commercial sources and used without further purification unless indicated otherwise. The purity of *N*,*N*-carbonyl diimidazole (CDI) was determined by NMR before usage and recrystallized with acetonitrile if it was found to be <90%. The amberlyst-A21 resin was previously cleaned by suspending in three separate batches of MeOH (approximately equal to resin volume) for 2 h. Dowex 50WX8 resin was purified by vacuum filtering and washing with alternating volumes of methanol and tetrahydrofuran until no color was observed in the filtrate (approximately 3 equivalent volumes of solvent). BzMA and TFEMA were percolated through a small column of basic alumina prior to usage. These were stored at -10 ^{o}C over 4$\mathring{A}$ molecular sieves. PyMMA was dissolved in acetone, passed over a small column of basic alumina, dried under vacuum overnight, then stored at -10 ^{o}C. Before analysis by DLS, TEM, and fluorometry, the reaction aliquots were diluted in deionized water with sonication to a concentration of 0.2 mg/mL.

^{1}H and ^{13}C spectra were recorded in deuterated solvents on a Bruker AVANCE 500 NMR Spectrometer.

GPC measurements were done at a flow rate of 0.3 mL/min at 50 ^{o}C, on a GPC system equipped with Waters Alliance HPLC System, 2695 Separation Module with 2 Tosoh TSKgel Super HM-M columns and Waters 2414 Differential Refractometer (RI) and Waters 2998 Photodiode Array Detector (PDA) was used. Polystyrene standards (900–100,000 g/mol) were

used for the calibrations curve and data were processed using the Empower 3 software (Waters). The electrolytic salt, LiBr (0.01%) was added to minimize effects such as polymer aggregation and/or adsorption associated with the polymer or the columns, enabling normal fractionation to occur.

DLS - Aggregate size and zeta potential (ζ-potential) were determined by a Malvern Instruments Zetasizer Nano ZS using a He–Ne laser with a 633 nm wavelength, a detector angle of 173 at 25 ^{o}C using a He–Ne laser with a 633 nm wavelength. Measurements were done in triplicate to confirm reproducibility.

TEM - A JEOL 1230 TEM was operated at 100 kV using a Gatan Orius 831 bottom mounted CCD camera. TEM samples were prepared by adding 10 μL diluted nanoparticle solution to a 300 mesh Formvar/Cu grid. Water was wicked away with weighing paper, and the slide was then incubated on a drop of 1% uranyl acetate stain for 20 sec. Excess water was again wicked away, and the grids were dried at room temperature in a vacuum oven for 45 min before analysis. Image analysis was done using Fiji 2.1.2 and a custom Python 3.7 script.

3.3.2 GENERAL ESTERIFICATION PROCEDURE

BMPA dendron growth was adapted from previously reported procedures.[17] bMPA (1.5eq per hydroxyl group) was suspended in a solution of EtOAc (2 M relative to CDI), and CDI (1.65eq per hydroxyl group) was carefully added. After 1h stirring at rt and conformation of completion via NMR, CsF (0.24 eq per hydroxyl group) was added, followed by the alcohol initiator. The solution was heated at 50^{o}C overnight, or until completion was observed via ^{1}H NMR. The crude was stirred overnight with water added at a 5:1 volume ratio to EtOAc. This was diluted to a concentration of 0.2 M and washed with 0.25 M amount of the following solutions: 3x 1 M

$NaHSO_4$, 3x saturated $NaHCO_3$, and 1x brine. The organic layer was dried with anhydrous magnesium sulfate and concentrated under vacuum.

3.3.3 GENERAL DEPROTECTION PROCEDURE

The acetal-protected dendron was dissolved to a concentration of 6.7wt% in MeOH. Dowex resin was added at a 350% weight ratio relative to dendron. After the disappearance of the doublet at 1.4 ppm via ^{1}H, the resin was removed via vacuum filtration, and MeOH was removed in vacuo. Any residual water was removed via air-drying. If any impurities remained via ^{1}H, the hydroxyl-terminated dendron was either recrystallized in EtOAc or stirred with petroleum ether and charcoal and filtered over Celite.

3.3.4 GENERAL POLYMERIZATION PROCEDURE

The mCTA and solvent(s) were added to a gas-tight conical vial and sonicated and incubated 1h in a dark place. Initiator and monomer(s) were then added, and the solution was purged with Ar for 30 min. The vial was then placed in a 60^oC bath and monitored by NMR.

3.3.5 HEMOLYSIS ASSAY

Hemolysis was performed according to previously published protocols[23,25]. Briefly, LDBC NP, bare PLGA NP, IL-PLGA NPs, and IL-LDBC NPs at 1 mg/mL in 1x PBS pH 7.4. were combined with washed and isolated BALB/c red blood stocks (1:50 dilution from originally concentrated fraction from 250 µL of K2-EDTA treated whole blood) at a 1:10 (v/v) ratio in quadruplicate in a 96 clear-well COSTAR plate (final volume 200 uL/well). The samples were then incubated for 1 hour at 37 °C, and then centrifuged at 4 °C for 10 minutes at 500xg. 100 µL of supernatant was collected to measure peak hemolytic absorbance in quadruplicate at 405 nm by UV-Vis/fluorescent plate-reader. 20% Triton X-100 and 1x PBS pH 7.4 were used as positive and

negative internal controls at the same treatment dilution. The 1x PBS negative control was subtracted as a minimum baseline (0%) from all samples, and the Triton-X-100 positive control was used as a maximum baseline (100%) to calculate normalized hemolytic percentages with standard error of mean (n = 4). A two-tail t-test of means was used to determine significance between 2 samples at a time[23,25]

CHAPTER IV: MULTIFUNCTIONAL FLUORINE-19 MAGNETIC RESONANCE IMAGING NANOPARTICLES AS THERANOSTIC AGENTS

4.1 INTRODUCTION

As described in Chapter 1, MRI has emerged as a powerful diagnostic tool producing three-dimensional and cross-sectional images of living tissue with the advantage of being a noninvasive imaging technique for anatomy and physiological processes.[180] The clinical MRI is generally used to visualize spatial biodistribution of hydrogen atoms, mainly in water and lipid molecules. Paramagnetic contrast agents are often introduced in MRI to enhance image contrast between healthy and diseased tissue or to direct the status of organ function or blood flow.[181] Typical agents include chelates of $Gd^{3+,}$ Fe^{3+}, or Mn^{2+}. Paramagnetic contrast agents are function by reducing the relaxation times of local ^{1}H nuclei through magnetic interactions between unpaired electrons and hydrogen nuclei.[182] This causes a local change in contrast, which may distinguish between healthy and pathological tissues.

Although such contrast agents have significantly enhanced the performance and efficacy of MRI, many limitations remain. For instance, the high background signal from water and the intrinsic sources of contrast in tissue often prevent the discrimination of diseased tissue using ^{1}H relaxation agents.[183] In addition, the changes in contrast induced by indirect modulation by the contrast agents of the water protons are not readily related to the local concentration of the imaging agent in complex body conditions.[184] The alternative approach of directly observing the nuclear

spins of the contrast agent, rather than the neighboring spins, has significant advantages if the objective is to measure the local concentration of the contrast agents quantitatively. However, this approach is impractical if observing ^{1}H spins due to the overwhelming confounding signal from endogenous protons in the body. Additionally, the biological impact of traditional contrast agents is vastly misunderstood.[185] To overcome these encounters, there has been increasing interest in developing contrast agents containing biologically rare, biocompatible, and magnetically active nuclei such as ^{19}F, ^{23}Na, ^{31}P, etc.

The ^{19}F isotope appears to be the most promising imaging nucleus. It has a 100% natural abundance and nuclear spin (I) of ½. Additionally, the gyromagnetic ratio of ^{19}F is very close to hydrogen (40.08 vs 42.58 MHz/T of ^{1}H).[186-189] This means that the ^{19}F atoms can be successfully imagined by a standard ^{1}H MRI technique, requiring only minor tuning of the radio-frequency equipment and allowing simultaneous imaging of both ^{1}H and ^{19}F signals. ^{19}F chemical shifts are varied in a broad range (>350 ppm), and only trace quantities ($<10^{-6}$ M) of ^{19}F are present in the human body. They are immobilized in the solid phase (bones and teeth), leading to a very short background signal far below MRI detection limits. [190] In addition, the fluorine atom has a van der Waals radius of 1.47 Å, making it larger than the hydrogen atom, which has a van der Waals radius of 1.20 Å.[191] Fluorine is as space-filling as oxygen yet is much less polarizable. Interestingly enough, introducing fluorine into a polymer provides novel behavior due to high electronegativity (4.0 on the Pauling scale), high ionization potential, and low polarizability of the fluorine atom.[192]

Despite its undeniable potential, ^{19}F MRI is still underutilized, primarily due to toxicity issues, low fluorine content, water-solubility, and often unfavorable physical/biological properties.[193-195] Therefore, the development of new ^{19}F MRI contrast agents represent an ongoing challenge and critical need in biomedical diagnostic research. The usage of nanoparticles as

imaging probes has several advantages over traditional imaging agents. Loading ability is one of the key advantages where the concentration of the imaging agent can be controlled within each nanoparticle system during the synthesis. Additionally, the tunability of the surface of the nanoparticles can potentially extend the circulation time of the imaging agent in the blood or target a specific location within the body. Finally, nanoparticles can act as multifunctional contrast agents since they have more properties that can be used simultaneously in multiple imaging techniques, especially in MRI.

As described in chapter 3, PISA technique open new pathways for the autonomous creation of biomimetic nanoparticles.[180] Combination of both ^{19}F MRI and PISA techniques offers additional advantages to numerous biomedical research fields, particularly MRI agents' design, to understand the stability of nanoparticles based upon different fluorine content and the factors affecting cellular uptake. The study described herein aims to prepare partly fluorinated polymeric nanoparticles in a one-pot reaction using aqueous RAFT polymerization to determine their potential as ^{19}F MRI contrast agents.

4.2 RESULTS AND DISCUSSION

4.2.1 DESIGN AND SYNTHESIS

^{19}F MRI depends on the use of a fluorinated contrast agent. Applicable ^{19}F MRI contrast agents should satisfy several critical criteria, such as a single ^{19}F resonance peak for maximum sensitivity and minimum imaging artifact, appreciable fluorine content for high sensitivity and low toxicity, sufficiently long spin-spin relaxation time (T_2) and high signal to noise ratio (SNR) for optimal imagine.[196-199] From our previous results in chapter 3, we used our cationic dendritic chain transfer agent (mCTA-8-ala) to produce multiple morphologies, including vesicles at a 17:83

hydrophilic to hydrophobic ratio. Here we used mCTA-8ala to synthesize fluorinated linear dendritic block copolymer pBz_HF using 1,1,1,3,3,3-hexafluoropropan-2-yl methacrylate (HFMA) and hydrophobic monomer BzMA. As explain in chapter 3, BzMA provides stable hydrophobic segment to the nanoaggregates via pi-pi staking between phenyl groups. Surface amine groups from the mCTA-8ala will provide higher water solubility for the polymer and higher cellular uptake for the resulting polymer nanoparticles.

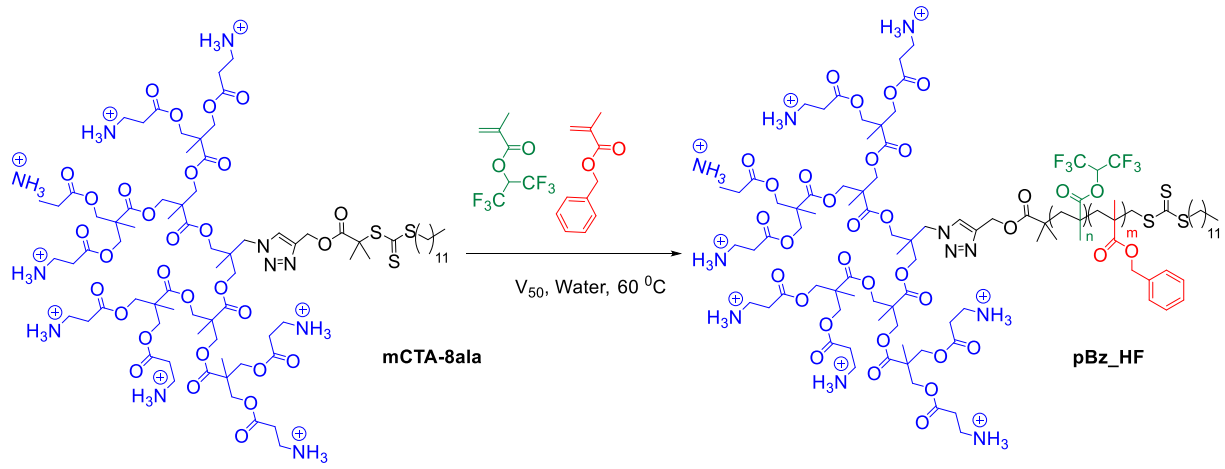

Figure 23. Synthetic route for the preparation of pBz_HF, n is the number of HFMA units, and m is the number of BzMA units. By changing HFMA (n) to BZMA (m) ratio (n:m) into 1:5, 1:10, and 1:20, we synthesized P(Bz_HF_5), P(Bz_HF_10), and P(Bz_HF_20)

A general synthetic scheme for the pBz_HF is shown in Figure 23. The water-soluble 2,2'-azobis(2-methylpropionamidine) dihydrochloride (V50) was used as the initiator. Controlling the amount of fluorine in the polymer is essential as its concentration contributes to the MRI signal as well as toxicity. To ensure that the fluorine amount was enough to achieve a distinct MRI signal without exhibiting a cytotoxic response as a nanoparticle, we developed a library of fluorinated LDBCs by changing HFMA (n) to BzMA (m) ratio (n:m) into 1:5, 1:10, and 1:20, which results in P(Bz_HF_5), P(Bz_HF_10) and P(Bz_HF_20), respectively.

4.2.2 CHARACTERIZATION OF POLYMERS

The synthesis and characterization of mCTA 8ala are shown in Chapter 3 and Appendix B. The final products were confirmed by ^{1}H and ^{19}F NMR spectroscopy displayed in Appendix C (Fig. 105-119). The molar mass and the degree of polymerization (DP) were calculated using proton NMR spectra for all the polymers (Synthesis, Appendix C). ^{19}F NMR was conducted to confirm the absence of free HFMA monomer in the reaction mixture and the presence of fluorinated polymer. GPC was utilized to confirm the molar masses of the polymers (Table 1 and Fig 120-122, Appendix C).

4.2.3 SELF-ASSEMBLY AND MORPHOLOGY

Tabulation of nanoaggregate characteristics is provided in Table 2. The CAC of the nanoparticles was evaluated by the pyrene probe method.[200] The CAC for the fluorinated polymers ranged from 1.26 to 15.85 mg/L, providing relatively low CAC values, and they are comparable to those found in the literature and correlate to the candidacy of these fluorinated nanoparticles as potential biomaterials. As the three polymers have the same hydrophobic segment and different amount of fluorine contain, CAC value increased with the fluorine amount. P(Bz_HF_5) which has the highest amount of fluorine has the highest CAC value (15.85 mg/L), and P(Bz_HF_20) which has the lowest amount of fluorine has the lowest CAC value (1.26 mg/L), with the P(Bz_HF_10) having an intermediate CAC value of 11.22 mg/L. This is due to hydrophobic nature of fluorinated compound.[201] Having a higher fluorine amount increases the hydrophobicity which leads the higher CAC value.[202-203] A low CAC value illustrates a more stable nanoaggregate system and a resistance to dissociation upon dilution in the blood.[200] Based on CAC values, the results indicate that P(Bz_HF_20) forms more stable nanoparticles compared to P(Bz_HF_5) and P(Bz_HF_10).

Table 3 CAC values, the average hydrodynamic diameter of the dendritic aggregates by TEM and DLS (in number and intensity), and surface charge

Polymer	CAC / (mg L^{-1})	R_{DLS} /nm	PDI	R_{TEM} / nm	Nagg	ζ-potential (mV)
P(Bz_HF_5)	15.85 ± 1.32	191.0 ± 48.2	0.12	160.4	21	33.6 ± 3.9
P(Bz_HF_10)	11.22 ± 0.59	135.3 ± 34.1	0.05	154.2	18	31.1 ± 3.9
P(Bz_HF_20)	1.26 ± 0.45	165.2 ± 38.7	0.04	175.3	17	30.5 ± 4.8

The particle size of the dendritic aggregates in aqueous media was studied by DLS which provides an estimate of the particle size as its hydrodynamic radius. To examine the morphology of the aggregates and to support the particle size data obtained by the DLS, TEM analysis was conducted

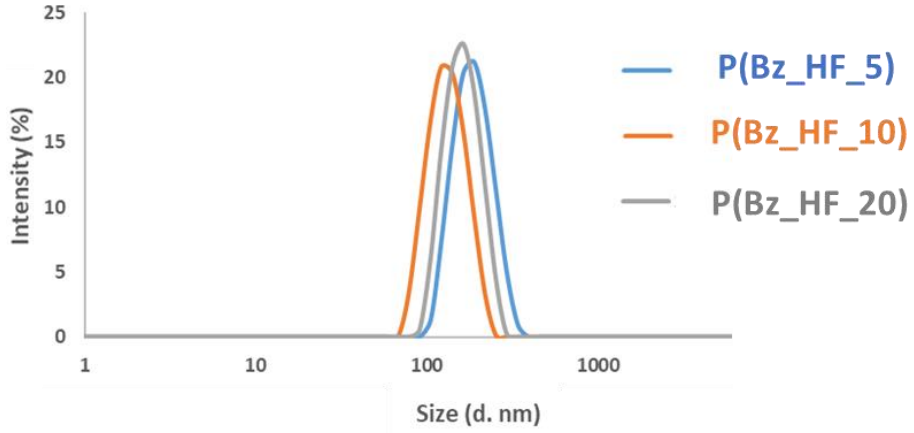

Figure 24. DLS spectra, Size distribution by intensity

Polymer system P(Bz_HF_5) has a larger particle size with an intensity average diameter 191.0 ± 48.2 nm, with 0.12 PDI (Fig. 123-125, Appendix C). For the polymer system P(Bz_HF_10), intensity average diameter 135.3 ± 34.1 nm, with 0.05 PDI (Fig. 126-128) and polymer system P(Bz_HF_20) shows intensity average diameter 165.2 ± 38.7 nm with 0.04 PDI

(Fig. 129-131, Appendix C). Based on the PDI value, all three polymer nanoparticles show a narrow distribution of PDI values below 0.2.

TEM analysis indicated polymer nanoparticles of P(Bz_HF_5), P(Bz_HF_10), and P(Bz_HF_20) as uniform monodispersed spherical aggregates (Fig. 25) with an average particle size of 160.4 nm, 154.2 nm, and 175.3 nm. It is essential to understand that TEM gives the size of nanoparticles in dried form. At the same time, DLS tells the hydrodynamic diameter, which is the size of the nanoparticle plus the liquid layer around the particle. Additionally, the presence of bigger particles may contribute to an increase in light scattering, shifting the measured particle size towards larger values in DLS. For the biomedical field, DLS is a more appropriate size distribution analysis. Overall particle size analysis indicates that all three polymer nanoparticles produce nanoparticles within a favourable range for cellular uptake.[202] All particle sizes are below 200 nm, which indicates that they can escape physiological barriers, take advantage of the EPR effect, possess high potential for prolonged circulation and reduced filtration by the liver and spleen.

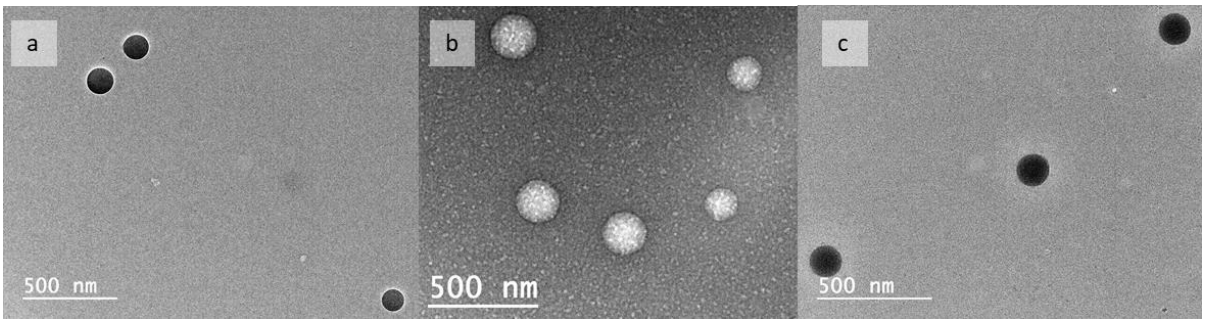

Figure 25. Nanoparticles formed by (a) P(Bz_HF_5), (b) P(Bz_HF_10), and (c) P(Bz_HF_20) under TEM

The surface charge is significant for the stability of nanoparticles in suspension and contributes to the adsorption of nanoparticles onto the cell membrane. After the adsorption of

nanoparticles, the endocytotic uptake rate depends on the particle size. The surface charge is commonly expressed as a zeta potential, which is measured by the laser Doppler electrophoresis technique. P(Bz_HF_5), P(Bz_HF_10), and P(Bz_HF_20) have a zeta potential of 33.6 ± 3.9, 31.1 ± 3.9, and 30.5 ± 4.8, respectively. Generally, particles with positive surface charges below 15 mV display the ideal properties such as decreased macrophage uptake,[203] higher tumor retention, and longer circulation time.[45] In addition, the ideal surface charge depends on factors such as cell type, cellular uptake mechanism, and intracellular localization of nanoparticles.[204] There have been reported studies that explain the ability of cationic nanoparticles to stay in a tumor for a prolonged time due to favorable electrostatic interactions that can be made between cationic nanoparticles and the negatively charged cell membrane at the stage of cellular uptake.[205] The surface charge values for P(Bz_HF) nanoparticles are higher compared to the ideal value (15 mV) expected. Additionally, the values are similar within the different amounts of fluorine content, indicating the surface charge is not much dependent on fluorine content for the three polymer systems.

An aggregation number (N_{agg}) explains the average number of individual polymer units present in a spherical nanoaggregate once the CAC has been reached. N_{agg} is essential in this study because it affords the average fluorine percentage inside a nanoparticle. P(Bz_HF_5), P(Bz_HF_10), and P(Bz_HF_20) have N_{agg} of 21, 18, and 17, respectively. The fluorescence quenching technique was carried out to calculate the N_{agg} of the nanoparticles. This technique is based on quenching of pyrene fluorescence by hydrophobic Benzophenone quencher.[206] N_{agg} was calculated by changing the quencher concentration using Equation 3. Where I_0 = fluorescence intensities of pyrene in the absence of quencher, I = fluorescence intensities of pyrene in the presence of quencher, C_p = molar concentration of the polymer, C_{CAC} = critical aggregation concentration, and C_q = molar concentration of the quencher.

$$\ln(I_0/I) = [N_{agg} / (C_p - C_{CAC})] \times C_q \quad (3)$$

4.2.4 CYTOTOXICITY

It is essential to evaluate the cytotoxicity of the nanoparticles to see their potential as a nanocarrier. After physiochemical characterization, we evaluated the effects of nanoparticles on cell viability against HEK cells using the Lactate Dehydrogenase (LDH) assay (Fig. 26). LDH is an enzyme that catalyzes the interconversion between pyruvate and lactate.[207] If there is any tissue damage, cells release LDH into the bloodstream. Since LDH is a steady enzyme, it has been usually used to evaluate the damage and toxicity towards tissue and cells. HEK cells were selected as a representation of human cell interactions.

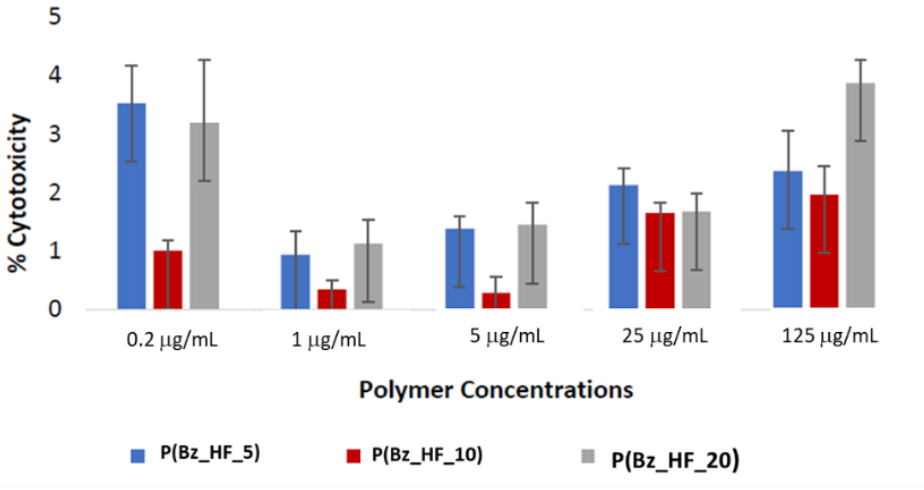

Figure 26. Cell viability after treatment with nanoparticles. The LDH assay determined cytotoxicity (percentage). Error bars denote the standard error, while letter denotes significance groups as determined by Tukey HSD ($p \leq 0.05$)

Among the three polymer nanoparticle systems, we found that P(Bz_HF_10) shows the minimum cytotoxicity. At 0.2 µg/mL, we can see the increased cytotoxicity compared to other

higher concentrations. It is essential to note that 0.2 µg/mL is below the CAC value; so at this concentration, there is no nanoparticle formation. From 1 µg/mL to 125 µg/mL, we found that cytotoxicity slowly increases with the concentration. P(Bz-HF_5), which has the highest amount of fluorine, shows the highest cytotoxicity at a concentration between 1 – 25 µg/mL. At 125 µg/mL concentration, P(Bz-HF_20) shows the highest cytotoxicity, but that is only 1.5% compared to P(Bz_HF_5). Overall, the observed cell cytotoxicity for the three nanoparticles systems was < 5 %, which indicates P(Bz_HF) nanoparticles are generally non-toxic to living human cells. (Fig. 26)

4.2.5 HEMOLYSIS ASSAY

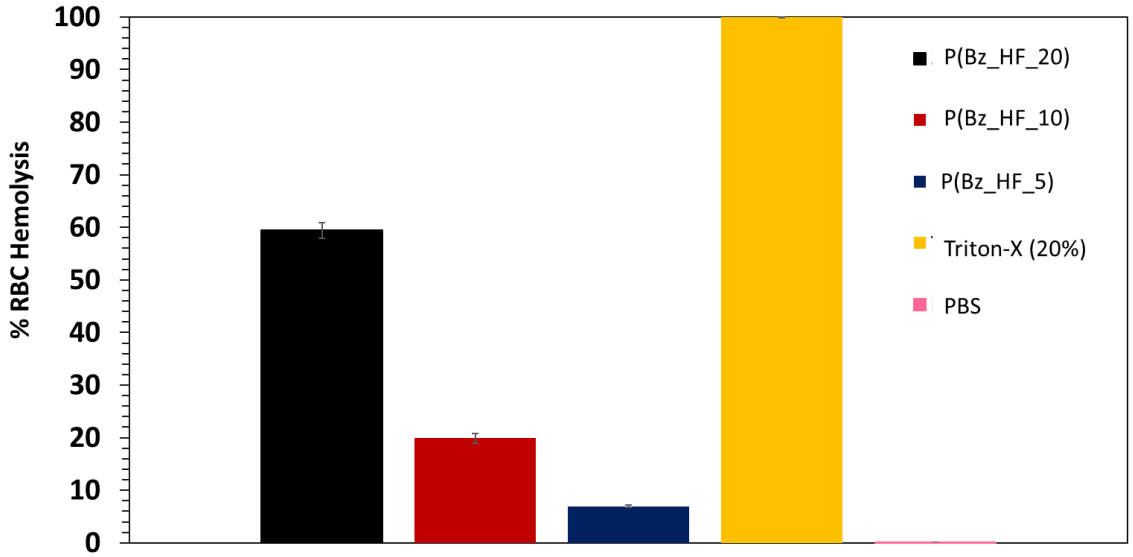

Figure 27. Hemolysis assay on mouse red blood cells at 125 µg/mL concentration. Average % Red Blood Cell (RBC) hemolysis in response to nanoparticles ex-vivo with standard error of the mean (SEM) (n = 4)

As discussed in Chapter 3.2.3, we measured the intravenous (IV) biocompatibility of the P(Bz_HF) nanoparticles via hemolysis assay on mouse red blood cells (Fig. 27). We used a nonionic detergent Triton-X as the negative control and PBS as a positive control for the hemolysis

assay. We found that P(Bz_HF_20) shows the highest RBC hemolysis (59%). The nanoparticle systems P(Bz_HF_5) and P(Bz_HF_10) show the lower RBC hemolysis of 7% and 20%. For clinic application, hemolysis is concerning; therefore, additional modifications to the surface of the nanoparticles are needed.[217]

4.2.6 RELAXATION TIMES (T_1/T_2)

In In order to evaluate their potential as ^{19}F MRI contrast agents, the fluorinated nanoparticles were examined by ^{19}F NMR. Samples were dispersed in H_2O/D_2O (90/10, v/v). As displayed in Fig 106, 111, and 116 in Appendix C, only one peak was observed in each spectrum, confirming a single ^{19}F chemical environment in the nanoparticles. The ^{19}F NMR relaxation times spin-lattice (T_1) and spin-spin (T_2) of the nanoparticles were measured and listed in Table 2.

Table 4. NMR Properties of the Fluorinated Polymeric Nano-objects in D_2O

Polymer	T_1 / ms	T_2 / ms
P(Bz_HF_5)	2695	946
P(Bz_HF_10)	2750	1450
P(Bz_HF_20)	2543	634

The spin−spin relaxation time T_2 is an important parameter determining the resultant MRI performance. A longer T_2 relaxation time is vital for producing intense ^{19}F MRI signals. T_2 relaxation usually proceeds more rapidly than T_1 recovery, and different biological tissues have different T_1 and T_2. For example, fluids have the longest T_1 and T_2; water-based tissues (T_1,1500-2000 ms range and T_2, 40-200 ms range), while fat-based tissues are in the (T_1, 400-1200 ms range

and T_2, 10-100 ms range). T_1 relaxation times ranged from 2543 s to 2750 s and T_2 relaxation times ranged from 634 ms to 1450 ms. P(Bz_HF_20) shows the shortest T_2 relaxation time and P(Bz_HF_10) shows the highest T_1 relaxation time. The MRI intensity (or signal-to-noise ratio, SNR) was found to be linearly dependent on the concentration of polymers. At 10 mg/mL SNR ranging from 277 to 725 (Fig 141-143, Appendix C), which is higher relative to SNR values reported for high-resolution MRI.[207] Additionally, the sensitivity of the contrast agent is dependent on intracellular ^{19}F concentration and MRI system hardware and acquisition parameters, all of which contribute to potential low SNR. Due to the higher SNR of the fluorinated nanoparticles systems, we check the potential of encapsulating a NIR secondary imaging agent.

4.2.7 PRELIMINARY ENCAPSULATION STUDIES

In order to assess the potential of a secondary imaging agent and hydrophobic loading ability, encapsulation studies were conducted with a novel hydrophobic cyanine-based photothermal imaging agent, C3 produced by Delcamp and co-workers (Fig.28a).[208] Cyanine-based dyes are generally used as imaging agents for photoacoustic and near-infrared fluorescence imaging. They can transform absorbed near-infrared (NIR) photons to heat as a photothermal agent and lower energy NIR photons for an image-guided combinatorial phototherapeutic agent. However, several bottlenecks limit the application of cyanine dyes, such as solubility and instability in aqueous media, which increase their imaging and therapeutic potential.

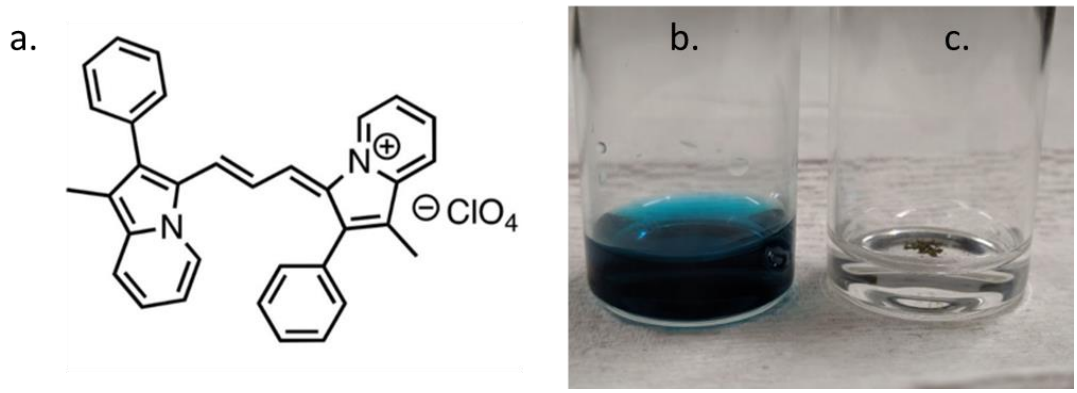

Figure 28. (a) Structure of NIR theranostic agent C3, (b) C3-loaded P(Bz_HF_10) nanoparticles, (c) dispersion of C3 in H_2O

Without the presence of fluorinated polymer, the dye was completely insoluble in water, forming a separate layer on the water surface (Fig. 28c). After encapsulating the dye into P(Bz_HF_10), we can see the solubility of C3 in polymer nanoparticle solution (Fig 28b). The reported DL% of P(Bz_HF_5), P(Bz_HF_10), and P(Bz_HF_20) is 8.96 %, 8.12 %, and 7.63 %, respectively. The reported EE% of P(Bz_HF_5), P(Bz_HF_10), and P(Bz_HF_20) is 24.61 %, 24.10 % and 20.65 % respectively. These DL% and EE% highlight the potential of uploading hydrophobic cargo and secondary imaging agents into fluorinated nanoparticles.

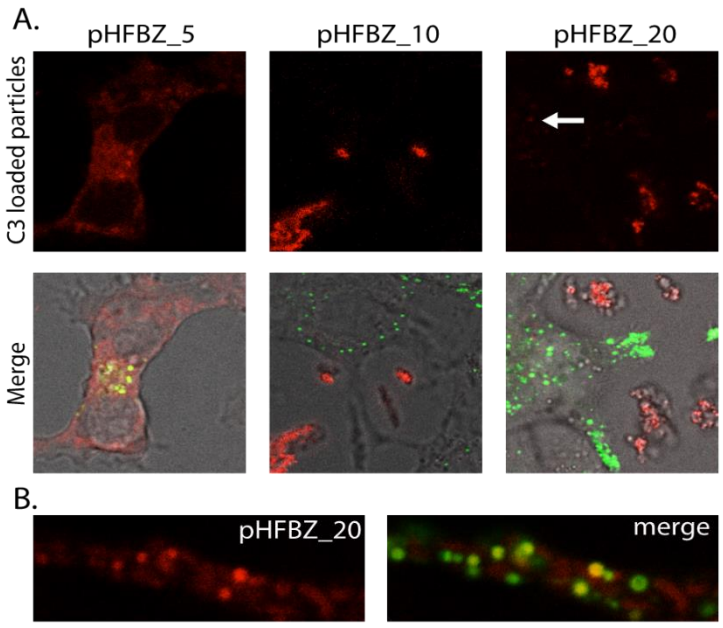

Figure 29. Cellular distribution of P(Bz_HF) derivates: a) imaging of C3 dye-loaded P(Bz_HF) particles. In HEK 293 cells: Top panels show C3 fluorescence, bottom panel merge C3 fluorescence (red), lysotracker green (green), and phase contrast. The white arrow shows C3 fluorescence on the interior of the cell. b) STED microscopy of cell lamellipodia showing C3 fluorescence (red) localized to lysosomes (green) and to presumptive endosomal bodies

C3-loaded fluorinated nanoparticles were then assessed as potential biological imaging agents. C3 dye fluorescence was measured after trafficking into HEK cells (Fig. 29). Simultaneously, LysoTracker green was used to track the distribution and accumulation of dye-loaded nanoparticles in the cellular organelles. LysoTracker Green is a fluorescent dye that stains acidic compartments in live cells with excitation/emission maxima 504/511 nm. In a review of the overlapped fluorescence images of C3 and LysoTracker, P(Bz_HF_5) shows efficient loading with some accumulation in lysosomes but generalized cell labeling, P(Bz_HF_10) and P(Bz_HF_20) were found as aggregates amongst cells with a small portion observed to be entering cells for P(Bz_HF_20) nanoparticles.

4.2.8 CONCLUSIONS AND FUTURE WORK

This work presents a successful attempt to prepare partly fluorinated polymeric nanoparticles in a one-pot reaction using aqueous RAFT polymerization. Transmission electron microscopy (TEM) and dynamic light scattering (DLS) analyses indicate nanoparticle sizes ranging from 120 to 180 nm with zeta-potential values ranging from 30.5 to 33.6 mV. Nanoparticles exhibit a single resonance in the ^{19}F NMR spectrum with relatively short MRI relaxation times. Additionally, these nanomaterials displayed minimal cell toxicity as well as potential for dual imaging and therapy. These results afford pathways toward building next-generation multifunctional ^{19}F MRI cell tracking nanomaterials.

4.3 EXPERIMENTAL SECTION

4.3.1 MATERIALS AND METHOD

Common solvents, HPLC solvents, and reagents were purchased from commercial suppliers (Sigma-Aldrich and Fisher Scientific) and used without additional purification. Benzyl methacrylate (BzMA) and 1,1,1,3,3,3-Hexafluoroisopropyl methacrylate (HFMA) were percolated through a small column of basic alumina before usage.

^{1}H spectra were collected using a Bruker Avance 300 or 400 MHz spectrometer. Chemical shifts (δ) are denoted in parts per million (ppm) relative to an internal standard (tetramethylsilane-TMS) and referenced to a protonated solvent obtained from Cambridge Isotope Laboratories, Inc.

^{19}F NMR spectra were collected using a Bruker Avance 400 MHz spectrometer with H_2O/D_2O (90/10, v/v) as solvent. Solution spectra were measured under the following measurements conditions: 90° pulse width 15 μs, relaxation delay 1 s, acquisition time 0.73, and 128 scans.

^{19}F spin−spin relaxation times (T_2) were measured using the Carr−Purcell−Meiboom−Gill (CPMG) pulse sequence at 298 K. The samples were dissolved in H_2O/D_2O (90/10, v/v) at a concentration of 1-10 mg/mL. The 90° pulse was determined by dividing with a 360° pulse width, at which the NMR signal is zero. The relaxation delay was 1 s, and the number of scans was 64. Only values for the major peaks are reported. For each measurement, the echo times were from 2 to 770 ms and 16 points were collected, which could be described by exponential functions for the calculation of T_2.

^{19}F spin−lattice (T_1) relaxation times were measured using the standard inversion−recovery pulse sequence. For each measurement, the relaxation delay was 2 s, and the number of scans was 32. Only values for the major peaks are reported. For each measurement, the recovery times were from 2 ms to 3 s, and 16 points were acquired. Values for the major peak at around −72.8 ppm are reported.

Gel permeation chromatography (GPC) measurements were done using DMF, and measurements were done at a flow rate of 0.8 mL/min at 55 ℃. A Shimadzu 20A GPC system equipped with two PSS SDV analytical 1000 Å columns and a differential refractive index detector were used. The data was evaluated using Astra 7.0 software. The GPC system was calibrated using Polymethylmethacrylate (PMMA) standards.

A JEOL 1230 TEM was used at 100 kV to obtain electron microscopy images using a bottom-mounted charge-coupled device (CCD) camera (Gatan Orius 831).

4.3.2 GENERAL SYNTHESIS

The mCTA was prepared using our previously published work (PISA paper). The mCTA, HFMA, V50, and water were added to a gas-tight conical vial and sonicated, and incubated 1 h in

a dark place. Then the solution was purged with Ar for 30 min and then the vial was placed in a 60 ^{0}C bath and monitored using NMR. After completion of polymerization, the polymer was purified by dialysis against Milli-Q water for 24 h and freeze dried. Then the same RAFT polymerization method explains above was carried out with the BzMA. The final reaction mixture was purified using size exclusion chromatography (Sephadex LH-20) to obtain the pHFBz polymer systems.

4.3.3 CHARACTERIZATION OF POLYMERS

The molar mass and the degree of polymerization (DP) were calculated using proton NMR spectra for all the polymers. DMSO-D6 was used as the solvent with TMS as the internal standard. ^{19}F NMR carried out to confirm the absence of free HFMA monomer in the reaction mixture and the presence of fluorinated polymer. GPC was utilized to confirm the molar masses calculated by NMR and obtain the dispersity (Đ) of the polymers.

4.3.4 PREPARATION AND CHARACTERIZATION OF NANOPARTICLES

Polymer systems were formed into nanoparticles via a previously reported nanoprecipitation method. 1 mg of the polymer was dissolved in THF (200 µL), and the resulting solution was added dropwise to a vial containing MilliQ water (2 mL) while sonicating. THF was allowed to evaporate under constant nitrogen flow. Nanoformulations were allowed to equilibrate for 12 h before testing.

Particle size and zeta potential (ζ-potential) measurements were carried out on a Zetasizer Nano ZS (Malvern Instrument) using a He−Ne laser (633 nm) detector angle of 173° at 25 °C. Concentration was kept 0.5 mg/mL for all the systems, and all measurements were done in triplicate to assure consistency. Morphologies of the nanoparticles were obtained by environmental TEM.

4.3.5 CRITICAL AGGREGATION CONCENTRATION

For the measurement of the critical aggregation concentration (CAC), pyrene (1.7 mg, 8.41 μmol) was dissolved in 3 mL of acetone, and 40 μL of the solution was added to 40 mL of deionized water. A series of concentrations of the nanoaggregate suspension ranging from 10^{-8} mg L^{-1} to 10^{2} mg L^{-1} was prepared by dilutions of 2 mL per sample. Pyrene solution (2 mL) was added to each vial, and these solutions were equilibrated for 48 h in a dark area. The fluorescence spectra were obtained on a Varian Cary fluorometer from Agilent Technologies. An emission wavelength of 390 nm was used for pyrene, and the excitation spectra were recorded from 300 to 380 nm. The ratio of emission intensities at 338 and 333 nm was graphed as a function of the log of the concentration. The CAC was determined as the concentration at the intercept of the lines for the two linear regions of the obtained graphs.

4.3.6 DETERMINATION OF THE AGGREGATION NUMBER (N_{AGG})

The fluorescence quenching technique was carried out to calculate the N_{agg} of the nanoparticles. This technique based on quenching of pyrene fluorescence by hydrophobic Benzophenone quencher. (DOI: 10.18433/j3zc73) N_{agg} was calculated by changing the quencher concentration using the following equation. Where I_0 = fluorescence intensities of pyrene in the absence of quencher, I = fluorescence intensities of pyrene in the presence of quencher, C_p = molar concentration of the polymer, C_{CAC} = critical aggregation concentration and C_q = molar concentration of the quencher.

$$\ln(I_0/I) = [N_{agg} / (C_p - C_{CAC})] \times C_q$$

4.3.7 ENCAPSULATION STUDIES

Chemical structures, absorbance, and emission profiles for each dye are given in the appendix C. 1 mg of C3 dye and 2 mg of the polymer was dissolved in THF (200 μL). The

nanoprecipitation method stated above (preparation and characterization of nanoparticles) was followed to form dye-loaded nanoparticles. After the 12 h equilibrating period, the unloaded dye was filtered out using a 0.45 μm syringe filter. Water was then removed by freeze-drying. The resulting crude (dye-loaded nanoparticles) was redissolved in THF (10 mL) to solubilize the encapsulated dye. The amount of encapsulated dye was estimated using a Cary 6000 UV−visible spectrophotometer and a standard calibration curve obtained from free dye in THF.

The encapsulation efficiency (EE%) and loading efficiency (DL%) were calculated for each dye using the following equations. M_C = mass of the dye in the nanoparticle, M_P = mass of LDBC, and M_{Ci} = mass of the dye initially added.

$$DL\ (\%) = 100 \times \frac{(Mc)}{(Mp + Mc)}$$

$$EE\ (\%) = 100\ \times \frac{(Mc)}{(Mci)}$$

4.3.8 IN VITRO CELL UPTAKE AND CYTOTOXICITY ASSAY

Human embryonic kidney (HEK293) cells were used for cytotoxity assay. HEK cells were grown under the standard conditions (37 °C, 5% CO_2, DMEM media with 10% FBS). Then the nanoparticles were added to tissue culture media and allowed 24 h incubation period. A LysoTracker Green DND-26 (Invitrogen) staining was performed to image lysosomes simultaneously. The distribution of dyes in the cells was visualized with a laser scanning confocal microscope (Zeiss LSM 510 META). Cytotoxicity of the nanoparticles (dye loaded and unloaded) was then evaluated with a CyQUANT LDH Cytotoxicity Assay Kit (Invitrogen) using a microplate reader BioTek Synergy H1. Tukey honestly significant difference (HSD) test was performed to calculate differences in viability between loaded and unloaded particles at different concentrations.

4.3.9 HEMOLYSIS ASSAY

Hemolysis was performed according to previously published protocols[23,25]. Briefly, LDBC NP, bare PLGA NP, IL-PLGA NPs, and IL-LDBC NPs at 1 mg/mL in 1x PBS pH 7.4. were combined with washed and isolated BALB/c red blood stocks (1:50 dilution from originally concentrated fraction from 250 µL of K2-EDTA treated whole blood) at a 1:10 (v/v) ratio in quadruplicate in a 96 clear-well COSTAR plate (final volume 200 uL/well). The samples were then incubated for 1 hour at 37 °C, and then centrifuged at 4 °C for 10 minutes at 500xg. 100 µL of supernatant was collected to measure peak hemolytic absorbance in quadruplicate at 405 nm by UV-Vis/fluorescent plate-reader. 20% Triton X-100 and 1x PBS pH 7.4 were used as positive and negative internal controls at the same treatment dilution. The 1x PBS negative control was subtracted as a minimum baseline (0%) from all samples, and the Triton-X-100 positive control was used as a maximum baseline (100%) to calculate normalized hemolytic percentages with standard error of mean (n=4). A two-tail t-test of means was used to determine significance between 2 samples at a time[23,25].

REFERENCES

REFERENCES

1) Sikwal, D. R.; Kalhapure, R. S.; Govender, T. An Emerging Class of Amphiphilic Dendrimers for Pharmaceutical and Biomedical Applications: Janus Amphiphilic Dendrimers. European Journal of Pharmaceutical Sciences 2017, 97, 113–134.

2) GENERAL. Science 1897, 5 (118), 547–549.

3) Selin, M.; Peltonen, L.; Hirvonen, J.; Bimbo, L. M. Dendrimers and Their Supramolecular Nanostructures for Biomedical Applications. Journal of Drug Delivery Science and Technology 2016, 34, 10–20.

4) Wooley, K. L.; Hawker, C. J.; Frechet, J. M. J. Unsymmetrical Three-Dimensional Macromolecules: Preparation and Characterization of Strongly Dipolar Dendritic Macromolecules. J. Am. Chem. Soc. 1993, 115 (24), 11496–11505.

5) Peterca, M.; Percec, V.; Leowanawat, P.; Bertin, A. Predicting the Size and Properties of Dendrimersomes from the Lamellar Structure of Their Amphiphilic Janus Dendrimers. J. Am. Chem. Soc. 2011, 133 (50), 20507–20520.

6) Percec, V.; Leowanawat, P.; Sun, H.-J.; Kulikov, O.; Nusbaum, C. D.; Tran, T. M.; Bertin, A.; Wilson, D. A.; Peterca, M.; Zhang, S.; Kamat, N. P.; Vargo, K.; Moock, D.; Johnston, E. D.; Hammer, D. A.; Pochan, D. J.; Chen, Y.; Chabre, Y. M.; Shiao, T. C.; Bergeron-Brlek, M.; André, S.; Roy, R.; Gabius, H.-J.; Heiney, P. A. Modular Synthesis of Amphiphilic Janus Glycodendrimers and Their Self-Assembly into Glycodendrimersomes

and Other Complex Architectures with Bioactivity to Biomedically Relevant Lectins. J. Am. Chem. Soc. 2013, 135 (24), 9055–9077.

7) Zhang, S.; Sun, H.-J.; Hughes, A. D.; Moussodia, R.-O.; Bertin, A.; Chen, Y.; Pochan, D. J.; Heiney, P. A.; Klein, M. L.; Percec, V. Self-Assembly of Amphiphilic Janus Dendrimers into Uniform Onion-like Dendrimersomes with Predictable Size and Number of Bilayers. Proceedings of the National Academy of Sciences 2014, 111 (25), 9058–9063.

8) Acton, A. L.; Fante, C.; Flatley, B.; Burattini, S.; Hamley, I. W.; Wang, Z.; Greco, F.; Hayes, W. Janus PEG-Based Dendrimers for Use in Combination Therapy: Controlled Multi-Drug Loading and Sequential Release. Biomacromolecules 2013, 14 (2), 564–574.

9) Ouyang, L.; Ma, L.; Li, Y.; Pan, J.; Guo, L. Synthesis of First Generation Janus-Type Dendrimers Bearing Asp Oligopeptides and Naproxen. Arkivoc 2010, 2010 (2), 256–266.

10) Guo, L.; Pan, J.; Ma, L.; Zhao, Y.; Zhao, J.; Ouyang, L. Design and Synthesis of Novel Janus Dendrimers as Lipophilized Antioxidants. Synlett 2013, 24 (08), 1011–1015.

11) Salmen, J.; Banys-Paluchowski, M.; Fehm, T. Bone-Targeted Therapy. Geburtshilfe Frauenheilkd 2015, 75 (06), 584–587.

12) Fuchs, S.; Pla-Quintana, A.; Mazères, S.; Caminade, A.-M.; Majoral, J.-P. Cationic and Fluorescent “Janus” Dendrimers. Org. Lett. 2008, 10 (21), 4751–4754.

13) Filippi, M.; Patrucco, D.; Martinelli, J.; Botta, M.; Castro-Hartmann, P.; Tei, L.; Terreno, E. Novel Stable Dendrimersome Formulation for Safe Bioimaging Applications. Nanoscale 2015, 7 (30), 12943–12954.

14) Esfand, R.; Tomalia, D. A. Poly(Amidoamine) (PAMAM) Dendrimers: From Biomimicry to Drug Delivery and Biomedical Applications. Drug Discovery Today 2001, 6 (8), 427–436.

15) He, C.; Hu, Y.; Yin, L.; Tang, C.; Yin, C. Effects of Particle Size and Surface Charge on Cellular Uptake and Biodistribution of Polymeric Nanoparticles. Biomaterials 2010, 31 (13), 3657–3666.

16) Gulino, A. Nanoparticle-Based Delivery of Small Interfering RNA: Challenges for Cancer Therapy. IJN 2012, 3637.

17) Lin, J.; Zhang, H.; Chen, Z.; Zheng, Y. Penetration of Lipid Membranes by Gold Nanoparticles: Insights into Cellular Uptake, Cytotoxicity, and Their Relationship. ACS Nano 2010, 4 (9), 5421–5429.

18) Fröhlich, E. The Role of Surface Charge in Cellular Uptake and Cytotoxicity of Medical Nanoparticles. IJN 2012, 5577.

19) Soenen, S. J.; Rivera-Gil, P.; Montenegro, J.-M.; Parak, W. J.; De Smedt, S. C.; Braeckmans, K. Cellular Toxicity of Inorganic Nanoparticles: Common Aspects and Guidelines for Improved Nanotoxicity Evaluation. Nano Today 2011, 6 (5), 446–465.

20) Abdalla, A. M. E.; Xiao, L.; Ullah, M. W.; Yu, M.; Ouyang, C.; Yang, G. Current Challenges of Cancer Anti-Angiogenic Therapy and the Promise of Nanotherapeutics. Theranostics, 2018, 8, 533–548.

21) Lei, C.; Davoodi, P.; Zhan, W.; Chow, P. K.-H.; Wang, C.-H. Development of Nanoparticles for Drug Delivery to Brain Tumor: The Effect of Surface Materials on Penetration Into Brain Tissue. Journal of Pharmaceutical Sciences 2019, 108 (5), 1736–1745.

22) Olsson, P. A. Signature Fatty Acids Provide Tools for Determination of the Distribution and Interactions of Mycorrhizal Fungi in Soil. FEMS Microbiology Ecology 1999, 29 (4), 303–310.

23) Stenström, P.; Andrén, O.; Malkoch, M. Fluoride-Promoted Esterification (FPE) Chemistry: A Robust Route to Bis-MPA Dendrons and Their Postfunctionalization. Molecules 2016, 21 (3), 366.

24) Worrell, B. T.; Malik, J. A.; Fokin, V. V. Direct Evidence of a Dinuclear Copper Intermediate in Cu(I)-Catalyzed Azide-Alkyne Cycloadditions. Science 2013, 340 (6131), 457–460.

25) Chandrasiri, I.; Abebe, D. G.; Gupta, S.; Williams, J. S. D.; Rieger, W. D.; Simms, B. L.; Yaddehige, M. L.; Noh, Y.; Payne, M. E.; Fortenberry, A. W.; Smith, A. E.; Ilavsky, J.; Grayson, S. M.; Schneider, G. J.; Watkins, D. L. Synthesis and Characterization of Polylactide-PAMAM "Janus-type" Linear-dendritic Hybrids. J. Polym. Sci. Part A: Polym. Chem. 2019, 57 (13), 1448–1459.

26) Tyrrell, Z. L.; Shen, Y.; Radosz, M. Fabrication of Micellar Nanoparticles for Drug Delivery through the Self-Assembly of Block Copolymers. Progress in Polymer Science 2010, 35 (9), 1128–1143.

27) Cho, E. J.; Holback, H.; Liu, K. C.; Abouelmagd, S. A.; Park, J.; Yeo, Y. Nanoparticle Characterization: State of the Art, Challenges, and Emerging Technologies. Mol. Pharmaceutics 2013, 10 (6), 2093–2110.

28) Banik, B. L.; Fattahi, P.; Brown, J. L. Polymeric Nanoparticles: The Future of Nanomedicine. WIREs Nanomed Nanobiotechnol 2015, 8 (2), 271–299.

29) Lobner, D. Comparison of the LDH and MTT Assays for Quantifying Cell Death: Validity for Neuronal Apoptosis Journal of Neuroscience Methods 2000, 96 (2), 147–152

30) Weinstein, S.; Toker, I. A.; Emmanuel, R.; Ramishetti, S.; Hazan-Halevy, I.; Rosenblum, D.; Goldsmith, M.; Abraham, A.; Benjamini, O.; Bairey, O.; Raanani, P.; Nagler, A.;

Lieberman, J.; Peer, D. Harnessing RNAi-Based Nanomedicines for Therapeutic Gene Silencing in B-Cell Malignancies. Proc Natl Acad Sci USA 2015, 113 (1), E16–E22.

31) Warren, N. J.; Armes, S. P. Polymerization-Induced Self-Assembly of Block Copolymer Nano-Objects via RAFT Aqueous Dispersion Polymerization. J. Am. Chem. Soc. 2014, 136 (29), 10174–10185.

32) Penfold, N. J. W.; Yeow, J.; Boyer, C.; Armes, S. P. Emerging Trends in Polymerization-Induced Self-Assembly. ACS Macro Lett. 2019, 8 (8), 1029–1054.

33) Lovett, J. R.; Ratcliffe, L. P. D.; Warren, N. J.; Armes, S. P.; Smallridge, M. J.; Cracknell, R. B.; Saunders, B. R. A Robust Cross-Linking Strategy for Block Copolymer Worms Prepared via Polymerization-Induced Self-Assembly. Macromolecules 2016, 49 (8), 2928–2941.

34) Saha, R. N.; Vasanthakumar, S.; Bende, G.; Snehalatha, M. Nanoparticulate Drug Delivery Systems for Cancer Chemotherapy. Molecular Membrane Biology 2010, 27 (7), 215–231.

35) Liu, C.; Hong, C.-Y.; Pan, C.-Y. Polymerization Techniques in Polymerization-Induced Self-Assembly (PISA). Polym. Chem. 2020, 11 (22), 3673–3689.

36) Canning, S. L.; Smith, G. N.; Armes, S. P. A Critical Appraisal of RAFT-Mediated Polymerization-Induced Self-Assembly. Macromolecules 2016, 49 (6), 1985–2001.

37) Yeow, J.; Boyer, C. Photoinitiated Polymerization-Induced Self-Assembly (Photo-PISA): New Insights and Opportunities. Adv. Sci. 2017, 4 (7), 1700137.

38) Parrott, M. C.; Benhabbour, S. R.; Saab, C.; Lemon, J. A.; Parker, S.; Valliant, J. F.; Adronov, A. Synthesis, Radiolabeling, and Bio-Imaging of High-Generation Polyester Dendrimers. J. Am. Chem. Soc. 2009, 131 (8), 2906–2916.

39) Aughan, R. A.; Gannon, N. P.; Garcia-Smith, R.; Licon-Munoz, Y.; Barberena, M. A.; Bisoffi, M.; Trujillo, K. A. β-Alanine Suppresses Malignant Breast Epithelial Cell Aggressiveness through Alterations in Metabolism and Cellular Acidity in Vitro. Molecular Cancer 2014, 13 (1), 14.

40) Zhang, X.; Rieger, J.; Charleux, B. Effect of the Solvent Composition on the Morphology of Nano-Objects Synthesized via RAFT Polymerization of Benzyl Methacrylate in Dispersed Systems. Polym. Chem. 2012, 3 (6), 1502.

41) Wang, K.; Wang, Y.; Zhang, W. Synthesis of Diblock Copolymer Nano-Assemblies by PISA under Dispersion Polymerization: Comparison between ATRP and RAFT. Polym. Chem. 2017, 8 (41), 6407–6415.

42) Jones, E. R.; Semsarilar, M.; Wyman, P.; Boerakker, M.; Armes, S. P. Addition of Water to an Alcoholic RAFT PISA Formulation Leads to Faster Kinetics but Limits the Evolution of Copolymer Morphology. Polym. Chem. 2016, 7 (4), 851–859.

43) Six, J.L.; Ferji, K. Polymerization Induced Self-Assembly: An Opportunity toward the Self-Assembly of Polysaccharide-Containing Copolymers into High-Order Morphologies. Polym. Chem. 2019, 10 (1), 45–53.

44) Piogé, S.; Tran, T. N.; McKenzie, T. G.; Pascual, S.; Ashokkumar, M.; Fontaine, L.; Qiao, G. Sono-RAFT Polymerization-Induced Self-Assembly in Aqueous Dispersion: Synthesis of LCST-Type Thermosensitive Nanogels. Macromolecules 2018, 51 (21), 8862–8869.

45) Sedlacek, O.; Jirak, D.; Vit, M.; Ziołkowska, N.; Janouskova, O.; Hoogenboom, R. Fluorinated Water-Soluble Poly(2-Oxazoline)s as Highly Sensitive 19F MRI Contrast Agents. Macromolecules 2020, 53 (15), 6387–6395.

46) Zhao, W.; Ta, H. T.; Zhang, C.; Whittaker, A. K. Polymerization-Induced Self-Assembly (PISA) - Control over the Morphology of 19F-Containing Polymeric Nano-Objects for Cell Uptake and Tracking. Biomacromolecules 2017, 18 (4), 1145–1156.

47) Knight, J. C.; Edwards, P. G.; Paisey, S. J. Fluorinated Contrast Agents for Magnetic Resonance Imaging; a Review of Recent Developments. RSC Adv. 2011, 1 (8), 1415.

48) Temme, S.; Bönner, F.; Schrader, J.; Flögel, U. 19 Magnetic Resonance Imaging of Endogenous Macrophages in Inflammation. WIREs Nanomed Nanobiotechnol 2012, 4 (3), 329–343.

49) Srinivas, M.; Heerschap, A.; Ahrens, E. T.; Figdor, C. G.; Vries, I. J. M. de. 19F MRI for Quantitative in Vivo Cell Tracking. Trends in Biotechnology 2010, 28 (7), 363–370.

50) Tirotta, I.; Mastropietro, A.; Cordiglieri, C.; Gazzera, L.; Baggi, F.; Baselli, G.; Bruzzone, M. G.; Zucca, I.; Cavallo, G.; Terraneo, G.; Baldelli Bombelli, F.; Metrangolo, P.; Resnati, G. A Superfluorinated Molecular Probe for Highly Sensitive in Vivo19F-MRI. J. Am. Chem. Soc. 2014, 136 (24), 8524–8527.

51) Partlow, K. C.; Chen, J.; Brant, J. A.; Neubauer, A. M.; Meyerrose, T. E.; Creer, M. H.; Nolta, J. A.; Caruthers, S. D.; Lanza, G. M.; Wicldine, S. A. 19 F Magnetic Resonance Imaging for Stem/Progenitor Cell Tracking with Multiple Unique Perfluorocarbon Nanobeacons. FASEB j. 2007, 21 (8), 1647–1654.

52) Neal, M. A.; Pippard, B. J.; Hollingsworth, K. G.; Maunder, A.; Dutta, P.; Simpson, A. J.; Blamire, A. M.; Wild, J. M.; Thelwall, P. E. Optimized and Accelerated 19 F-MRI of Inhaled Perfluoropropane to Assess Regional Pulmonary Ventilation. Magn Reson Med 2019, 82 (4), 1301–1311.

53) Sedlacek, O.; Jirak, D.; Galisova, A.; Jager, E.; Laaser, J. E.; Lodge, T. P.; Stepanek, P.; Hruby, M. 19F Magnetic Resonance Imaging of Injectable Polymeric Implants with Multiresponsive Behavior. Chem. Mater. 2018, 30 (15), 4892–4896.

54) Anselmo, A. C.; Zhang, M.; Kumar, S.; Vogus, D. R.; Menegatti, S.; Helgeson, M. E.; Mitragotri, S. Elasticity of Nanoparticles Influences Their Blood Circulation, Phagocytosis, Endocytosis, and Targeting. ACS Nano 2015, 9 (3), 3169–3177.

55) Talelli, M.; Barz, M.; Rijcken, C. J. F.; Kiessling, F.; Hennink, W. E.; Lammers, T. Core-Crosslinked Polymeric Micelles: Principles, Preparation, Biomedical Applications and Clinical Translation. Nano Today 2015, 10 (1), 93–117.

56) Israelachvili, J. N.; Mitchell, D. J.; Ninham, B. W. Theory of Self-Assembly of Hydrocarbon Amphiphiles into Micelles and Bilayers. Journal of the Chemical Society, Faraday Transactions 2, 1976, 72, 1525.

57) Canning, S. L.; Smith, G. N.; Armes, S. P. A Critical Appraisal of RAFT-Mediated Polymerization-Induced Self-Assembly. Macromolecules, 2016, 49, 1985–2001

58) lanazs, A.; Armes, S. P.; Ryan, A. J. Self-Assembled Block Copolymer Aggregates: From Micelles to Vesicles and Their Biological Applications. Macromol. Rapid Commun. 2009, 30 (4–5), 267–277.

59) Israelachvili, J. N.; Mitchell, D. J.; Ninham, B. W. Theory of Self-Assembly of Lipid Bilayers and Vesicles. Biochim. Biophys. Acta - Biomembr. 1977, 470 (2), 185–201.

60) Mai, Y.; Eisenberg, A. Self-Assembly of Block Copolymers. Chem. Soc. Rev. 2012, 41 (18), 5969.

61) Lu, X.-Y.; Wu, D.-C.; Li, Z.-J.; Chen, G.-Q. Polymer Nanoparticles; 2011; pp 299–323

62) Kataoka, K.; Harada, A.; Nagasaki, Y. Block Copolymer Micelles for Drug Delivery: Design, Characterization and Biological Significance. Adv. Drug Deliv. Rev. 2001, 47 (1), 113–131.

63) Torchilin, V. P. Micellar Nanocarriers: Pharmaceutical Perspectives. Pharm. Res. 2006, 24 (1), 1–16.

64) Aliabadi, H. M.; Lavasanifar, A. Polymeric Micelles for Drug Delivery. Expert Opin. Drug Deliv. 2006, 3 (1), 139–162.

65) Lu, Y.; Park, K. Polymeric Micelles and Alternative Nanonized Delivery Vehicles for Poorly Soluble Drugs. Int. J. Pharm. 2013, 453 (1), 198–214.

66) Washington, K. E.; Kularatne, R. N.; Karmegam, V.; Biewer, M. C.; Stefan, M. C. Recent Advances in Aliphatic Polyesters for Drug Delivery Applications. Wiley Interdiscip. Rev. Nanomedicine Nanobiotechnology 2017, 9 (4), e1446.

67) Nagaya, T.; Nakamura, Y. A.; Choyke, P. L.; Kobayashi, H. Fluorescence-Guided Surgery. Frontiers in Oncology, 2017, 7.

68) Landau, M. J.; Gould, D. J.; Patel, K. M. Advances in Fluorescent-Image Guided Surgery. Annals of Translational Medicine, 2016, 4, 392–392

69) Wang, S.; Li, B.; Zhang, F. Molecular Fluorophores for Deep-Tissue Bioimaging. ACS Central Science, 2020, 6, 1302–1316

70) Barroso, M. M. Quantum Dots in Cell Biology. Journal of Histochemistry & Cytochemistry, 2011, 59, 237–251.

71) Cao, J.; Zhu, B.; Zheng, K.; He, S.; Meng, L.; Song, J.; Yang, H. Recent Progress in NIR-II Contrast Agent for Biological Imaging. Frontiers in Bioengineering and Biotechnology, 2020, 7.

72) Yang, Q.; Ma, H.; Liang, Y.; Dai, H. Rational Design of High Brightness NIR-II Organic Dyes with S-D-A-D-S Structure. Accounts of Materials Research, 2021, 2, 170–183.

73) Stamentović, V.; Collado, D.; Perez-Inestrosa, E. Photophysical Properties and Bioimaging Application of an Aminonaphthalimide-Squaraine Non-Conjugated System. Spectrochimica Acta Part A: Molecular and Biomolecular Spectroscopy, 2022, 267, 120546.

74) Rizvi, S. B.; Ghaderi, S.; Keshtgar, M.; Seifalian, A. M. Semiconductor Quantum Dots as Fluorescent Probes for in Vitro and in Vivo Bio-Molecular and Cellular Imaging. Nano Reviews, 2010, 1, 5161.

75) de Crespigny, A.; Bou-Reslan, H.; Nishimura, M. C.; Phillips, H.; Carano, R. A. D.; D'Arceuil, H. E. 3D Micro-CT Imaging of the Postmortem Brain. Journal of Neuroscience Methods, 2008, 171, 207–213.

76) Bydder, G. M. The Agfa Mayneord Lecture: MRI of Short and UltrashortT2andT2* Components of Tissues, Fluids and Materials Using Clinical Systems. The British Journal of Radiology, 2011, 84, 1067–1082.

77) Busato, A.; Fumene Feruglio, P.; Parnigotto, P. P.; Marzola, P.; Sbarbati, A. In Vivo Imaging Techniques: A New Era for Histochemical Analysis. European Journal of Histochemistry, 2016.

78) Sedlacek, O.; Jirak, D.; Vit, M.; Ziołkowska, N.; Janouskova, O.; Hoogenboom, R. Fluorinated Water-Soluble Poly(2-Oxazoline)s as Highly Sensitive 19F MRI Contrast Agents. Macromolecules 2020, 53 (15), 6387–6395.

79) Zhao, W.; Ta, H. T.; Zhang, C.; Whittaker, A. K. Polymerization-Induced Self-Assembly (PISA) - Control over the Morphology of 19F-Containing Polymeric Nano-Objects for Cell Uptake and Tracking. Biomacromolecules 2017, 18 (4), 1145–1156.

80) Knight, J. C.; Edwards, P. G.; Paisey, S. J. Fluorinated Contrast Agents for Magnetic Resonance Imaging; a Review of Recent Developments. RSC Adv. 2011, 1 (8), 1415.

81) Temme, S.; Bönner, F.; Schrader, J.; Flögel, U. 19 Magnetic Resonance Imaging of Endogenous Macrophages in Inflammation. WIREs Nanomed Nanobiotechnol 2012, 4 (3), 329–343.

82) Srinivas, M.; Heerschap, A.; Ahrens, E. T.; Figdor, C. G.; Vries, I. J. M. de. 19F MRI for Quantitative in Vivo Cell Tracking. Trends in Biotechnology 2010, 28 (7), 363–370.

83) D. R. Sikwal, R. S. Kalhapure and T. Govender, Eur J Pharm Sci, 2017, 97, 113-134.

84) Caminade, R. Laurent, B. Delavaux-Nicot and J.-P. Majoral, New J. Chem., 2012, 36, 217-226.

85) V. Percec, D. A. Wilson, P. Leowanawat, C. J. Wilson, A. D. Hughes, M. S. Kaucher, D. A. Hammer, D. H. Levine, A. J. Kim and F. S. Bates, Science, 2010, 328, 1009-1014.

86) M. Selin, L. Peltonen, J. Hirvonen and L. M. Bimbo, Journal of Drug Delivery Science and Technology, 2016, 34, 10-20.

87) K. L. Wooley, C. J. Hawker and J. M. J. Frechet, J. Am. Chem. Soc., 1993, 115, 11496-11505.

88) M. Peterca, V. Percec, P. Leowanawat and A. Bertin, J. Am. Chem. Soc., 2011, 133, 20507-20520.

89) V. Percec, P. Leowanawat, H.-J. Sun, O. Kulikov, C. D. Nusbaum, T. M. Tran, A. Bertin, D. A. Wilson, M. Peterca and S. Zhang, J. Am. Chem. Soc., 2013, 135, 9055-9077.

90) S. Zhang, H.-J. Sun, A. D. Hughes, R.-O. Moussodia, A. Bertin, Y. Chen, D. J. Pochan, P. A. Heiney, M. L. Klein and V. Percec, Proceedings of the National Academy of Sciences, 2014, 111, 9058-9063.

91) Z. Yang, A. H. Muller, C. Xu, P. S. Doyle, J. M. DeSimone, J. Lahann, F. Sciortino, S. Glotzer, L. Hong and D. A. Aarts, Janus particle synthesis, self-assembly and applications, Royal Society of Chemistry, 2012.

92) L. Ouyang, L. Ma, Y. Li, J. Pan and L. Guo, ARKIVOC: Online Journal of Organic Chemistry, 2010.

93) J. Pan, L. Ma, Y. Zhao, J. Zhao, L. Ouyang and L. Guo, Synlett, 2013, 24, 1011-1015.

94) J. Salmen, M. Banys-Paluchowski and T. Fehm, Geburtshilfe und Frauenheilkunde, 2015, 75, 584.

95) S. Fuchs, A. Pla-Quintana, S. Mazeres, A.-M. Caminade and J.-P. Majoral, Org. Lett., 2008, 10, 4751-4754.

96) M. Filippi, D. Patrucco, J. Martinelli, M. Botta, P. Castro-Hartmann, L. Tei and E. Terreno, Nanoscale, 2015, 7, 12943-12954.

97) M. Labieniec-Watala and C. Watala, J. Pharm. Sci., 2015, 104, 2-14.

98) A. L. Acton, C. Fante, B. Flatley, S. Burattini, I. W. Hamley, Z. Wang, F. Greco and W. Hayes, Biomacromolecules, 2013, 14, 564-574.

99) E. Fröhlich, International journal of nanomedicine, 2012, 7, 5577.

100) Y. Hu, X. Gong, J. Zhang, F. Chen, C. Fu, P. Li, L. Zou and G. Zhao, Polymers, 2016, 8, 99.

101) K. Kobayashi, J. Wei, R. Iida, K. Ijiro and K. Niikura, Polym. J., 2014, 46, 460-468.

102) B. Ozpolat, A. K. Sood and G. Lopez-Berestein, Advanced drug delivery reviews, 2014, 66, 110-116.

103) B. Ozpolat, A. K. Sood and G. Lopez-Berestein, Journal of internal medicine, 2010, 267, 44-53.

104) T. Stylianopoulos, M.-Z. Poh, N. Insin, M. G. Bawendi, D. Fukumura, L. L. Munn and R. K. Jain, Biophys. J., 2010, 99, 1342-1349.

105) H. Cabral, Y. Matsumoto, K. Mizuno, Q. Chen, M. Murakami, M. Kimura, Y. Terada, M. Kano, K. Miyazono and M. Uesaka, Nature nanotechnology, 2011, 6, 815-823.

106) B. L. Banik, P. Fattahi and J. L. Brown, WIREs Nanomedicine and Nanobiotechnology, 2016, 8, 271-299.

107) S. Taabache and A. Bertin, Polymers, 2017, 9, 280.

108) T. Delmas, A.-C. Couffin, P. A. Bayle, F. De Crecy, E. Neumann, F. Vinet, M. Bardet, J. Bibette and I. Texier, J. Colloid Interface Sci., 2011, 360, 471-481.

109) A. F. Thünemann and S. General, J. Controlled Release, 2001, 75, 237-247.

110) S. R. Youngren, R. K. Tekade, B. Gustilo, P. R. Hoffmann and M. B. Chougule, BioMed research international, 2013, 2013.

111) L. Espana-Serrano and M. B. Chougule, Molecular Therapy-Nucleic Acids, 2016, 5, e384.

112) R. Esfand and D. A. Tomalia, Drug Discovery Today, 2001, 6, 427-436.

113) I. Chandrasiri, D. G. Abebe, S. Gupta, J. S. D. Williams, W. D. Rieger, B. L. Simms, M. L. Yaddehige, Y. Noh, M. E. Payne and A. W. Fortenberry, J. Polym. Sci., Part A: Polym. Chem., 2019, 57, 1448-1459.

114) (114). L. J. Fox, R. M. Richardson and W. H. Briscoe, Adv. Colloid Interface Sci., 2018, 257, 1-18.

115) J. Bugno, H.-j. Hsu and S. Hong, Journal of drug targeting, 2015, 23, 642-650.

116) C. C. De Carvalho and M. J. Caramujo, Molecules, 2018, 23, 2583.

117) S. García-Gallego, D. Hult, J. V. Olsson and M. Malkoch, Angew. Chem. Int. Ed., 2015, 54, 2416-2419.

118) D. Lombardo, M. A. Kiselev, S. Magazù and P. Calandra, Advances in Condensed Matter Physics, 2015, 2015, 151683.

119) J. Košmrlj, Click triazoles, Springer, 2012.

120) S. Shukla, S. K. Shukla, P. P. Govender and N. Giri, RSC advances, 2016, 6, 94325-94351.

121) B. Lu, X. Lv and Y. Le, Polymers, 2019, 11, 304.

122) L. Piñeiro Maseda, M. d. l. M. Novo Rodríguez and W. Al-Soufi, 2015.

123) H. Yin, S.-W. Kang and Y. H. Bae, Macromolecules, 2009, 42, 7456-7464.

124) A. Lancelot, R. Clavería-Gimeno, A. Velázquez-Campoy, O. Abian, J. L. Serrano and T. Sierra, Eur. Polym. J., 2017, 90, 136-149.

125) E. J. Cho, H. Holback, K. C. Liu, S. A. Abouelmagd, J. Park and Y. Yeo, Molecular pharmaceutics, 2013, 10, 2093-2110.

126) C. He, Y. Hu, L. Yin, C. Tang and C. Yin, Biomaterials, 2010, 31, 3657-3666.

127) F. S. Mozar and E. H. Chowdhury, Current Pharmaceutical Design, 2018, 24, 3283-3296.

128) A. Chung, Q. Gao and W. J. Kao, Biomaterials, 2007, 28, 285-298.

129) M. E. Eichhorn, I. Ischenko, S. Luedemann, S. Strieth, A. Papyan, A. Werner, H. Bohnenkamp, E. Guenzi, G. Preissler and U. Michaelis, International journal of cancer, 2010, 126, 1235-1245.

130) S. Weinstein, I. A. Toker, R. Emmanuel, S. Ramishetti, I. Hazan-Halevy, D. Rosenblum, M. Goldsmith, A. Abraham, O. Benjamini and O. Bairey, Proceedings of the National Academy of Sciences, 2016, 113, E16-E22.

131) P. C. Naha, S. P. Mukherjee and H. J. Byrne, International journal of environmental research and public health, 2018, 15, 338.

132) R. S. Navath, A. R. Menjoge, B. Wang, R. Romero, S. Kannan and R. M. Kannan, Biomacromolecules, 2010, 11, 1544-1563.

133) S. Kannan, P. Kolhe, V. Raykova, M. Glibatec, R. M. Kannan, M. Lieh-Lai and D. Bassett, Journal of Biomaterials Science, Polymer Edition, 2004, 15, 311-330.

134) A. Janaszewska, J. Lazniewska, P. Trzepiński, M. Marcinkowska and B. Klajnert-Maculewicz, Biomolecules, 2019, 9.

135) S. Lee, M. C. Choi, K. Al Adem, S. Lukman and T.-Y. Kim, Scientific Reports, 2020, 10, 5120.

136) Bolu, B. S.; Sanyal, R.; Sanyal, A., Drug Delivery Systems from Self-Assembly of Dendron-Polymer Conjugates †. Molecules 2018, 23, 1570.

137) Chen, W.; Kretzschmann, A.; Tian, W.; Wu, S., Nonlinear Supramolecular Polymers for Therapeutic Applications. Advanced Therapeutics 2019, 2, 1800103.

138) Hsu, H.-J.; Bugno, J.; Lee, S.-r.; Hong, S., Dendrimer-Based Nanocarriers: A Versatile Platform for Drug Delivery. WIREs Nanomedicine and Nanobiotechnology 2017, 9, e1409.

139) Yasen, W.; Dong, R.; Aini, A.; Zhu, X., Recent Advances in Supramolecular Block Copolymers for Biomedical Applications. Journal of Materials Chemistry B 2020, 8, 8219-8231.

140) Funkhouser, J., Reinventing Pharma: The Theranostic Revolution. Current Drug Discovery 2002, 17-19.

141) Amoabediny, G.; Haghiralsadat, F.; Naderinezhad, S.; Helder, M. N.; Akhoundi Kharanaghi, E.; Mohammadnejad Arough, J.; Zandieh-Doulabi, B., Overview of Preparation Methods of Polymeric and Lipid-Based (Niosome, Solid Lipid, Liposome) Nanoparticles: A Comprehensive Review. International Journal of Polymeric Materials and Polymeric Biomaterials 2018, 67, 383-400.

142) B.K. Johnson, R.K. Prud'homme, Mechanism for rapid self-assembly of block copolymer nanoparticles, Phys. Rev. Lett. 91(11) (2003) 118302.

143) Hanemann, T.; Szabó, D. V., Polymer-Nanoparticle Composites: From Synthesis to Modern Applications. Materials 2010, 3, 3468-3517.

144) Lv, F.; An, Z.; Wu, P., Scalable Preparation of Alternating Block Copolymer Particles with Inverse Bicontinuous Mesophases. Nature Communications 2019, 10, 1397.

145) Khor, S. Y.; Quinn, J. F.; Whittaker, M. R.; Truong, N. P.; Davis, T. P., Controlling Nanomaterial Size and Shape for Biomedical Applications Via Polymerization-Induced Self-Assembly. Macromolecular Rapid Communications 2019, 40, 1800438.

146) Penfold, N. J. W.; Yeow, J.; Boyer, C.; Armes, S. P., Emerging Trends in Polymerization-Induced Self-Assembly. ACS Macro Letters 2019, 8, 1029-1054.

147) Canning, S. L.; Smith, G. N.; Armes, S. P., A Critical Appraisal of Raft-Mediated Polymerization-Induced Self-Assembly. 2016, 49, 1985-2001.

148) Lowe, A. B., Raft Alcoholic Dispersion Polymerization with Polymerization-Induced Self-Assembly. 2016.

149) Armes, S. P.; Perrier, S.; Zetterlund, P. B., Introduction to Polymerization-Induced Self Assembly. Polymer Chemistry 2021, 12, 8-11.

150) Charleux, B.; Delaittre, G.; Rieger, J.; D'Agosto, F., Polymerization-Induced Self-Assembly: From Soluble Macromolecules to Block Copolymer Nano-Objects in One Step. Macromolecules 2012, 45, 6753-6765.

151) Warren, N. J.; Armes, S. P., Polymerization-Induced Self-Assembly of Block Copolymer Nano-Objects Via Raft Aqueous Dispersion Polymerization. Journal of the American Chemical Society 2014, 136, 10174-10185.

152) Siirilä, J.; Häkkinen, S.; Tenhu, H., The Emulsion Polymerization Induced Self-Assembly of a Thermoresponsive Polymer Poly(N -Vinylcaprolactam). 2018, 10, 766-775.

153) Zhou, J.; Yao, H.; Ma, J., Recent Advances in Raft-Mediated Surfactant-Free Emulsion Polymerization. Polymer Chemistry 2018, 9, 2532-2561.

154) Carlsson, L.; Fall, A.; Chaduc, I.; W\aagberg, L.; Charleux, B.; Malmström, E.; D'Agosto, F.; Lansalot, M.; Carlmark, A., Modification of Cellulose Model Surfaces by Cationic Polymer Latexes Prepared by Raft-Mediated Surfactant-Free Emulsion Polymerization. Polymer Chemistry 2014, 5, 6076-6086.

155) Malkoch, M.; Malmström, E.; Hult, A., Rapid and Efficient Synthesis of Aliphatic Ester Dendrons and Dendrimers. Macromolecules 2002, 35, 8307-8314.

156) Malkoch, M.; García-Gallego, S., Chapter 2 Bis-Mpa Dendrimers and Other Dendritic Polyesters. In Dendrimer Chemistry: Synthetic Approaches Towards Complex Architectures, The Royal Society of Chemistry: 2020; pp 21-57.

157) Derry, M. J.; Fielding, L. A.; Armes, S. P., Industrially-Relevant Polymerization-Induced Self-Assembly Formulations in Non-Polar Solvents: Raft Dispersion Polymerization of Benzyl Methacrylate. Polymer Chemistry 2015, 6, 3054-3062.

158) Guida, V., Thermodynamics and Kinetics of Vesicles Formation Processes. 2010, 161, 77-88.

159) Cunningham, V. J.; Alswieleh, A. M.; Thompson, K. L.; Williams, M.; Leggett, G. J.; Armes, S. P.; Musa, O. M. Poly(Glycerol Monomethacrylate)–Poly(Benzyl Methacrylate) Diblock Copolymer Nanoparticles via RAFT Emulsion Polymerization: Synthesis, Characterization, and Interfacial Activity. Macromolecules, 2014, 47, 5613–5623.

160) Cui, H.; Chen, Z.; Zhong, S.; Wooley, K. L.; Pochan, D. J., Block Copolymer Assembly Via Kinetic Control. Science 2007, 317, 647-650.

161) Rieger, J., Guidelines for the Synthesis of Block Copolymer Particles of Various Morphologies by Raft Dispersion Polymerization. Macromolecular Rapid Communications 2015, 36, 1458-1471.

162) Walter, M. V.; Malkoch, M., Simplifying the Synthesis of Dendrimers: Accelerated Approaches. Chemical Society Reviews 2012, 41, 4593-4609.

163) Arseneault, M.; Wafer, C.; Morin, J.-F., Recent Advances in Click Chemistry Applied to Dendrimer Synthesis. Molecules (Basel, Switzerland) 2015, 20, 9263-9294.

164) Pei, Y.; Noy, J.-M.; Roth, P. J.; Lowe, A. B., Thiol-Reactive Passerini-Methacrylates and Polymorphic Surface Functional Soft Matter Nanoparticles Via Ethanolic Raft Dispersion Polymerization and Post-Synthesis Modification. 2015, 6, 1928-1931.

165) Zhao, W.; Ta, H. T.; Zhang, C.; Whittaker, A. K., Polymerization-Induced Self-Assembly (Pisa) - Control over the Morphology of 19f-Containing Polymeric Nano-Objects for Cell Uptake and Tracking. Biomacromolecules 2017, 18, 1145-1156.

166) Yaddehige, M. L.; Chandrasiri, I.; Barker, A.; Kotha, A. K.; Dal Williams, J. S.; Simms, B.; Kucheryavy, P.; Abebe, D. G.; Chougule, M. B.; Watkins, D. L. Structural and Surface Properties of Polyamidoamine (PAMAM) – Fatty Acid-based Nanoaggregates Derived from Self-assembling Janus Dendrimers. ChemNanoMat, 2020, 6, 1833–1842. (167). Mai, Y.; Eisenberg, A., Self-Assembly of Block Copolymers. Chemical Society Reviews 2012, 41, 5969-5985.

167) Johnson, B. K.; Prud'homme, R. K., Mechanism for Rapid Self-Assembly of Block Copolymer Nanoparticles. Physical Review Letters 2003, 91, 118302.

168) Feng, H.; Lu, X.; Wang, W.; Kang, N.-G.; Mays, J. W., Block Copolymers: Synthesis, Self-Assembly, and Applications. Polymers 2017, 9, 494.

169) Zaquen, N.; Azizi, W. A. A. W.; Yeow, J.; Kuchel, R. P.; Junkers, T.; Zetterlund, P. B.; Boyer, C., Alcohol-Based Pisa in Batch and Flow: Exploring the Role of Photoinitiators. Polymer Chemistry 2019, 10, 2406-2414.

170) Stenström, P.; Manzanares, D.; Zhang, Y.; Ceña, V.; Malkoch, M., Evaluation of Amino-Functional Polyester Dendrimers Based on Bis-Mpa as Nonviral Vectors for Sirna Delivery. Molecules 2018, 23, 2028.

171) Stenström, P.; Hjorth, E.; Zhang, Y.; Andrén, O. C. J.; Guette-Marquet, S.; Schultzberg, M.; Malkoch, M., Synthesis and in Vitro Evaluation of Monodisperse Amino-Functional Polyester Dendrimers with Rapid Degradability and Antibacterial Properties. Biomacromolecules 2017, 18, 4323-4330.

172) Pei, Y.; Lowe, A. B., Polymerization-Induced Self-Assembly: Ethanolic Raft Dispersion Polymerization of 2-Phenylethyl Methacrylate. Polymer Chemistry 2014, 5, 2342-2351.

173) Khor, S. Y.; Truong, N. P.; Quinn, J. F.; Whittaker, M. R.; Davis, T. P., Polymerization-Induced Self-Assembly: The Effect of End Group and Initiator Concentration on Morphology of Nanoparticles Prepared Via Raft Aqueous Emulsion Polymerization. ACS Macro Letters 2017, 6, 1013-1019.

174) Jones, E. R.; Semsarilar, M.; Wyman, P.; Boerakker, M.; Armes, S. P., Addition of Water to an Alcoholic Raft Pisa Formulation Leads to Faster Kinetics but Limits the Evolution of Copolymer Morphology. 2015, 7, 851-859.

175) Rajagopal, K.; Mahmud, A.; Christian, D. A.; Pajerowski, J. D.; Brown, A. E.; Loverde, S. M.; Discher, D. E., Curvature-Coupled Hydration of Semicrystalline Polymer Amphiphiles Yields Flexible Worm Micelles but Favors Rigid Vesicles: Polycaprolactone-Based Block Copolymers. Macromolecules 2010, 43, 9736-9746.

176) Evans, B. C.; Nelson, C. E.; Yu, S. S.; Beavers, K. R.; Kim, A. J.; Li, H.; Nelson, H. M.; Giorgio, T. D.; Duvall, C. L. Ex Vivo</Em> Red Blood Cell Hemolysis Assay for the Evaluation of PH-Responsive Endosomolytic Agents for Cytosolic Delivery of Biomacromolecular Drugs. Journal of Visualized Experiments, 2013.

177) Pham, C. T. N.; Thomas, D. G.; Beiser, J.; Mitchell, L. M.; Huang, J. L.; Senpan, A.; Hu, G.; Gordon, M.; Baker, N. A.; Pan, D.; Lanza, G. M.; Hourcade, D. E. Application of a Hemolysis Assay for Analysis of Complement Activation by Perfluorocarbon Nanoparticles. Nanomedicine: Nanotechnology, Biology and Medicine, 2014, 10, 651–660.

178) Amin, K.; Dannenfelser, R.-M. In Vitro Hemolysis: Guidance for the Pharmaceutical Scientist. Journal of Pharmaceutical Sciences, 2006, 95, 1173–1176.

179) Zhao, W.; Ta, H. T.; Zhang, C.; Whittaker, A. K. Polymerization-Induced Self-Assembly (PISA) - Control over the Morphology of 19F-Containing Polymeric Nano-Objects for Cell Uptake and Tracking. Biomacromolecules 2017, 18 (4), 1145–1156.

180) Sedlacek, O.; Jirak, D.; Vit, M.; Ziołkowska, N.; Janouskova, O.; Hoogenboom, R. Fluorinated Water-Soluble Poly(2-Oxazoline)s as Highly Sensitive 19F MRI Contrast Agents. Macromolecules 2020, 53 (15), 6387–6395.

181) Piogé, S.; Tran, T. N.; McKenzie, T. G.; Pascual, S.; Ashokkumar, M.; Fontaine, L.; Qiao, G. Sono-RAFT Polymerization-Induced Self-Assembly in Aqueous Dispersion: Synthesis of LCST-Type Thermosensitive Nanogels. Macromolecules 2018, 51 (21), 8862–8869.

182) Knight, J. C.; Edwards, P. G.; Paisey, S. J. Fluorinated Contrast Agents for Magnetic Resonance Imaging; a Review of Recent Developments. RSC Adv. 2011, 1 (8), 1415.

183) Temme, S.; Bönner, F.; Schrader, J.; Flögel, U. 19 Magnetic Resonance Imaging of Endogenous Macrophages in Inflammation. WIREs Nanomed Nanobiotechnol 2012, 4 (3), 329–343.

184) Srinivas, M.; Heerschap, A.; Ahrens, E. T.; Figdor, C. G.; Vries, I. J. M. de. 19F MRI for Quantitative in Vivo Cell Tracking. Trends in Biotechnology 2010, 28 (7), 363–370.

185) Tirotta, I.; Mastropietro, A.; Cordiglieri, C.; Gazzera, L.; Baggi, F.; Baselli, G.; Bruzzone, M. G.; Zucca, I.; Cavallo, G.; Terraneo, G.; Baldelli Bombelli, F.; Metrangolo, P.; Resnati, G. A Superfluorinated Molecular Probe for Highly Sensitive in Vivo19F-MRI. J. Am. Chem. Soc. 2014, 136 (24), 8524–8527.

186) Partlow, K. C.; Chen, J.; Brant, J. A.; Neubauer, A. M.; Meyerrose, T. E.; Creer, M. H.; Nolta, J. A.; Caruthers, S. D.; Lanza, G. M.; Wicldine, S. A. 19 F Magnetic Resonance Imaging for Stem/Progenitor Cell Tracking with Multiple Unique Perfluorocarbon Nanobeacons. FASEB j. 2007, 21 (8), 1647–1654.

187) Neal, M. A.; Pippard, B. J.; Hollingsworth, K. G.; Maunder, A.; Dutta, P.; Simpson, A. J.; Blamire, A. M.; Wild, J. M.; Thelwall, P. E. Optimized and Accelerated 19 F-MRI of Inhaled Perfluoropropane to Assess Regional Pulmonary Ventilation. Magn Reson Med 2019, 82 (4), 1301–1311.

188) Moore, T. L.; Rodriguez-Lorenzo, L.; Hirsch, V.; Balog, S.; Urban, D.; Jud, C.; Rothen-Rutishauser, B.; Lattuada, M.; Petri-Fink, A. Nanoparticle Colloidal Stability in Cell Culture Media and Impact on Cellular Interactions. Chem. Soc. Rev. 2015, 44 (17), 6287–6305.

189) Shi, H.; He, X.; Yuan, Y.; Wang, K.; Liu, D. Nanoparticle-Based Biocompatible and Long-Life Marker for Lysosome Labeling and Tracking. Anal. Chem. 2010, 82 (6), 2213–2220.

190) Griffiths, G.; Hoflack, B.; Simons, K.; Mellman, I.; Kornfeld, S. The Mannose 6-Phosphate Receptor and the Biogenesis of Lysosomes. Cell 1988, 52 (3), 329–341.

191) Duong, T.; Li, X.; Yang, B.; Schumann, C.; Albarqi, H. A.; Taratula, O.; Taratula, O. Phototheranostic Nanoplatform Based on a Single Cyanine Dye for Image-Guided Combinatorial Phototherapy. Nanomedicine Nanotechnology, Biol. Med. 2017, 13 (3), 955–963.

192) Smith, B. R.; Gambhir, S. S. Nanomaterials for In Vivo Imaging. Chem. Rev. 2017, 117 (3), 901–986.

193) Lu, Y.; Zhang, E.; Yang, J.; Cao, Z. Strategies to Improve Micelle Stability for Drug Delivery. Nano Res. 2018, 11 (10), 4985–4998.

194) Nelemans, L. C.; Gurevich, L. Drug Delivery with Polymeric Nanocarriers—Cellular Uptake Mechanisms. Materials (Basel). 2020, 13 (2), 366.

195) Hornig, S.; Heinze, T.; Becer, C. R.; Schubert, U. S. Synthetic Polymeric Nanoparticles by Nanoprecipitation. J. Mater. Chem. 2009, 19 (23), 3838.

196) Chandrasiri, I.; Abebe, D. G.; Loku Yaddehige, M.; Williams, J. S. D.; Zia, M. F.; Dorris, A.; Barker, A.; Simms, B. L.; Parker, A.; Vinjamuri, B. P.; Le, N.; Gayton, J. N.; Chougule, M. B.; Hammer, N. I.; Flynt, A.; Delcamp, J. H.; Watkins, D. L. Self-Assembling PCL–PAMAM Linear Dendritic Block Copolymers (LDBCs) for Bioimaging and Phototherapeutic Applications. ACS Appl. Bio Mater. 2020, 3 (9), 5664–5677.

197) Ulbrich, K.; Holá, K.; Šubr, V.; Bakandritsos, A.; Tuček, J.; Zbořil, R. Targeted Drug Delivery with Polymers and Magnetic Nanoparticles: Covalent and Noncovalent Approaches, Release Control, and Clinical Studies. Chem. Rev. 2016, 116 (9), 5338–5431.

198) Deng, C.; Jiang, Y.; Cheng, R.; Meng, F.; Zhong, Z. Biodegradable Polymeric Micelles for Targeted and Controlled Anticancer Drug Delivery: Promises, Progress and Prospects. Nano Today 2012, 7 (5), 467–480.

199) Ballesteros, C. A. S.; Correa, D. S.; Zucolotto, V. Polycaprolactone Nanofiber Mats Decorated with Photoresponsive Nanogels and Silver Nanoparticles: Slow Release for Antibacterial Control. Mater. Sci. Eng. C 2020, 107, 110334.

200) Mavila, S.; Eivgi, O.; Berkovich, I.; Lemcoff, N. G. Intramolecular Cross-Linking Methodologies for the Synthesis of Polymer Nanoparticles. Chem. Rev. 2016, 116 (3), 878–961.

201) Dalvi, V. H.; Rossky, P. J. Molecular Origins of Fluorocarbon Hydrophobicity. Proceedings of the National Academy of Sciences, 2010, 107, 13603–13607.

202) Zhang, Y., Wang, Y., Zhang, H. et al. Synthesis and Surface-Active Behavior of New Fluorinated Hyperbranched Polymer. J Surfact Deterg 17, 967–975 (2014).

203) Wang, C., Li, X., Du, B. et al. Preparation and properties of a novel waterborne fluorinated polyurethane–acrylate hybrid emulsion. Colloid Polym Sci 292, 579–587 (2014).

204) Ranathunge, T. A.; Yaddehige, M. L.; Varma, J. H.; Smith, C.; Nguyen, J.; Owolabi, I.; Kolodziejczyk, W.; Hammer, N. I.; Hill, G.; Flynt, A.; Watkins, D. L. Heteroacene-Based Amphiphile as a Molecular Scaffold for Bioimaging Probes. Frontiers in Chemistry, 2021, 9.

205) Buwalda, S.; Al Samad, A.; El Jundi, A.; Bethry, A.; Bakkour, Y.; Coudane, J.; Nottelet, B. Stabilization of Poly(Ethylene Glycol)-Poly(ε-Caprolactone) Star Block Copolymer Micelles via Aromatic Groups for Improved Drug Delivery Properties. J. Colloid Interface Sci. 2018, 514, 468–478.

206) Sedlacek, O.; Jirak, D.; Galisova, A.; Jager, E.; Laaser, J. E.; Lodge, T. P.; Stepanek, P.; Hruby, M. 19F Magnetic Resonance Imaging of Injectable Polymeric Implants with Multiresponsive Behavior. Chem. Mater. 2018, 30 (15), 4892–4896.

207) Pavlova, O.S., Gulyaev, M.V., Anisimov, N.V. et al. New Aspects of Biodistribution of Perfluorocarbon Emulsions in Rats: Thymus Imaging. Appl Magn Reson 51, 1625–1635 (2020).

208) Ndaleh, D.; Smith, C.; Loku Yaddehige, M.; Shaik, A. K.; Watkins, D. L.; Hammer, N. I.; Delcamp, J. H. Shortwave Infrared Absorptive and Emissive Pentamethine-Bridged Indolizine Cyanine Dyes. The Journal of Organic Chemistry, 2021, 86, 15376–15386.

209) Gayton, J.; Autry, S. A.; Meador, W.; Parkin, S. R.; Hill, G. A., Jr.; Hammer, N. I.; Delcamp, J. H. Indolizine-Cyanine Dyes: Near Infrared Emissive Cyanine Dyes with Increased Stokes Shifts. The Journal of Organic Chemistry, 2018, 84, 687–697.

210) D. A. Tomalia, A. M. Naylor and W. A. Goddard III, Angewandte Chemie International Edition in English, 1990, 29, 138-175.

211) I. J. Majoros, C. R. Williams, D. A. Tomalia and J. R. Baker, Macromolecules, 2008, 41, 8372-8379.

212) J. W. Lee, J. H. Kim, B.-K. Kim, J. H. Kim, W. S. Shin and S.-H. Jin, Tetrahedron, 2006, 62, 9193-9200.

213) C. Gao, M. Liu, S. Lü, X. Zhang and Y. Chen, Materials Research Express, 2014, 1, 015005.

214) B. Kumar, M. A. Aga, A. Rouf, B. A. Shah and S. C. Taneja, RSC Advances, 2014, 4, 21121-21130.

215) J. Sun, W. Birnbaum, J. Anderski, M.-T. Picker, D. Mulac, K. Langer and D. Kuckling, Biomacromolecules, 2018, 19, 4677-4690.

216) P. Wu, M. Malkoch, J. N. Hunt, R. Vestberg, E. Kaltgrad, M. G. Finn, V. V. Fokin, K. B. Sharpless and C. J. Hawker, Chem. Commun., 2005, DOI: 10.1039/B512021G, 5775-5777.

217) García-Gallego, S.; Hult, D.; Olsson, J. V.; Malkoch, M., Fluoride-Promoted Esterification with Imidazolide-Activated Compounds: A Modular and Sustainable Approach to Dendrimers. Angewandte Chemie International Edition 2015, 54, 2416-2419.

218) Xu, Y.; Deng, M.; Zhang, H.; Tan, S.; Li, D.; Li, S.; Luo, L.; Liao, G.; Wang, Q.; Huang, J.; Liu, J.; Yang, X.; Wang, K. Selection of Affinity Reagents to Neutralize the Hemolytic

Toxicity of Melittin Based on a Self-Assembled Nanoparticle Library. ACS Applied Materials & Interfaces, 2020, 12, 16040–16049.

APPENDIX

APPENDIX A: SUPPLEMENTARY INFORMATION FOR CHAPTER 2

SYNTHETIC DETAILS

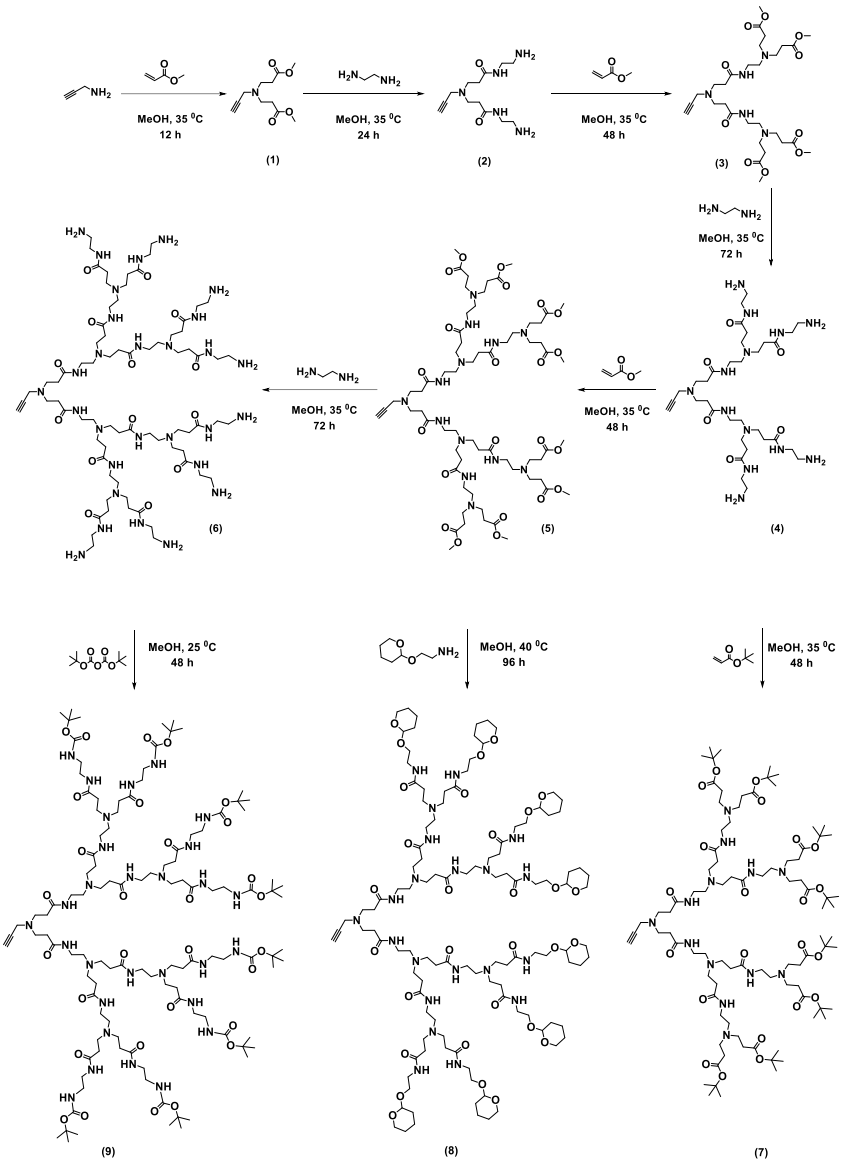

Scheme 1. Synthesis of hydrophilic dendron

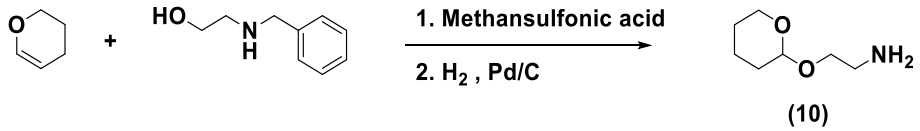

Scheme 2. Synthesis of ((tetrahydro-2H-pyran-2-yl)oxy)methanamine

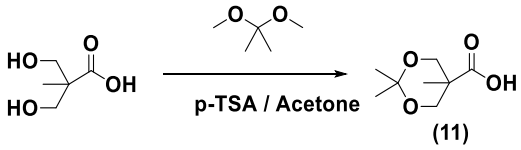

Scheme 3. Synthesis of 2,2,5-trimethyl-1,3-dioxane-5-carboxylic acid

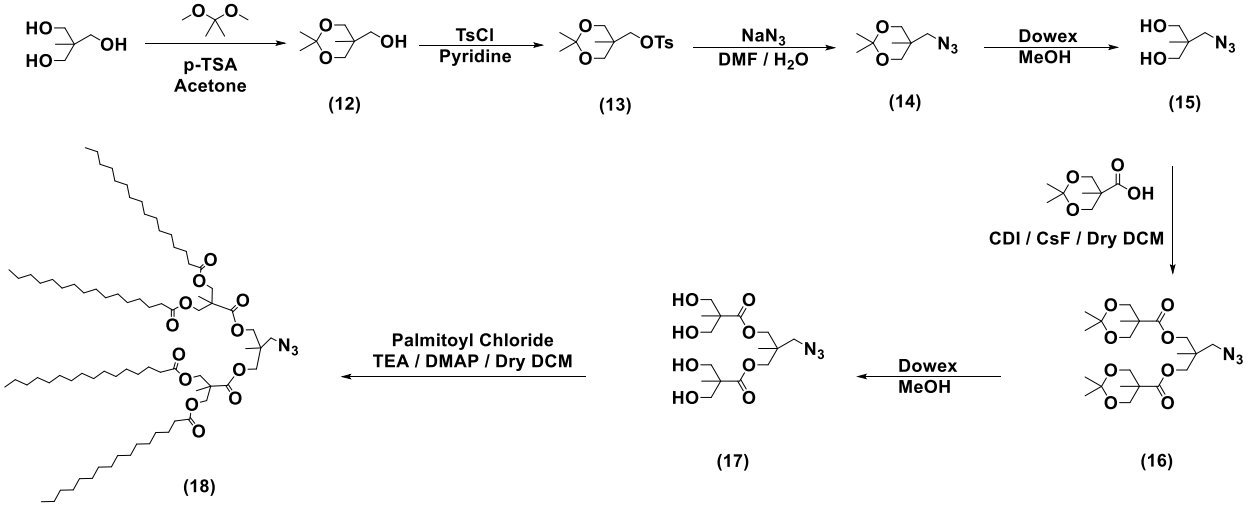

Scheme 4. Synthesis of hydrophobic dendron

PAMAM synthesis procedures were adapted from previously reported procedures.[208- 214] All NMR spectra were matched with the corresponding reported spectra and ppm value.

P-PAMAM-G-0.5 (1)

To the stirred solution of propargyl amine (5.10 g, 0.08 mmol) in 50 mL of methanol, methyl acrylate (MA) (35.38 g, 0.41 mmol) in 150 mL of methanol was added dropwise under-salted ice. After the completion of the addition, the reaction mixture was allowed to come to room temperature and then was subjected to heating at 35 ^{o}C overnight. Upon ^{1}H NMR confirmation of completion, MA was co-evaporated in-vacuo three times with butanol, three washes with reagent alcohol, and three with MeOH until complete removal was confirmed by ^{1}H NMR in $CDCl_3$ with 97% yield. ^{1}H NMR (500 MHz, $CDCl_3$) δ 3.65 (d, *J* = 3.5 Hz, 6H), 2.82 (q, *J* = 7.0, 5.3 Hz, 4H), 2.45 (q, *J* = 7.0, 5.2 Hz, 4H), 2.19 (t, *J* = 2.9 Hz, 1H).

P-PAMAM-G-1.0 (2)

To the stirred solution of ethylenediamine (EDA) (52.10 g, 0.86 mmol) in 100 mL of methanol, compound 1 (5.09 g, 0.02 mmol) in 50 mL of methanol was added dropwise under-salted ice. After the completion of the addition, the reaction mixture was allowed to come to room temperature and then was subjected to heating at 35 ^{o}C overnight. Upon ^{1}H NMR confirmation of completion, MA was co-evaporated in-vacuo three times each with butanol, reagent alcohol, and MeOH until complete removal was confirmed by ^{1}H NMR in MeOD with 90% yield. ^{1}H NMR (500 MHz, MeOD) δ 3.58 (t, J = 6.5 Hz, 5H), 3.53 – 3.47 (m, 2H), 3.28 (t, J = 6.2 Hz, 4H), 2.86 (t, J = 6.7 Hz, 5H), 2.75 (t, J = 6.2 Hz, 5H), 2.65 (t, J = 2.6 Hz, 1H), 2.41 (t, J = 6.7 Hz, 4H), 2.20 (t, *J* = 2.9 Hz, 1H).

P-PAMAM-G-1.5 (3)

To the stirred solution of MA (53.30 g, 0.62 mmol) in 200 mL of methanol, compound 2 (5.94 g, 0.06 mmol) in 50 mL in methanol was added dropwise under-salted ice. After the completion of the addition, the reaction mixture was allowed to come to room temperature and then was subjected to heating at 35 ^{o}C for two days. Upon ^{1}H NMR confirmation of completion, MA was co-evaporated in-vacuo three times with butanol, three with reagent alcohol, and three with MeOH until complete removal was confirmed by ^{1}H NMR in $CDCl_3$ with 95% yield. ^{1}H NMR (500 MHz, $CDCl_3$) δ 3.70 (d, J = 1.5 Hz, 13H), 3.49 (d, J = 2.2 Hz, 2H), 3.32 (q, J = 5.8 Hz, 4H), 2.88 (t, J = 6.7 Hz, 4H), 2.79 (t, J = 6.6 Hz, 9H), 2.57 (t, J = 6.0 Hz, 3H), 2.46 (t, J = 6.7 Hz, 9H), 2.41 (t, J = 6.8 Hz, 4H), 2.19 (t, *J* = 2.9 Hz, 1H).

P-PAMAM-G-2.0 (4)

To the stirred solution of EDA (47.56 g, 792 mmol) in 100 mL of methanol, compound 3 (12.51g, 9.87 mmol) in 60 mL in methanol was added dropwise under-salted ice. After the completion of the addition, the reaction mixture was allowed to come to room temperature and then it was subjected to heating at 35 ^{o}C for three days. Upon ^{1}H NMR confirmation of completion, MA was co-evaporated in-vacuo three times with butanol, three with reagent alcohol, and three with MeOH until complete removal was confirmed by ^{1}H NMR in MeOD with 91% yield. ^{1}H NMR (500 MHz, $CDCl_3$) δ 3.56 (t, J = 6.7 Hz, 12H), 3.39 (t, J = 4.7 Hz, 2H), 3.21 (m, J = 12.0, 6.0 Hz, 8H), 2.76 (t, J = 5.9 Hz, 8H), 2.69 (dd, J = 11.0, 4.7 Hz, 8H), 2.47 (t, J = 6.2 Hz, 2H), 2.29 (d, J = 21.8 Hz, 18H), 2.20 (t, *J* = 2.9 Hz, 1H).

P-PAMAM-G-2.5 (5)

To the stirred solution of MA (71.84 g, 834 mmol) in 150 mL of methanol, compound 4 (12.45 g, 16.7 mmol) in 60 mL in methanol was added dropwise under-salted ice. After the

completion of the addition, the reaction mixture was allowed to come to room temperature and then it was subjected to heating at 35 ^{o}C for four days. Upon ^{1}H NMR confirmation of completion, MA was co-evaporated in-vacuo three times with butanol, three with reagent alcohol, and three with MeOH until complete removal was confirmed by ^{1}H NMR in $CDCl_3$ with 94% yield. ^{1}H NMR (300 MHz, $CDCl_3$) δ 3.68 (s, 24H), 3.47 (s, 2H), 3.30 (d, J = 5.8 Hz, 12H), 2.79 (dt, J = 13.6, 6.5 Hz, 28H), 2.57 (dt, J = 12.2, 6.0 Hz, 12H), 2.44 (t, J = 6.7 Hz, 16H), 2.38 (t, J = 6.3 Hz, 12H), 2.19 (t, *J* = 2.9 Hz, 1H).

P-PAMAM-G-3.0 (6)

To the stirred solution of EDA (34.31 g, 571 mmol) in 70 mL of methanol, compound 5 (10.24 g, 7.14 mmol) in 50 mL in methanol was added dropwise under-salted ice. After the completion of the addition, the reaction mixture was allowed to come to room temperature and then it was subjected to heating at 35 ^{o}C for four days. Upon ^{1}H NMR confirmation of completion, MA was co-evaporated in-vacuo three times with butanol, three with reagent alcohol, and three with MeOH until complete removal was confirmed by ^{1}H NMR in MeOD with an 88% yield. ^{1}H NMR (500 MHz, MeOD) δ 3.57 (t, J = 6.7 Hz, 4H), 3.39 – 3.34 (m, 16H), 3.32 – 3.26 (m, 28H), 2.81 (tq, J = 12.8, 6.4 Hz, 48H), 2.61 (q, J = 6.8 Hz, 14H), 2.39 (t, J = 7.0 Hz, 30H).

P-PAMAM-TBE (7)

To the stirred solution of compound 4 (22.00 g, 29.7 mmol) in 110 mL of methanol, tertbutyl acrylate (TBA) (190.53 g, 149 mmol) in 380 mL methanol was added dropwise under-salted ice. After the complete addition of TBA, the reaction was allowed to warm to room temperature. The reaction continued at room temperature for two days. Upon ^{1}H NMR confirmation of completion, a single rotovap ensued. The PAMAM product was dissolved into a

minimal amount of DCM, which was followed by precipitation via separatory funnel into 5x mL of stirring, pure hexane. After settling, the hexane layer was decanted, and the remaining product was air-dried. This precipitation, decanting, and the air-drying process was repeated twice more. A final ^{1}H NMR ensured the removal of TBA with 90% yield. ^{1}H NMR (500 MHz, $CDCl_3$) δ 3.47 (s, 2H), 3.35 (s, 18H), 3.26 (s, 26H), 2.74 (s, 24H), 2.56 (d, J = 15.4 Hz, 14H), 2.37 (s, 28H), 2.19 (t, *J* = 2.9 Hz, 1H), 1.45 (s, 72H).

P-PAMAM-THP (8)

To the stirred solution of compound 5 (15.06 g, 9.04 mmol) in 150 mL of methanol, ((tetrahydro-2H-pyran-2-yl)oxy)methanamine (THP) (11) (36.85 g, 181 mmol) in 120 mL in methanol was added dropwise under-salted ice. After the complete addition of THP, the reaction was allowed to warm to room temperature. The reaction continued at room temperature for 24 h and then at 40 ^{o}C for 72 h. Upon ^{1}H NMR confirmation of completion, a single rotovap ensued. The PAMAM product was dissolved into a minimal amount of DCM which was followed by precipitation via separatory funnel into 5x mL of stirring, pure hexane. After settling, the hexane layer was decanted, and the remaining product was air-dried. This precipitation, decanting, and the air-drying process was repeated twice more. It was further purified using size exclusion chromatography (Sephadex LH-20). A final ^{1}H NMR ensured the removal of excess THP with 81% yield. ^{1}H NMR (500 MHz, $CDCl_3$) δ 4.57 (s, 8H), 3.94 – 3.67 (m, 16H), 3.64 (s, 2H), 3.57 – 3.18 (s, 38H), 2.93 – 2.42 (m, 26H), 2.41 – 2.26 (s, 12H), 2.23 (s, 1H), 1.93 – 1.67 (m, 48H).

P-PAMAM-BOC (9)

To the stirred solution of compound 6 (16.25 g, 9.83 mmol) in 150 mL of methanol, di-tert-butyl dicarbonate (Boc Anhydride) (25.75 g, 118 mmol) in 120 mL in methanol was added

dropwise under-salted ice. After the complete addition of Boc Anhydride, the reaction was allowed to warm to room temperature. The reaction continued at room temperature for two days. Upon ^{1}H NMR confirmation of completion, a single rotovap ensued. The PAMAM product was dissolved into a minimal amount of DCM which was followed by precipitation via separatory funnel into 5x mL of stirring, pure hexane. After settling, the hexane layer was decanted, and the remaining product was air-dried. This precipitation, decanting, and the air-drying process was repeated twice more. A final ^{1}H NMR ensured the removal of Boc Anhydride with a 92% yield. ^{1}H NMR (400 MHz, $CDCl_3$) δ 3.62 (s, 2H), 3.32 (q, J = 5.6 Hz, 18H), 3.24 (t, J = 6.2 Hz, 28H), 2.80 – 2.65 (m, 28H), 2.53 (q, J = 7.9, 6.0 Hz, 14H), 2.36 (q, J = 9.0, 6.7 Hz, 28H), 2.23 (s, 1H), 1.42 (s, 72H).

((tetrahydro-2H-pyran-2-yl)oxy)methanamine (10)

This procedure was adapted from previously reported procedures.[211] To the stirred solution of 2-Benzylaminoethanol (5.00 g, 33.1 mmol) in 17 mL of DCM at 0 ^{o}C, methanesulfonic acid (3.50 g, 36.4 mmol) was added at 15 ^{o}C. After 45 min 3,4-dihydro-2H-pyran (4.73 g, 56.2 mmol) was added at 10-15 ^{o}C. It was stirred for 1 h at 15 ^{o}C. Upon ^{1}H NMR confirmation of completion, 3 N caustic solution (17 mL, 49.1 mmol) was added at 5-10 ^{o}C. The phases were separated, and the organic layer was concentrated in the vacuum line. The oily yellow crude product was purified by short path distillation at 3 x 10^3 mbar and 117-125 ^{o}C. 1.0 g of crude product was dissolved in 15 mL of ethanol and Pd/C (5 wt%, 327 mg, 0.154 mmol) was added at room temperature overnight under hydrogen balloon. Upon ^{1}H NMR confirmation of completion, the reaction mixture was filtered through a celite pad. Then the filtrate was concentrated in vacuum to give 0.53 g of compound 11 with 86 % yield. ^{1}H NMR (500 MHz, $CDCl_3$) δ 4.66 – 4.58 (m, 1H), 3.94 – 3.75 (m, 2H), 3.64 (dt, *J* = 16.4, 5.9 Hz, 1H), 3.58 – 3.40 (m, 2H), 2.90 (q, *J* = 11.8, 8.7 Hz, 2H), 1.89 – 1.69 (m, 2H), 1.61 – 1.56 (m, 4H).

2,2,5-trimethyl-1,3-dioxane-5-carboxylic acid (11)

This procedure was adapted from previously reported procedures.[212] To the stirred solution of 3-hydroxy-2-(hydroxymethyl)-2-methylpropanoic acid (100.06 g, 750 mmol) in 500 mL of acetone, 2,2-dimethoxy-propane (DMP) (116.47 g, 1120 mmol) and p-toluenesulfonic acid (PTSA) (7.10 g, 40.0 mmol) were added under room temperature. After the completion of the addition, the reaction mixture was stirred 5 h. Then it was filtered through an amberlyst column and the solvent was evaporated at room temperature. The residue was recrystallized using CH_2Cl_2 to give (2) white crystals with 92% yield. ^{1}H NMR (500 MHz, $CDCl_3$) δ 4.27 – 4.17 (m, 2H), 3.76 – 3.66 (m, 2H), 1.55 – 1.39 (m, 6H), 1.23 (d, J = 2.8 Hz, 3H).

(2,2,5-trimethyl-1,3-dioxan-5-yl)methanol (12)

This procedure was adapted from previously reported procedures.[213] To the stirred solution of 2-(hydroxymethyl)-2-methylpropane-1,3-diol (10.10 g, 80.1 mmol) in 50 mL of acetone, 2,2-dimethoxy-propane (DMP) (13.14 g, 126 mmol) and PTSA (0.79 g, 0. 4.14 mmol) were added under room temperature. After the completion of the addition, the reaction mixture was stirred 4 h. Then it was filtered through an amberlyst column and the solvent was evaporated, and the residue was put under 60 ^{o}C and full vacuum for 2 h. Then it was put under vacuum overnight to give (4) as a colourless liquid with 96% yield. ^{1}H NMR (500 MHz, $CDCl_3$) δ 3.67 (d, *J* = 5.3 Hz, 4H), 3.60 (d, *J* = 11.8 Hz, 2H), 1.44 (s, 3H), 1.40 (s, 3H), 0.83 (s, 3H).

(2,2,5-trimethyl-1,3-dioxan-5-yl)methyl 4-methylbenzenesulfonate (13)

This procedure was adapted from previously reported procedures.[214] Compound (12) (10.89 g, 68.0 mmol) was dissolved in 34 mL of pyridine and it was added dropwise to the stirred solution of p-toluenesulfonyl chloride (35.70 g, 187 mmol) in 48 mL of pyridine at 0 ^{o}C under

nitrogen. After the complete addition, reaction mixture was stirred 48 h at room temperature. Then the reaction mixture was added dropwise to 100 mL of 40% ammonium chloride solution at 0 ^{o}C. After complete addition, it was allowed to stir at room temperature for 2 h. Then it was filtered and washed with DI water until the pyridine smell was gone. Then the residue was dissolved in 25 mL of DCM and extracted with half saturated ammonium chloride and saturated NaCl solution. Yellow DCM solution was dried with anhydrous sodium sulfate. Then the solvent was evaporated, and the residue was placed under full vacuum for 12 h to give (5) as a yellow solid with 89% yield. ^{1}H NMR (500 MHz, $CDCl_3$) δ 7.86 – 7.79 (m, 2H), 7.38 (d, *J* = 7.6 Hz, 2H), 4.11 (s, 2H), 3.58 (s, 4H), 2.47 (s, 3H), 1.39 (d, *J* = 4.8 Hz, 3H), 1.25 (d, *J* = 4.7 Hz, 3H), 0.84 (s, 3H).

5-(azidomethyl)-2,2,5-trimethyl-1,3-dioxane (14)

This procedure was adapted from previously reported procedures.[214] Compound 13 (14.60 g, 46.4 mmol), NaN_3 (12.07 g, 186 mmol), water (10 mL), and DMF (80 mL) were stirred at 110 °C for 48 h under reflux. The mixture was poured into 150 ml water and extracted four times with Et_2O (4 × 200 mL). The organic phase was dried over anhydrous $MgSO_4$ and the solvent was removed under reduced pressure. The residue was purified by column chromatography with silica gel (100 g) and ethyl acetate/n-hexane (1:4) to give 7.48 g of a colourless liquid with an 87% yield. ^{1}H NMR (500 MHz, $CDCl_3$) δ 3.58 (d, J = 2.8 Hz, 4H), 3.51 (s, 2H), 1.40 (d, J = 13.8 Hz, 6H), 0.81 (d, J = 1.1 Hz, 3H).

2-(azidomethyl)-2-methylpropane-1,3-diol (15)

This procedure was adapted from previously reported procedures.[213] Compound (14) (7.05 g, 40.3 mmol) was dissolved in 35 mL of methanol. 7.00 g of a Dowex, H^+ resin was added, and the reaction mixture was stirred for 12 h at 50 ^{o}C. When the reaction was complete the Dowex, H+

resin was filtered off in a vacuum filter under a low vacuum and carefully washed with methanol. The methanol was evaporated to give 5.41 g of white crystals with a 93% yield. ^{1}H NMR (400 MHz, $CDCl_3$) δ 3.73 – 3.58 (m, 4H), 3.56 – 3.43 (m, 2H), 2.19 (s, 2H), 0.89 (d, J = 2.0 Hz, 3H).

A-MPA-4-AC (16)

This procedure was adapted from previously reported procedures.[214] Compound 11 (6.48 g, 37.2 mmol), 1,1'-carbonyldiimidazole (CDI) (9.05 g, 55.8 mmol) were dissolved in 30 ml of ethyl acetate and it was stirred 1 h at 50 °C. CsF (0.75 g, 4.93 mmol), Compound (15) (1.80 g, 12.4 mmol) were dissolved in 10 ml of ethyl acetate separately and it was slowly added to the reaction mixture under nitrogen at 50 ^{o}C. It was stirred 12 h. When the reaction was complete 200 mL DI water was added and allowed to stir 2 h at room temperature. Then it was extracted with 1 M HCl (200 mL x 3), 1 M $NaHSO_4$ (200 mL x 3), 10% Na_2CO_3, saturated NaCl (200 mL) and it was dried under anhydrous $MgSO_4$. Ethyl acetate was evaporated to give 5.22 g of colourless oil liquid with a 92% yield. ^{1}H NMR (500 MHz, $CDCl_3$) δ 4.21 (d, J = 11.7 Hz, 4H), 4.13 – 4.09 (m, 4H), 3.68 (d, J = 11.7 Hz, 4H), 3.42 – 3.39 (m, 2H), 1.43 (d, J = 32.2 Hz, 12H), 1.18 (d, J = 1.6 Hz, 6H), 1.08 (d, J = 1.5 Hz, 3H).

A-MPA-4-OH (17)

This procedure was adapted from previously reported procedures.[214] Compound (16) (5.00 g, 10.9 mmol) was dissolved in 20 mL of methanol. 5.00 g of a Dowex, H^+ resin was added, and the reaction mixture was stirred for 12 h at 50 ^{o}C. When the reaction was complete the Dowex, H^+ resin was filtered off in a vacuum filter under a low vacuum and carefully washed with methanol. The methanol was evaporated to give 3.96 g of colourless liquid with a 96% yield. ^{1}H NMR (300

MHz, $CDCl_3$) δ 4.09 (s, 4H), 3.88 (d, J = 11.2 Hz, 4H), 3.78 – 3.67 (m, 4H), 3.43 (s, 4H), 3.38 (s, 2H), 1.12 – 1.09 (m, 6H), 1.09 – 1.07 (m, 3H).

A-MPA-4-FA (18)

This procedure was adapted from previously reported procedures.[211] To the stirred solution of (17) (3.25 g, 8.61 mmol), TEA (13.94 g, 138 mmol), 4-dimethylaminopyridine (DMAP) (3.15 g, 25.8 mmol) in 50 ml DCM at 0 ^oC under nitrogen, palmitoyl chloride (18.93 g, 68.9 mmol) was dissolved in 20 ml DCM and it was added dropwise. After the complete addition, it was stirred 12 h at room temperature. 150 ml of DI water was added, and it was stirred 1 h. Then the DCM layer was separated, and it was dried under anhydrous $MgSO_4$. DCM was evaporated to give yellow residue further purified by the Sephadex-LH-20 column in DCM to give 10.86 g of yellow solid with a 91% yield. ^1H NMR (300 MHz, $CDCl_3$) δ 4.22 (d, J = 1.5 Hz, 8H), 4.01 (s, 4H), 3.32 (s, 2H), 2.30 (t, J = 7.5 Hz, 8H), 1.59 (t, J = 7.4 Hz, 8H), 1.31 (d, J = 5.8 Hz, 104H), 1.04 – 0.99 (m, 3H), 0.91 – 0.86 (m, 18H).

Reported below are the full synthetic details for the preparation of macromolecules

Synthesis of FA-PAMAM-TBE and FA-PAMAM-COOH

To the stirred solution of P-PAMAM-TBE (2.50 g, 1.32 mmol), A-MPA-4-FA (1.67 g, 1.29 mmol) in 25 ml of DMF, CuBr (374.0 mg, 2.61 mmol) was added under nitrogen flushing. After complete addition, PMDETA (452.2 mg, 2.61 mmol) was added and allowed to stir under nitrogen at 35 ^oC for 48 h. The reaction mixture was precipitated to 200 mL diethyl ether. After settling, the diethyl ether layer was decanted, and the remaining product was air-dried. This precipitation, decanting, and the air-drying process was repeated twice more. The crude product was dissolved in 100 mL of DCM. It was extracted with 0.1 M EDTA solution. It was further

purified using size exclusion chromatography (Sephadex LH-20) to give FA-PAMAM-TBE as a yellow solid. Then 2.10 g of FA-PAMAM-TBE was dissolved in 30 mL of chloroform and 3.0 mL (10% v/v) of TFA was added dropwise and stirred for 45 minutes. The reaction mixture was air-dried and dissolved in 8 mL of chloroform. It was added dropwise to 500 mL of diethyl ether and stirred for 2 h. It was filtered and precipitation procedure was repeated three times. Finally, the resulting yellow solid was put under the vacuum for 24 h to obtain the pure product with 82% yield. The formation of the FA-PAMAM-COO^- was confirmed via disappearance of TBE groups (1.40 ppm) (Fig. 53)

^{1}H NMR for FA-PAMAM-TBE (400 MHz, $CDCl_3$) δ 7.82 (s, 1H), 5.91-5.60 (m, 4H), 4.39 (s, 2H), 4.29 (s, 2H), 4.26 (s, 4H), 4.22 (s, 8H), 4.01 (s, 8H), 3.32 (m, 18H), 3.22 (m, 26H), 2.84 (s, 24H), 2.47 (s, 28H), 2.30 (t, 14H), 1.40 (s, 72H), 1.27 – 1.24 (m, 104H), 1.01 (s, 3H), 0.98 (s, 6H), 0.89 – 0.87 (m, 14H).^{13}C NMR (126 MHz, $CDCl_3$) δ 173.13, 171.92, 162.49, 142.91, 125.24, 66.00, 64.86, 52.81, 52.49, 51.60, 49.19, 46.47, 37.16, 36.42, 34.60, 29.65, 25.21, 24.81, 17.82, 14.05.

Synthesis of FA-PAMAM-BOC and FA-PAMAM-NH_3^+

To the stirred solution of P-PAMAM-Boc (3.20 g, 1.31 mmol), A-MPA-4-FA (2.72 g, 1.96 mmol) in 25 mL of DMF, CuBr (374.0 mg, 2.61 mmol) was added under nitrogen flushing. After complete addition, N,N,N′,N″,N″-Pentamethyldiethylenetriamine (PMDETA) (452.2 mg, 2.61 mmol) was added and allowed to stir under nitrogen at 35 ^oC for 48 h. The reaction mixture was precipitated to 200 ml diethyl ether. After settling, the diethyl ether layer was decanted, and the remaining product was air-dried. This precipitation, decanting, and the air-drying process was repeated twice more. The crude product was dissolved in 100 mL of DCM. It was extracted with

0.1 M EDTA solution. It was further purified using size exclusion chromatography (Sephadex LH-20) to give 3.95 g of FA-PAMAM-BOC. It was dissolved in 45 mL of chloroform and 4.5 mL (10% v/v) of trifluoroacetic acid (TFA) was slowly added and stirred for 45 minutes. The reaction mixture was air-dried and dissolved in 10 mL of chloroform. It was added dropwise to 500 mL of diethyl ether and stirred for 2 h. It was filtered and precipitation procedure was repeated three times. Finally, the resulting yellow solid was put under the vacuum for 24 hours to obtain the pure product with 86% yield. The formation of the FA-PAMAM-NH_3^+ was confirmed via disappearance of BOC groups (1.42 ppm) (Fig. 59).

^{1}H NMR for FA-PAMAM-Boc (500 MHz, $CDCl_3$) δ 7.87 (s, 1H), 5.91-5.60 (m, 6H), 4.40 (s, 3.29 -3.15 (m, 28H), 3.10 – 2.78 (m, 28H), 2.64-2.35 (m, 28H), 2.33-2.24 (q, 28H), 1.42 (s, 72H), 1.30-1.22 (m, 104H), 1.01 (s, 3H), 0.98 (s, 6H), 0.86 (t, 12H). ^{13}C NMR (101 MHz, Chloroform-*d*) δ 172.99, 172.07, 156.40, 144.29, 125.79, 78.99, 77.40, 64.87, 52.45, 47.84, 44.21, 33.97, 31.81, 29.58, 24.80, 22.56, 17.73, 13.95.

Synthesis of FA-PAMAM-THP and FA-PAMAM-OH

To the stirred solution of P-PAMAM-THP (1.04 g, 0.428 mmol), A-MPA-4-FA (0.86 g, 0.642 mmol) in 10 mL of DMF, CuBr (130.0 mg, 0.856 mmol) was added under nitrogen flushing. After complete addition, PMDETA (149.4 mg, 0.856 mmol) was added and allowed to stir under nitrogen at 35 ^{o}C for 48 h. The reaction mixture was precipitated to 200 mL diethyl ether. After settling, the diethyl ether layer was decanted, and the remaining product was air-dried. This precipitation, decanting, and the air-drying process was repeated twice more. The crude product was dissolved in 100 mL of DCM. It was extracted with 0.1 M EDTA solution. It was further purified using size exclusion chromatography (Sephadex LH-20) to give 1.27 g of a solid. Then

1.00 g of FA-PAMAM-THP was dissolved in 15 mL of chloroform and 2.0 mL of TFA was added dropwise and stirred for 60 minutes. The reaction mixture was air-dried and dissolved in 5 mL of chloroform. It was added dropwise to 250 mL of diethyl ether: methanol mixture (2:1) and stirred for 2 h. It was filtered and precipitation procedure was repeated three times. Finally, the resulting yellow solid was put under the vacuum for 24 h to obtain the pure product with a 79 % yield. The formation of the FA-PAMAM-OH was confirmed via disappearance of THP groups (4.60 ppm) (Fig. 65).

^{1}H NMR for FA-PAMAM-THP (400 MHz, $CDCl_3$) δ 7.89 (s, 1H), 4.60 (s, 8H), 4.25 (s, 8H), 4.01 (s, 8H), 3.89 (s, 28H), 3.55 (s, 18H), 2.32 (s, 12H), 1.90 – 1.57 (m, 48H), 1.36 – 1.23 (m, 104H), 1.02 (s, 3H) 0.91 (s, 18H). ^{13}C NMR (101 MHz, Chloroform-*d*) δ 174.10, 172.96, 162.45, 142.04, 125.99, 98.88, 77.32, 66.30, 65.08, 63.76, 54.91, 46.50, 39.57, 34.05, 31.95, , 29.72, 25.47, 22.73, 22.71, 19.69, 17.87, 13.96.

NMR SPECTRA

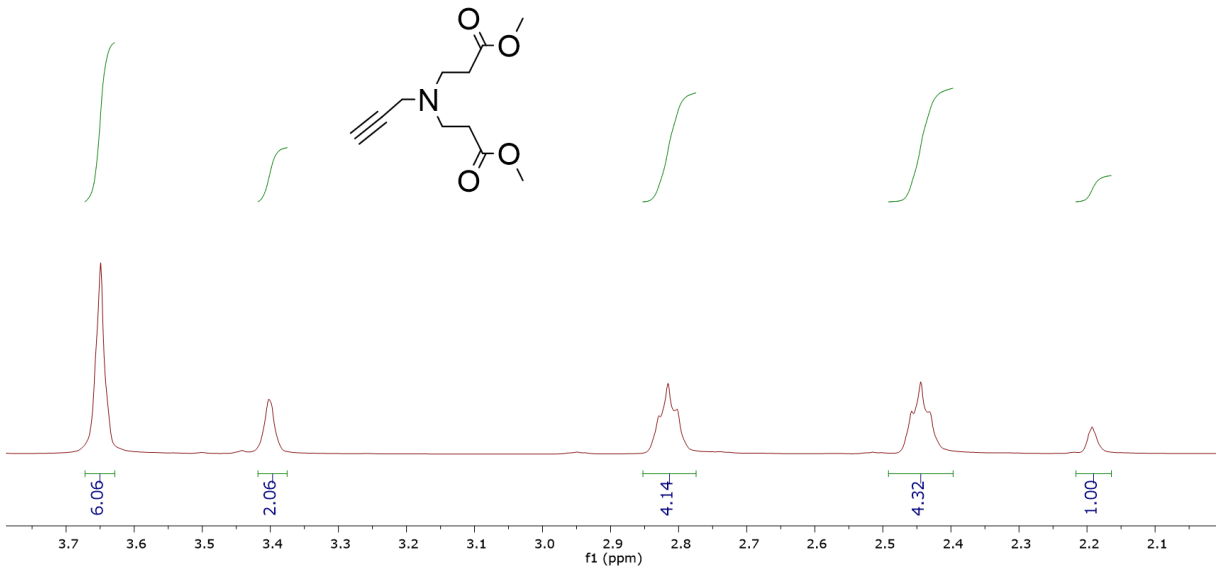

Figure 30. ^{1}H NMR for P-PAMAM-G0.5 (1) (500 MHz, $CDCl_3$)

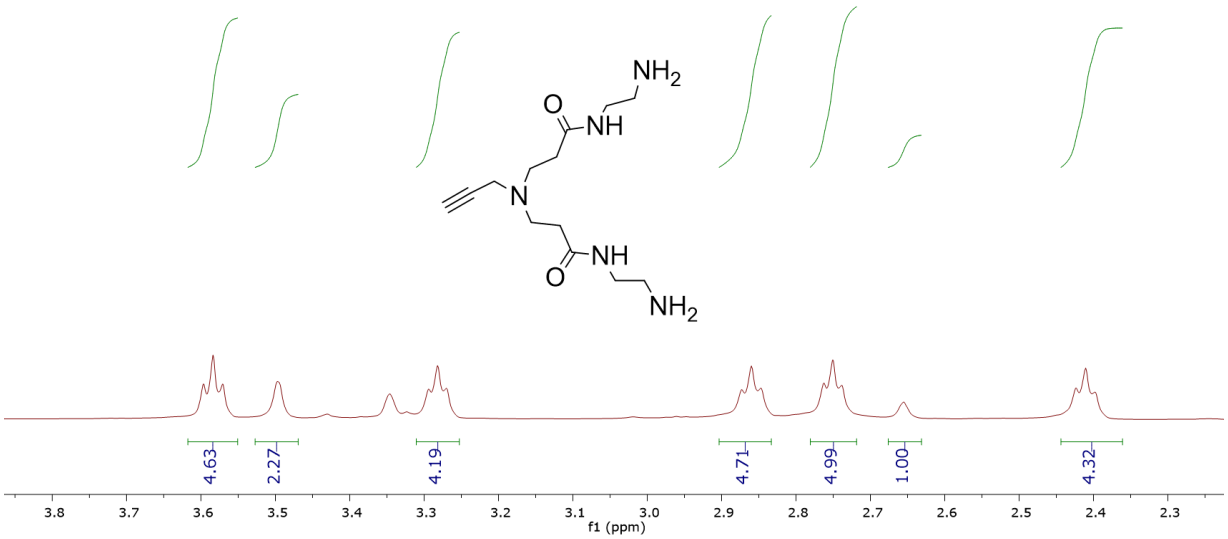

Figure 31. ^{1}H NMR for P-PAMAM-G1.0 (2) (500 MHz, MeOD)

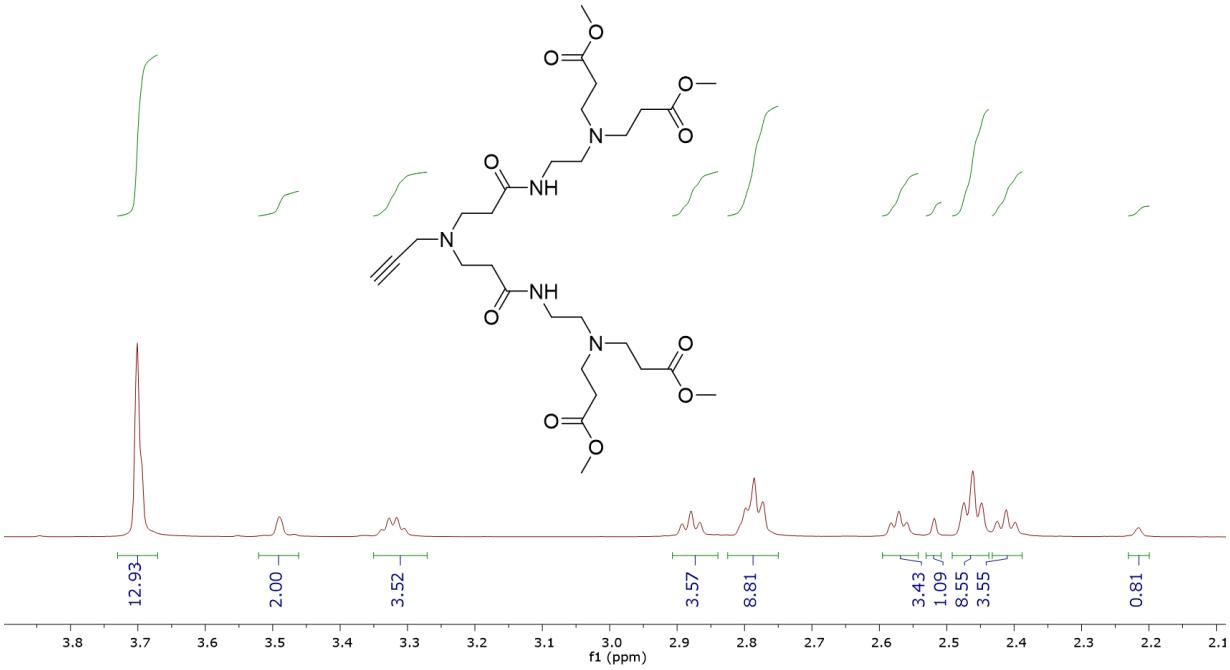

Figure 32. ^{1}H NMR for P-PAMAM-G1.5 (3) (500 MHz, $CDCl_3$)

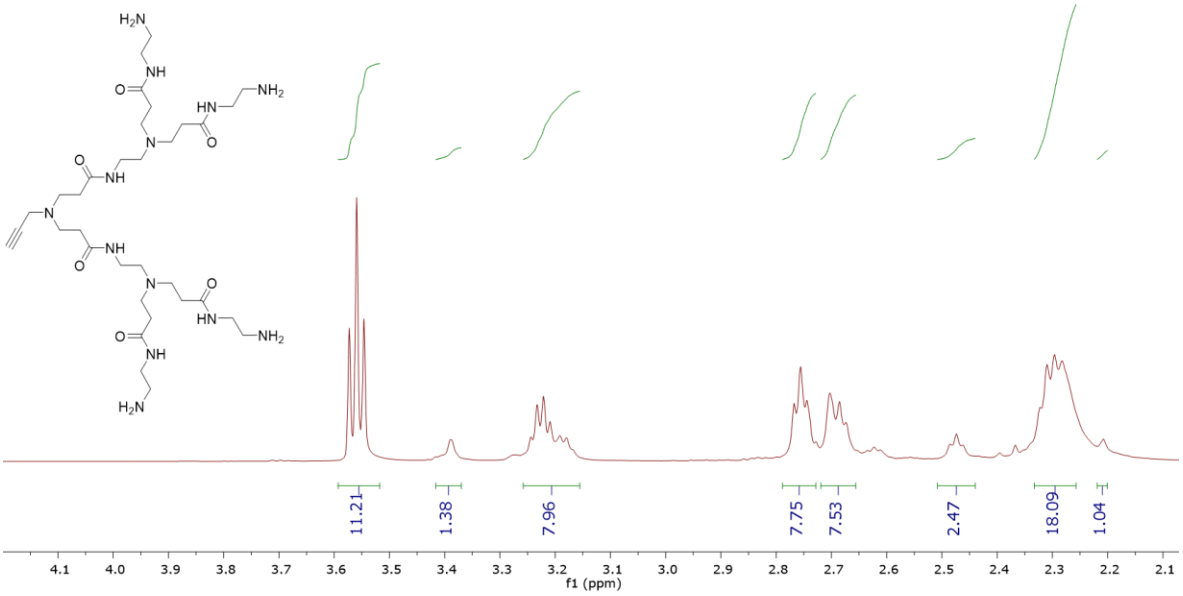

Figure 33. ^{1}H NMR for P-PAMAM-G2.0 (4) (500 MHz, MeOD)

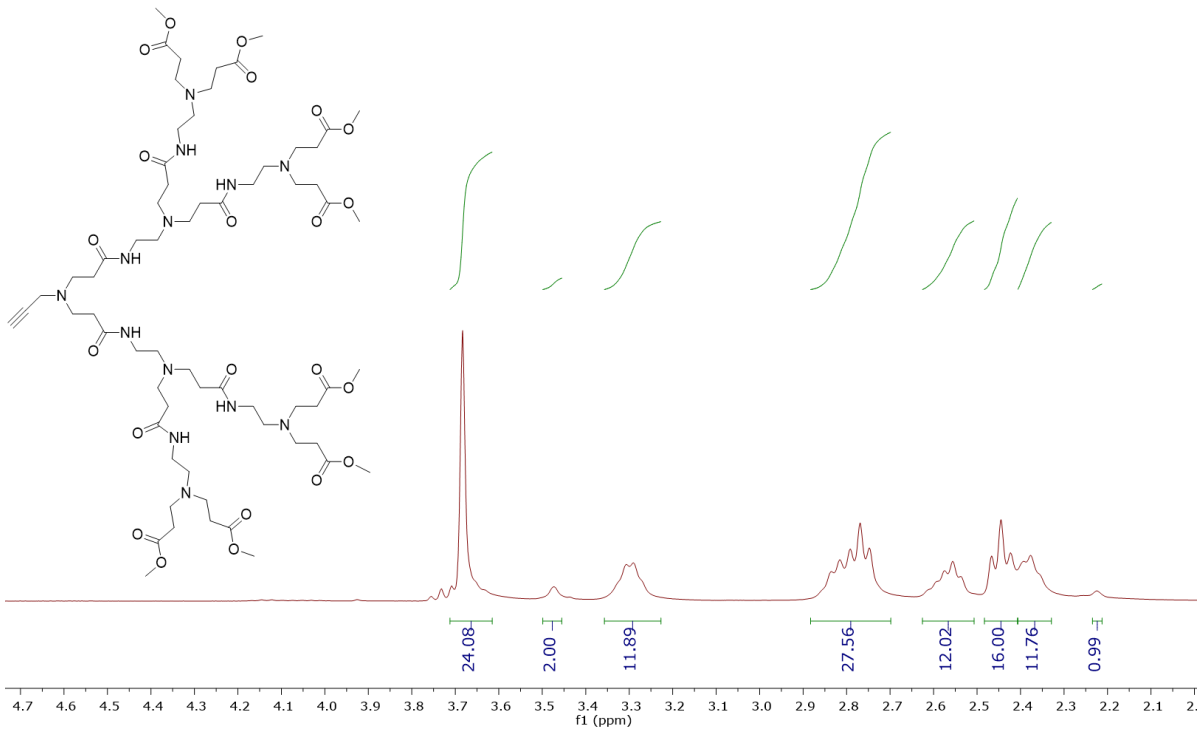

Figure 34. ^{1}H NMR for P-PAMAM-G2.5 (5) (300 MHz, $CDCl_3$)

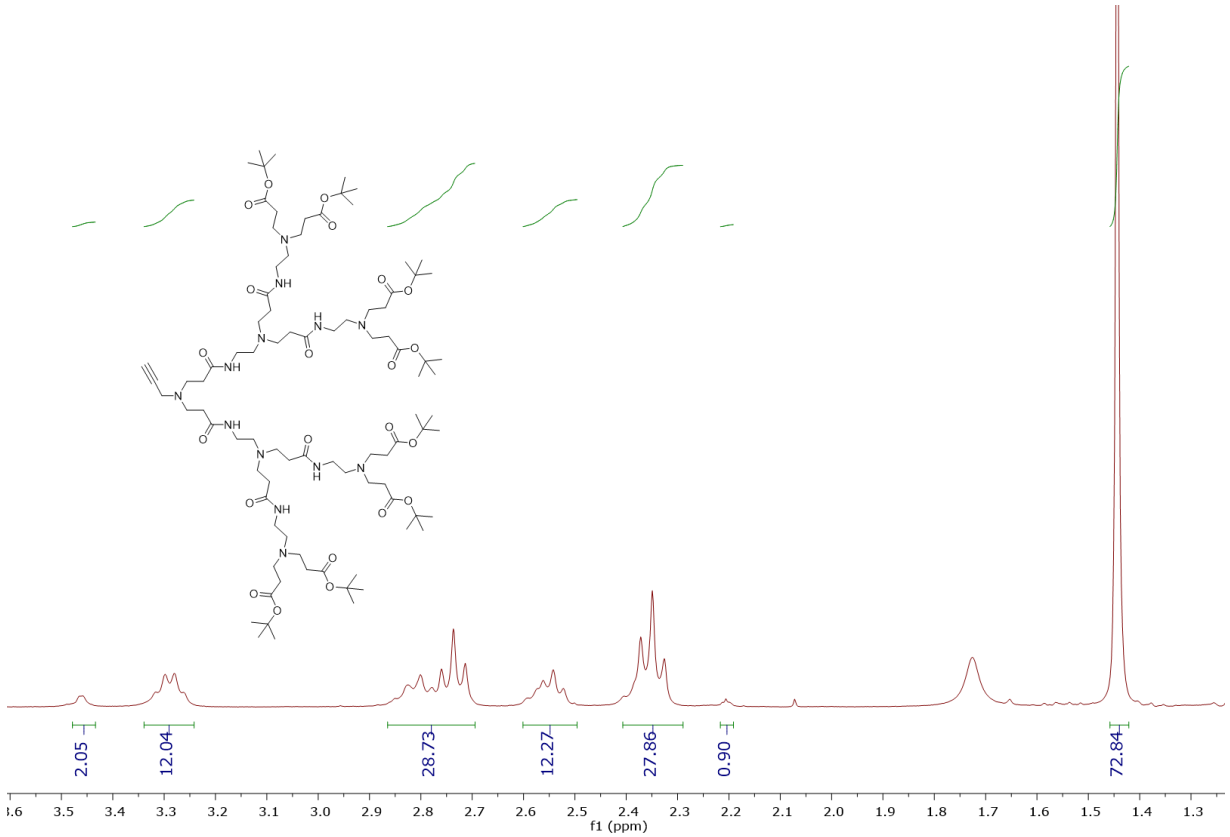

Figure 35. 1H NMR for P-PAMAM-TBE (500 MHz, CDCl3)

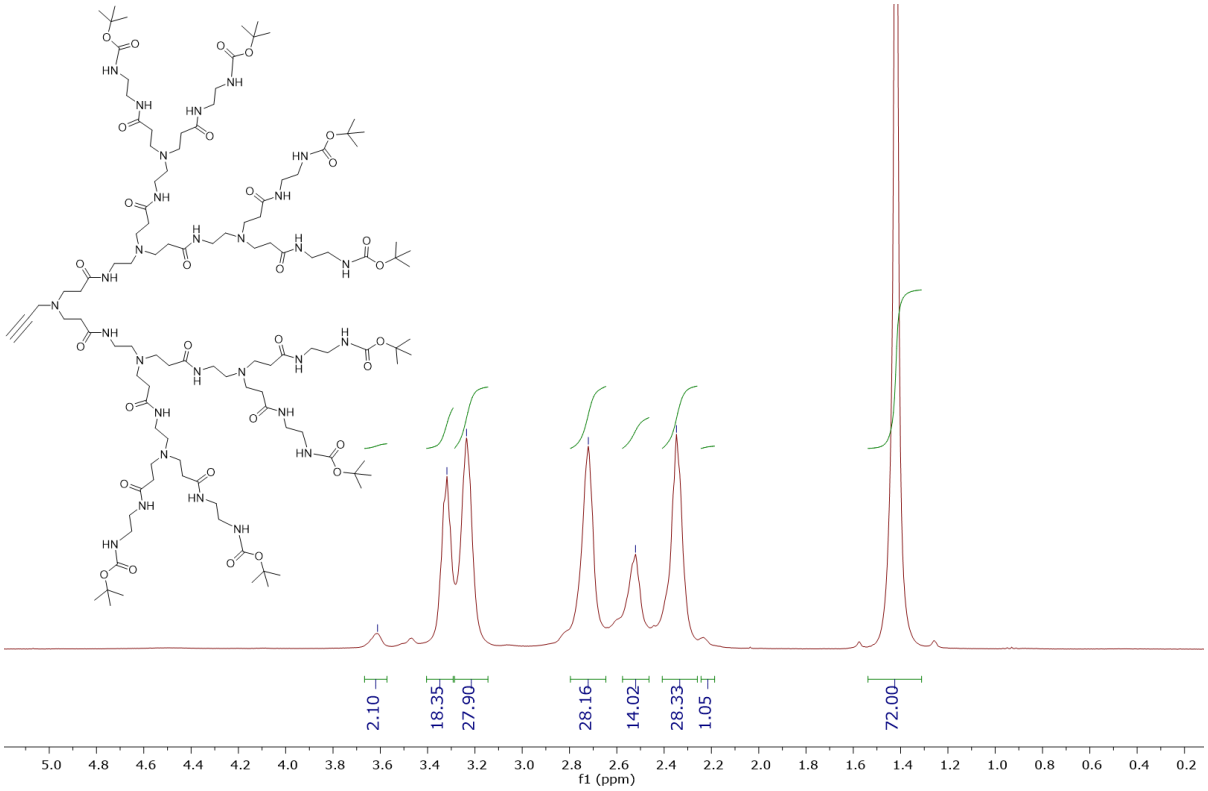

Figure 36. ^{1}H NMR for P-PAMAM-Boc (400 MHz, $CDCl_3$)

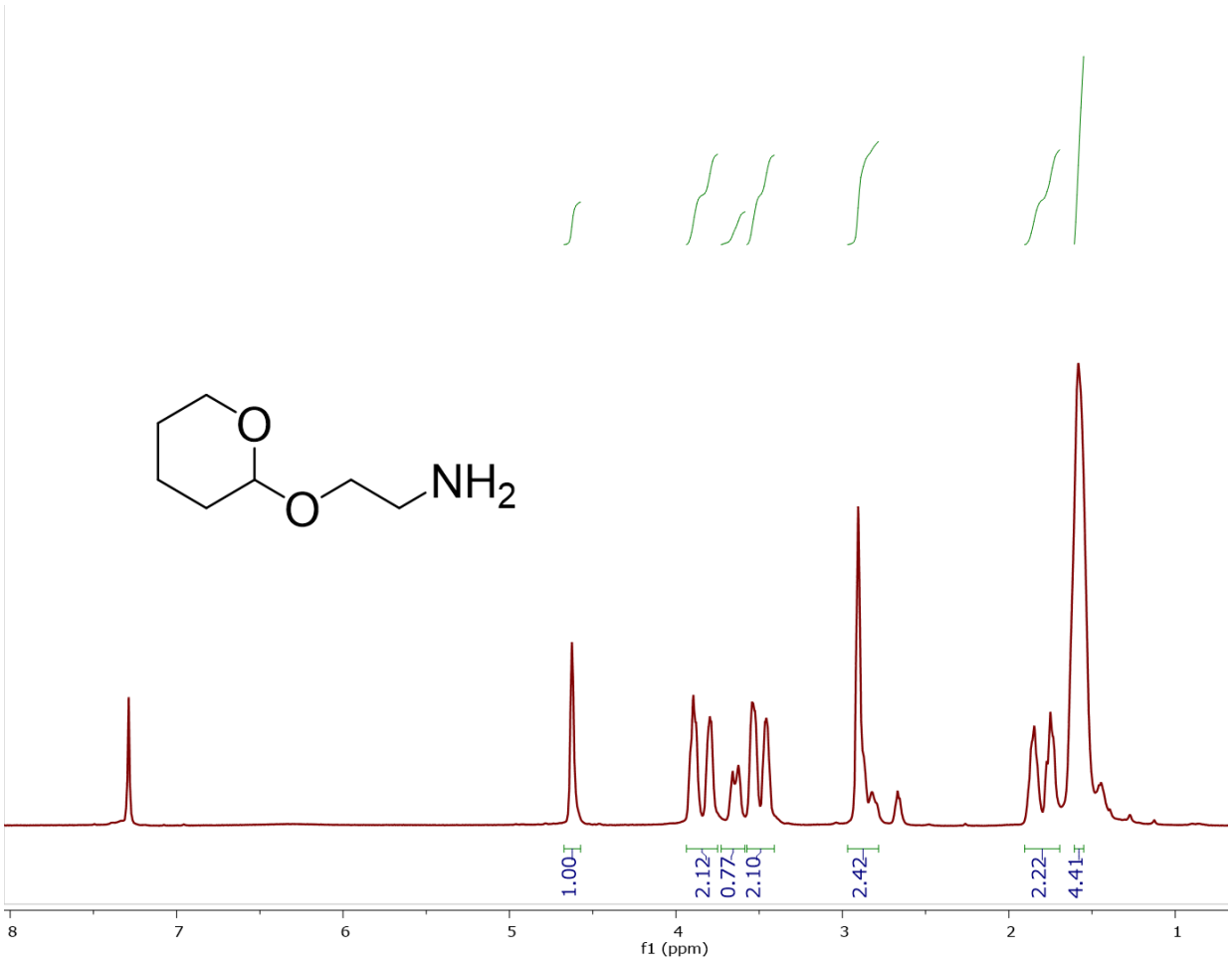

Figure 37. ^{1}H NMR for ((tetrahydro-2H-pyran-2-yl)oxy)methanamine (10) (500 MHz, $CDCl_3$)

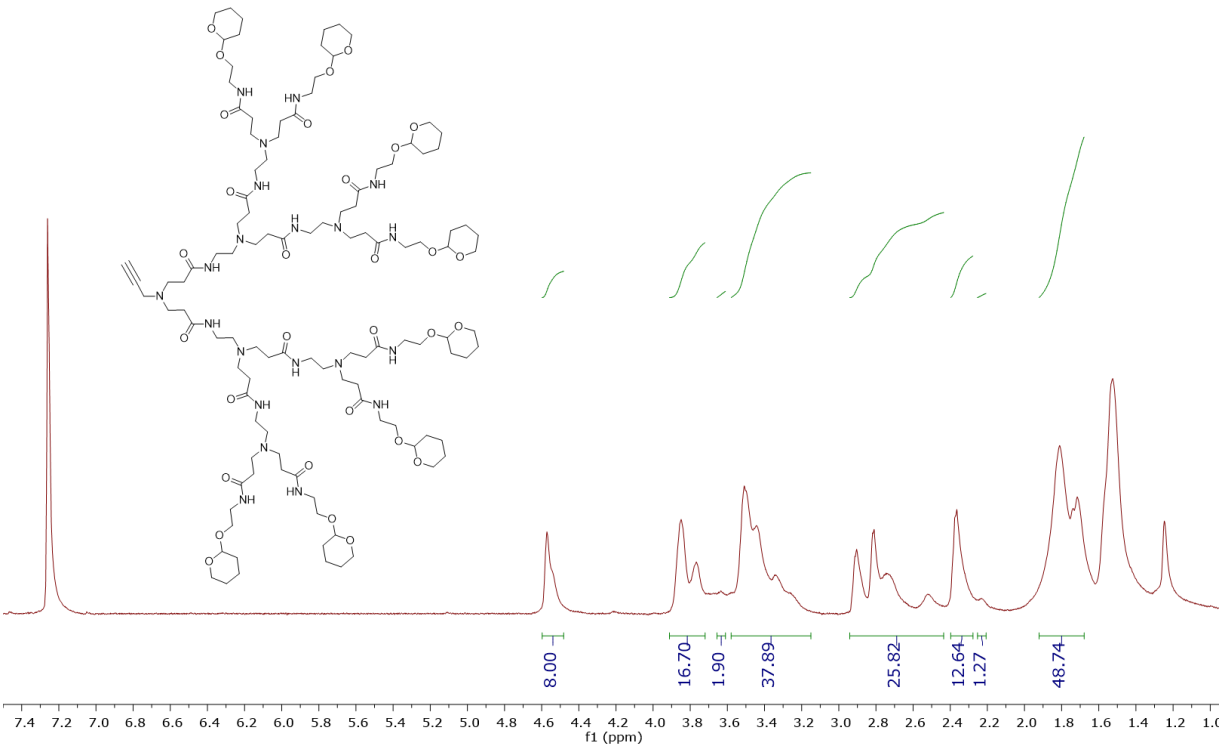

Figure 38. ^{1}H NMR for P-PAMAM-THP (500 MHz, $CDCl_3$)

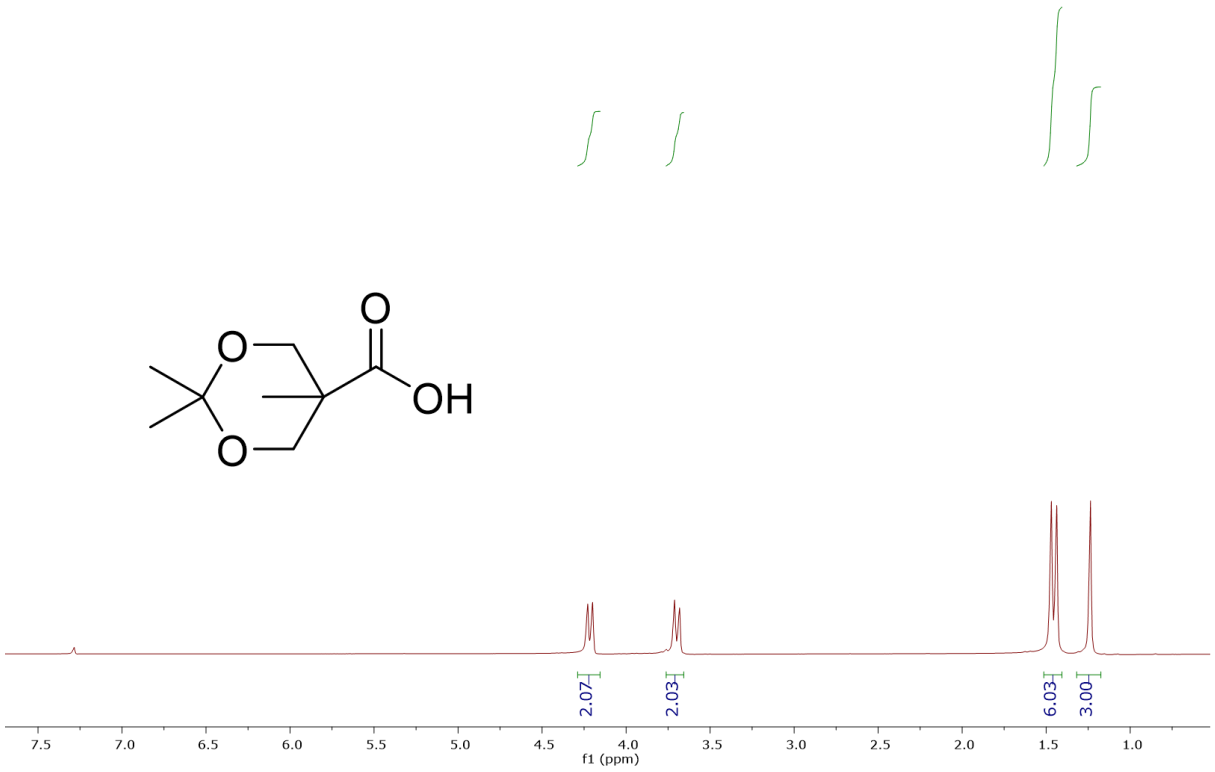

Figure 39. ^{1}H NMR for 2,2,5-trimethyl-1,3-dioxane-5-carboxylic acid (11) (500 MHz, $CDCl_3$)

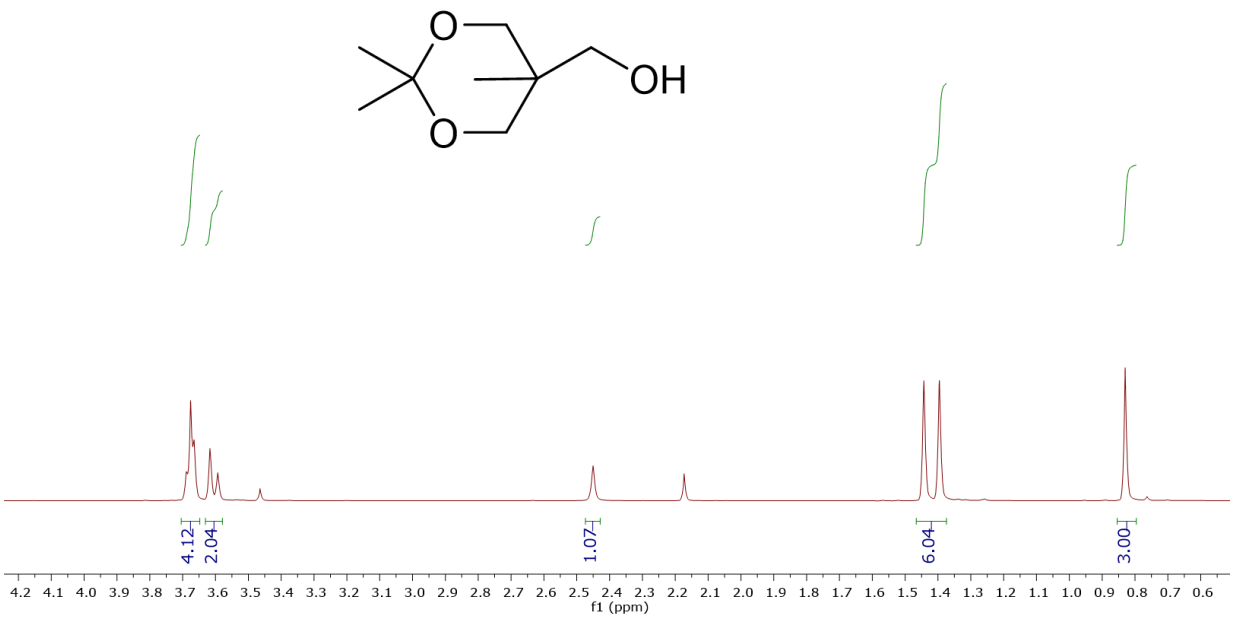

Figure 40. ^{1}H NMR for (2,2,5-trimethyl-1,3-dioxan-5-yl)methanol (12) (500 MHz, $CDCl_3$), solvent impurities acetone and methanol

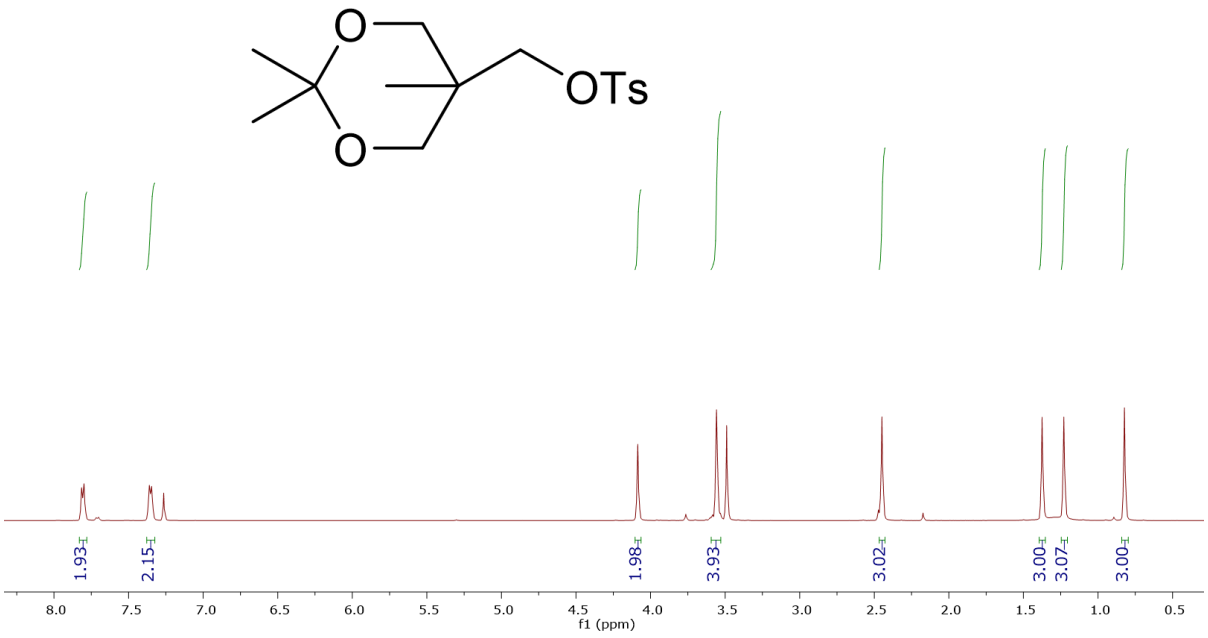

Figure 41. ^{1}H NMR for (2,2,5-trimethyl-1,3-dioxan-5-yl)methyl 4-methylbenzene sulfonate (13) (500 MHz, $CDCl_3$)

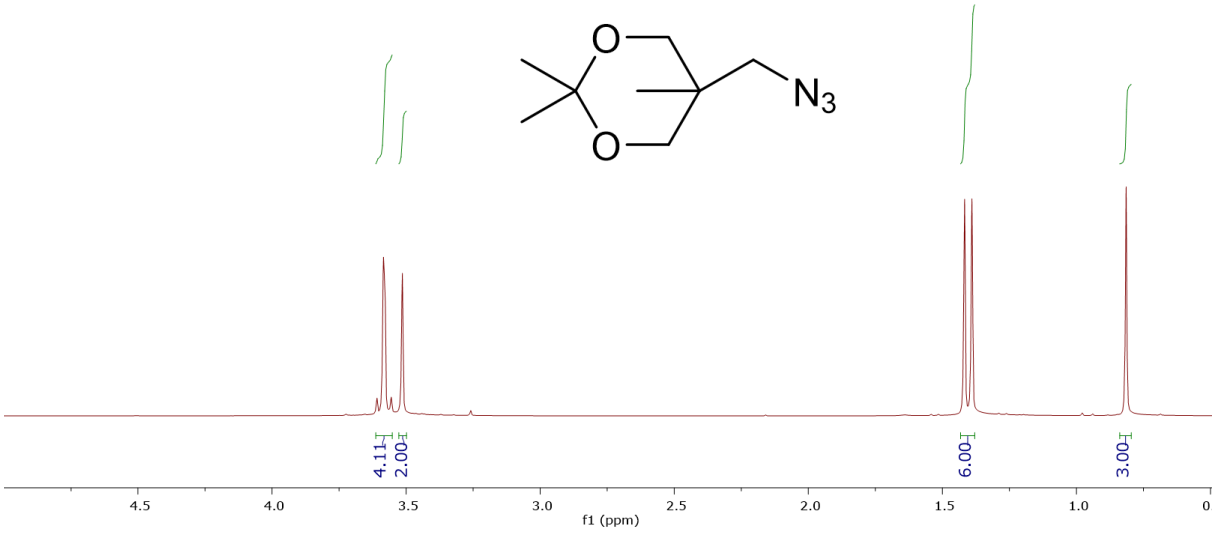

Figure 42. ^{1}H NMR for 5-(azidomethyl)-2,2,5-trimethyl-1,3-dioxane (14) (500 MHz, $CDCl_3$)

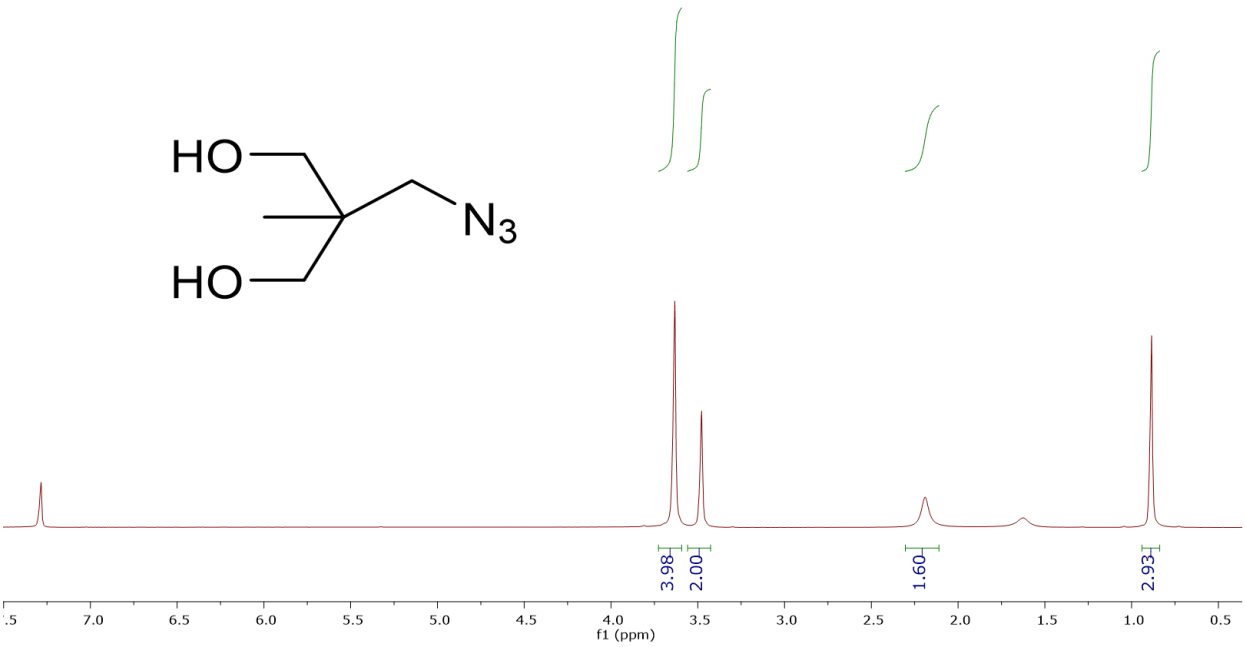

Figure 43. ^{1}H NMR for 2-(azidomethyl)-2-methylpropane-1,3-diol (15) (400 MHz, $CDCl_3$)

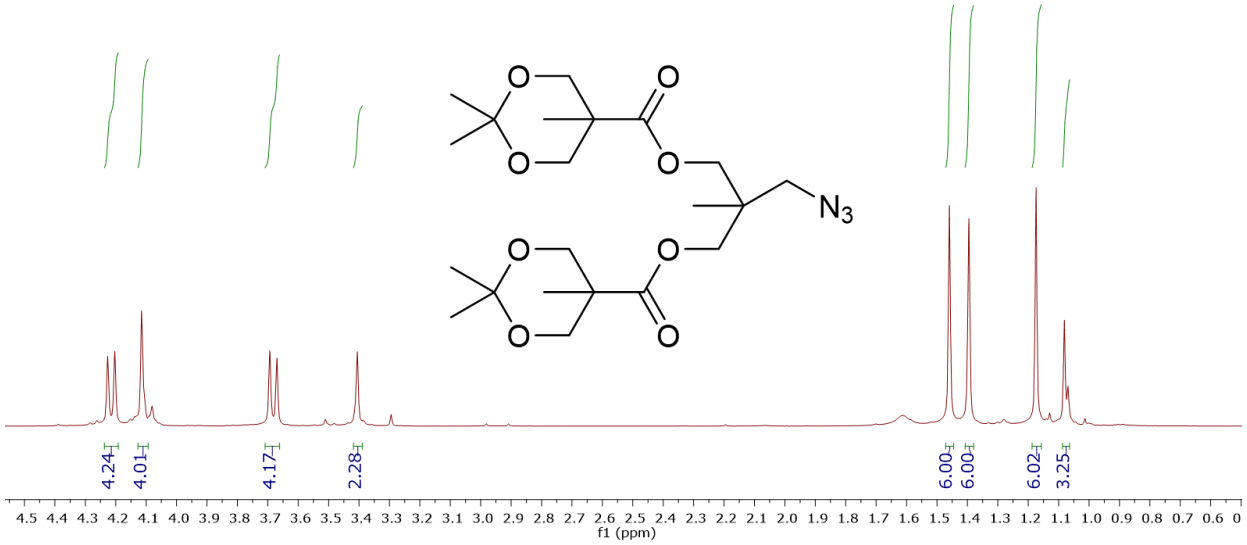

Figure 44. ^{1}H NMR for A-MPA-4-AC (16) (500 MHz, $CDCl_3$)

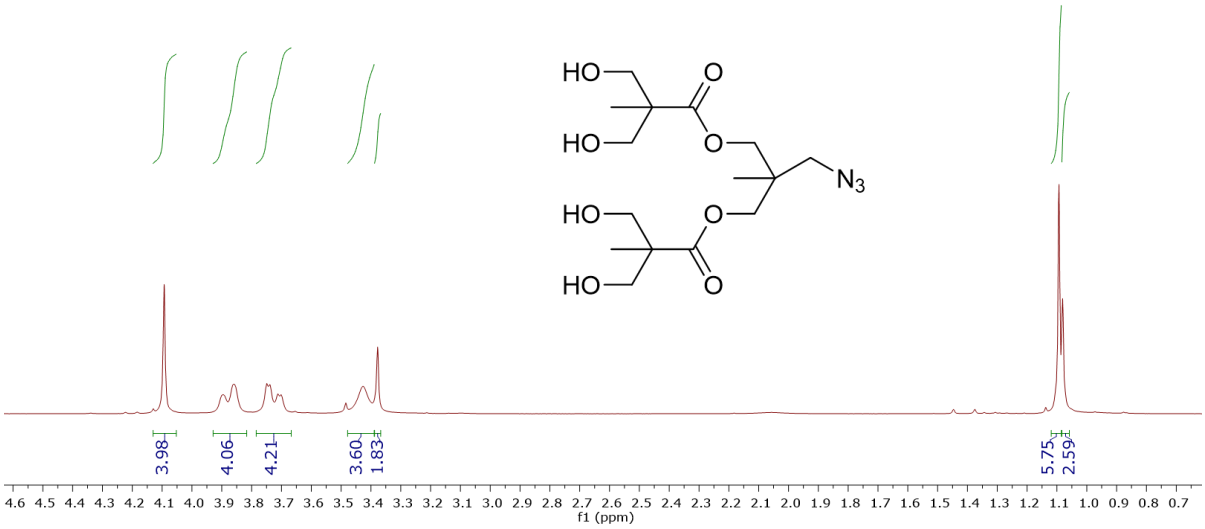

Figure 45. ^{1}H NMR for A-MPA-4-OH (17) (300 MHz, $CDCl_3$)

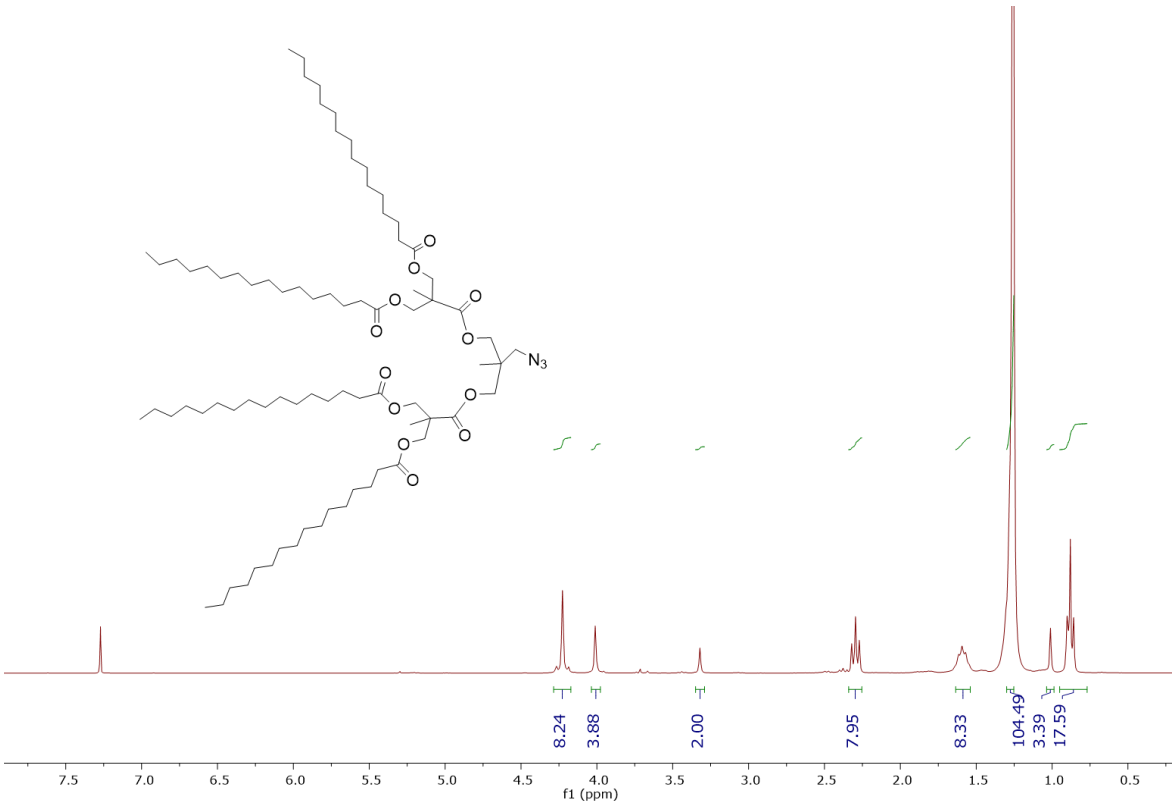

Figure 46. ^{1}H NMR for A-MPA-4-FA (18) (300 MHz, $CDCl_3$)

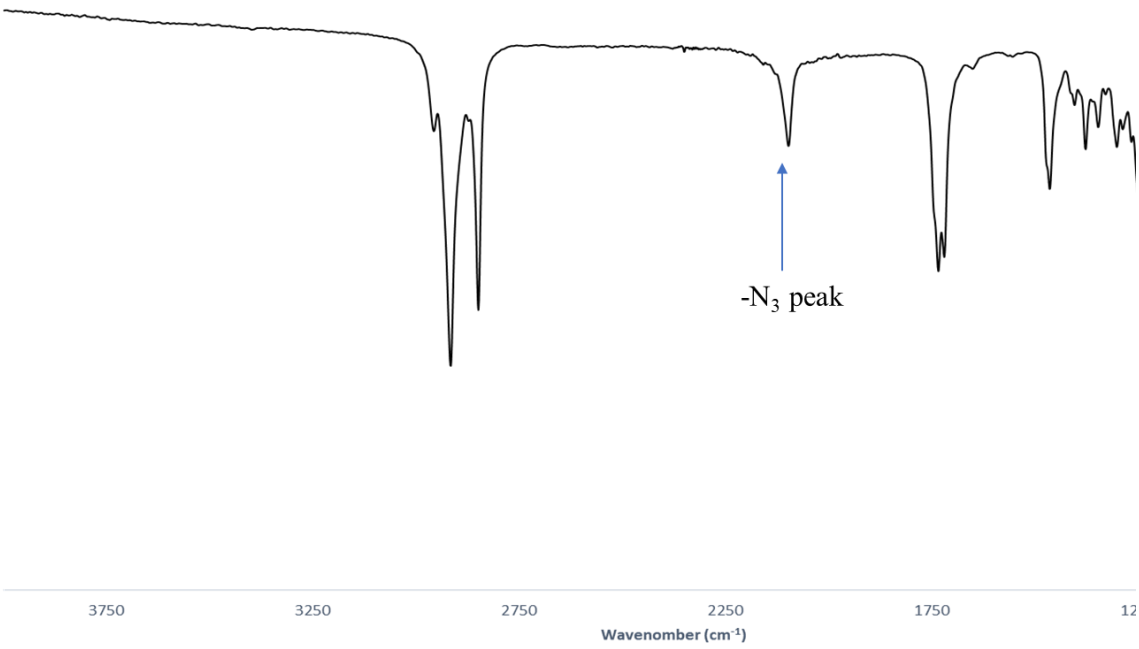

Figure 47. FTIR spectra for A-MPA-4-FA (18)

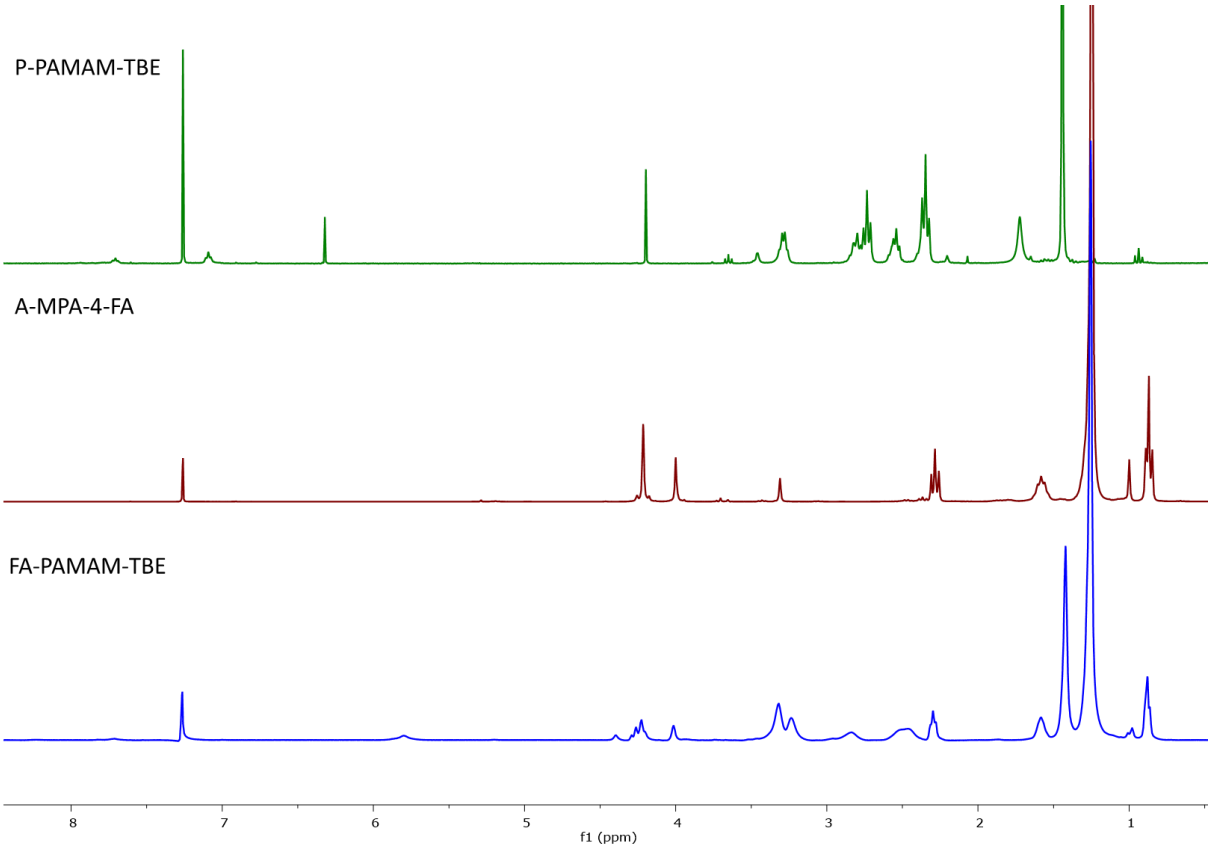

Figure 48. ^{1}H NMR comparison for FA-PAMAM-TBE with P-PAMAM-TBE and A-MPA-4-FA (500 MHz, $CDCl_3$)

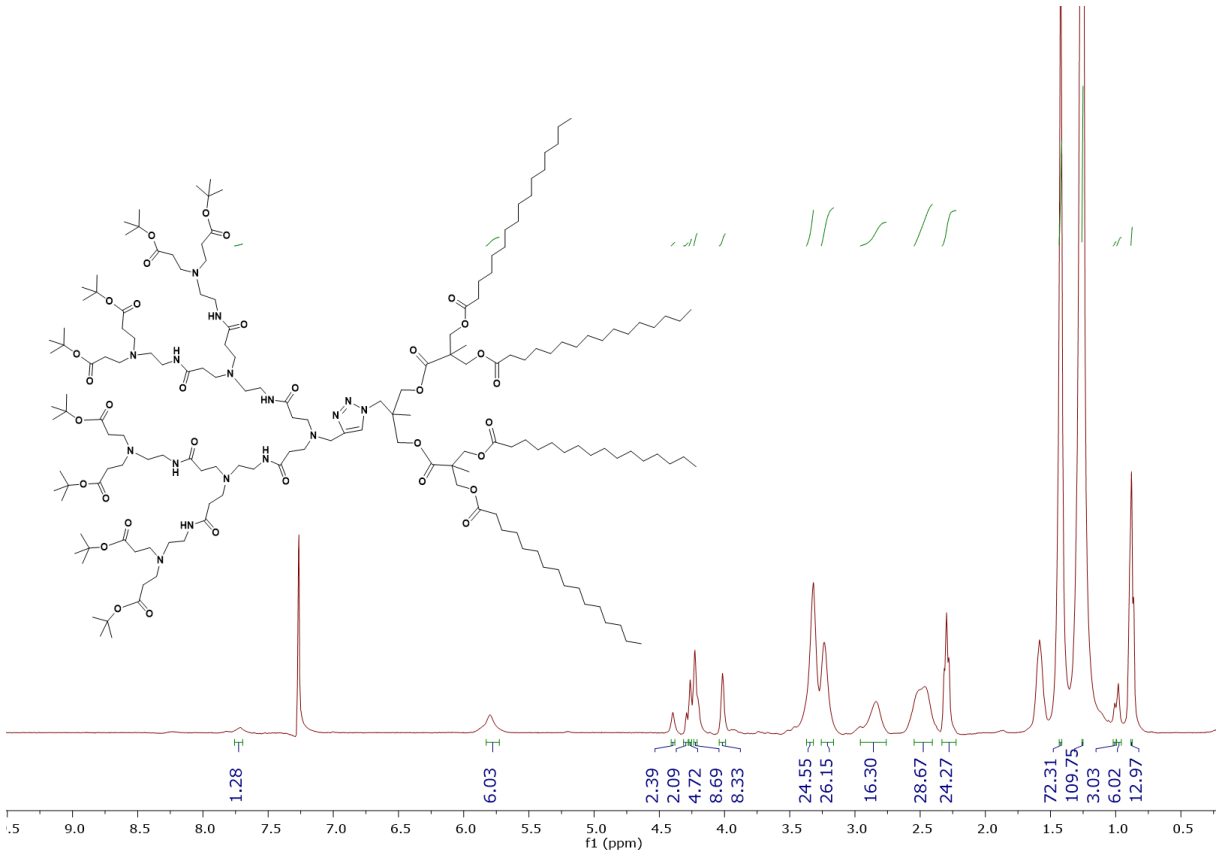

Figure 49. ^{1}H NMR for FA-PAMAM-TBE (500 MHz, $CDCl_3$)

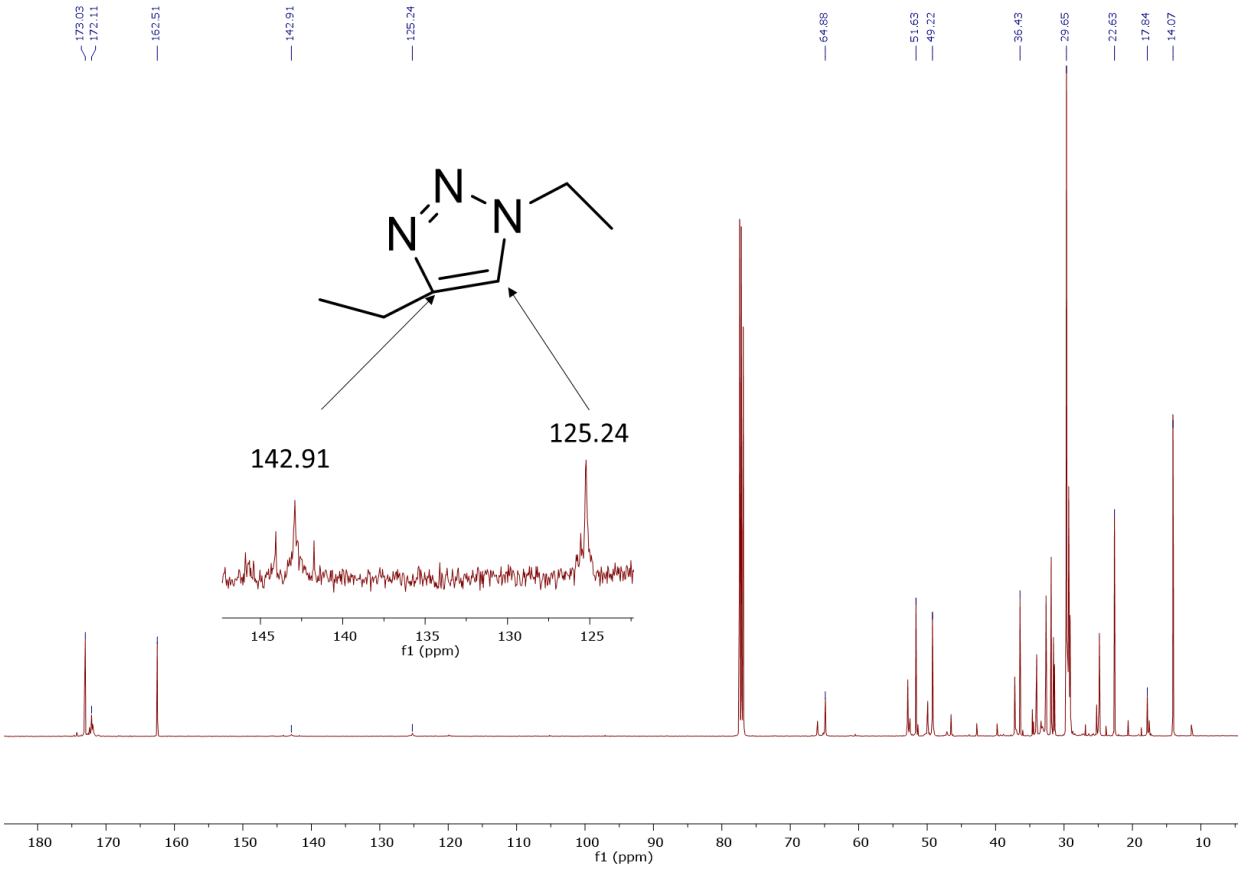

Figure 50. ^{13}C NMR for FA-PAMAM-TBE (300 MHz, $CDCl_3$)

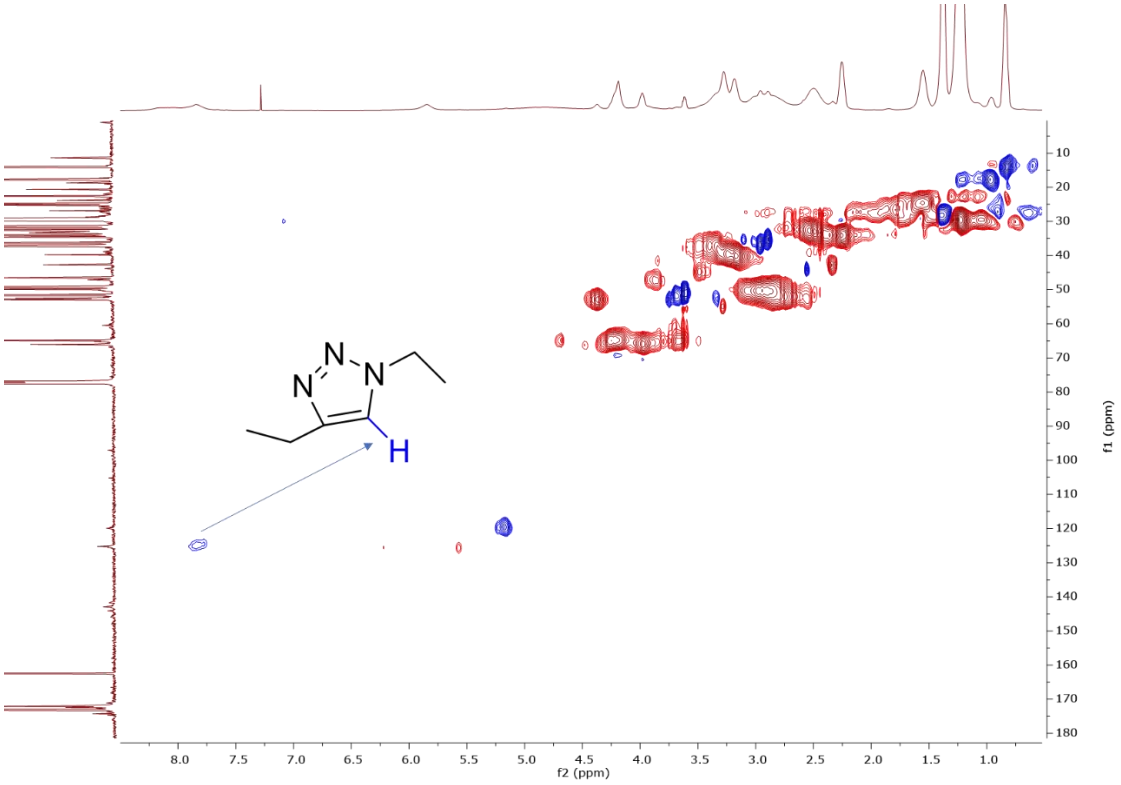

Figure 51. HSQC for FA-PAMAM-TBE (400 MHz, $CDCl_3$)

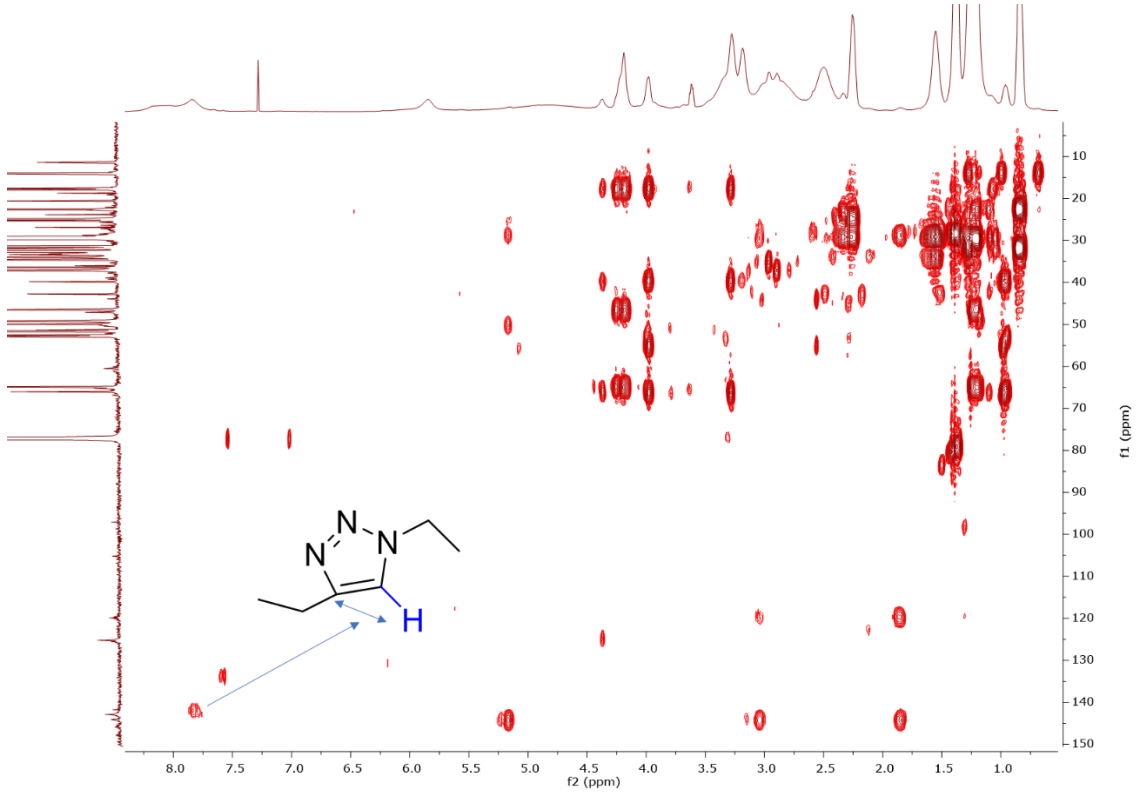

Figure 52. HMBC for FA-PAMAM-TBE (400 MHz, $CDCl_3$)

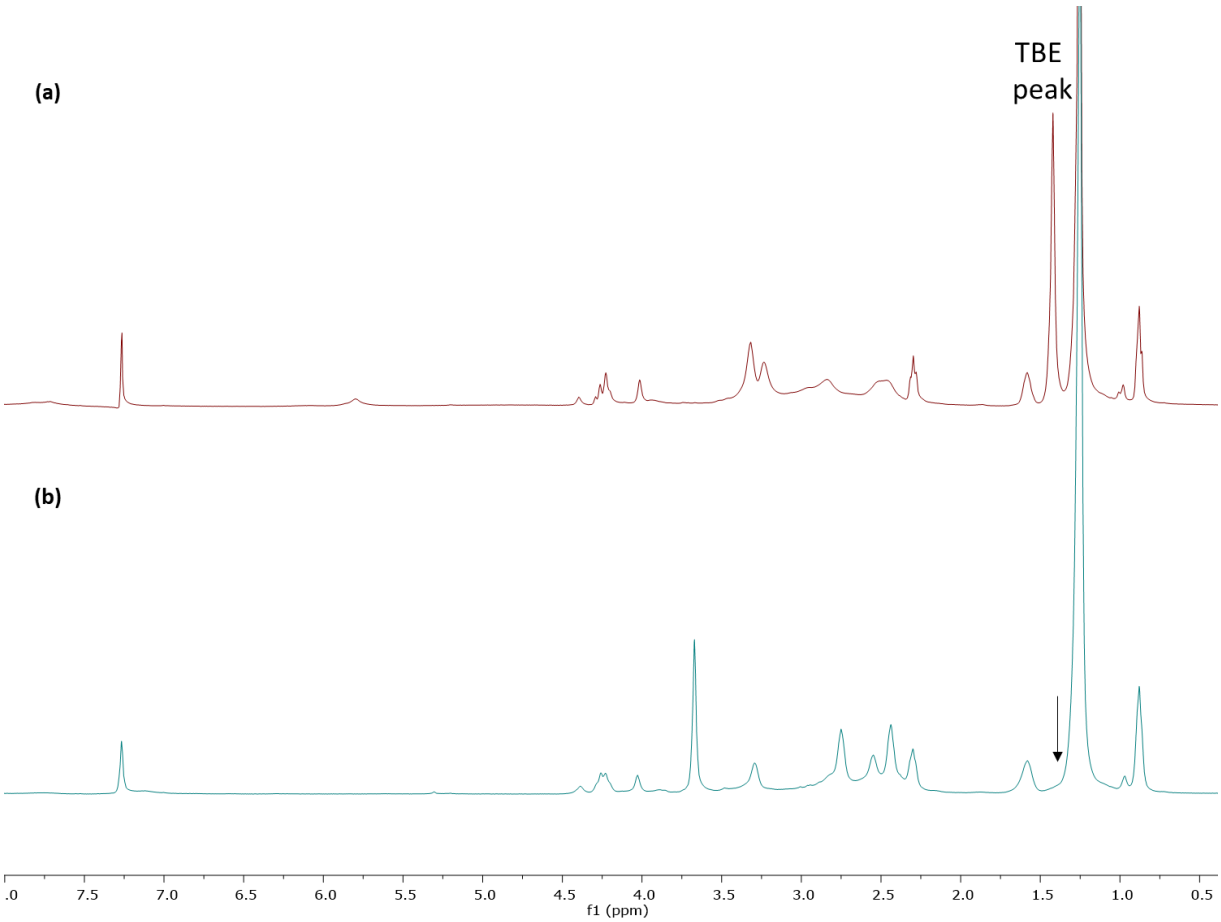

Figure 53. ^{1}H NMR comparison for (a) FA-PAMAM-TBE, (b) FA-PAMAM-COOH (500 MHz, $CDCl_3$), solvent impurities THF; arrow indicates that TBE (1.4 ppm) has been removed to reveal the carboxylic acid groups

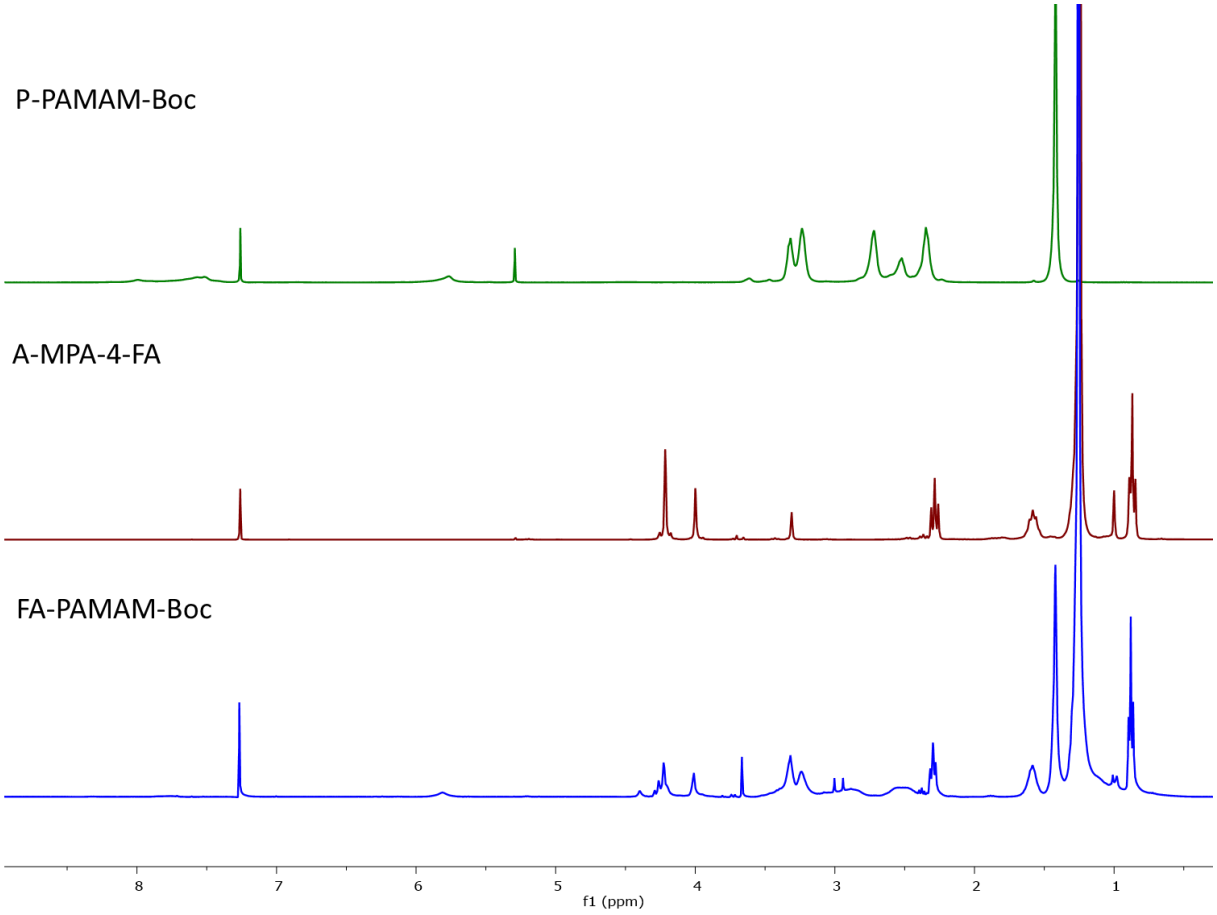

Figure 54. ^{1}H NMR comparison for FA-PAMAM-Boc with P-PAMAM-Boc and A-MPA-4-FA (500 MHz, $CDCl_3$), solvent impurities DMF, DCM and THF

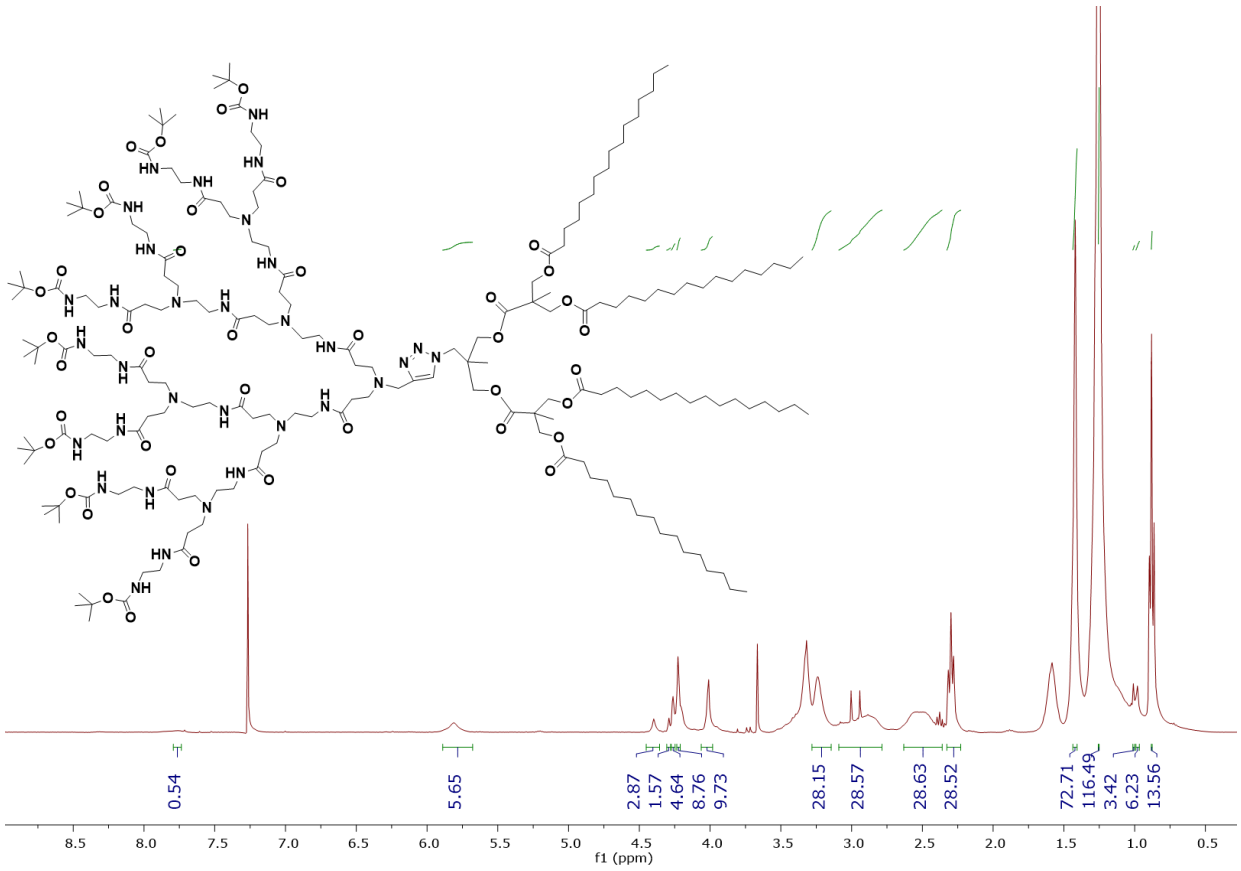

Figure 55. ^{1}H NMR for FA-PAMAM-Boc (500 MHz, $CDCl_3$), solvent impurities THF and DMF

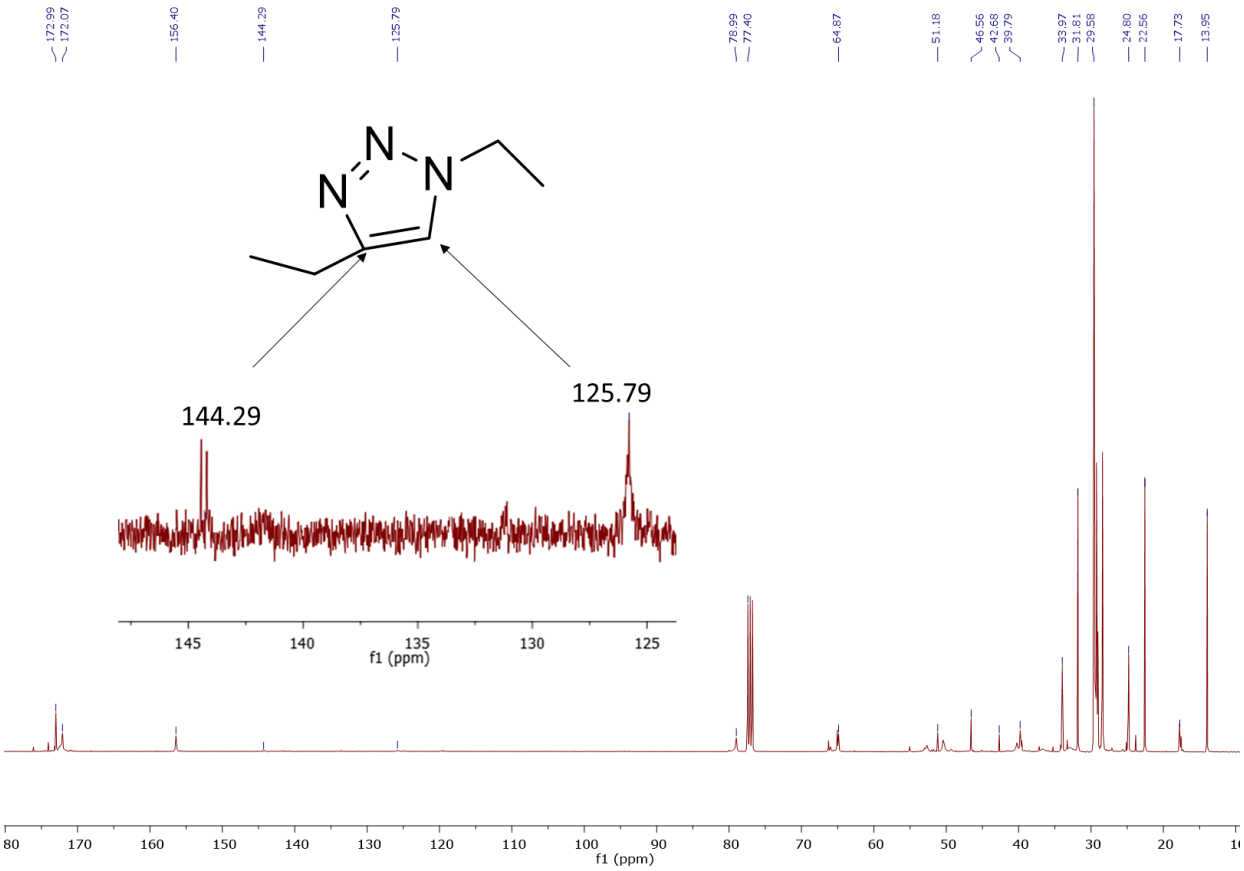

Figure 56. ^{13}C NMR for FA-PAMAM-BOC (400 MHz, $CDCl_3$)

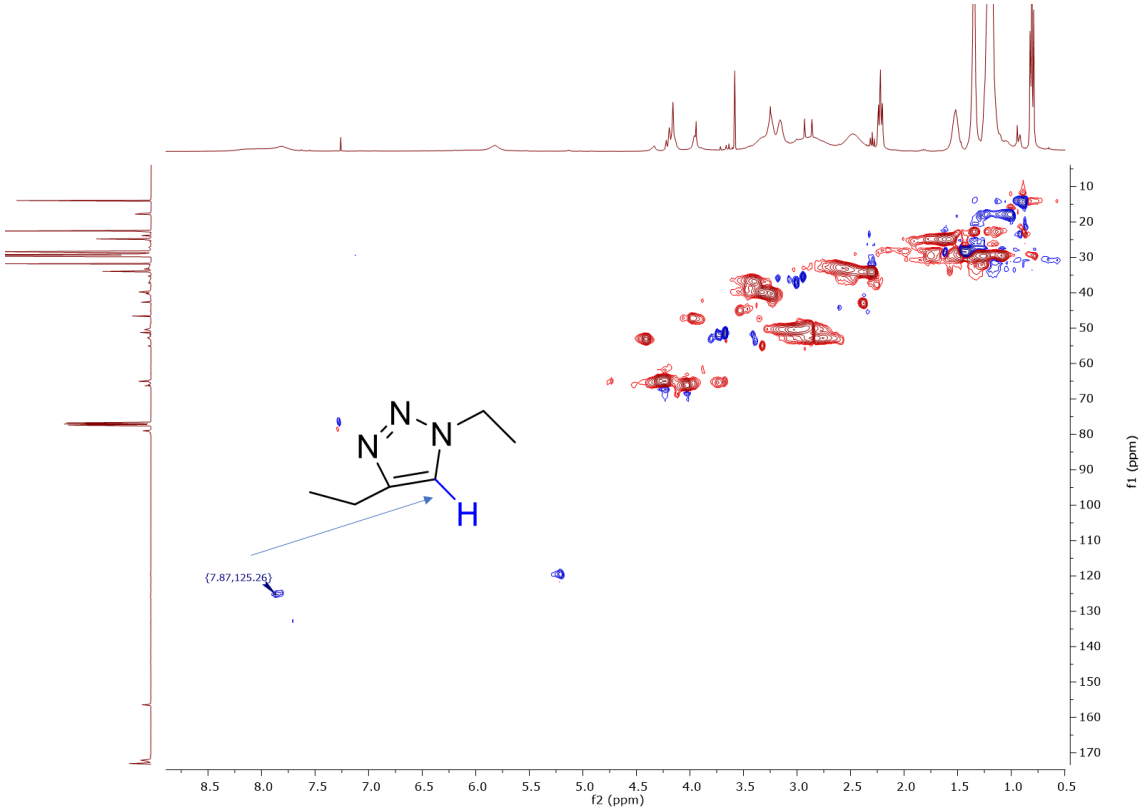

Figure 57. HSQC for FA-PAMAM-BOC (400 MHz, $CDCl_3$)

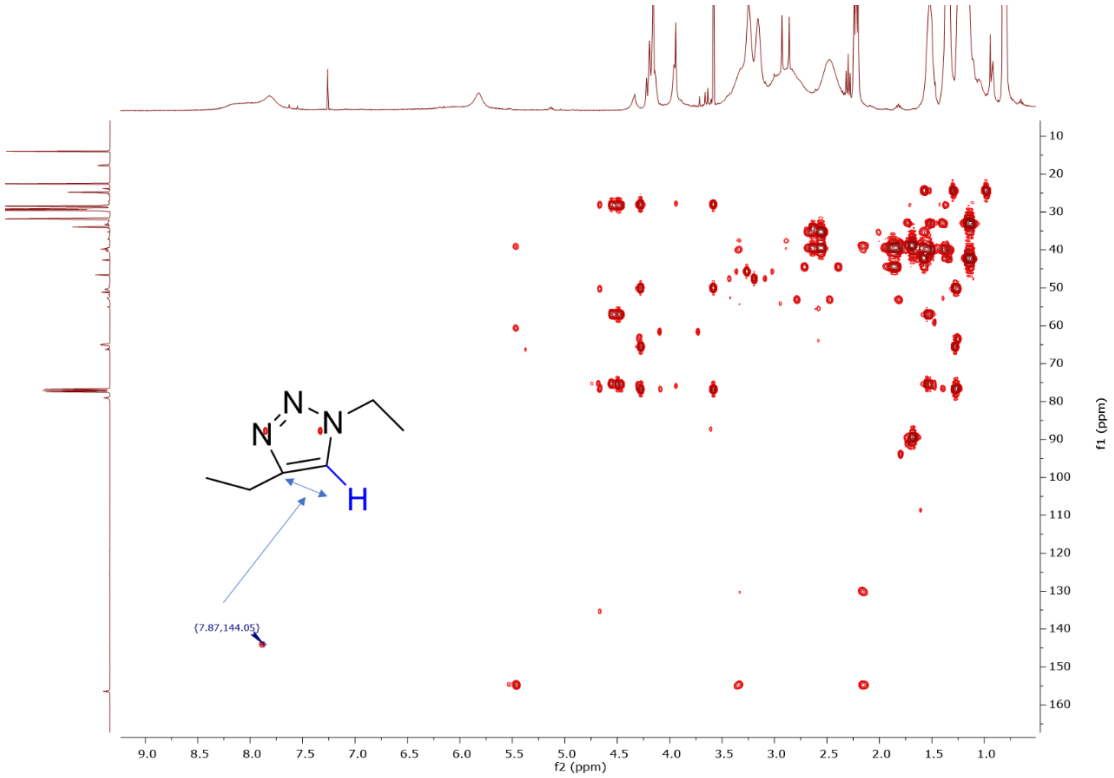

Figure 58. HMBC for FA-PAMAM-BOC (400 MHz, $CDCl_3$)

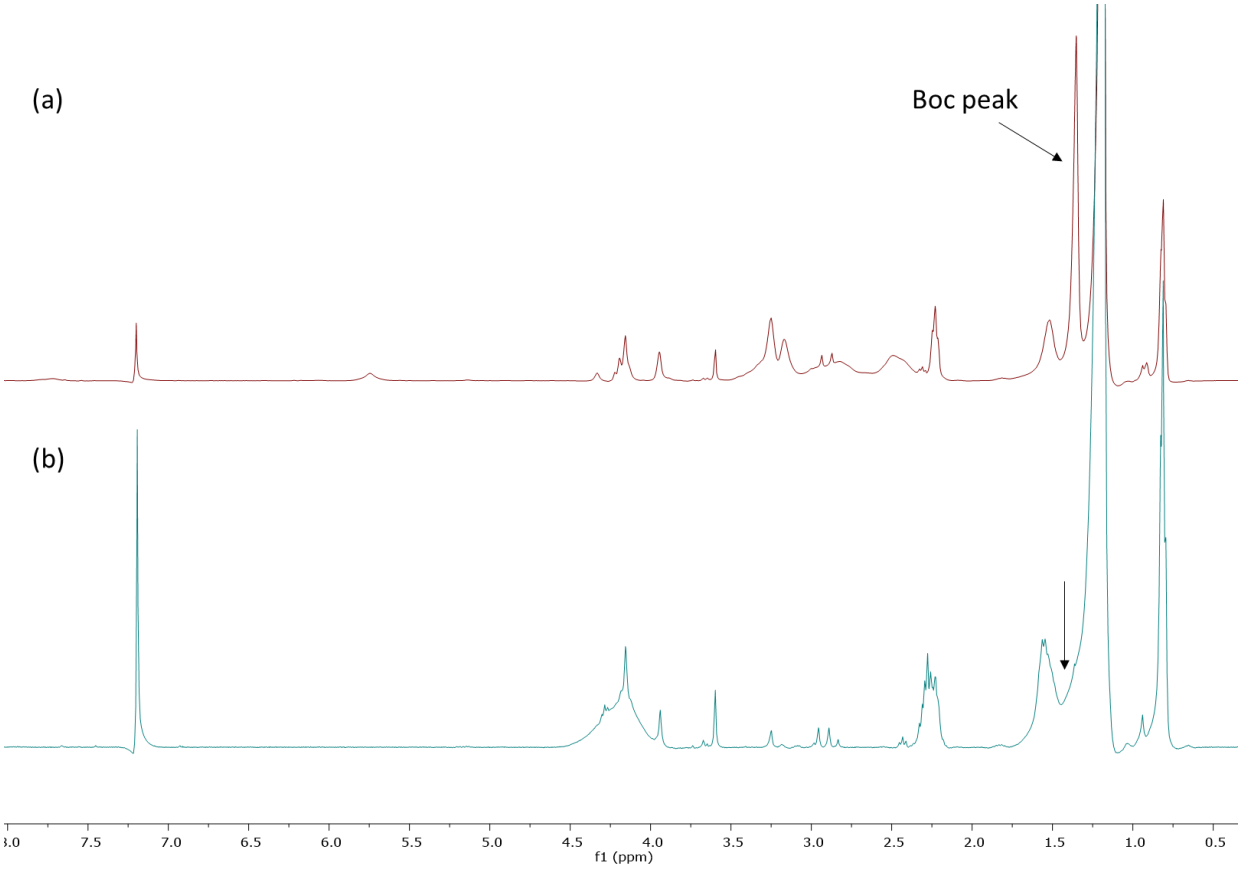

Figure 59. ^{1}H NMR comparison for (a) FA-PAMAM-BOC, (b) FA-PAMAM-NH_3^+ (500 MHz, $CDCl_3$) solvent impurities DMF; arrow indicates removal of Boc group (1.4 ppm) to reveal protonated amine groups. Broaden in NMR spectra due to H bonding and amphiphilic nature of the JD

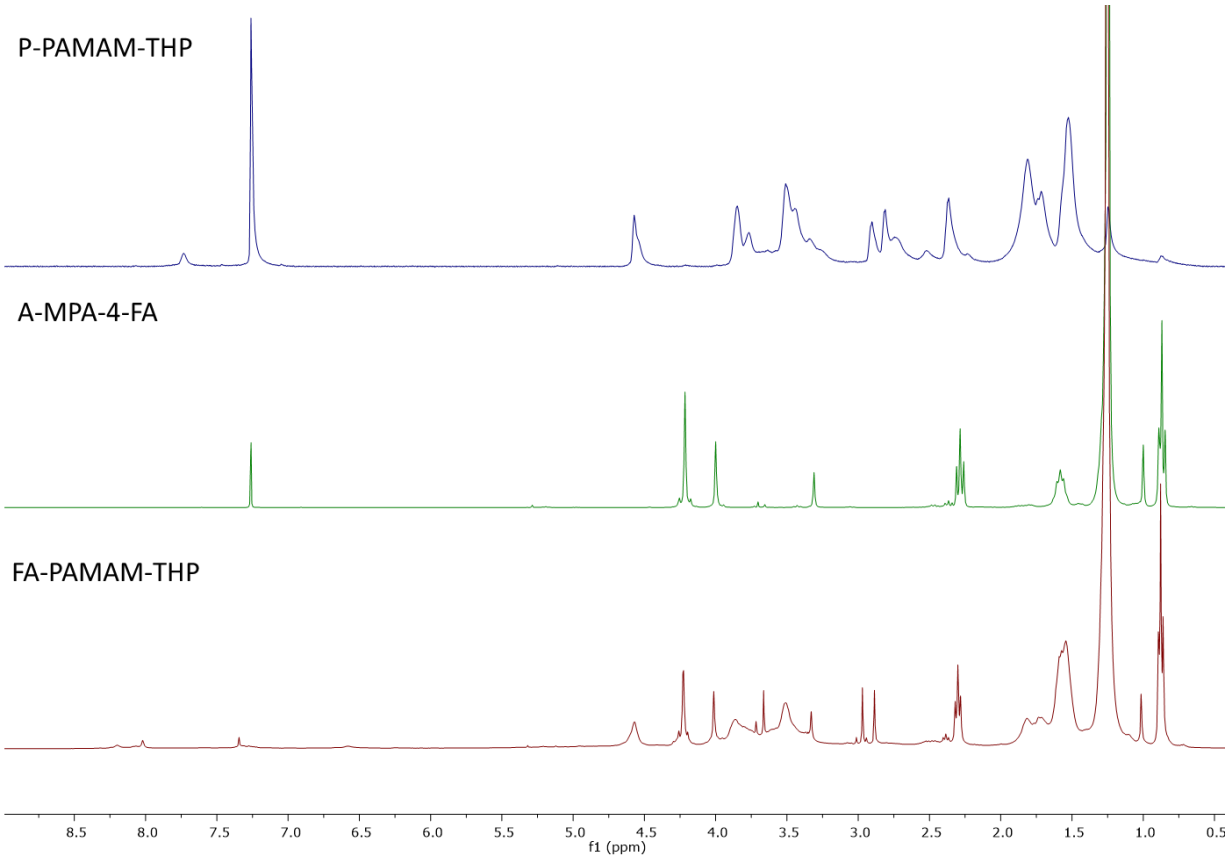

Figure 60. ^{1}H NMR comparison for FA-PAMAM-THP with P-PAMAM-THP and A-MPA-4-FA (500 MHz, $CDCl_3$), solvent impurities DMF and THF

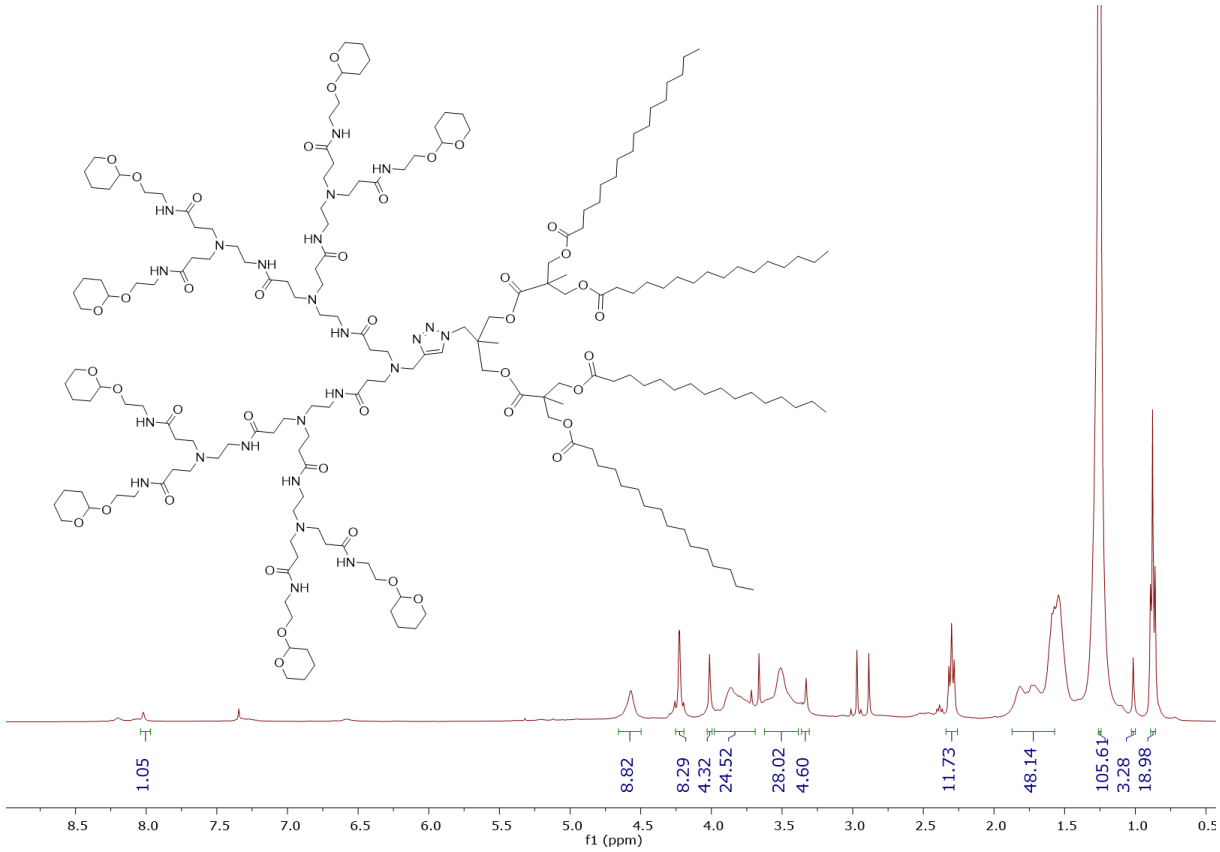

Figure 61. ^{1}H NMR for FA-PAMAM-THP (500 MHz, $CDCl_3$) solvent impurities DMF and THF

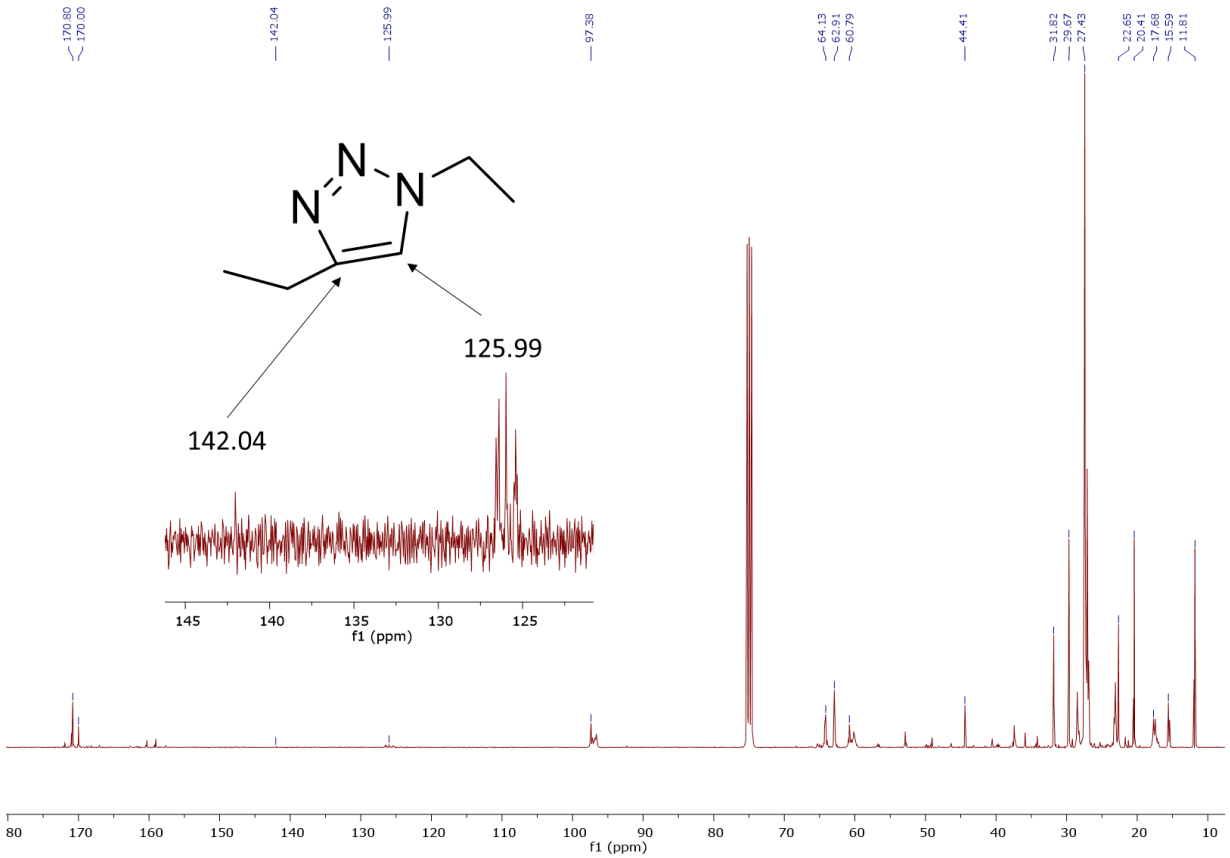

Figure 62. ^{13}C NMR for FA-PAMAM-THP (400 MHz, $CDCl_3$)

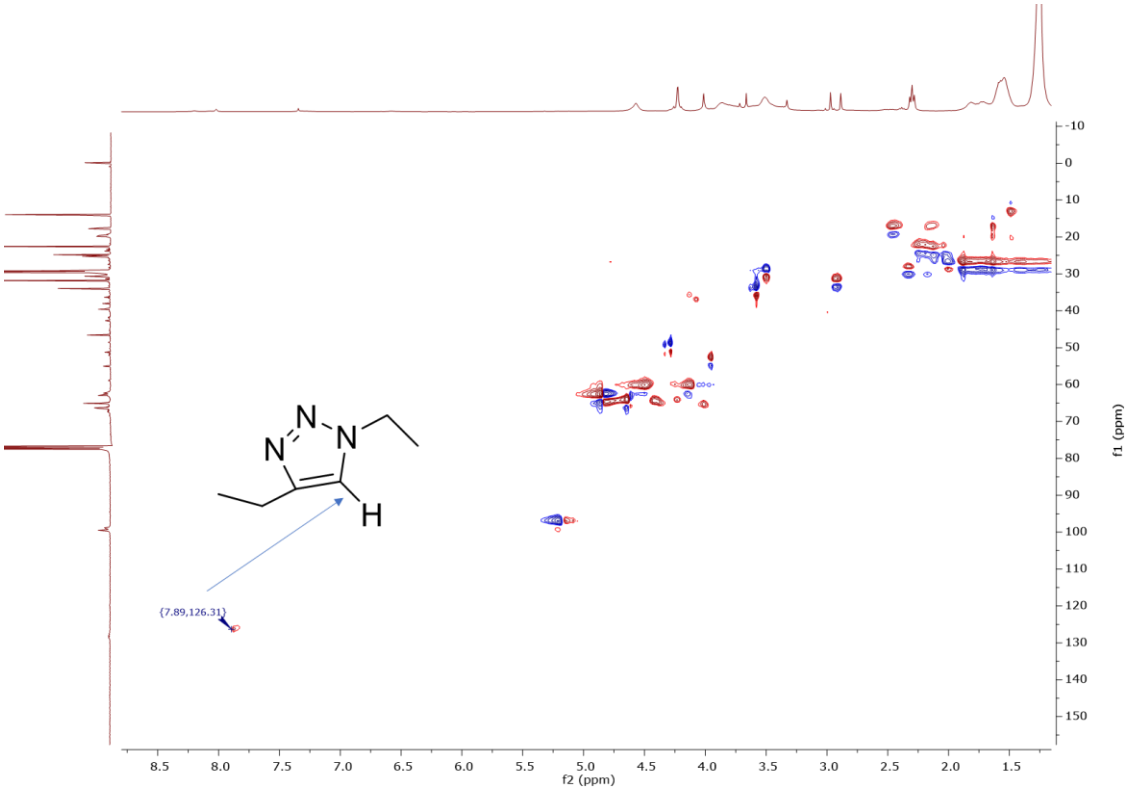

Figure 63. HSQC for FA-PAMAM-THP (400 MHz, $CDCl_3$)

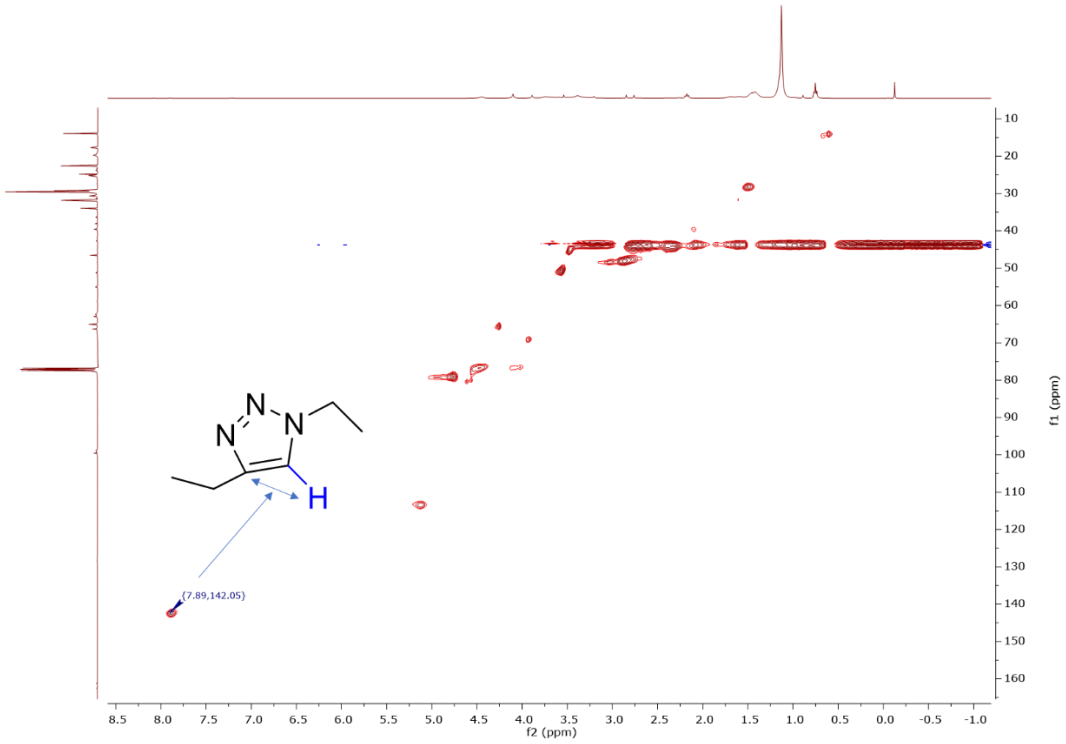

Figure 64. HMBC for FA-PAMAM-THP (400 MHz, $CDCl_3$)

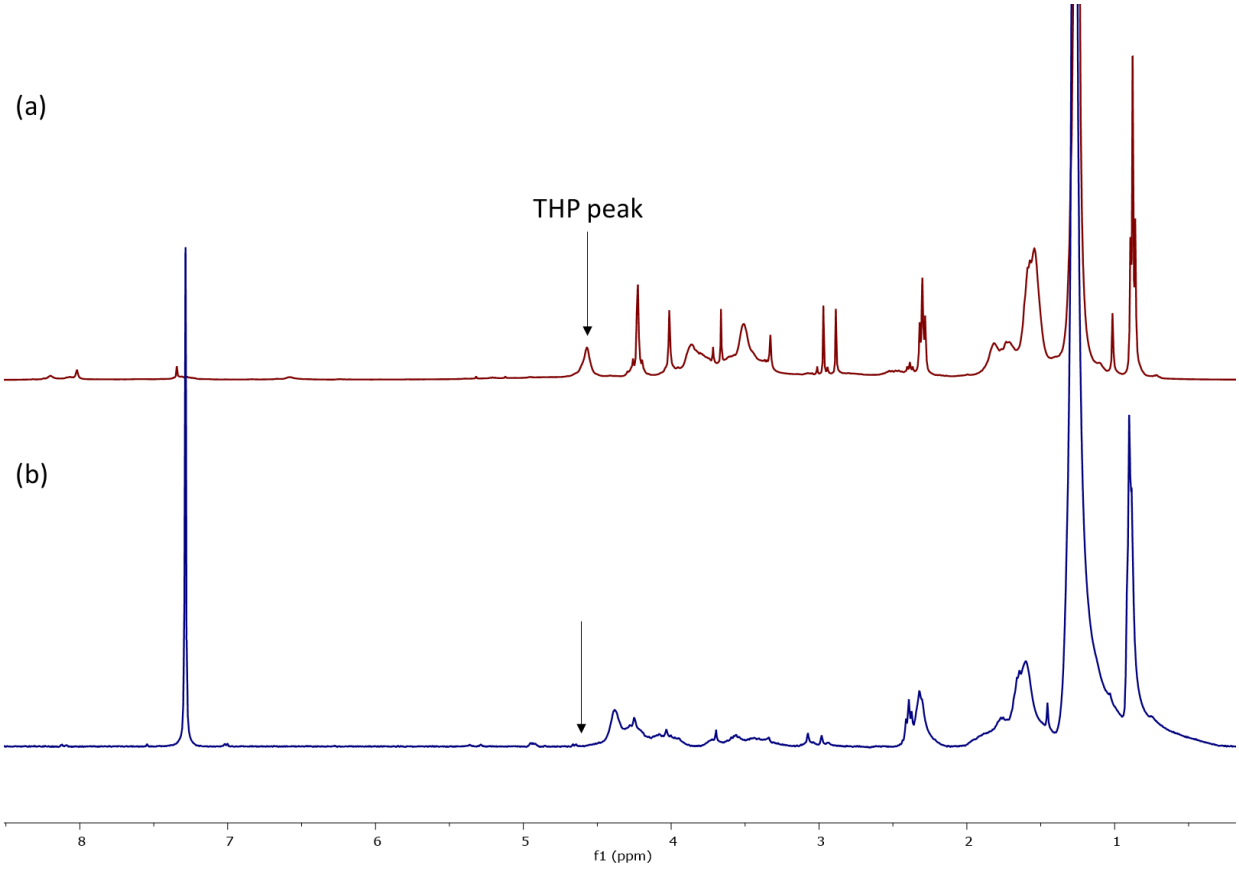

Figure 65. ^{1}H NMR comparison for (a) FA-PAMAM-THP, (b) FA-PAMAM-OH (500 MHz, $CDCl_3$) arrow indicates removal of THP group (4.6 ppm) to reveal hydroxyl groups. Broaden in NMR spectra due to H bonding and amphiphilic nature of the JD

GPC CHROMATOGRAMS

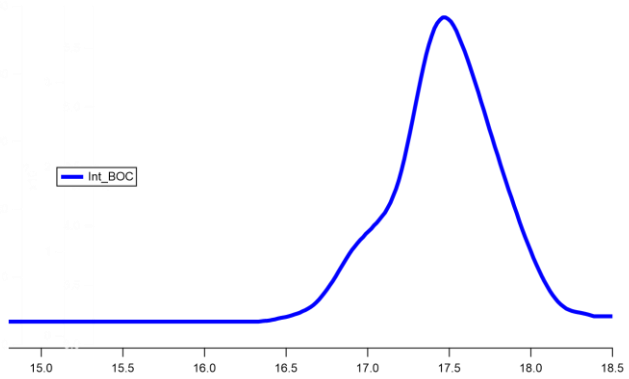

Figure 66. GPC chromatograms for FA-PAMAM-BOC in THF

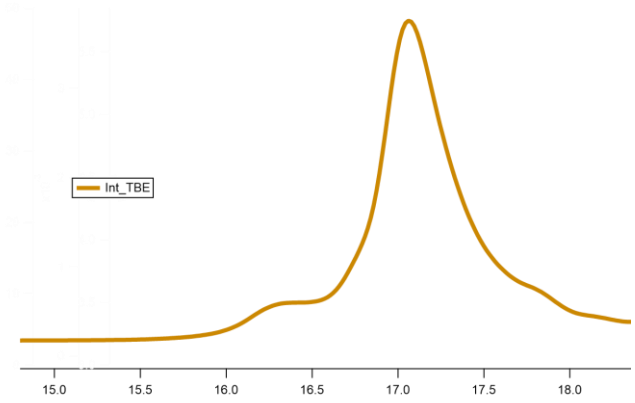

Figure 67. GPC chromatograms for FA-PAMAM-TBE in THF

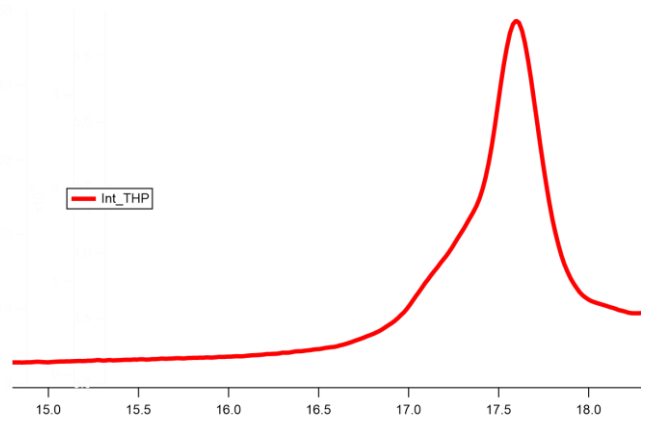

Figure 68. GPC chromatograms for FA-PAMAM-THP in THF

Table 5. Summary of average hydrodynamic diameter of the dendritic aggregates

Sample	R_{hDLS}(nm)		PDI	ζ-potential (mV)
	Number	Intensity		
FA-PAMAM-G3-NH_3^+	57.8 ± 16.7	103.7 ± 40.3	0.191	56.1 ± 6.5
FA-PAMAM-G3-OH	41.0 ± 9.0	53.3 ± 12.4 308.2 ± 85.1	0.469	8.5 ± 1.6
FA-PAMAM-G3-COO^-	93.1 ± 15.9	102.2 ± 14.1	0.882	-17.9 ± 2.6

DLS SPECTRA

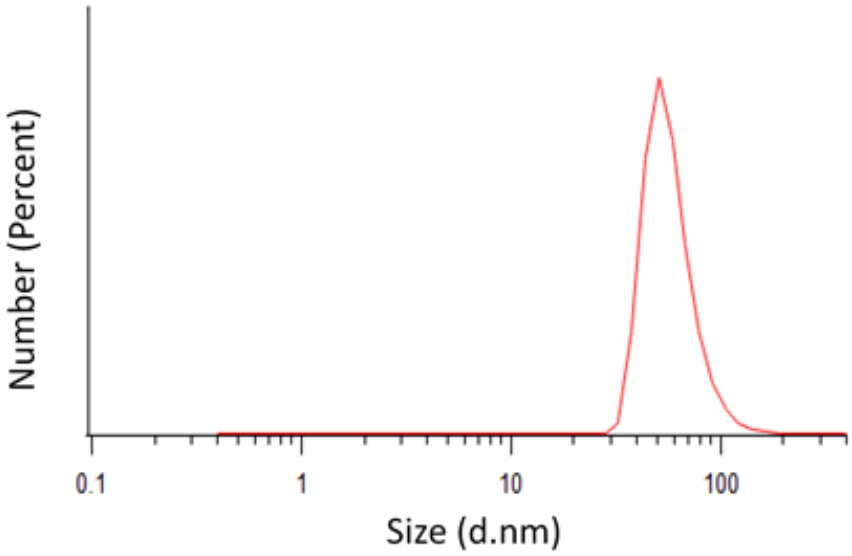

Figure 69. DLS spectra for FA-PAMAM-NH_3^+, Size distribution by number

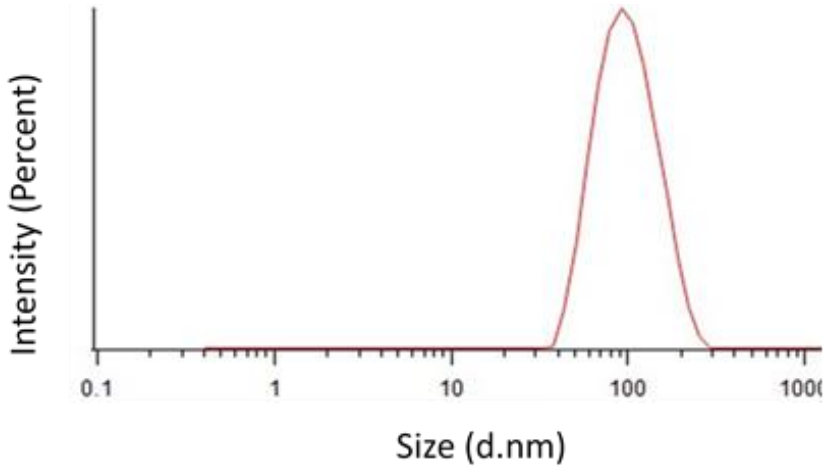

Figure 70. DLS spectra for FA-PAMAM-NH_3^+, Size distribution by intensity

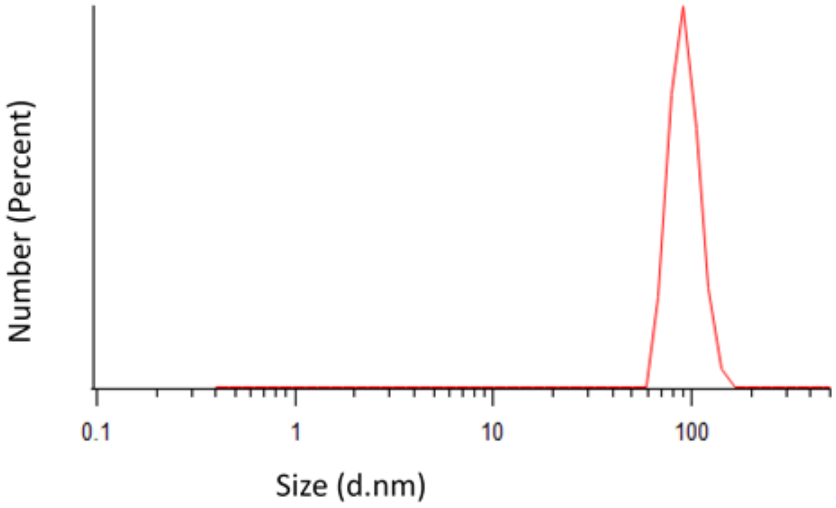

Figure 71. DLS spectra for FA-PAMAM-COO^-, Size distribution by number

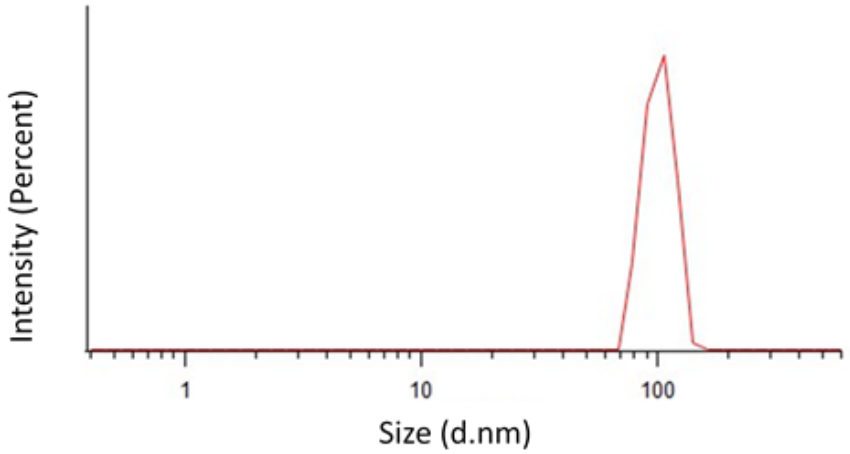

Figure 72. DLS spectra for FA-PAMAM-COO^-, Size distribution by intensity

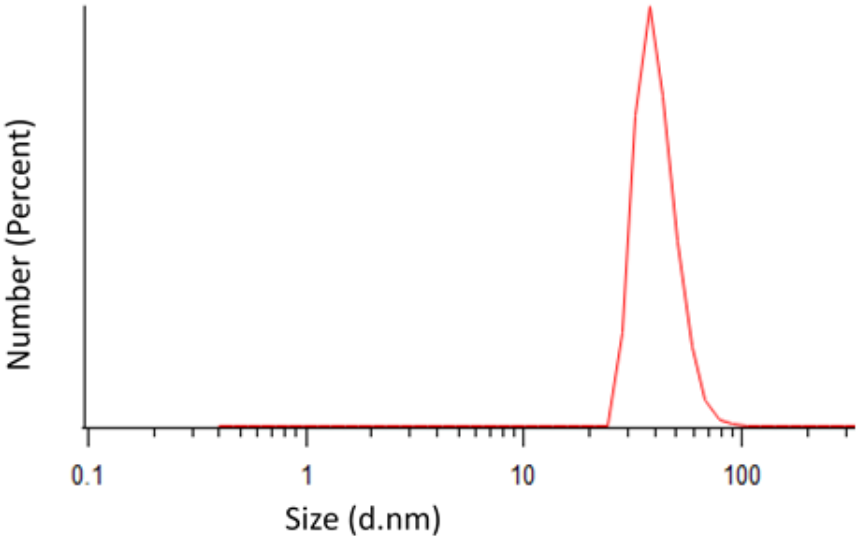

Figure 73. DLS spectra for FA-PAMAM-OH, Size distribution by number

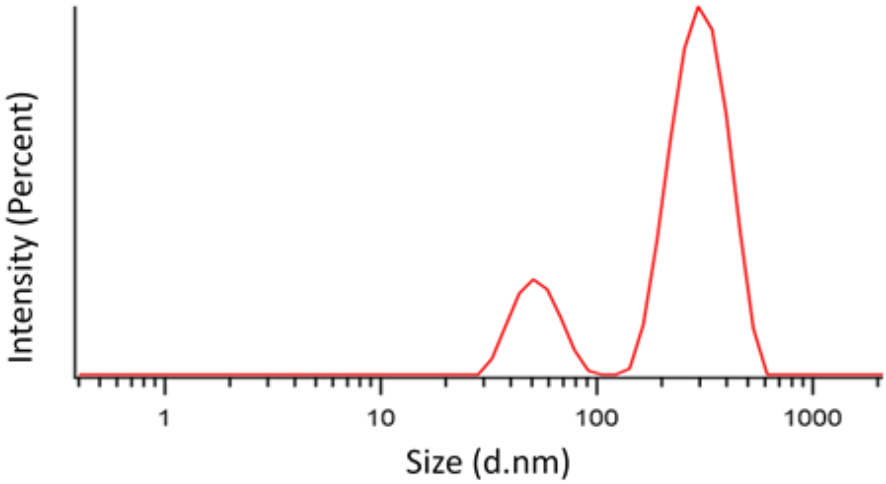

Figure 74. DLS spectra for FA-PAMAM-OH, Size distribution by intensity

CAC DATA

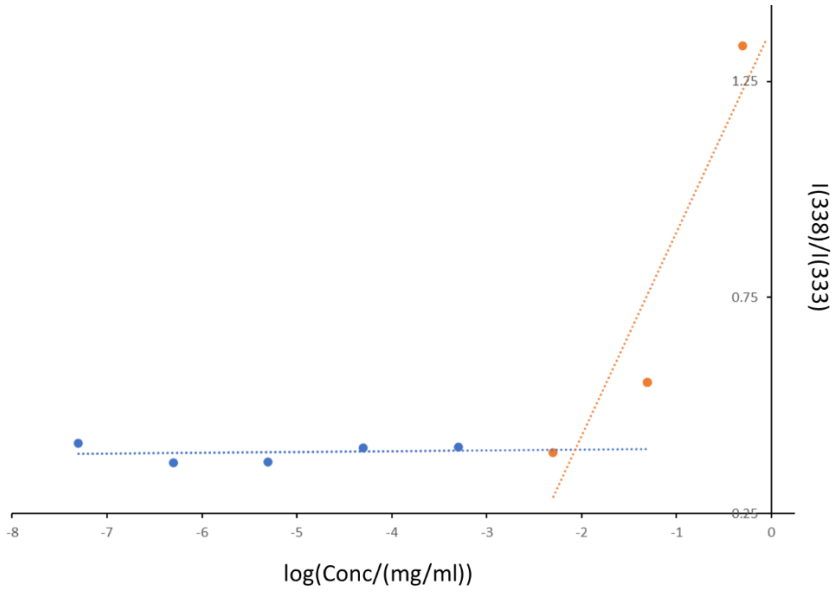

Figure 75. Excitation ratio vs. log concentration for FA-PAMAM-NH_3^+

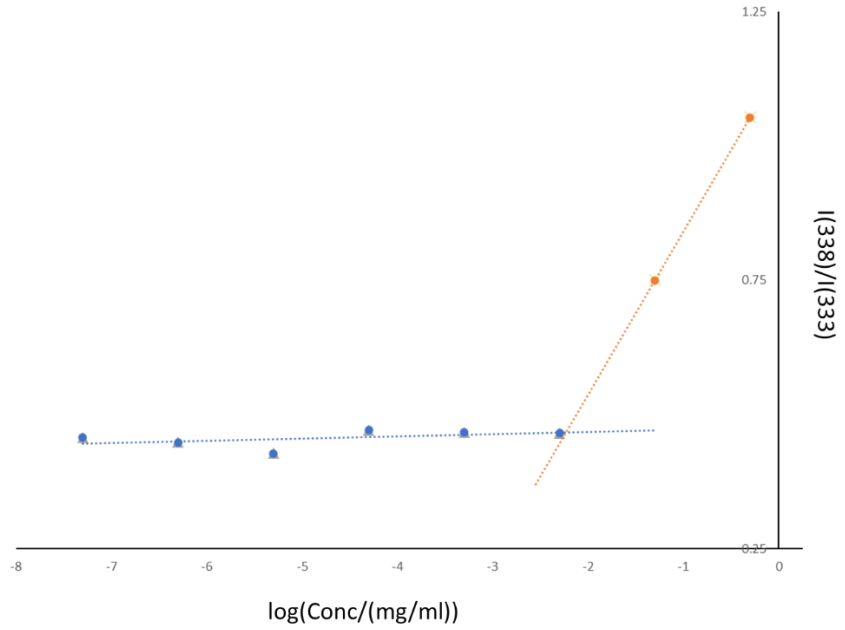

Figure 76. Excitation ratio vs. log concentration for FA-PAMAM-COO^-

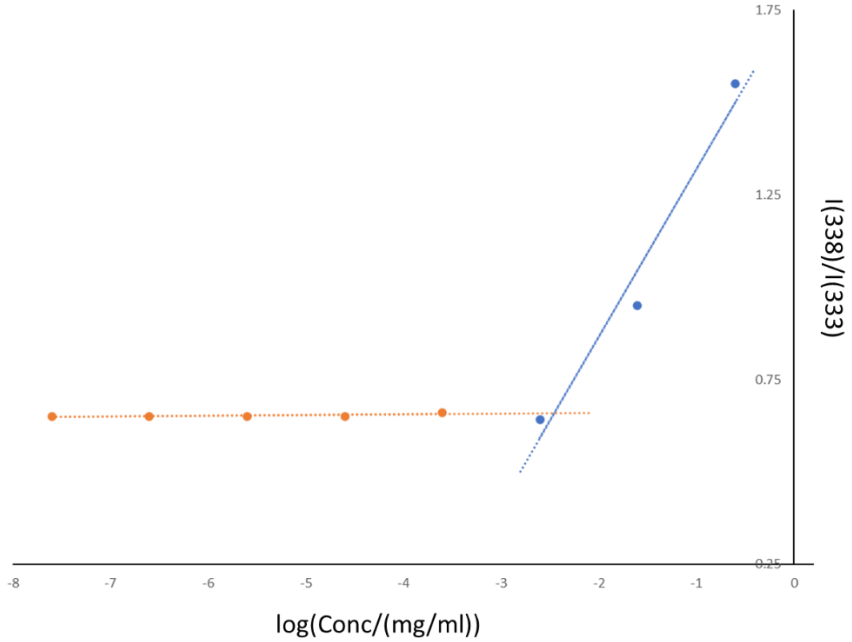

Figure 77. Excitation ratio vs. log concentration for FA-PAMAM-OH

APPENDIX B: SUPPLEMENTARY INFORMATION FOR CHAPTER 3

MATERIALS AND METHODS

All chemicals were purchased from commercial sources (Fisher Scientific) and used without further purification unless indicated otherwise. N-Boc alanine was purchased from Sigma Aldrich. The amberlyst-A21 resin was previously cleaned by suspending in three separate batches of MeOH (approximately equal to resin volume) for 2h. Dowex 50WX8 resin was purified by vacuum filtering and washing with alternating volumes of methanol and tetrahydrofuran until no color was observed in the filtrate (approximately 3 equivalent volumes of solvent). BzMA was percolated through a small column of basic alumina prior to usage. These were stored at -10 over molecular sieves. Before analysis by DLS, TEM, and/or fluorometry, the reaction aliquots were diluted in deionized water with sonication to a concentration of 0.2 mg/mL.

INSTRUMENTATION

NMR and spectra were recorded in deuterated solvents on a Bruker AVANCE 500 NMR Spectrometer. J values are expressed in Hz, and quoted chemical shifts are in ppm downfield from tetramethylsilane (TMS) reference using the residual protonated solvents as an internal standard. The signals have been designated as follows: s (singlet), d (doublet), t (triplet), m (multiplets). Analysis was done using MestreNova 14.0.

GPC measurements were done at a flow rate of 0.3 mL/min at 50, on a GPC system equipped with Waters Alliance HPLC System, 2695 Separation Module with 2 Tosoh TSKgel

Super HM-M columns and Waters 2414 Differential Refractometer (RI) and Waters 2998 Photodiode Array Detector (PDA) was used. Polystyrene standards (900–100,000 g/mol) were used for the calibrations curve, and data were processed using the Empower 3 software (Waters). Addition of the electrolytic salt, LiBr (0.01%), was done to minimize effects such as polymer aggregation and/or adsorption associated with the polymer or the columns, enabling normal fractionation to occur.1, 2, 3

DLS Aggregate size and zeta potential (Z-potential) were determined by a Malvern Instruments Zetasizer Nano ZS using a He–Ne laser with a 633 nm wavelength, a detector angle of 173 at 25 using a He–Ne laser with a 633 nm wavelength. Measurements were done in triplicate to ensure reproducibility.

TEM A JEOL 1230 TEM was operated at 100 kV using a Gatan Orius 831 bottom mounted CCD camera. TEM samples were prepared by adding 10 diluted nanoparticle solutions to a 300 mesh Formvar/Cu grid. Water was wicked away with weighing paper, and the slide was then incubated on a drop of 1% uranyl acetate stain for 20 sec. Excess water was again wicked away, and the grids were dried at room temperature in a vacuum oven for 45 min before analysis. Image analysis was done using Fiji 2.1.2 and a custom Python 3.7 script.

SYNTHETIC DESCRIPTION

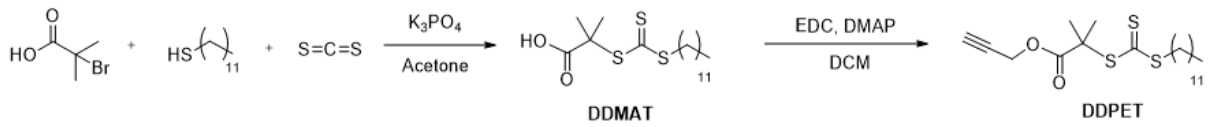

Figure 78. Synthesis of alkyne (linear) segment of mCTA

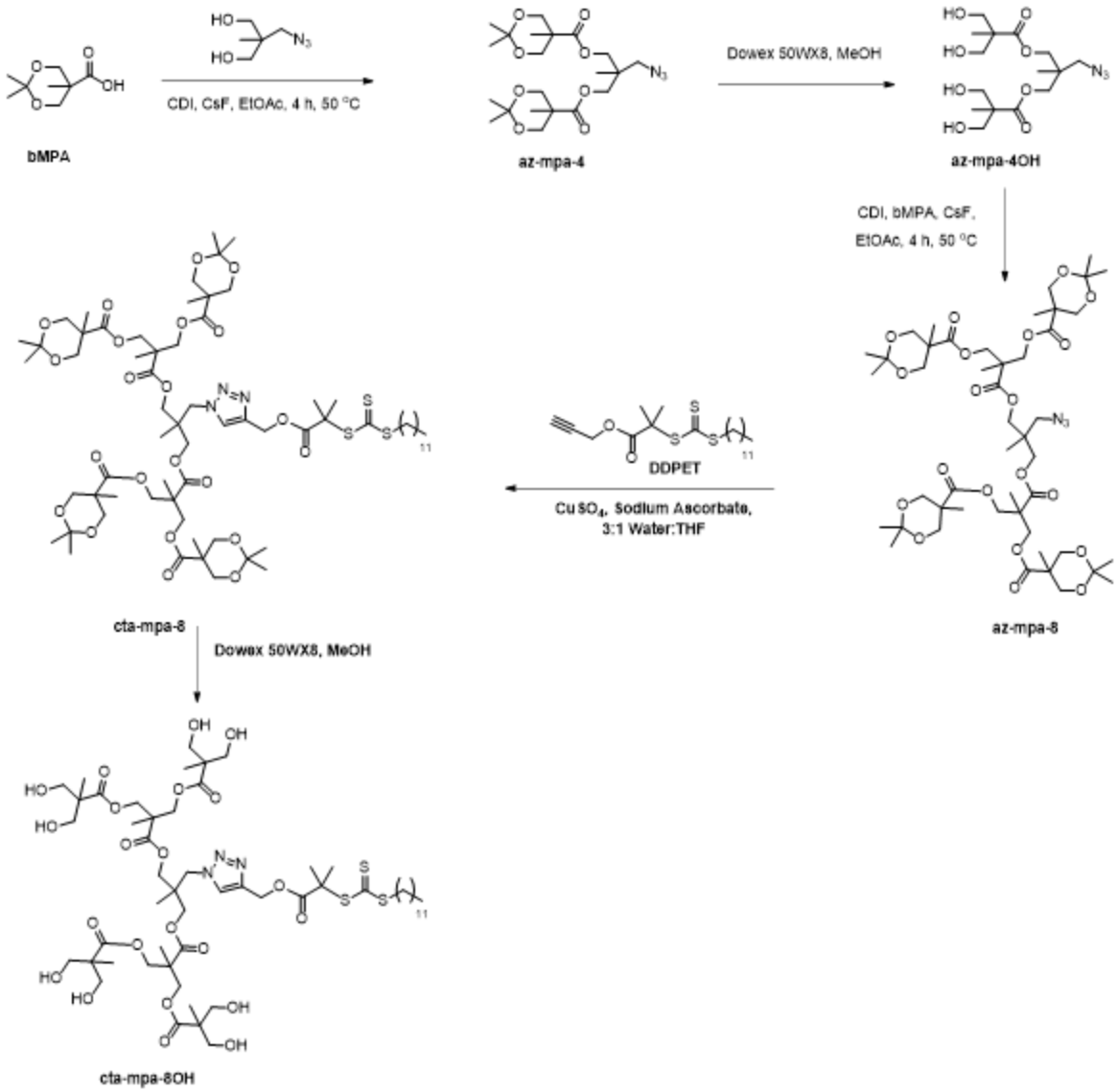

Figure 79. Synthesis of dendritic segment and coupling to from mCTA-8OH

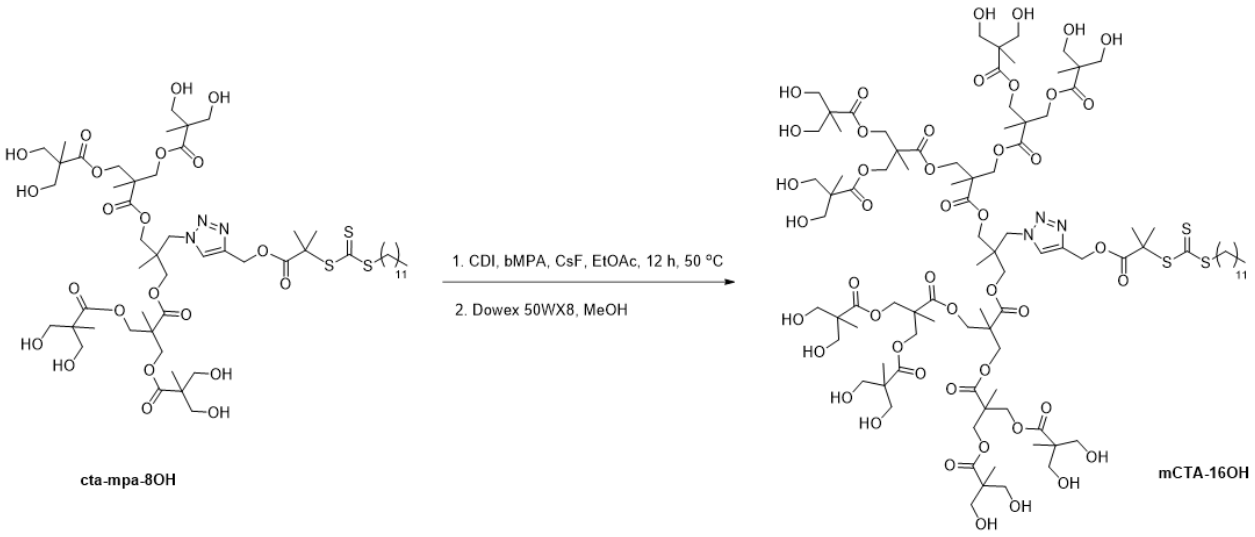

Figure 80. Synthesis of final mCTA-16OH

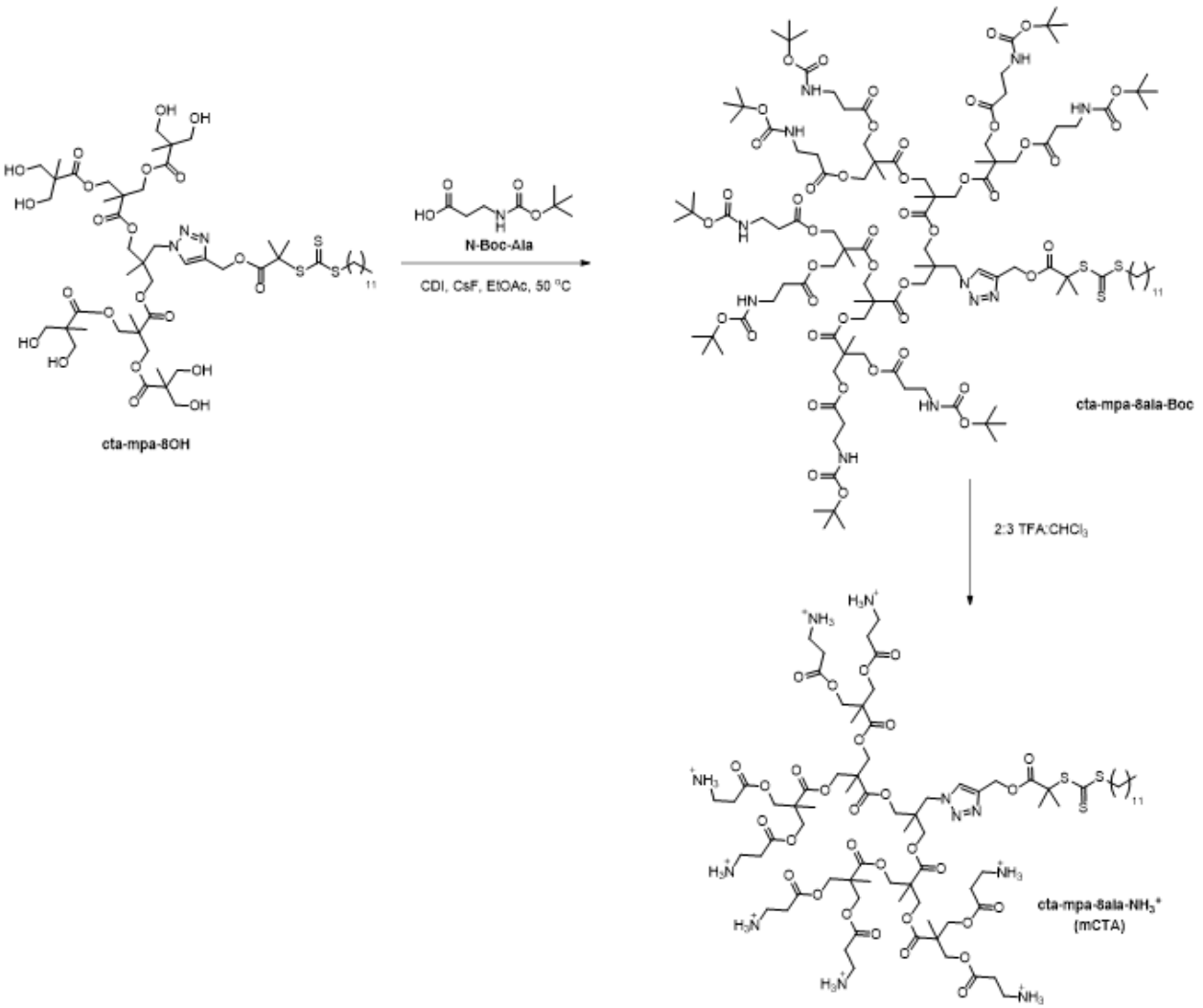

Figure 81. Synthesis of final mCTA-8ala

GENERAL ESTERIFICATION PROCEDURE

BMPA dendron growth was adapted from previously reported procedures.4, 5 bMPA (1.5eq per hydroxyl group) was suspended in a solution of EtOAc (2M relative to CDI), and N,N-carbonyl diimidazole (CDI, 1.65eq per hydroxyl group) was carefully added. After 1h stirring at rt and confirmation of completion via NMR, CsF (0.24eq per hydroxyl group) was added, followed by the alcohol initiator. The solution was heated overnight, or until completion was observed via NMR. After cooling to room temperature, the crude was stirred overnight with water added at a 5:1 volume ratio to EtOAc. This was diluted to a concentration of 0.2M and washed with 0.25M amount of the following solutions: 3x 1M, 3x saturated, and 1x brine. The organic layer was dried with magnesium sulfate and concentrated in vacuo.

GENERAL DEPROTECTION PROCEDURE

The acetal-protected dendron was dissolved to a concentration of 6.7wt% in MeOH. Dowex resin was added at a 350% weight ratio relative to dendron.[215] After the disappearance of the doublet at 1.4 ppm via, the resin was removed via vacuum filtration, and MeOH was removed in vacuo. Any residual water was removed via air-drying. If any impurities remained via, the hydroxyl-terminated dendron was recrystallized in EtOAc or stirred with petroleum ether and charcoal and filtered over Celite.

GENERAL POLYMERIZATION PROCEDURE

The mCTA and solvent(s) were added to a gas-tight conical vial, sonicated, and incubated for 1 h in a dark place. Initiator and monomer(s) were then added, and the solution was purged with Ar for 30 min. The vial was then placed in a 60 ^{0}C bath and monitored by NMR. Mn was first measured by ^{1}H NMR, using peaks 5.75, 4.87, and 4.65 ppm for pBzMA-OH and 5.75, 4.87, and

4.67 ppm for pBzMA-NH_3^+ as references. (Theoretical integration = 24). The peak at 4.87 ppm corresponds to the benzyl peak (CH2) of pBzMA and therefore equals 2*DP. All NMR were recorded in DMSO-d6. For pBzMA-NH_3^+ with mCTA-8ala, we found it imperative to maintain a low pH as alanine-functionalized bMPA has been shown to be relatively unstable at neutral/basic pH at elevated temperatures.6, 7 Given the pH sensitivity of this initiator, the pH of mCTA-8ala in water at a concentration of 0.37 M was maintained at about 1.7.

SYNTHESIS PROCEDURES

The bMPA monomer was made as previously described.5 Briefly, 2,2-bis(hydroxymethyl)propionic acid (100 g, 0.746 mol) was stirred in acetone (500 mL) and 2,2-dimethoxypropane (138 mL, 1.12 mol) at room temperature until the solution turned transparent. Then, para-toluene sulfonic acid (6.42g, 37.3 mmol) was added, and the reaction was stirred for 4 h. The crude was percolated through a column of Amberlyst-A21 resin. The eluent was conc in vacuo, dissolved in 300 mL DCM and stirred 6 h. Any solid that crashed out was removed by vacuum filtration over Celite. The filtrate was added dropwise to 1L of Hexanes and stirred for 30 min, then allowed to sit for 30 min. The resulting white solid was vacuum filtered, yielding bMPA as a white, amorphous solid. Yield = 79.6g (61.2%) 1H NMR (300 MHz, Chloroform-d) 4.20 (d, J = 12.0 Hz, 2H), 3.68 (d, J = 11.8 Hz, 2H), 1.48 – 1.39 (m, 6H), 1.22 (s, 3H).

Az-mpa-4 was grown by the general esterification procedure outlined above. After activating bMPA (14.9 g, 85.6 mmol) suspended in 43mL EtOAc with CDI (13.9g, 85.6 mmol), CsF (2.08g, 13.7 mmol) and 2-(azidomethyl)-2-methylpropane-1,3-diol (4.14 g, 28.5 mmol) were added and stirred overnight, yielding az-mpa-4 as a light-yellow oil. Yield = 11.9g (92%) 1H NMR (400 MHz, Chloroform-d) 4.21 (d, J = 11.6 Hz, 4H), 4.11 (s, 4H), 3.68 (d, J = 11.6 Hz, 5H), 3.40

(s, 2H), 1.42 (d, J = 25.7 Hz, 13H), 1.17 (s, 6H), 1.08 (s, 3H). Solvent impurities: EtOAc, Water. 13C NMR (75 MHz, Chloroform-d) 173.77, 98.16, 66.13, 65.94, 55.11, 42.23, 40.02, 25.82, 21.45, 18.45, 17.69.

Az-mpa-4OH: az-mpa-4 was deprotected using the general deprotection procedure outlined above. After overnight stirring, the crude was dried in-vacuo and suspended in petroleum ether. Enough activated charcoal was added to make the solution opaque, and this was stirred overnight. This was filtered over Celite and concentrated in-vacuo, quantitatively yielding az-mpa-4OH as a clear oil. 1H NMR (400 MHz, Methanol-d4) 4.06 (s, 4H), 3.73 (d, J = 10.7 Hz, 4H), 3.64 (d, J = 10.8 Hz, 4H), 3.45 (s, 2H), 1.20 (s, 6H), 1.07 (s, 3H). 13C NMR (101 MHz, MeOD) δ 174.82, 65.76,, 64.54, 55.04, 50.44, 50.21, 47.57, 47.35, 47.14, 39.41, 19.66, 16.74, 16.06, 13.21.

Az-mpa-8 was grown according to the general esterification procedure outlined above. After activating bMPA (15.7g, 90mmol) suspended in 45 EtOAc with CDI (16.1g, 99mmol), CsF (2.10g, 13.8mmol) and 5.66g az-mpa-4OH were added and stirred 3h, yielding az-mpa-8 as a honey-colored oil. Yield = 12.6g (84%). 1H NMR (300 MHz, Chloroform-d) 4.45 (s, 8H), 4.15 (d, J = 11.8 Hz, 8H), 4.02 (s, 4H), 3.63 (d, J = 12.0 Hz, 8H), 3.35 (s, 2H), 1.39 (d, J = 18.6 Hz, 2rH), 1.31 (s, 6H), 1.14 (s, 12H), 1.03 (s, 3H). Solvent impurities: acetone, EtOAc, water

DDMAT: Potassium phosphate (4.2 g, 1.1 Eq, 20 mmol) was suspended in acetone (60 mL) in a 2-neck, 100mL flask. N_2 gas was bubbled through the solution for 30 minutes. Dodecane-1-thiol (4.0 g, 4.73 mL, 1.1 eq, 20 mmol) was added over 25 minutes via syringe pump. Carbon disulfide (4.1 g, 3.24 mL, 3 eq, 54 mmol) was then added and stirred 10 minutes. 2-bromo-2-methylpropanoic acid (3.0 g, 1 eq, 18 mmol) was added under N2. This was stirred until completion by NMR. After 48h, Acetone was removed in-vacuo. The resulting yellow solid was dissolved in 200mL 1M HCl. The water layer was extracted with 2x200mL DCM. The combined

organic fractions were washed with 200mL water and 200mL Brine. The organic fractions were dried with MgSO4 and conc in-vacuo. The resulting orange solid was recrystallized with 30mL hexanes, yielding S-Dodecyl-S′-(α,α′-dimethyl-α′′-acetic acid)trithiocarbonate, (DDMAT) as a yellow crystal. Yield = 3.3g (50%). 1H NMR (300 MHz, Chloroform-d) 3.28 (t, J = 7.4 Hz, 2H), 1.73 (s, 6H), 1.66 (q, J = 7.6 Hz, 2H), 1.26 (s, 16H), 0.92 – 0.84 (m, 3H). 13C NMR (75 MHz, CDCl3) δ 220.51, 179.84, 55.54, 37.02, 31.99, 29.74, 29.72, 29.66, 29.56, 29.44, 29.21, 29.06, 27.90, 25.17, 22.77, 14.22.

DDPET: DDMAT (3.0 g, 1 eq, 8.2 mmol), EDC (2.4 g 1.5 eq, 12 mmol) and DMAP (1.5 g, 1.5 eq, 12 mmol) were combined and degassed in an oven-dried flask. 30 mL anhydrous DCM was added, and the solution was cooled to $0oC$. Propargyl alcohol (1.5 g, 1.6 mL, 3.3 eq, 27 mmol) was added dropwise. The reaction was allowed to warm to room temperature and stirred for 72h. The crude was diluted with 120 mL DCM and washed with 2x30 mL 1M $NaHSO4$, 2x30 mL water, and 1x30 mL brine. This yielded S-Dodecyl- S′-(α,α′-dimethyl-α′′-propargyl ester)trithiocarbonate (DDPET) as an orange oil. Yield = 3.18 g (96%) 1H NMR (300 MHz, Chloroform-d) 4.70 (d, J = 2.5 Hz, 2H), 3.27 (t, J = 7.4 Hz, 2H), 2.46 (t, J = 2.5 Hz, 1H), 1.71 (s, 6H), 1.66 (t, J = 7.5 Hz, 2H), 1.26 (s, 16H), 0.93 – 0.83 (m, 3H). Solvent impurities: water, acetone. 13C NMR (101 MHz, CDCl3) δ 220.88, 172.19, 77.31, 75.15, 55.53, 53.24, 36.93, 31.91, 29.63, 29.62, 29.55, 29.44, 29.34, 29.10, 28.93, 27.85, 25.18, 22.68, 14.13.

cta-mpa-8: az-mpa-8 (1.13 g, 1.13 mmol) and DDPET (545mg, 1.35mmol) were dissolved in THF (12mL) and water (4.1 mL) and degassed with $N2$ for 30 minutes. Copper(II) sulfate pentahydrate (155 mg, 620 μmol) was then added, followed by sodium citrate (290 mg, 1.47 mmol) This was stirred overnight at room temperature. The crude was dissolved in 15mL EtOAc followed by washing with 2x5mL 1% EDTA. This was then purified by flash chromatography (gradient

from 80:20 hexane: EtOAc to 0:100 hexane: EtOAc), yielding cta-mpa-8 as an orange oil. Yield = 806mg (51%). 1H NMR (400 MHz, Chloroform-d) 7.67 (s, 1H), 5.23 (s, 2H), 4.45 – 4.30 (m, 10H), 4.15 (t, J = 8.0 Hz, 8H), 4.02 (s, 4H), 3.63 (d, J = 11.8 Hz, 8H), 3.24 (t, J = 7.4 Hz, 2H), 1.73 – 1.62 (m, 6H), 1.38 (d, J = 28.9 Hz, 30H), 1.30 – 1.20 (m, 24H), 1.18 – 1.08 (m, 15H), 1.00 (s, 3H), 0.88 (t, J = 6.5 Hz, 3H). Solvent impurities: water, EtOAc.

cta-mpa-8OH: 806 mg cta-mpa-8 was deprotected using the general deprotection procedure. After 24h stirring, the crude vacuum filtered and dried in-vacuo, yielding ctampa-8OH (4.7) as a dark orange oil. Yield = 666 mg (94%). ^{1}H NMR (300 MHz, Methanol-d4) 8.05 (s, 1H), 5.24 (s, 2H), 4.55 (s, 2H), 4.35 (qd, J = 11.0, 3.0 Hz, 8H), 4.11 (s, 4H), 3.77 – 3.55 (m, 16H), 1.68 (s, 6H), 1.63 (d, J = 7.4 Hz, 2H), 1.36 (s, 6H), 1.32 (s, 16H), 1.17 (s, 12H), 1.06 (s, 3H), 0.96 – 0.86 (m, 3H). Solvent impurities: acetone, MeOH

mCTA-16OH was grown according to the general esterification procedure outlined above. After activating bMPA (0.34 g, 0.62 mmol) suspended in 4 mL EtOAc with CDI (0.31 g, 1.93 mmol), CsF (0.02 g, 0.13 mmol) and mCTA-8OH (0.21 g, 0.16 mmol) were added and stirred 12 h, yielding mCTA-16OH. This was deprotected using the general deprotection procedure outlined above. After overnight stirring, this was filtered over Celite and concentrated in-vacuo, quantitatively yielding mCTA-16-OH as a clear oil. Yield = 0.29 g (82%). ^{1}H NMR (400 MHz, DMSO) δ 8.07 (s, 1H), 5.15 (s, 2H), 4.67 (t, J = 5.4 Hz, 12H), 4.45 (s, 2H), 4.16 (s, 12H), 3.96 (s, 4H), 3.42 (qd, J = 14.0, 12.3, 7.1 Hz, 32H), 3.27 (d, J = 7.4 Hz, 2H), 1.60 (s, 6H), 1.21 (d, J = 13.4 Hz, 39H), 1.00 (s, 17H), 0.86 (d, J = 8.3 Hz, 9H).

cta-mpa-8ala-Boc: 666 mg cta-mpa-8OH was grown using a slightly modified variant of the general esterification procedure. After activating N-Boc alanine (1.22 g, 6.24 mmol) suspended in 7 mL EtOAc with CDI (1.15 g, 7.06 mmol), CsF (158 mg, 1.04 mmol) and cta-mpa-8OH (666

mg, 535 μmol) were added and stirred overnight, yielding cta-mpa-8ala- Boc as a dark orange resin. Yield = 1.17 g (84%). 1H NMR (300 MHz, Chloroform-d) 7.72 (s, 1H), 5.23 (s, 6H), 4.43 (s, 2H), 4.36 – 4.14 (m, 23H), 4.05 (s, 4H), 3.37 (d, J = 6.3 Hz, 14H), 3.24 (t, J = 7.4 Hz, 2H), 2.54 (t, J = 6.1 Hz, 16H), 1.43 (s, 72H), 1.31 (s, 6H), 1.29 – 1.21 (m, 30H), 1.03 (s, 3H), 0.91 – 0.84 (m, 3H). Solvent impurities: EtOAc, water

cta-mpa-8ala (cationic mCTA): cta-mpa-8ala-Boc (1.17 g) was dissolved in 6 mL $CHCl3$ and 4 mL TFA. This was stirred at rt for 1.5 h, then concentrated in-vacuo. The resulting crude was precipitated in 50 mL diethyl ether cooled to 0 oC, and the precipitate was dried in a vacuum oven at room temperature for 48h. Yield = 610 mg (88%). 1H NMR (300 MHz, DMSO-d6) 8.12 (s, 1H), 7.96 (s, 27H), 5.17 (s, 2H), 4.51 (s, 2H), 4.22 (d, J = 19.4 Hz, 24H), 3.98 (s, 4H), 3.11 – 2.96 (m, 18H), 2.67 (t, J = 7.1 Hz, 16H), 1.60 (s, 6H), 1.36 – 1.14 (m, 32H), 0.87 (dd, J = 14.6, 8.6 Hz, 6H). Solvent impurities: 1,4-dioxane

Ethanolic mCTA-8ala and BzMA GPC Study: Reaction Progress Over Time

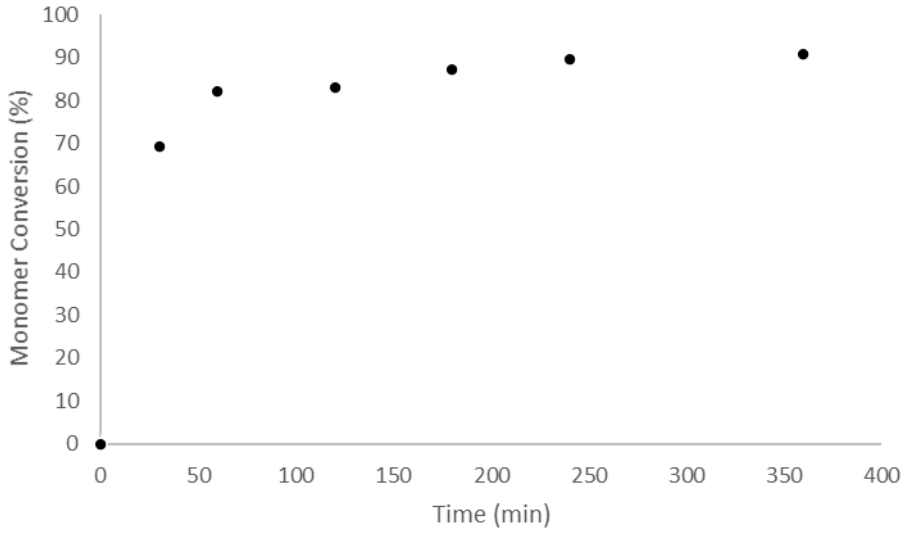

Figure 82. Monomer conversion versus time profile of pBzMA-16OH polymerization

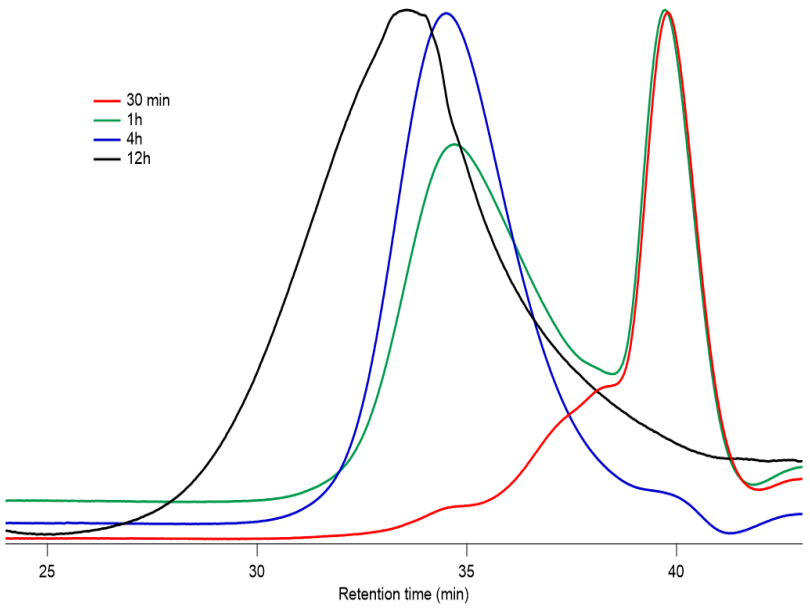

Figure 83. GPC trace of reaction over time

Ethanolic mCTA-16OH and BzMA NMR Study: Reaction Progress Over Time

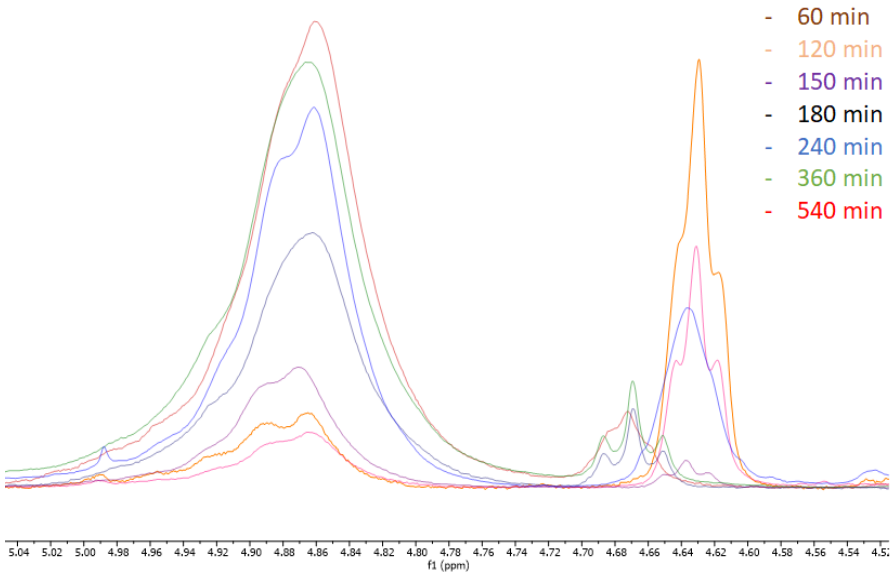

Figure 84. Superposition of ^{1}H NMR for aqueous pBzMA (4.88 pm) PISA indicating the incorporation of BzMA into mCTA (4.67 ppm); solvent DMSO-d6

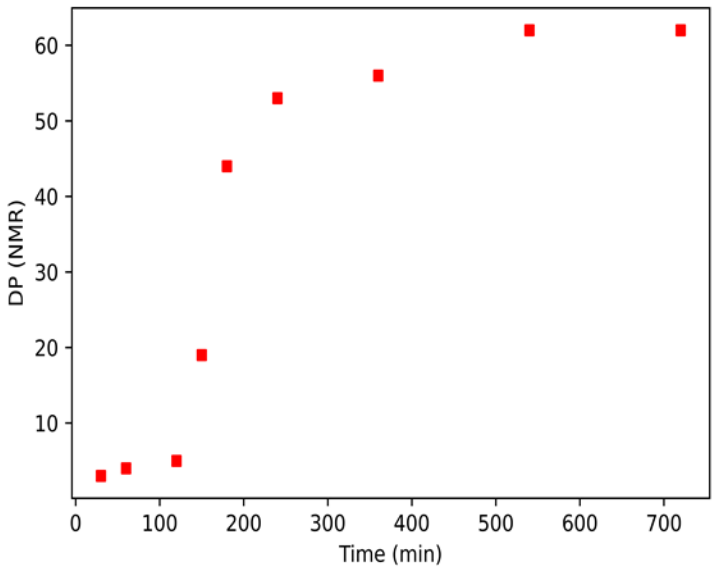

Figure 85. Kinetics of pBzMA-16OH

Aqueous mCTA-8ala and BzMA NMR Study: Reaction Progress Over Time

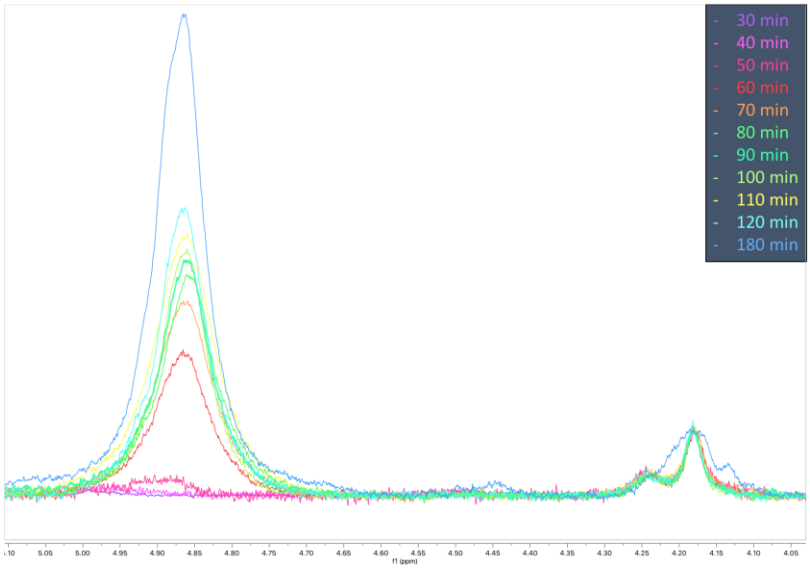

Figure 86. Superposition of 1H NMR for aqueous pBzMA (4.88 pm) PISA indicating the incorporation of BzMA into mCTA (4.18 ppm); solvent DMSO-d6

Transmission Electron Microscopy Images

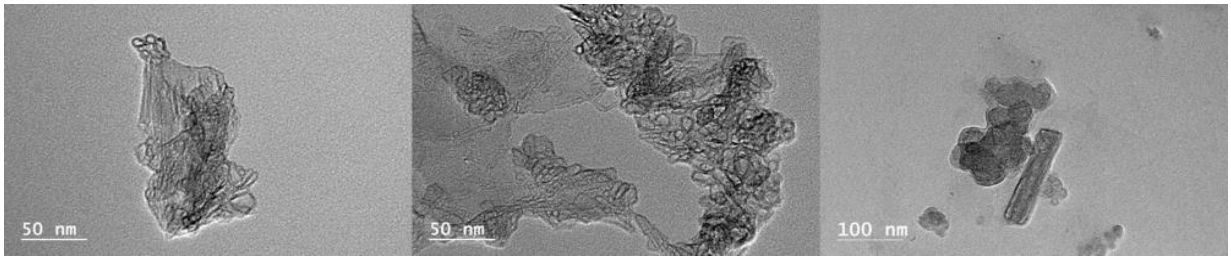

Figure 87. TEM of mCTA-8-ala in solution before PISA

NMR Spectra

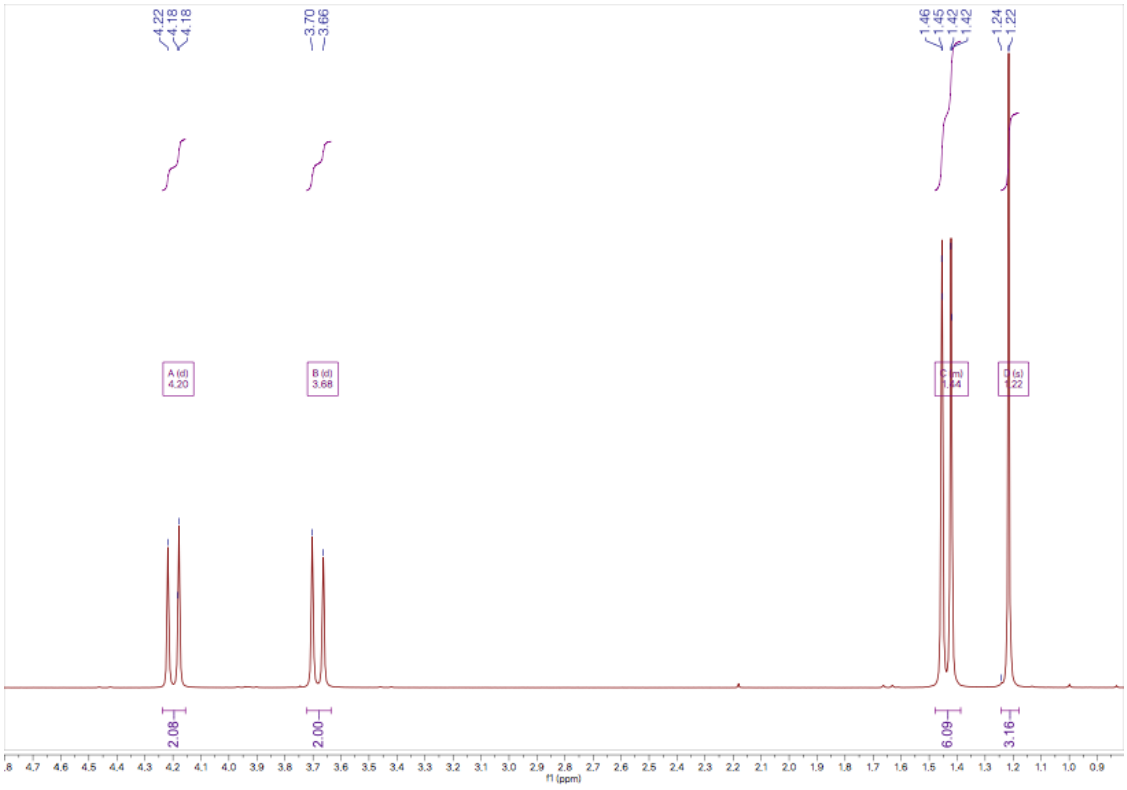

Figure 88. ^{1}H NMR of bMPA (400 MHz, $CDCl_3$)

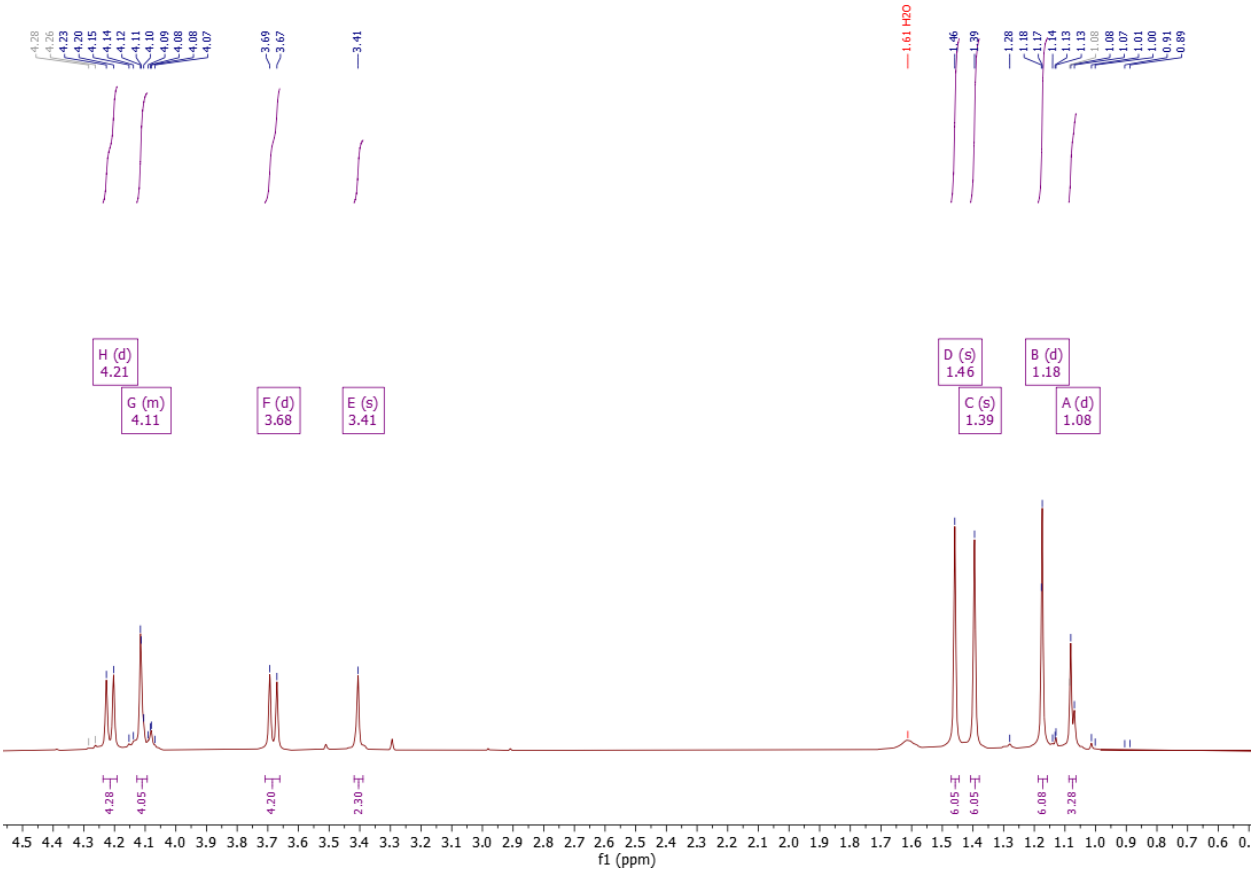

Figure 89. ^{1}H NMR of az-mpa-4 (400 MHz, $CDCl_3$)

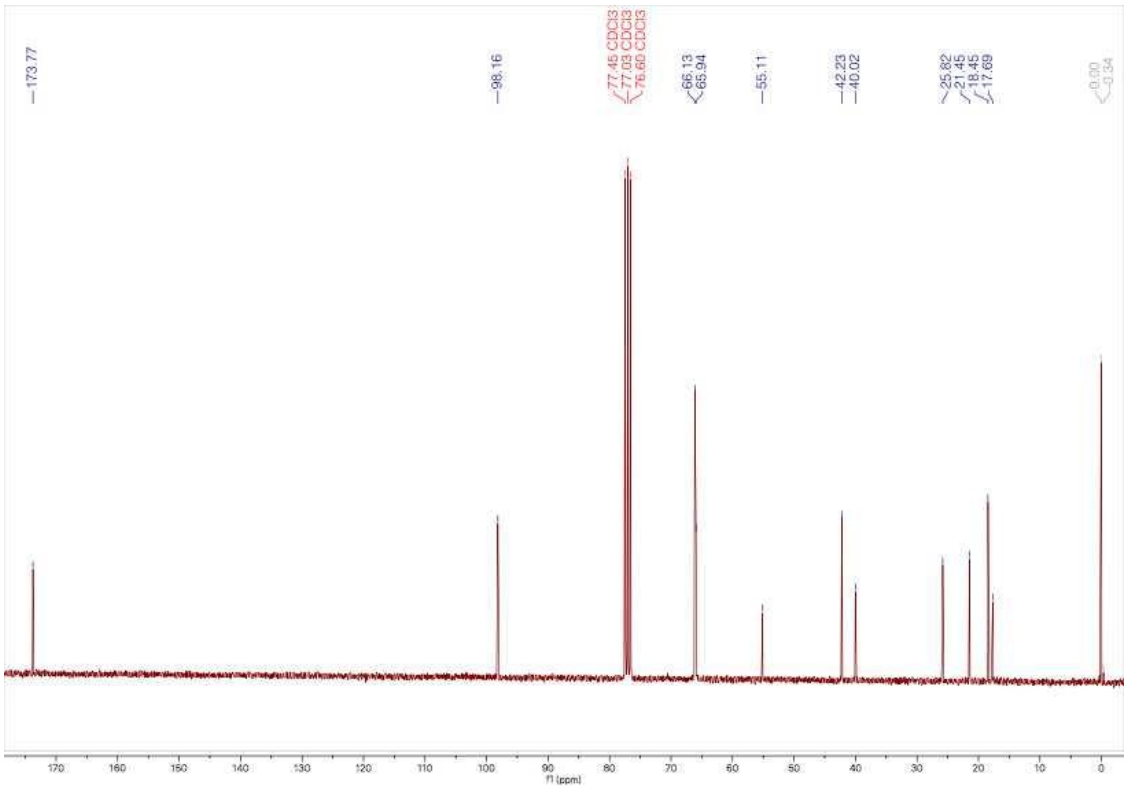

Figure 90. ^{13}C NMR of az-mpa-4 (400 MHz, $CDCl_3$)

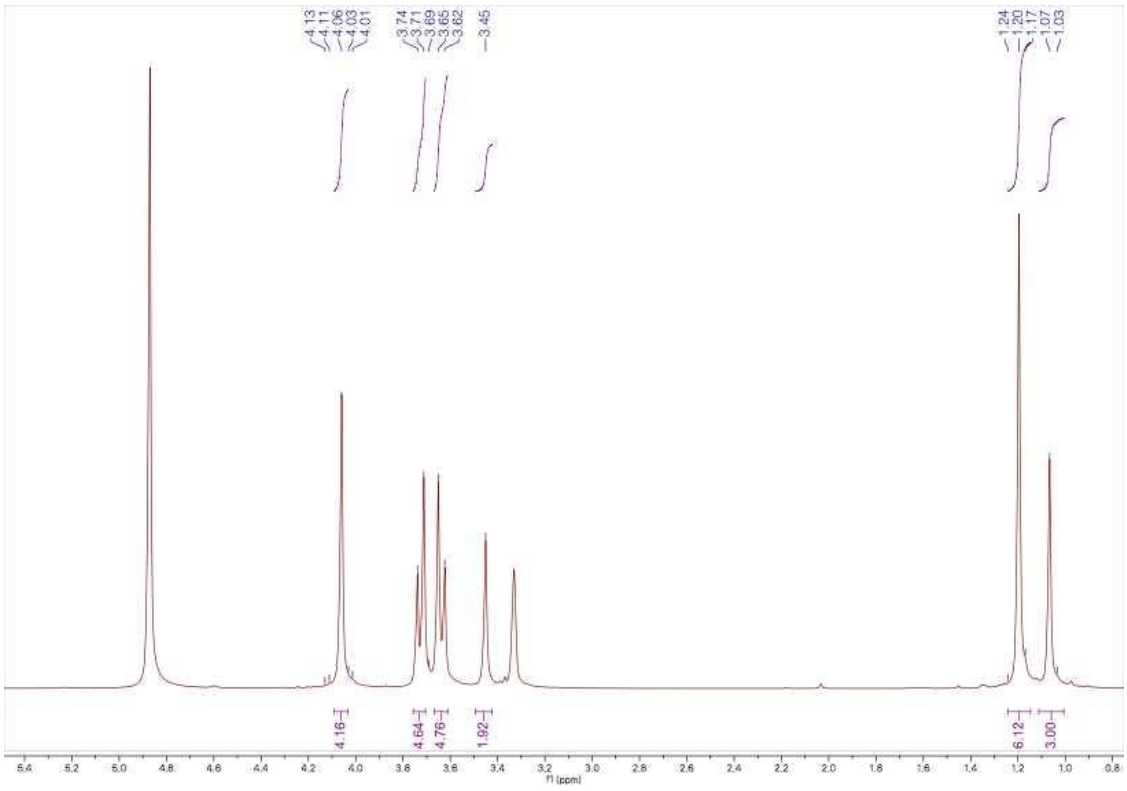

Figure 91. ^{1}H NMR of az-mpa-4OH (400 MHz, MeOD)

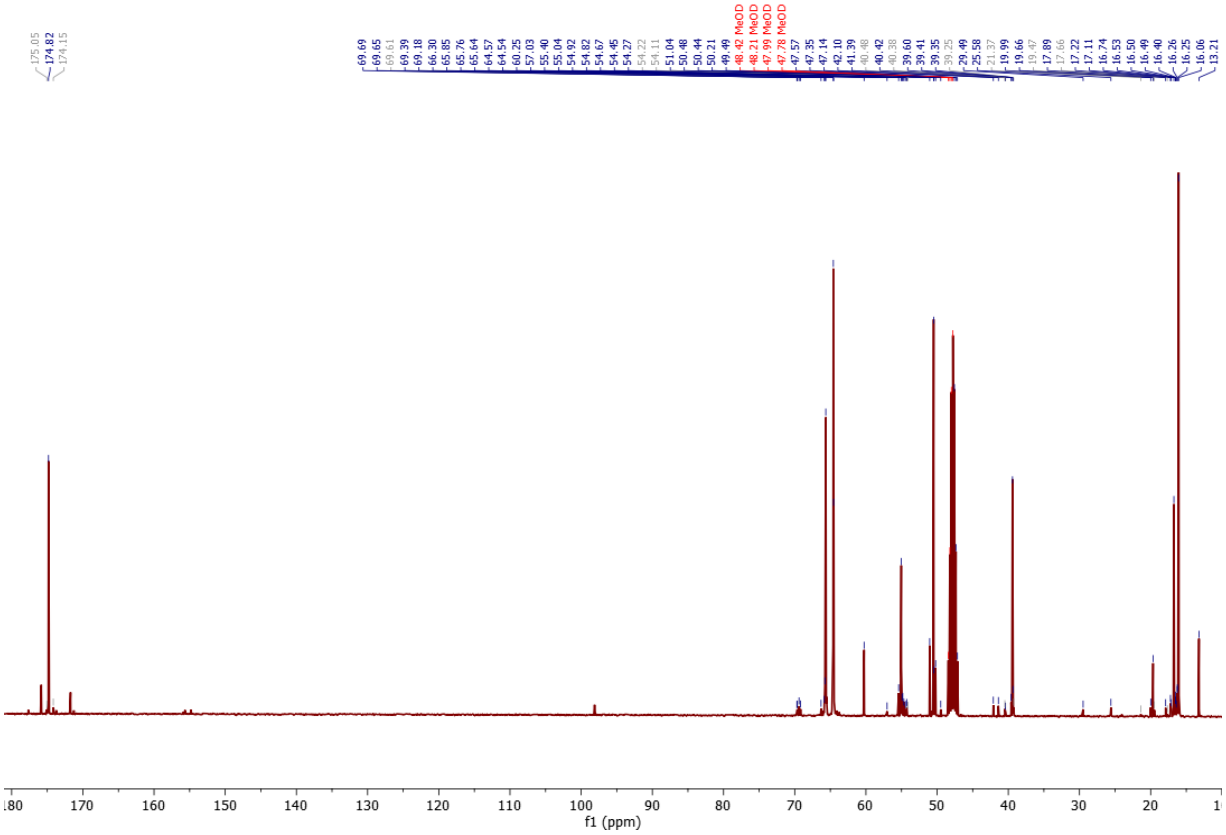

Figure 92. ^{13}C NMR of az-mpa-4OH (400 MHz, MeOD)

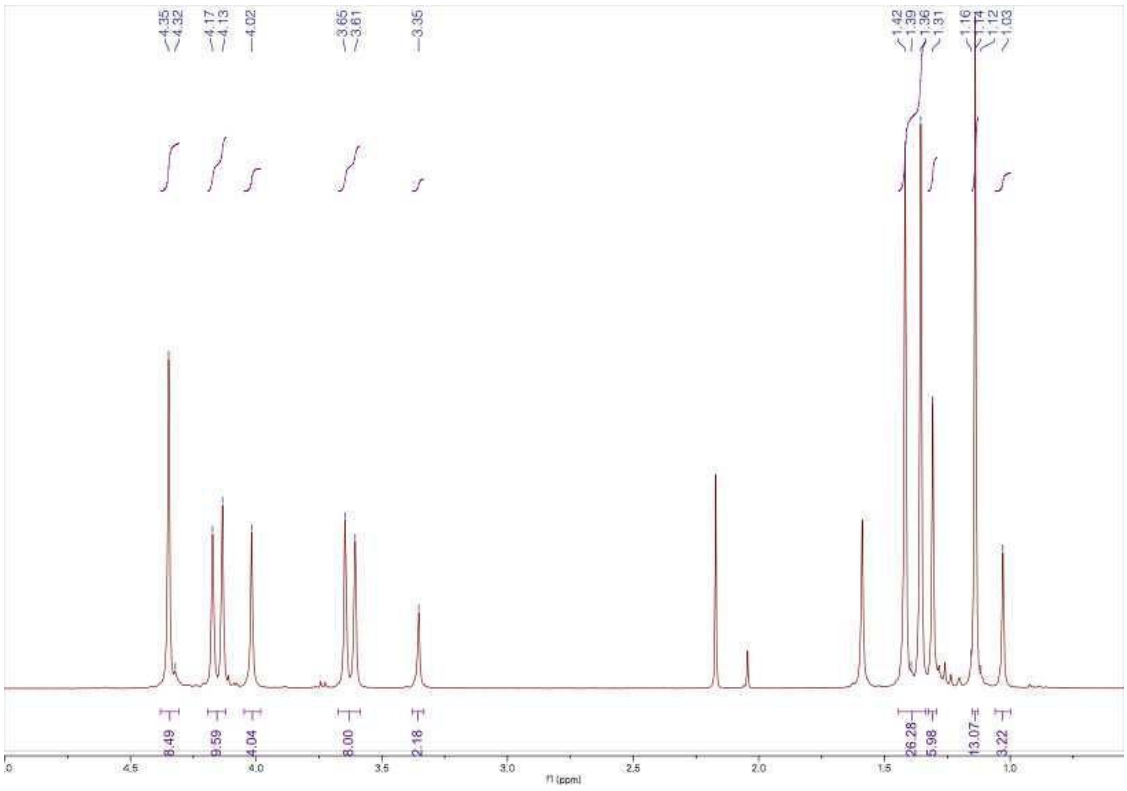

Figure 93. ^{1}H NMR of az-mpa-8 (400 MHz, $CDCl_3$)

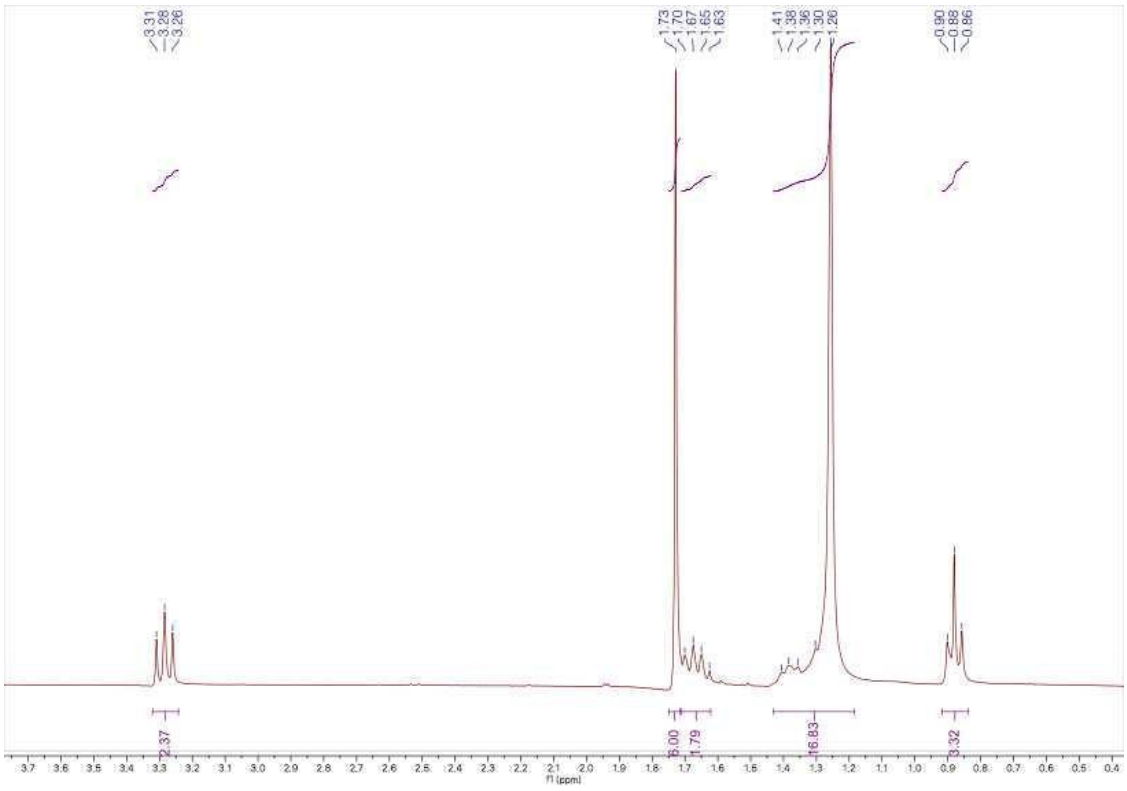

Figure 94. ^{1}H NMR of DDMAT (400 MHz, $CDCl_3$)

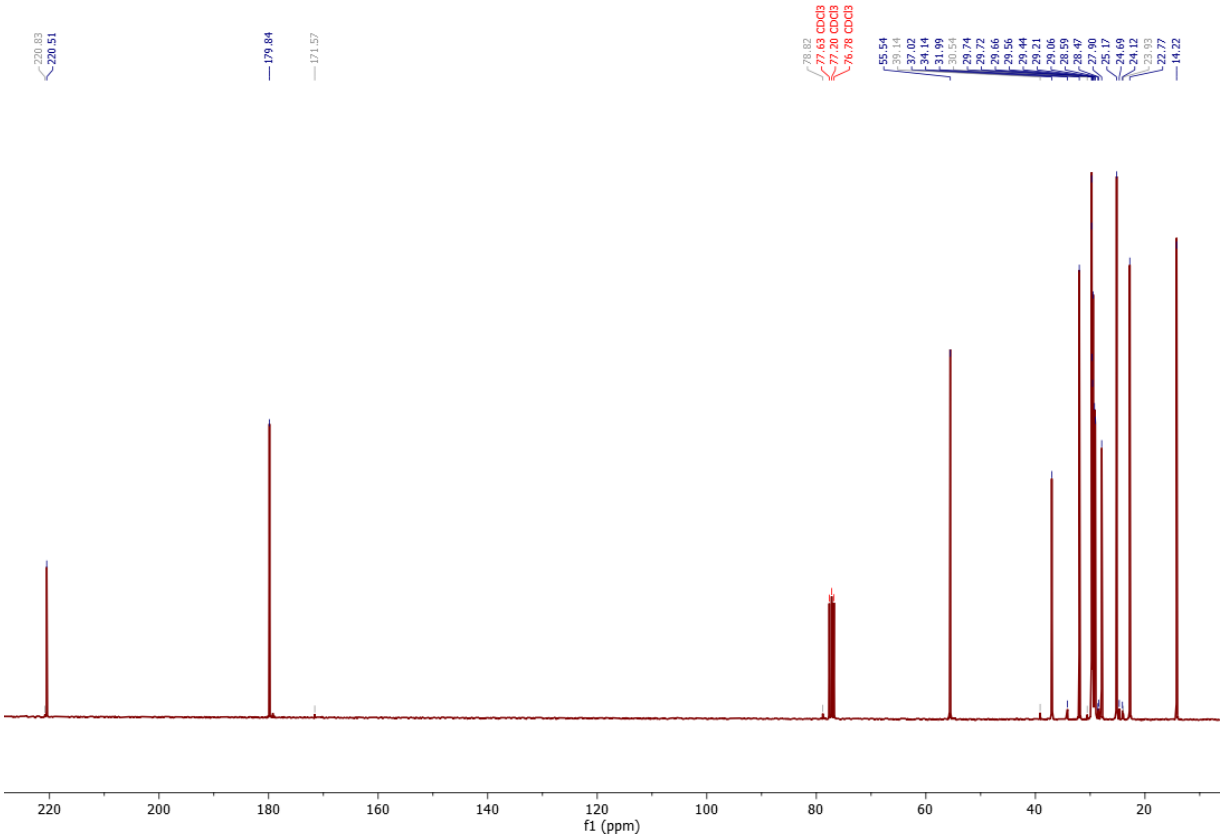

Figure 95. ^{13}C NMR of DDMAT (400 MHz, $CDCl_3$)

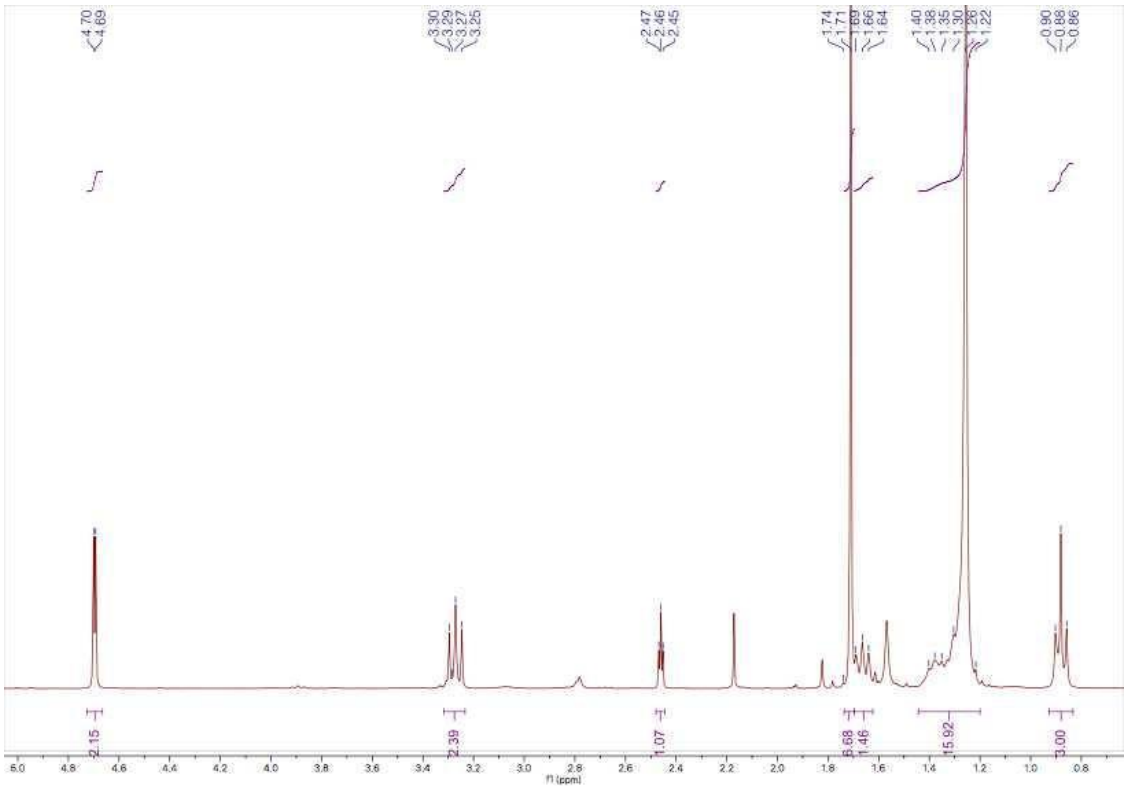

Figure 96. ^{1}H NMR of DDPET (400 MHz, $CDCl_3$)

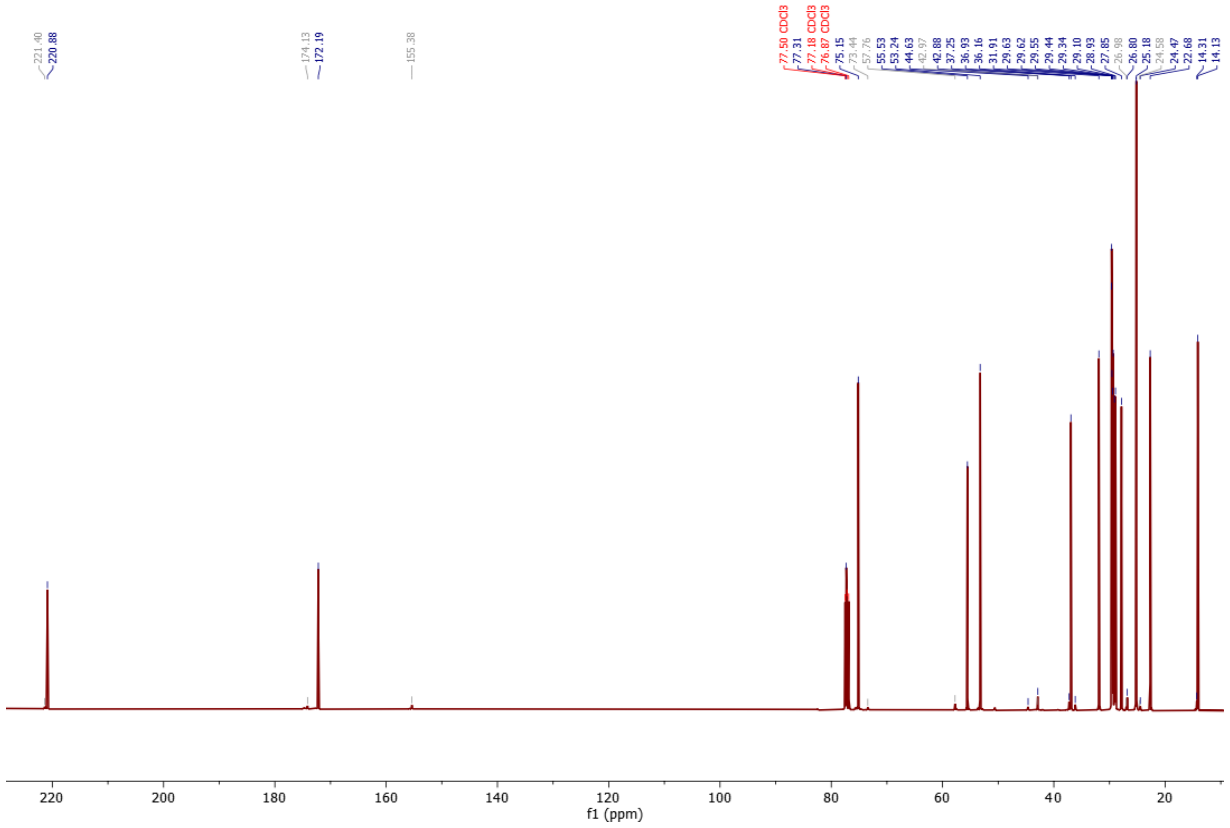

Figure 97. ^{13}C NMR of DDPET (400 MHz, $CDCl_3$)

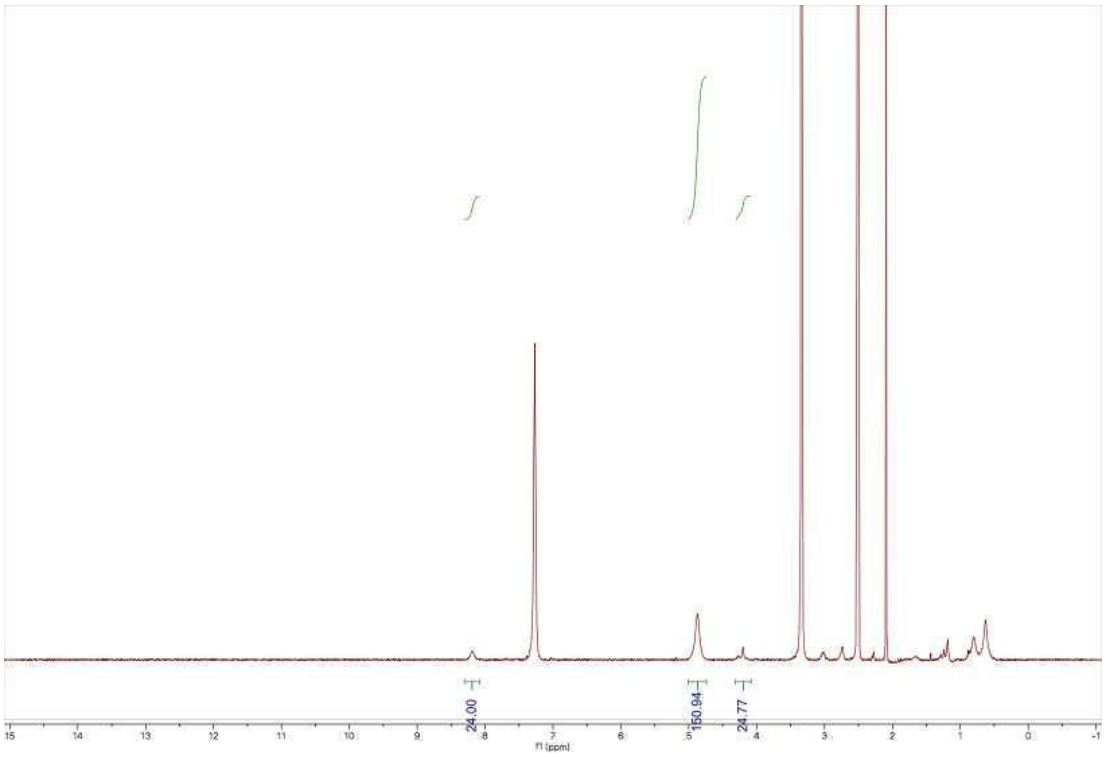

Figure 98. ^{1}H NMR of cta-mpa-8 (400 MHz, $CDCl_3$)

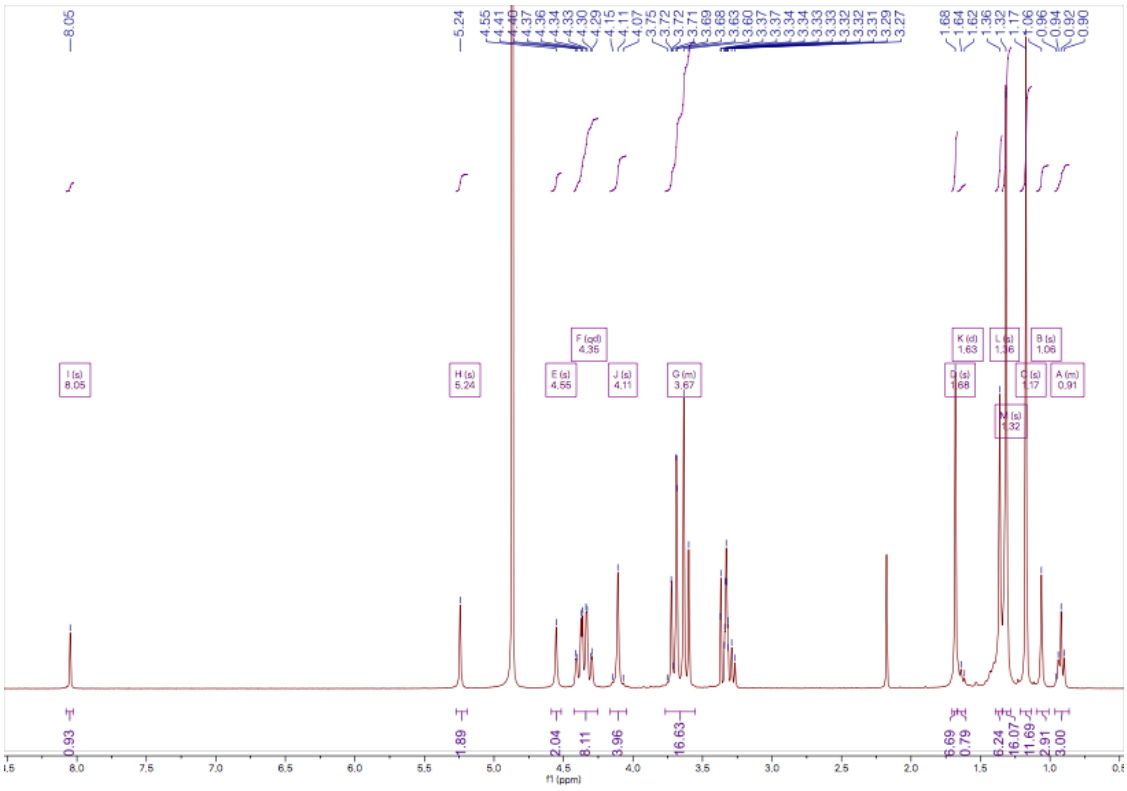

Figure 99. ^{1}H NMR of cta-mpa-8OH (400 MHz, $CDCl_3$)

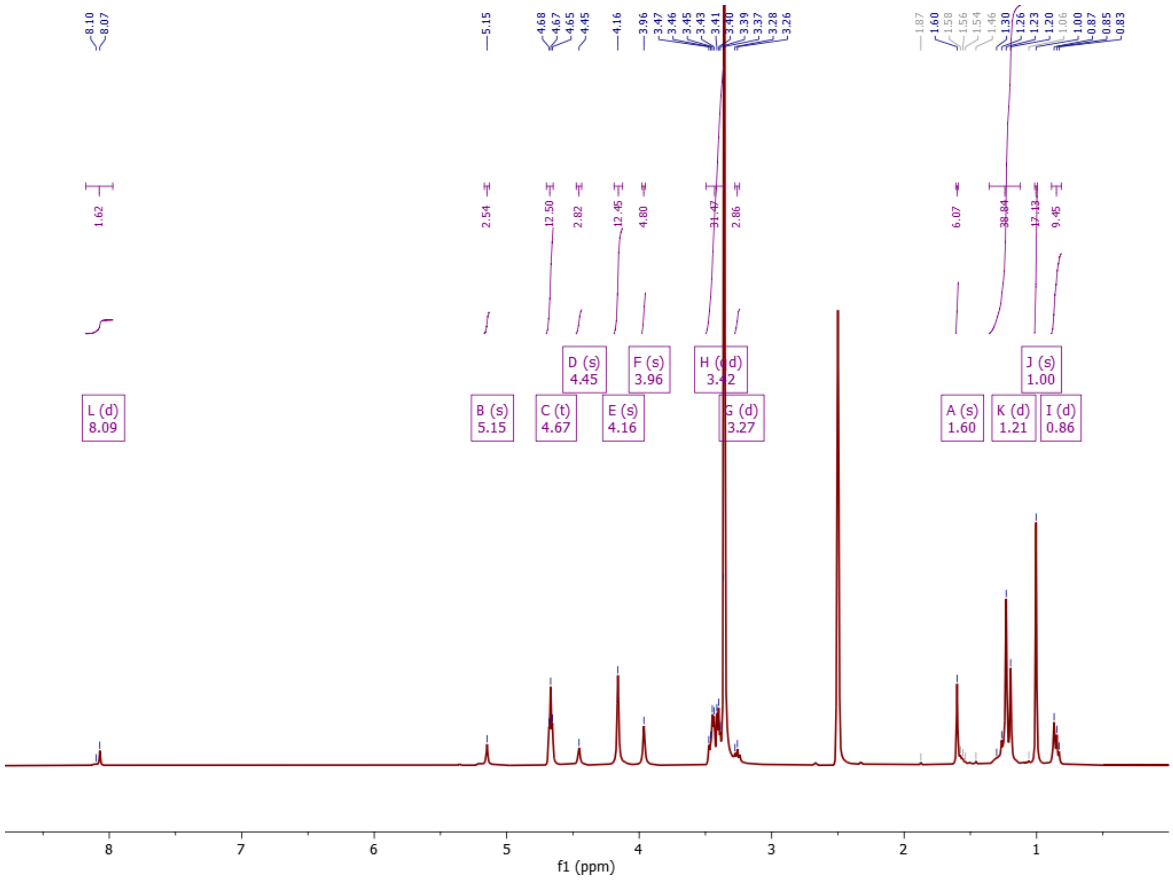

Figure 100. ^{1}H NMR of mCTA-16OH (400 MHz, DMSO-d6)

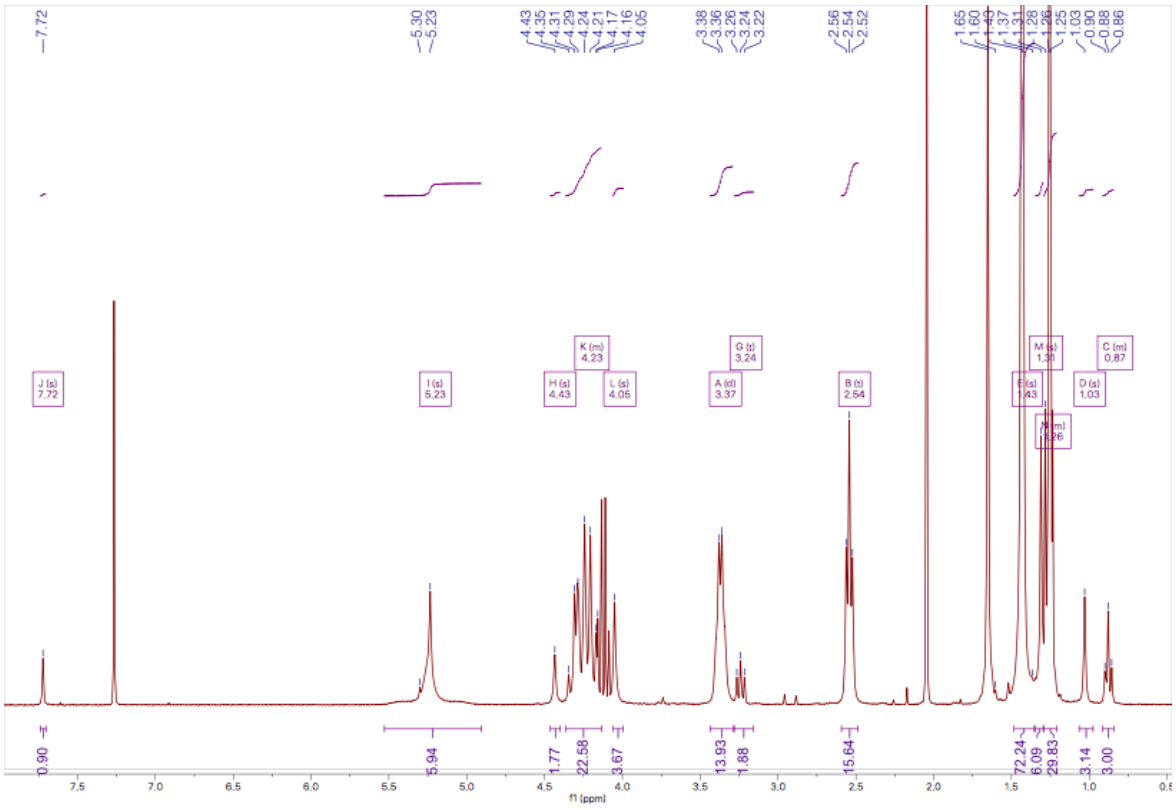

Figure 101. ^{1}H NMR of cta-mpa-8ala-Boc (400 MHz, $CDCl_3$)

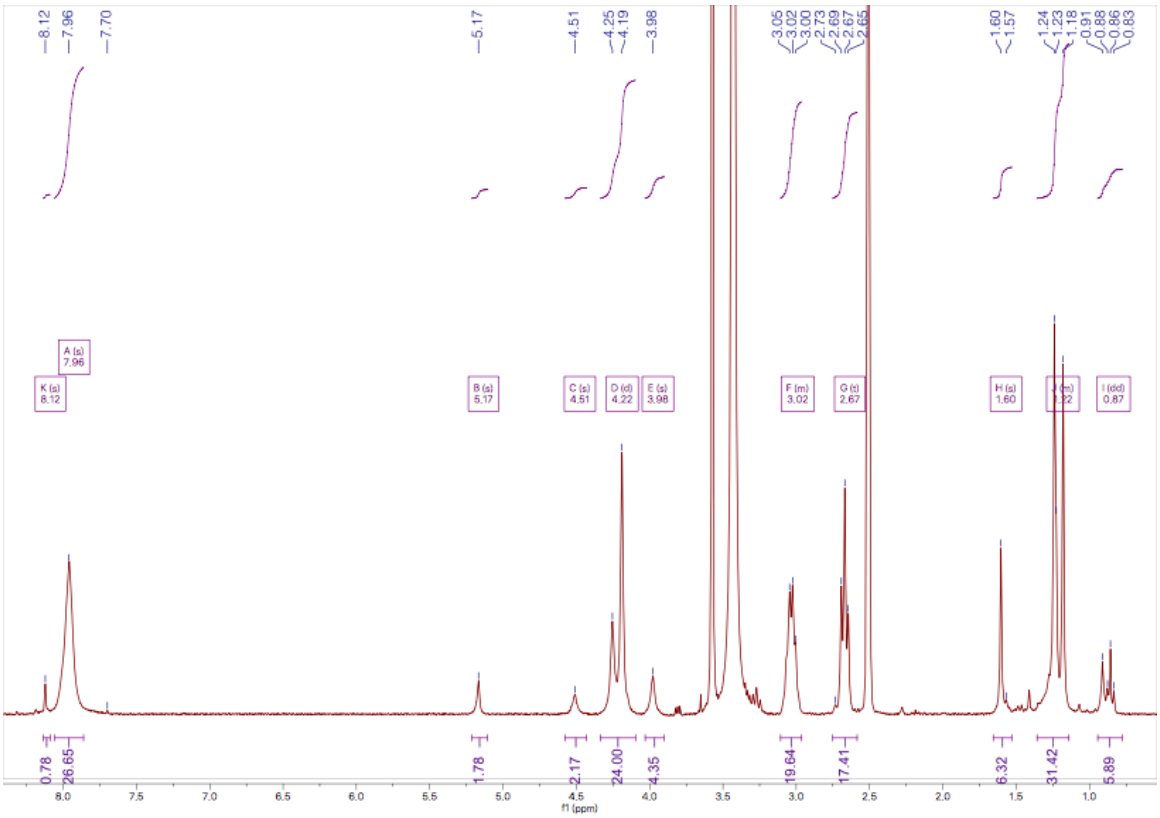

Figure 102. ^{1}H NMR of cta-mpa-8ala (cationic mCTA) (400 MHz, DMSO-d6)

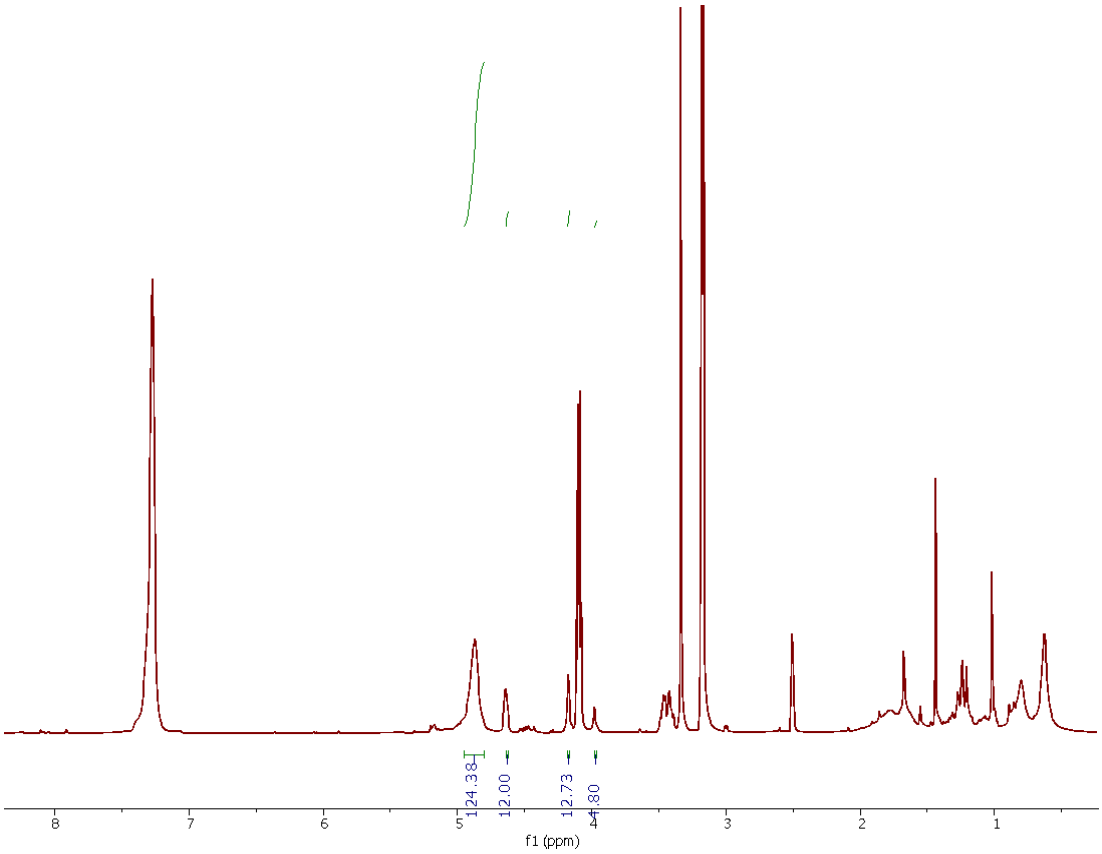

Figure 103. ^{1}H NMR of final timepoint for ethanol pBzMA PISA (400 MHz, DMSO-d6)

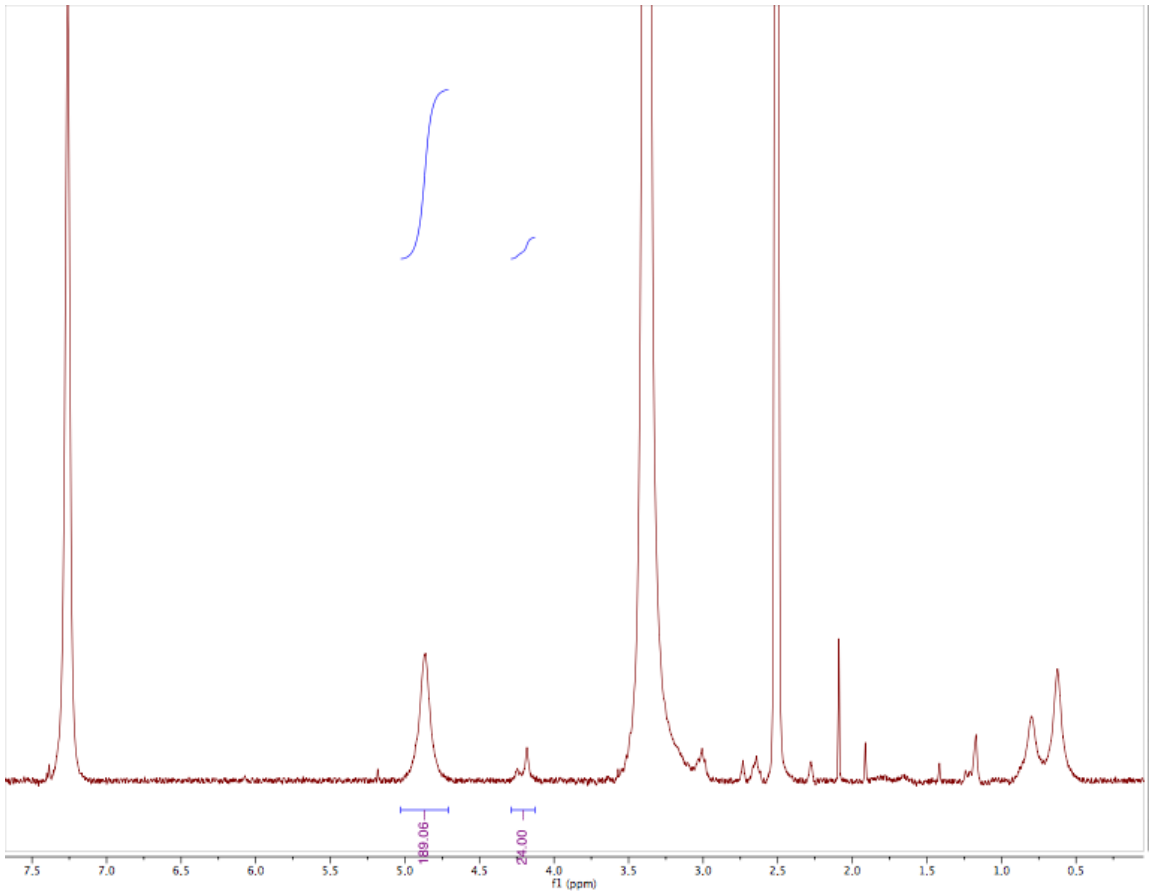

Figure 104. ^{1}H NMR of final timepoint for aqueous pBzMA PISA (400 MHz, DMSO-d6)

APPENDIX C: SUPPLEMENTARY INFORMATION FOR CHAPTER 4

SYNTHESIS OF P(BZ_HF_10)

The ^{19}F containing copolymer P(Bz_HF_5) was synthesized by RAFT polymerization using two steps (HFMA polymerization followed by BzMA polymerization). For the HFMA polymerization, mCTA-8ala (50.1 mg, 0.027 mmol), HFMA (33.2 mg, 0.137 mmol), 2,2′-Azobis(2-methylpropionamidine) dihydrochloride (V50) (1.5 mg, 0.005 mmol) and 2.1 mL Milli-Q water were added to a gas-tight conical vial and sonicated, and incubated 1 h in a dark place. Then the solution was purged with Ar for 30 min and then the vial was placed in a 60 ^{0}C bath. The overall monomer conversion was determined by ^{1}H NMR and ^{19}F NMR spectroscopy in DMSO-d6. ^{1}H NMR signals corresponding to the monomer (a – 1.95 ppm, b – 6.25 ppm, 6.04 ppm) were monitored as the reaction progressed. Peak b decreases with the time and peak a shifted to 0.9 ppm which showing the polymerization completion. (Fig. 1) ^{19}F NMR signals shows a shift of -72.8 ppm doublet peak of the monomer in to -73.6 ppm broad peak showing completion of the polymerization (Fig 2) The polymer was purified by dialysis against Milli-Q water for 24 h and freeze dried. The ^{1}H NMR shows the DP is 4 for HFMA (Fig 3). Then the resulting polymer used as mCTA for the BzMA polymerization, mCTA-8ala-pHF_4 (50.5 mg, 0.018 mmol), BzMA (130.0 mg, 0.737 mmol), V50 (1.5 mg, 0.005 mmol) and 2.1 mL Milli-Q water were added to a gas-tight conical vial and sonicated, and incubated 1 h in a dark place. Then the solution was purged with Ar for 30 min and then the vial was placed in a 60 ^{0}C bath. The overall monomer conversion was determined by ^{1}H NMR in DMSO-d6. ^{1}H NMR signals corresponding to the monomer (d – 5.20

ppm, c – 6.212 ppm, 5.85 ppm) were monitored as the reaction progressed. Peak c and d decrease with the time and new peak d* formed at 4.80 ppm which showing the polymerization completion. (Fig. 4). The final reaction mixture was purified using size exclusion chromatography (Sephadex LH-20). The ^{1}H NMR shows the DP is 42 for BzMA (Fig 5).

SYNTHESIS OF P(BZ_HF_5)

For the HFMA polymerization, mCTA-8ala (51.0 mg, 0.028 mmol), HFMA (65.5 mg, 0.280 mmol), V50 (1.5 mg, 0.005 mmol) and 2.5 mL Milli-Q water were added to a gas-tight conical vial and sonicated, and incubated 1 h in a dark place. Then the solution was purged with Ar for 30 min and then the vial was placed in a 60 ^{0}C bath. The overall monomer conversion was determined by ^{1}H NMR and ^{19}F NMR spectroscopy in DMSO-d6 as explained in synthesis of p(Bz_HF_10) (Fig. 6 and 7). The polymer was purified by dialysis against Milli-Q water for 24 h and freeze dried. The ^{1}H NMR shows the DP is 8 for HFMA (Fig 8). Then the resulting polymer used as mCTA for the BzMA polymerization, mCTA-8ala-pHF_8 (50.0 mg, 0.014 mmol), BzMA (95.5 mg, 0.542 mmol), V50 (0.8 mg, 0.003 mmol) and 2.1 mL Milli-Q water were added to a gas-tight conical vial and sonicated, and incubated 1 h in a dark place. Then the solution was purged with Ar for 30 min and then the vial was placed in a 60 ^{0}C bath. The overall monomer conversion was determined by ^{1}H NMR in DMSO-d6 (Fig. 9). The final reaction mixture was purified using size exclusion chromatography (Sephadex LH-20). The ^{1}H NMR shows the DP is 40 for BzMA (Fig 10).

SYNTHESIS OF P(BZ_HF_20)

For the HFMA polymerization, mCTA-8ala (52.5 mg, 0.028 mmol), HFMA (33.8 mg, 0.144 mmol), V50 (1.5 mg, 0.005 mmol) and 2.1 mL Milli-Q water were added to a gas-tight

conical vial and sonicated, and incubated 1 h in a dark place. Then the solution was purged with Ar for 30 min and then the vial was placed in a 60 ^{0}C bath. The overall monomer conversion was determined by ^{1}H NMR and ^{19}F NMR spectroscopy in DMSO-d6 as explained in synthesis of p(Bz_HF_10) (Fig. 11 and 12). The polymer was purified by dialysis against Milli-Q water for 24 h and freeze dried. The ^{1}H NMR shows the DP is 2 for HFMA (Fig 13). Then the resulting polymer used as mCTA for the BzMA polymerization, mCTA-8ala-pHF_2 (50.0 mg, 0.022 mmol), BzMA (153.7 mg, 0.872 mmol), V50 (1.1 mg, 0.004 mmol) and 2.1 mL Milli-Q water were added to a gas-tight conical vial and sonicated, and incubated 1 h in a dark place. Then the solution was purged with Ar for 30 min and then the vial was placed in a 60 ^{0}C bath. The overall monomer conversion was determined by ^{1}H NMR in DMSO-d6 (Fig. 14). The final reaction mixture was purified using size exclusion chromatography (Sephadex LH-20). The ^{1}H NMR shows the DP is 40 for BzMA (Fig 15).

NMR SPECTRA

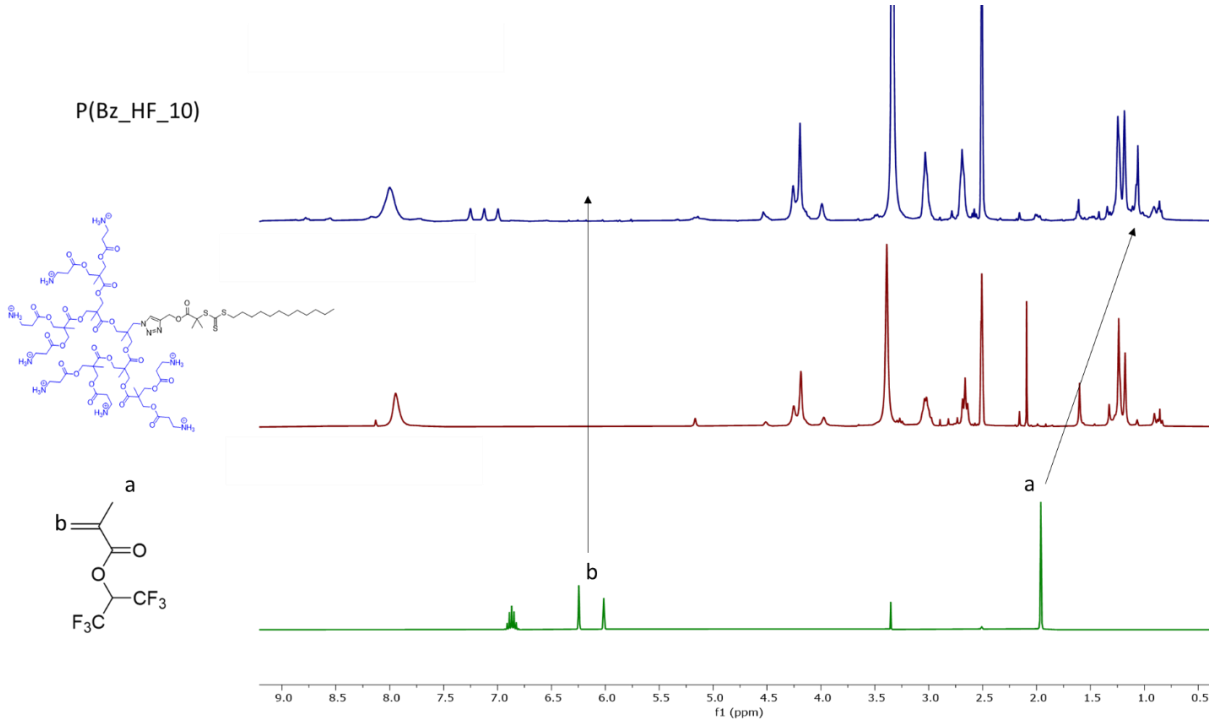

Figure 105. ^{1}H NMR comparison of HFMA, mCTA-8-ala and P(HF) (400 MHz, DMSO-d6)

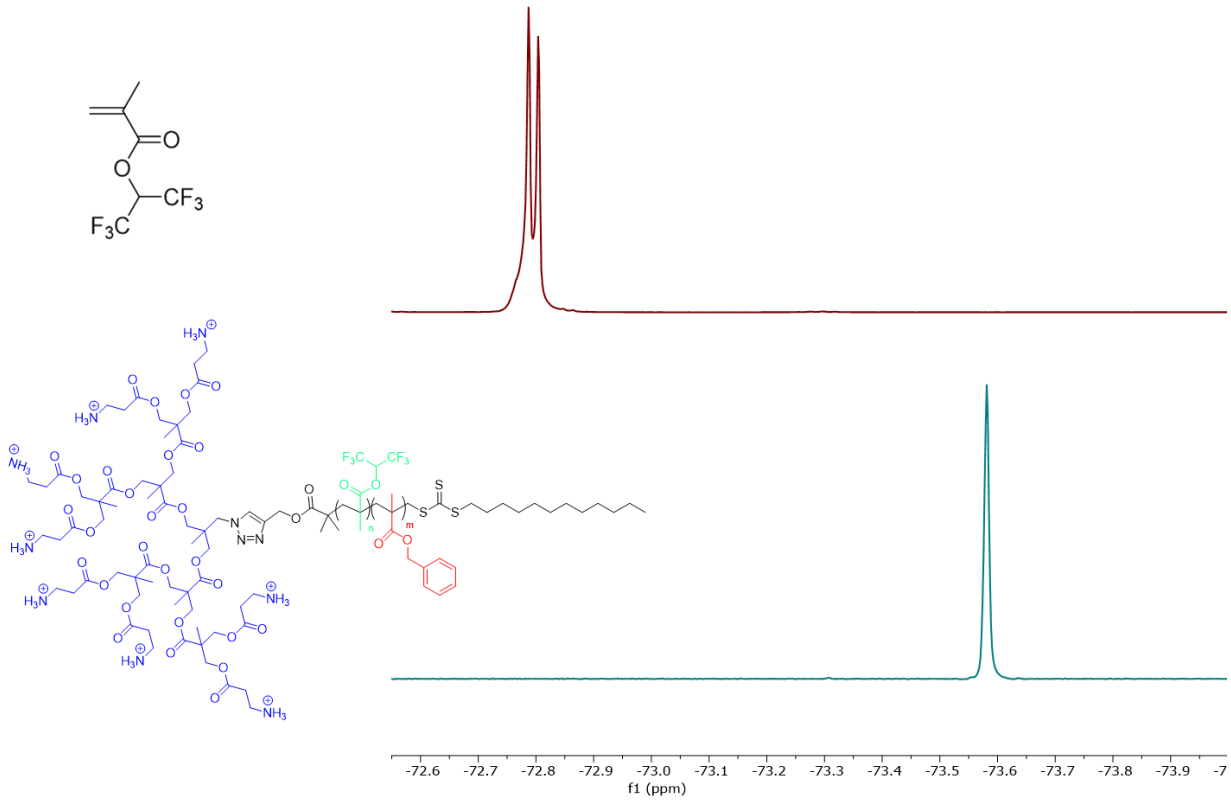

Figure 106. ^{19}F NMR comparison of HFMA and P(Bz_HF_10) (400 MHz, DMSO-d6)

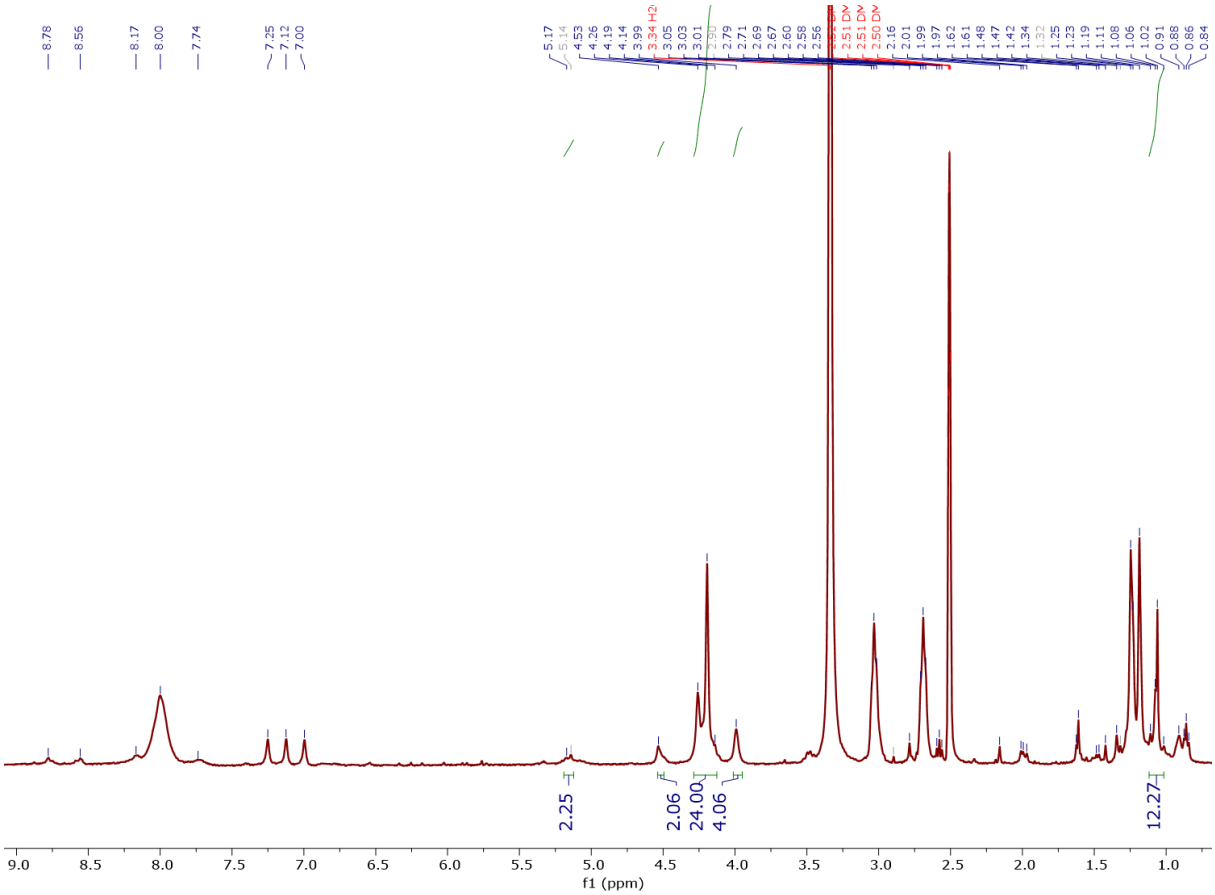

Figure 107. ^{1}H-NMR for pHF_10 (400 MHz, DMSO-d6)

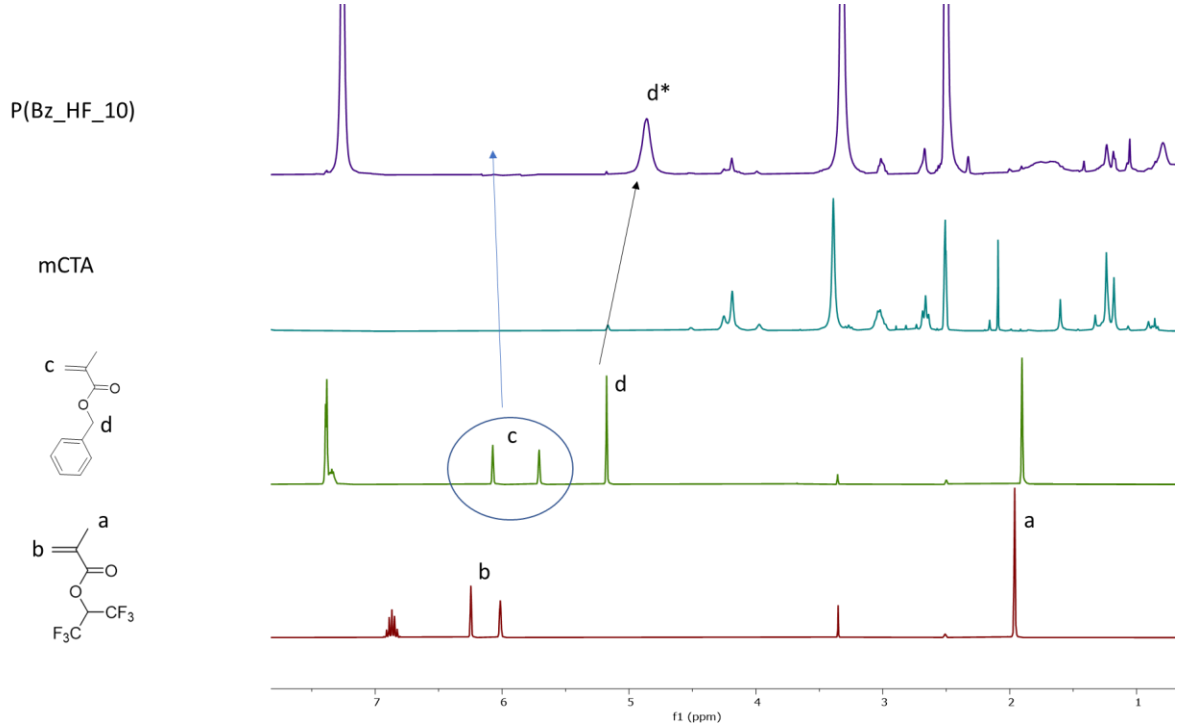

Figure 108. ^{1}H NMR comparison of HFMA, BzMA, mCTA-8-ala and P(Bz_HF_10) (400 MHz, DMSO-d6)

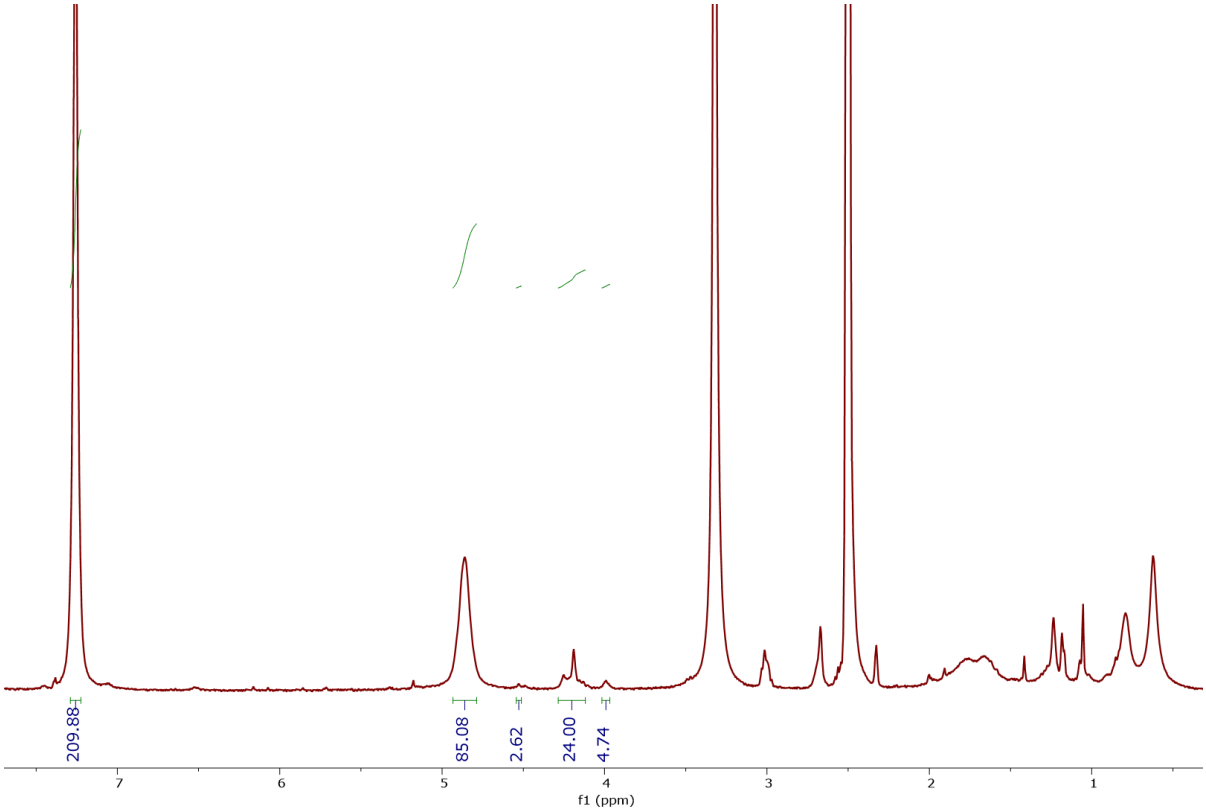

Figure 109. ^{1}H-NMR for pHF_10 (400 MHz, DMSO-d6)

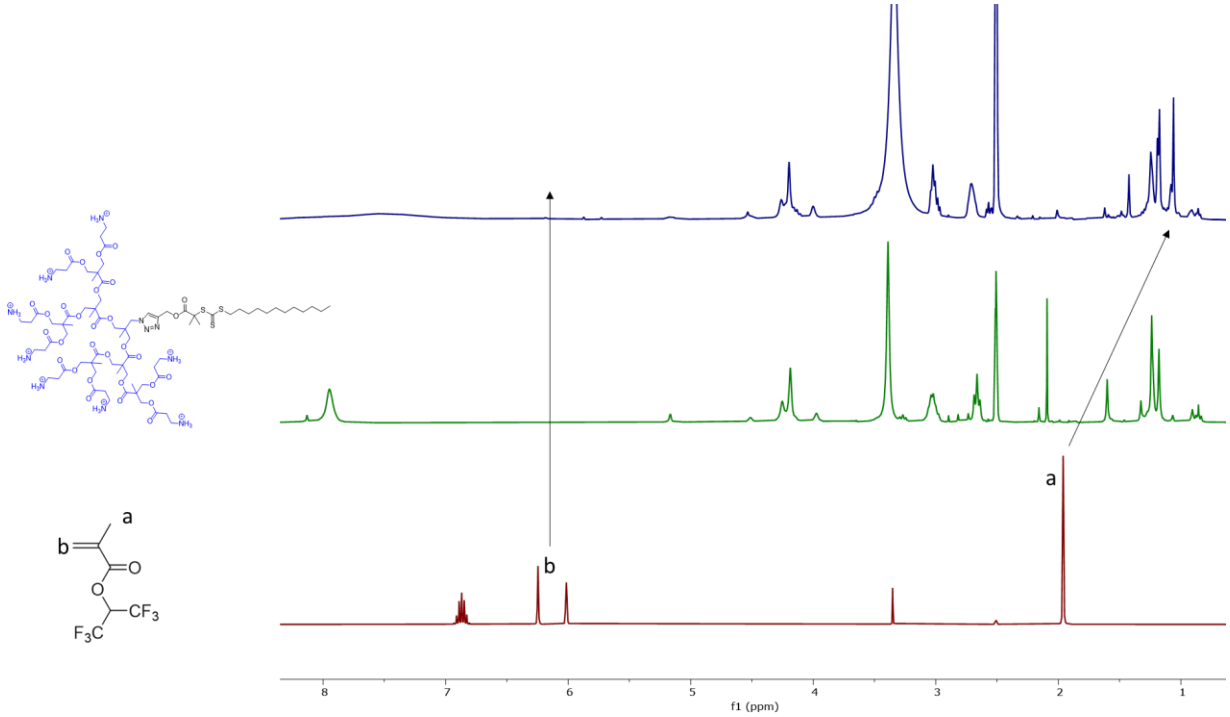

Figure 110. ^{1}H NMR comparison of HFMA, mCTA-8-ala and P(Bz_HF_5) (400 MHz, DMSO-d6)

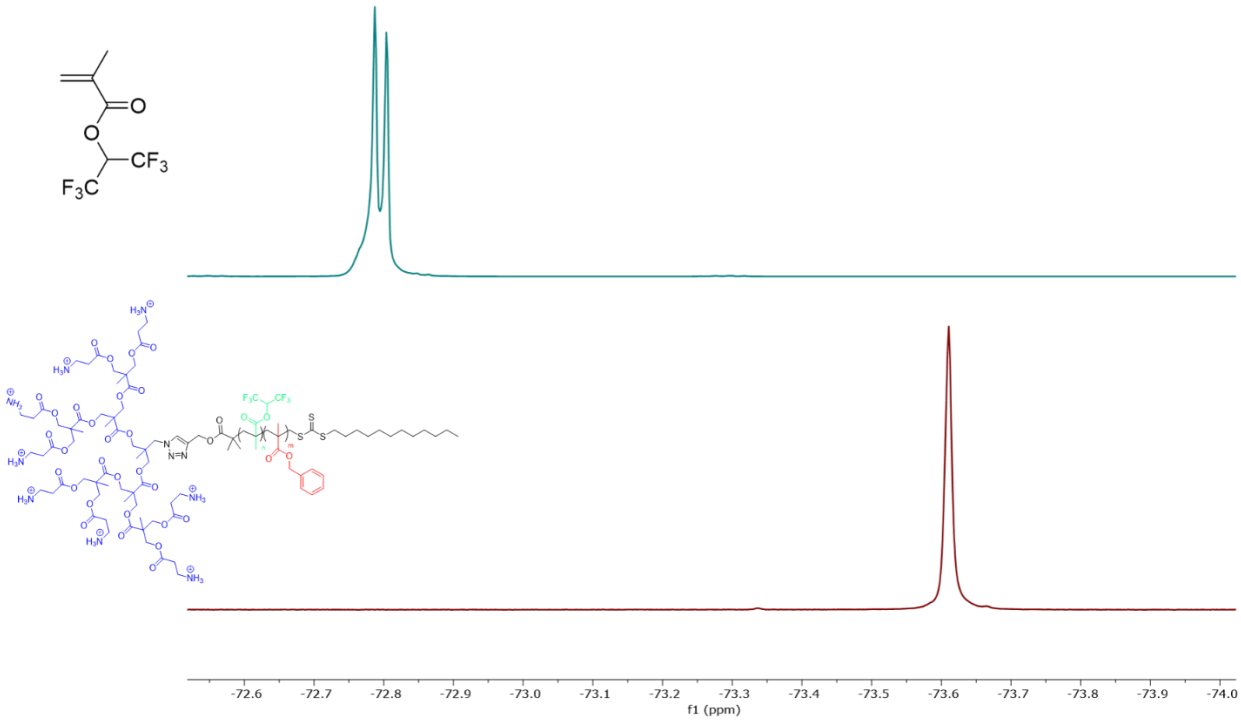

Figure 111. ^{19}F NMR comparison of HFMA and P(Bz_HF_5) (400 MHz, DMSO-d6)

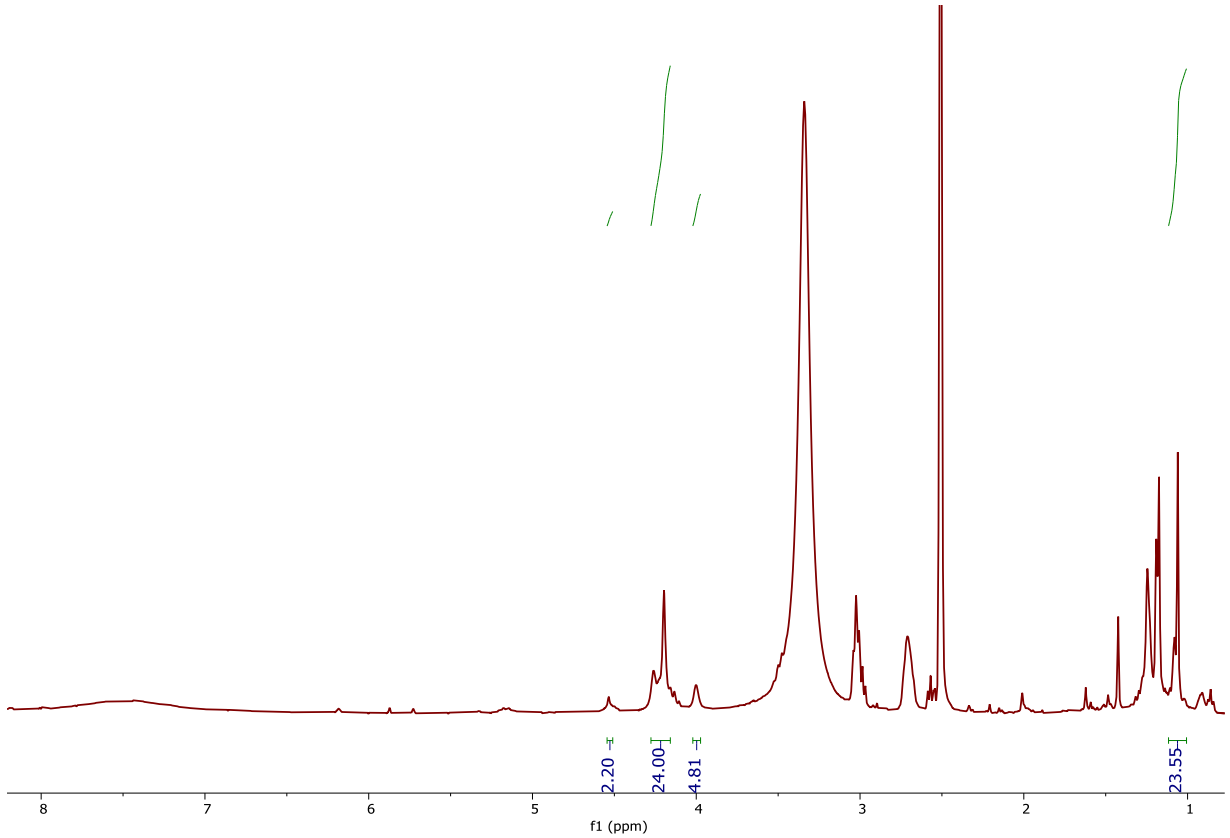

Figure 112. ^{1}H-NMR for P(HF_5) (400 MHz, DMSO-d6)

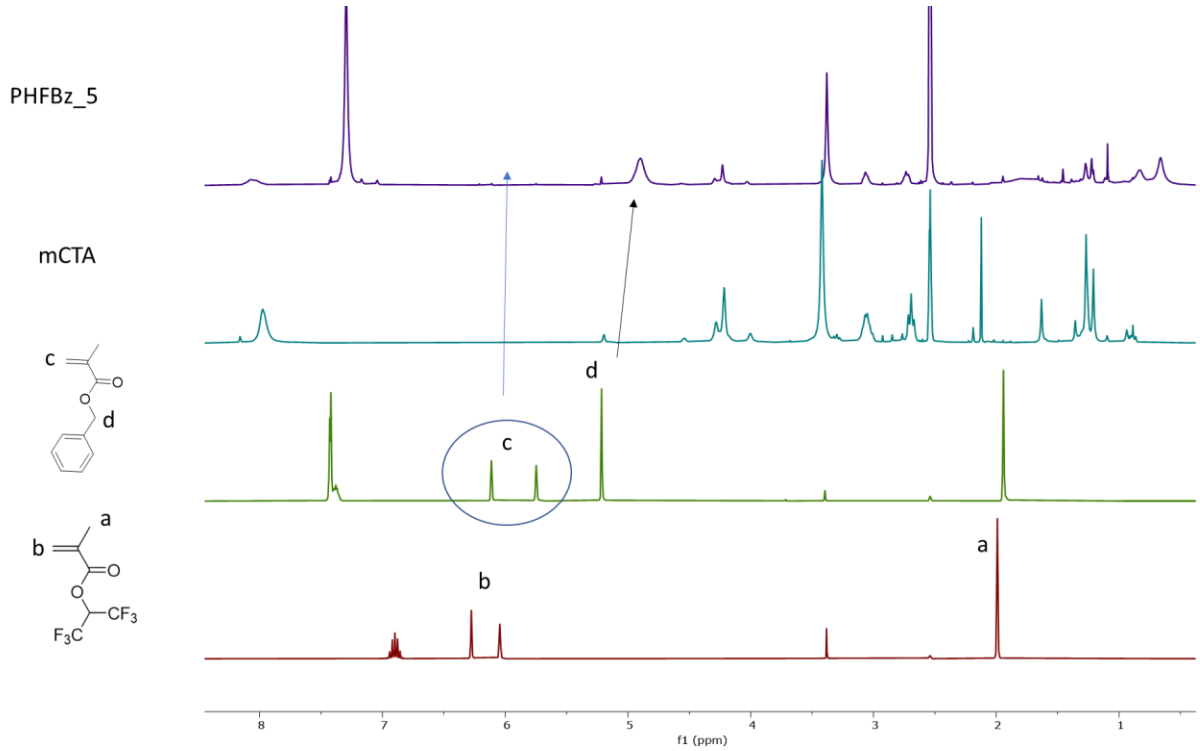

Figure 113. ^{1}H-NMR comparison of HFMA, BzMA, mCTA-8-ala and P(Bz_HF_5) (400 MHz, DMSO-d6)

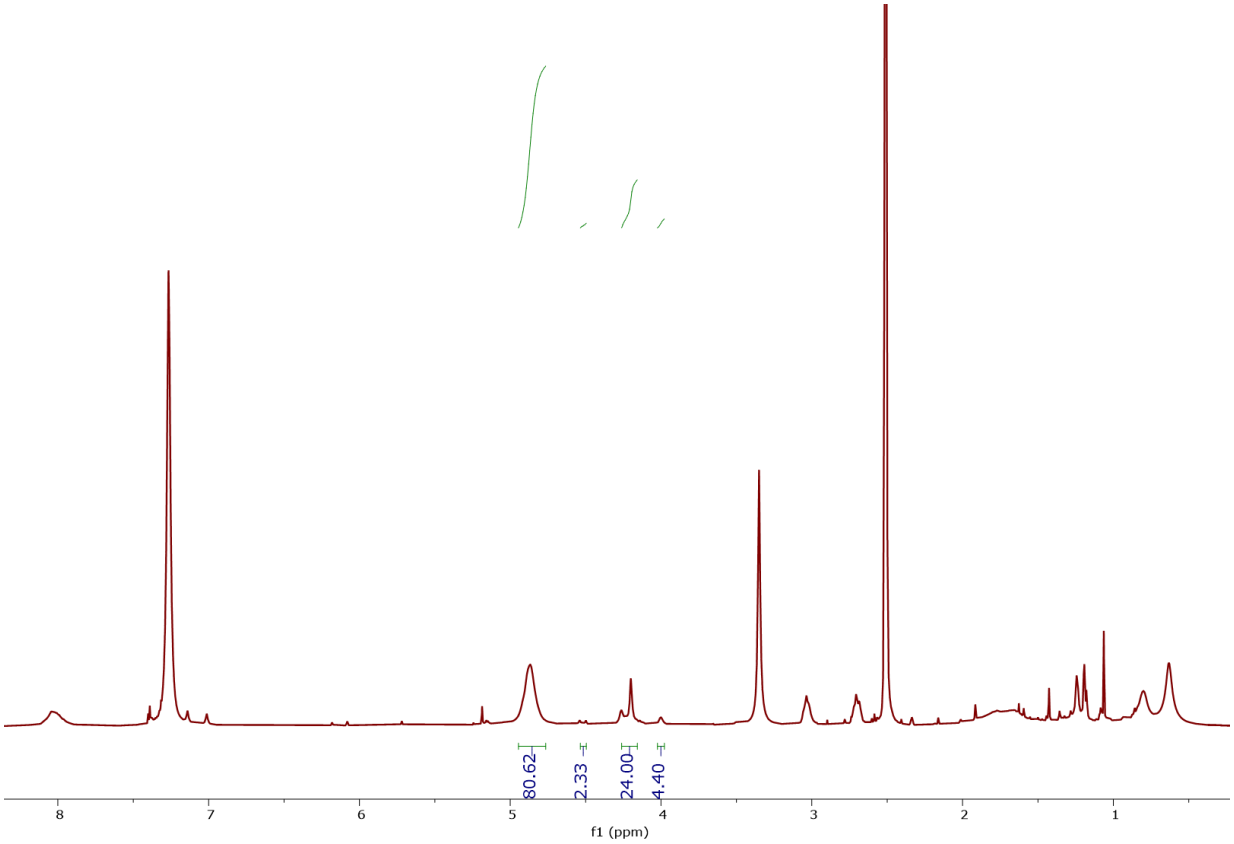

Figure 114. ^{1}H-NMR for P(Bz_HF_5) (400 MHz, DMSO-d6)

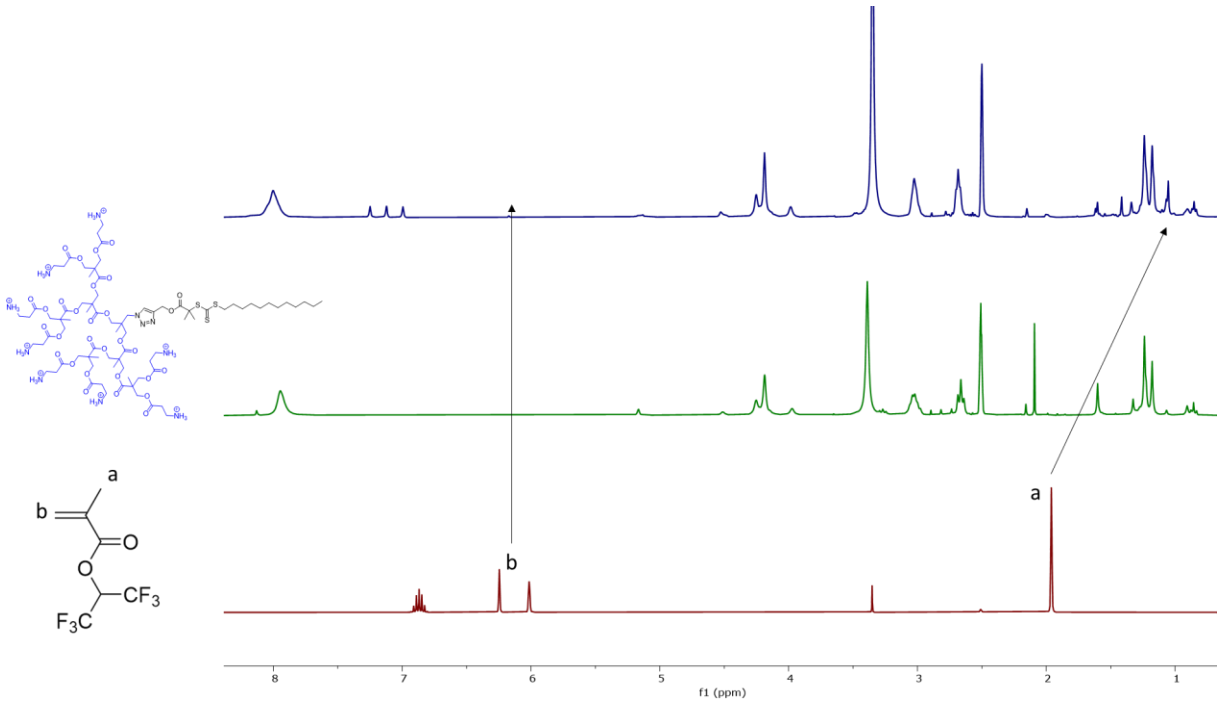

Figure 115. ^{1}H-NMR comparison of adding of HFMA, mCTA-8-ala and P(HF_20) (400 MHz, DMSO-d6)

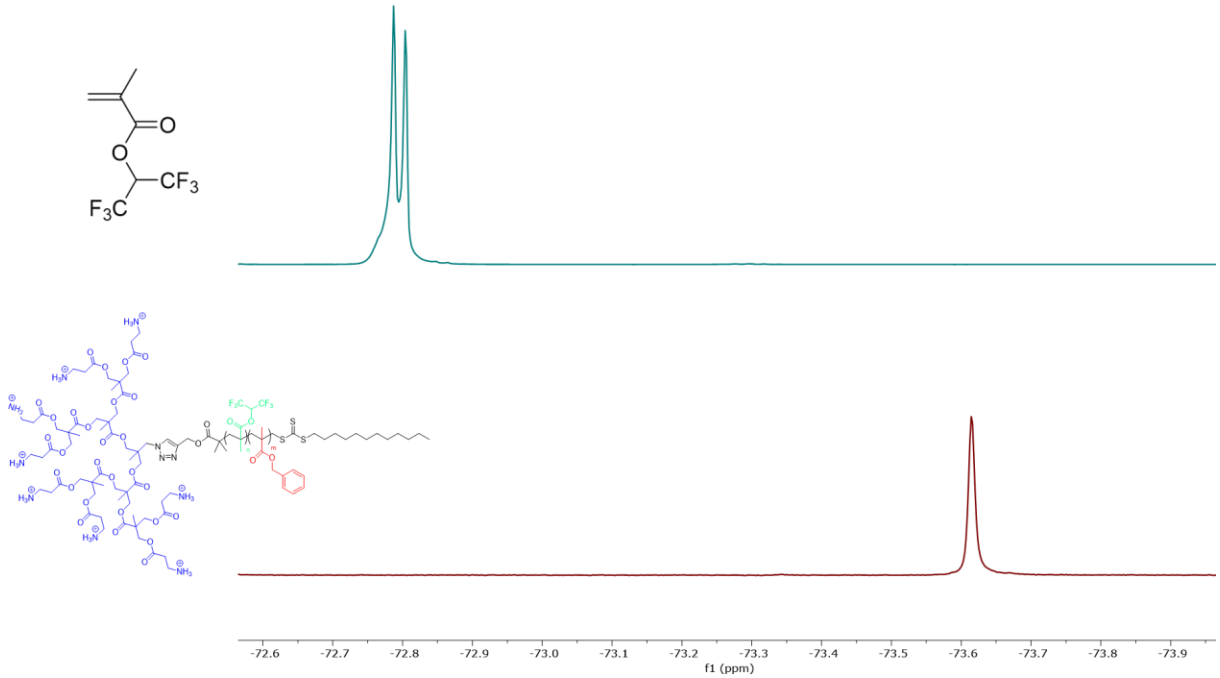

Figure 116. ^{19}F NMR comparison of HFMA and P(Bz_HF_20) (400 MHz, DMSO-d6)

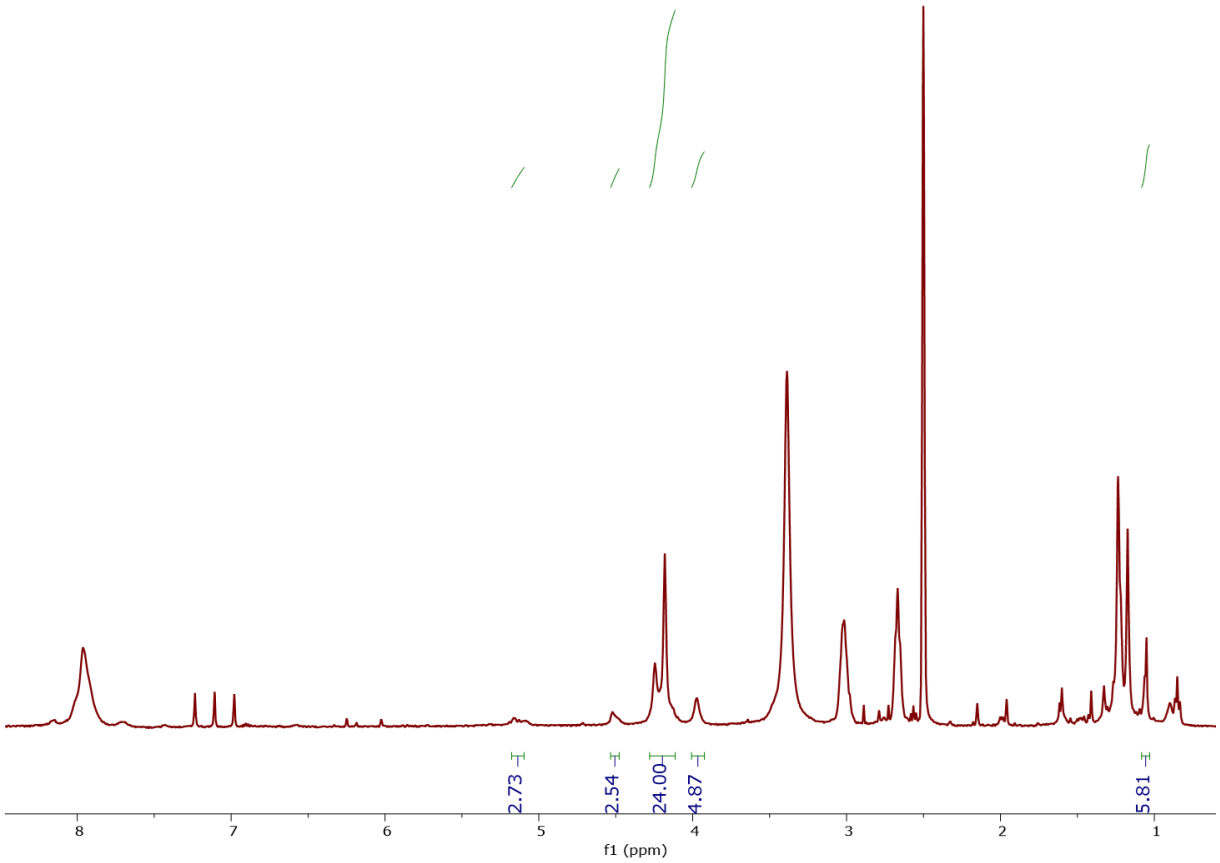

Figure 117. ^{1}H-NMR for P(HF_20) (400 MHz, DMSO-d6)

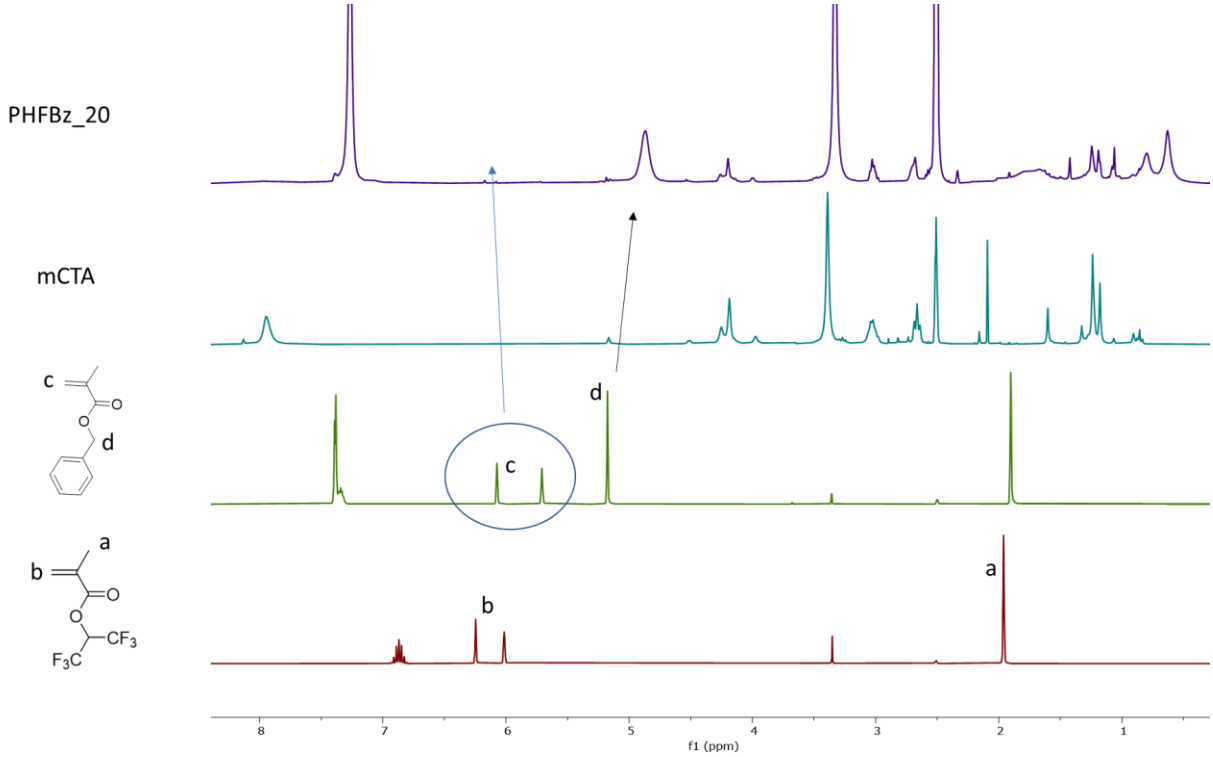

Figure 118. ^{1}H-NMR comparison of HFMA, BzMA, mCTA-8-ala and P(Bz_HF_20) (400 MHz, DMSO-d6)

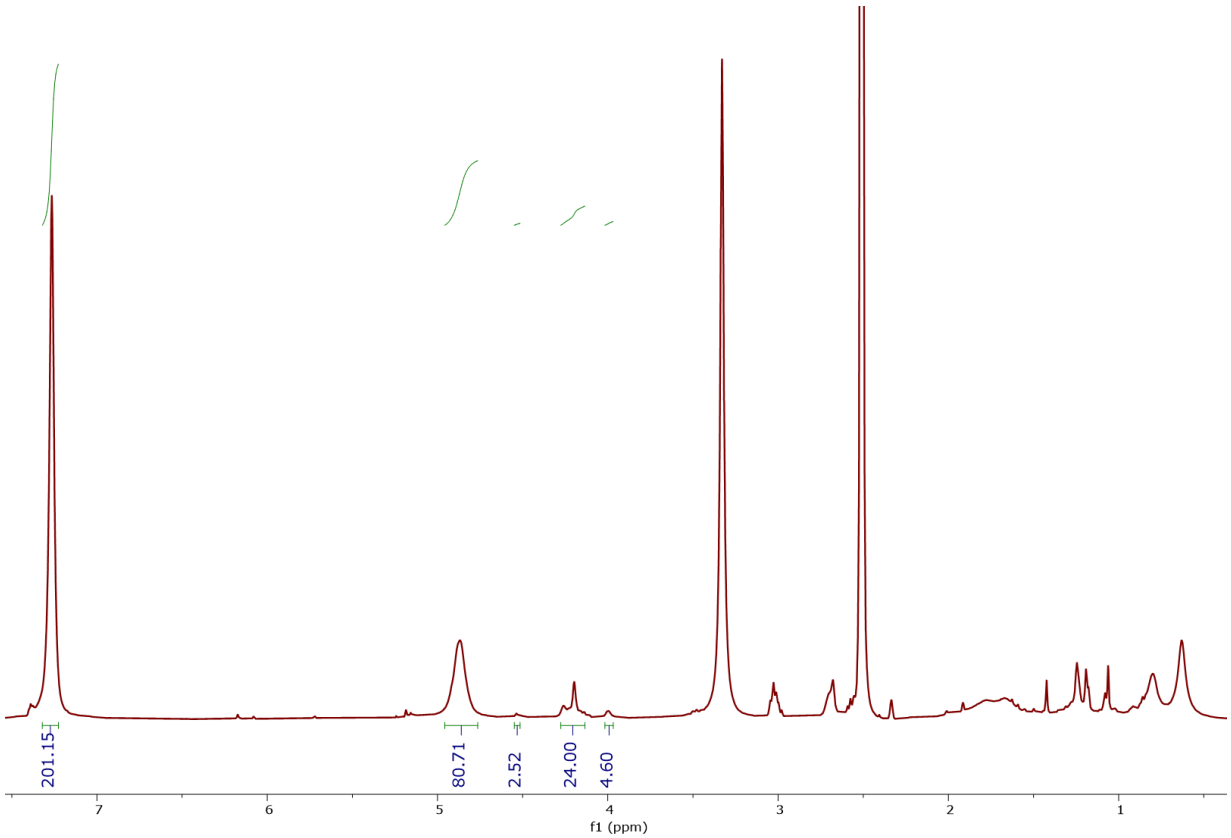

Figure 119. ^{1}H-NMR for P(Bz_HF_20) (400 MHz, DMSO-d6)

Table 6. Molecular weight characterization of JDs by GPC with DMF as the elution solvent

Polymer	Mn [g mol^{-1}]	Mw [g mol^{-1}]	Đ
P(Bz-HF-5)	5284	6973	1.320
P(Bz-HF-10)	8069	9804	1.215
P(Bz-HF-20)	6797	8079	1.189

M_n, M_w, Đ denote number average molar mass, weight average molar mass, and dispersity, respectively.

GPC CHROMATOGRAMS

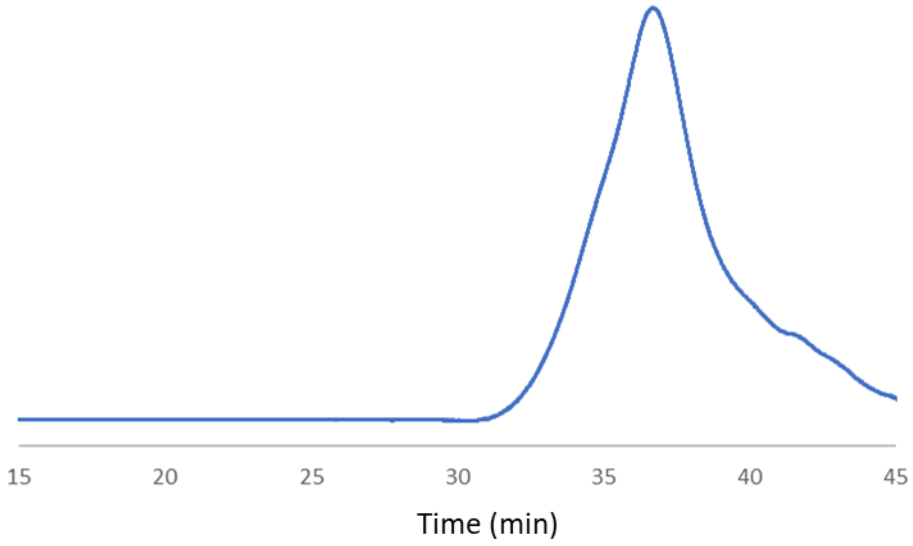

Figure 120. GPC chromatograms for P(Bz_HF_5)

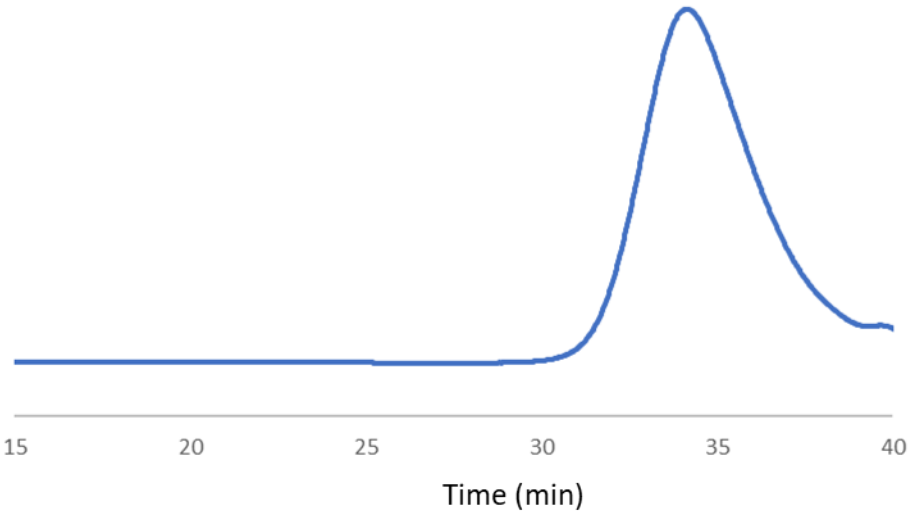

Figure 121. GPC chromatograms for P(Bz_HF_10)

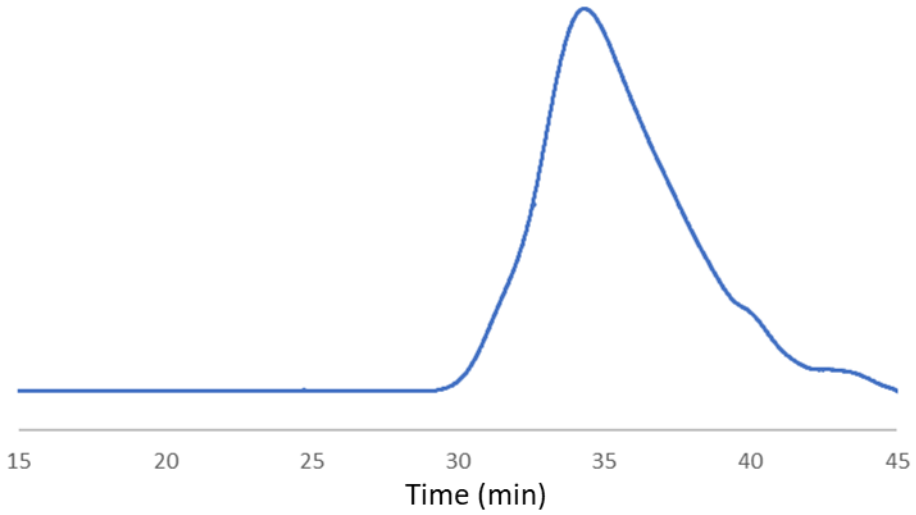

Figure 122. GPC chromatograms for P(Bz_HF_20)

Table 7. Summary of average hydrodynamic diameter of the dendritic aggregates

Sample	R_{hDLS}(nm)			PDI	ζ-potential (mV)
	Number	Intensity	Volume		
P(Bz_HF_5)	156.6 ± 42.35	191.0 ± 48.24	189.6 ± 53.74	0.115	33.6 ± 3.90
P(Bz_HF_10)	104.1 ± 26.73	135.3 ± 34.10	125.0 ± 36.86	0.054	31.1 ± 3.91
P(Bz_HF_20)	135.6 ± 34.93	165.2 ± 38.68	161.1 ± 43.73	0.035	30.5 ± 4.78

DLS SPECTRA

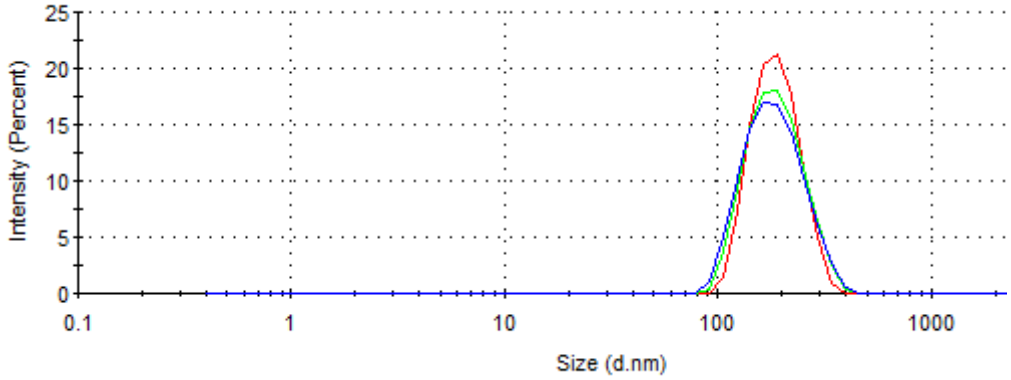

Figure 123. DLS spectra for P(Bz_HF_5), Size distribution by intensity

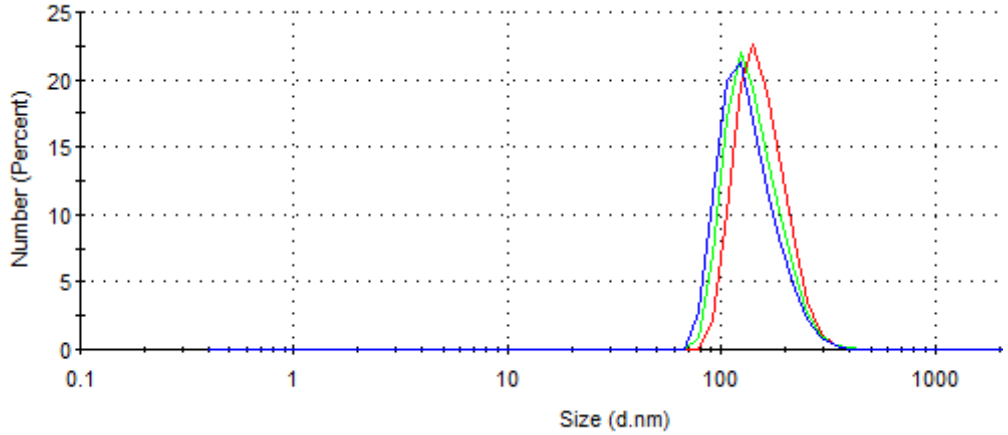

Figure 124. DLS spectra for P(Bz_HF_5), Size distribution by number

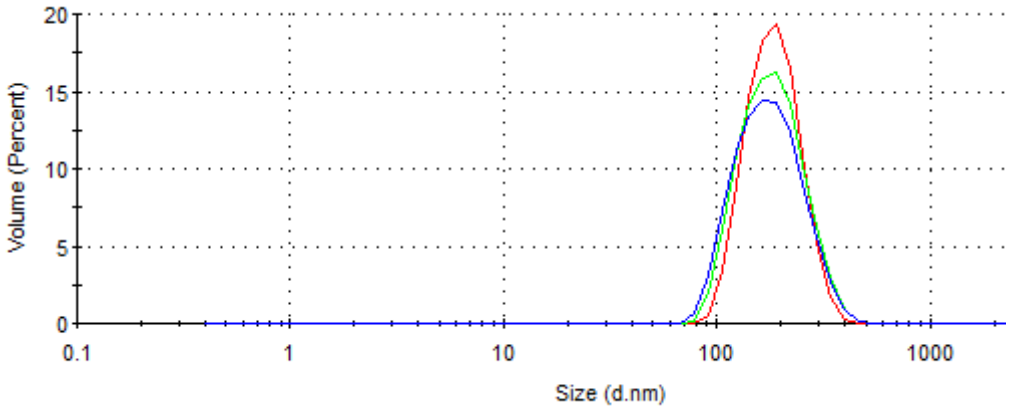

Figure 125. DLS spectra for P(Bz_HF_5), Size distribution by volume

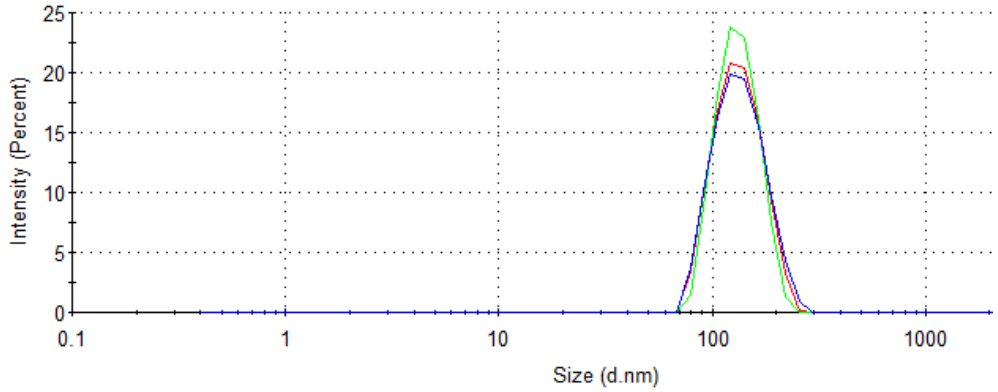

Figure 126. DLS spectra for P(Bz_HF_10), Size distribution by intensity

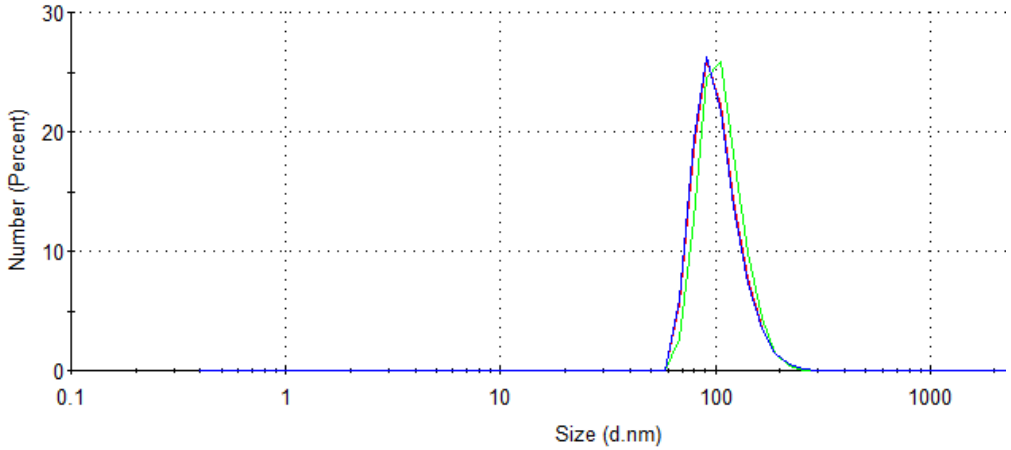

Figure 127. DLS spectra for P(Bz_HF_10), Size distribution by number

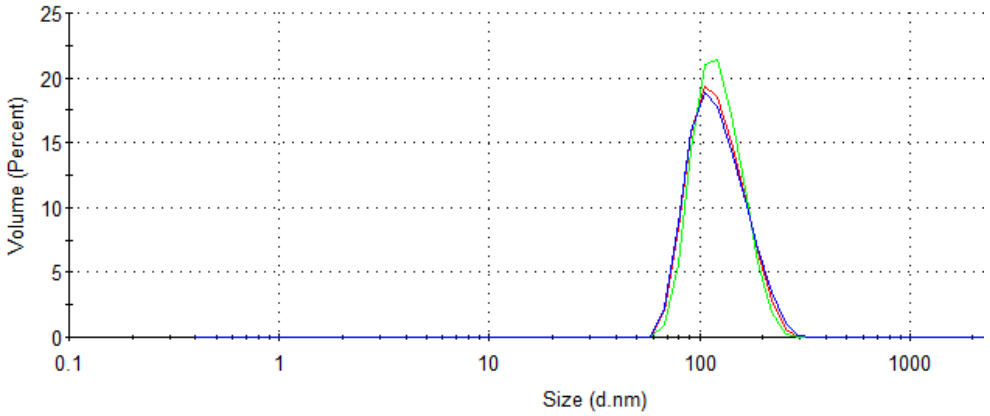

Figure 128. DLS spectra for P(Bz_HF_10), Size distribution by volume

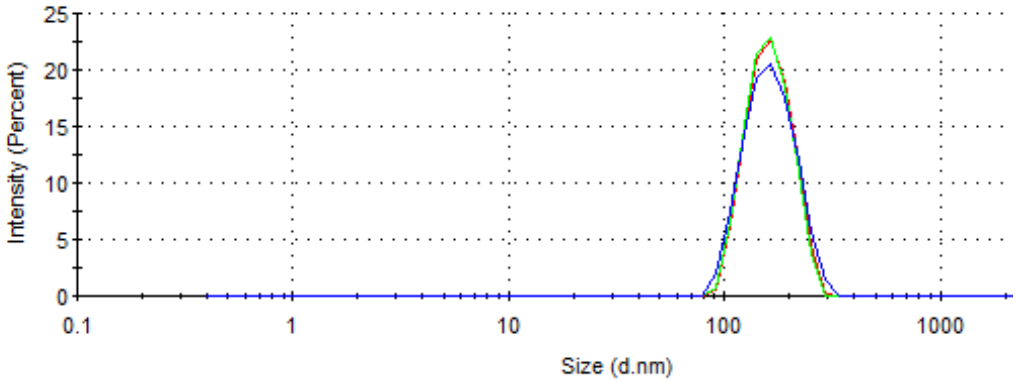

Figure 129. DLS spectra for P(Bz_HF_20), Size distribution by intensity

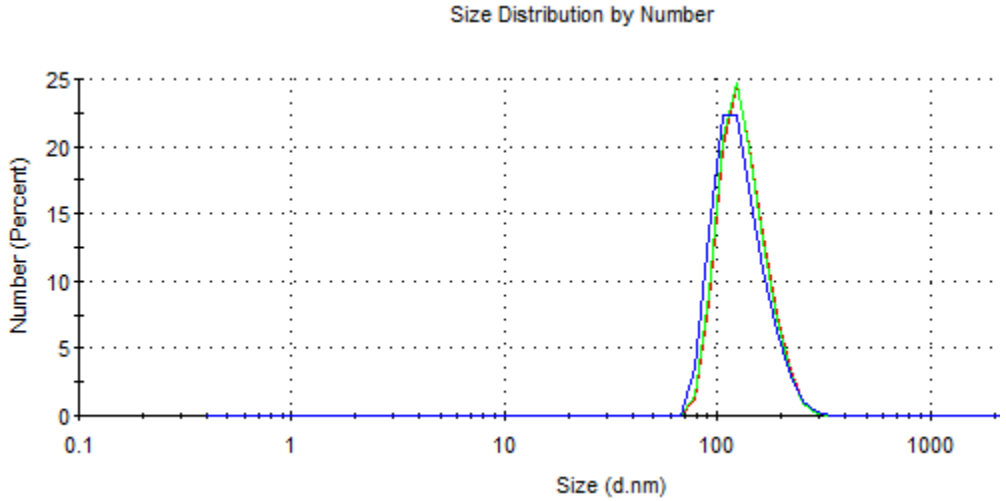

Figure 130. DLS spectra for P(Bz_HF_20), Size distribution by number

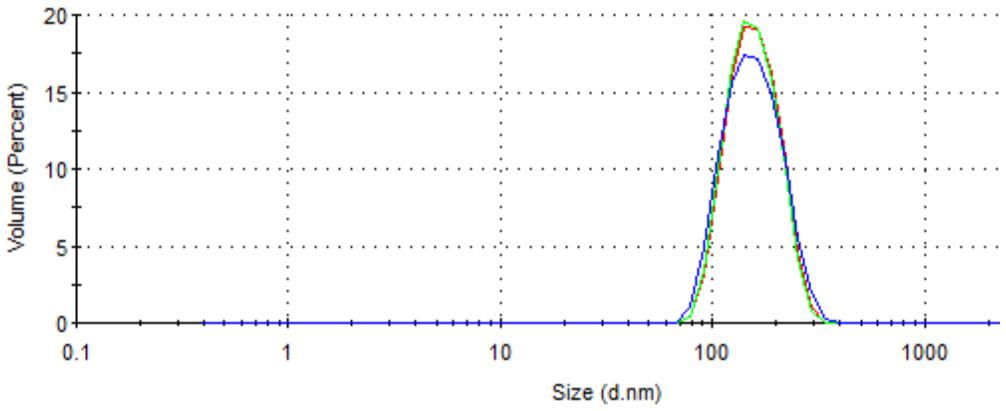

Figure 131. DLS spectra for P(Bz_HF_20), Size distribution by volume

CAC DATA

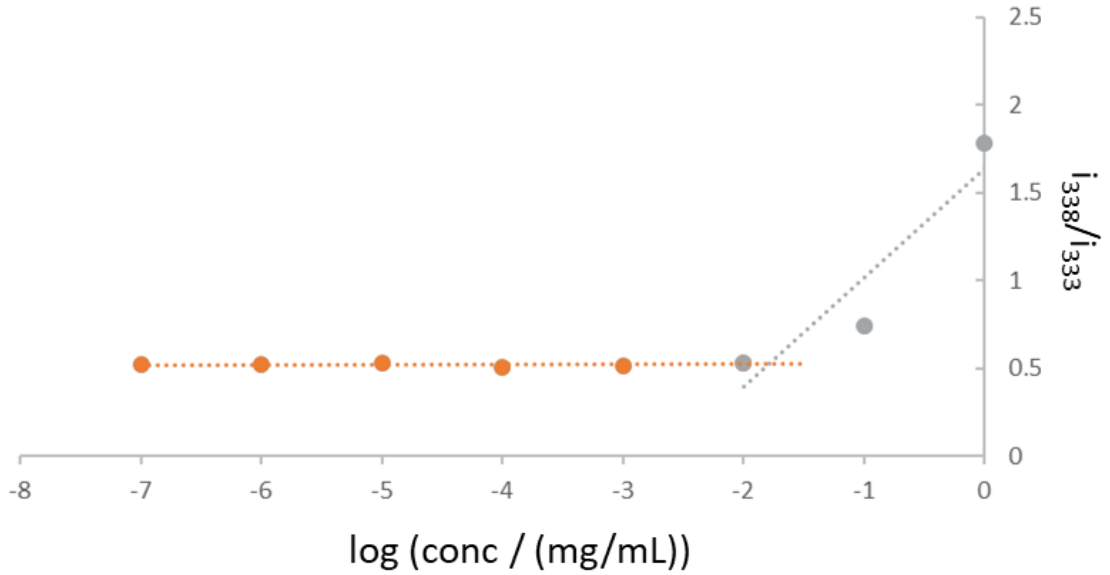

Figure 132. Excitation ratio vs. log concentration for P(Bz_HF_5)

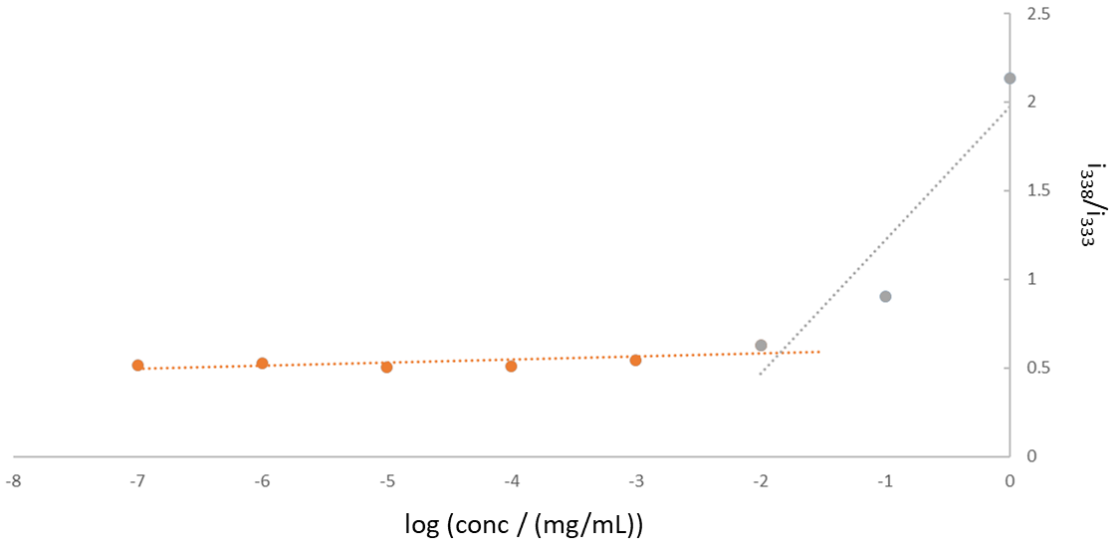

Figure 133. Excitation ratio vs. log concentration for P(Bz_HF_10)

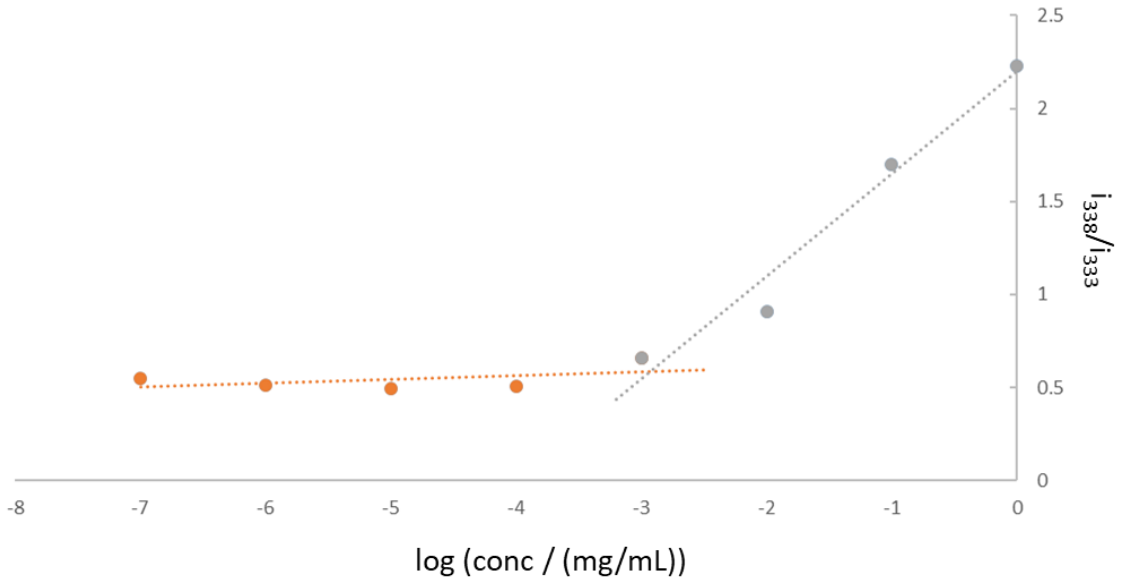

Figure 134. Excitation ratio vs. log concentration for P(Bz_HF_20)

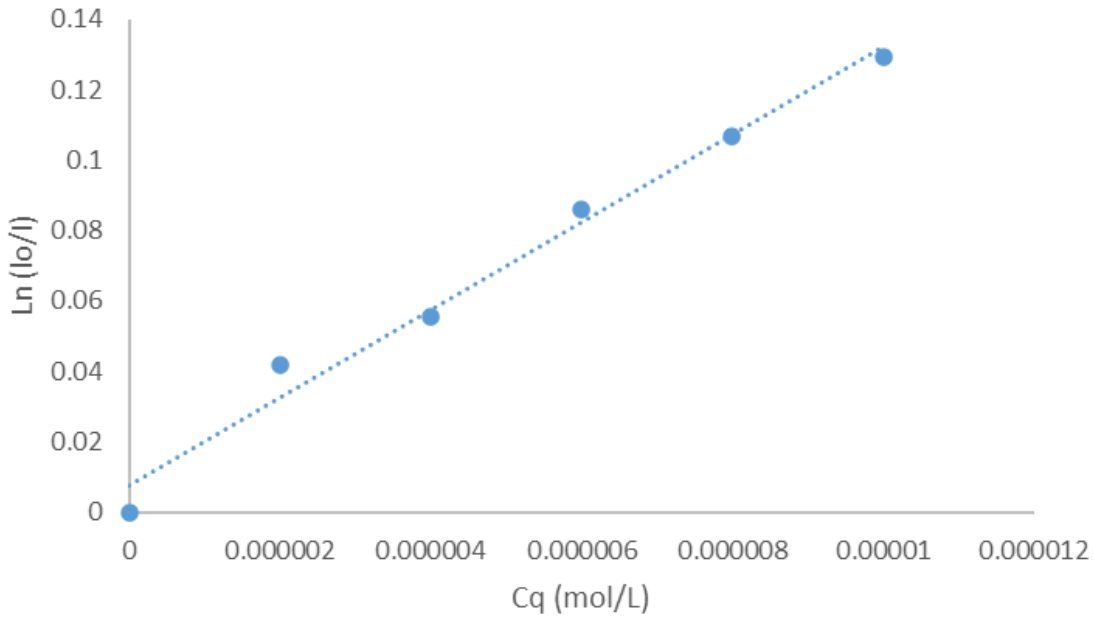

Figure 135. ln (I_0/I) of pyrene as a function of concentration of the quencher, benzophenone, in P(Bz_HF_5) aqueous solution at 25 ^{o}C

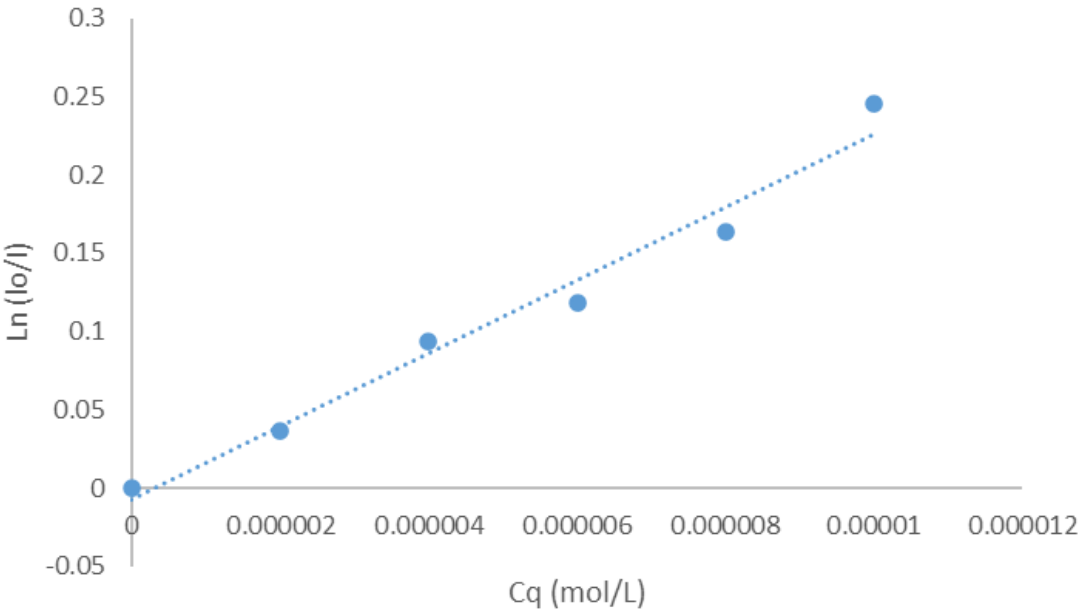

Figure 136. ln (I_0/I) of pyrene as a function of concentration of the quencher, benzophenone, in P(Bz_HF_10) aqueous solution at 25 ºC

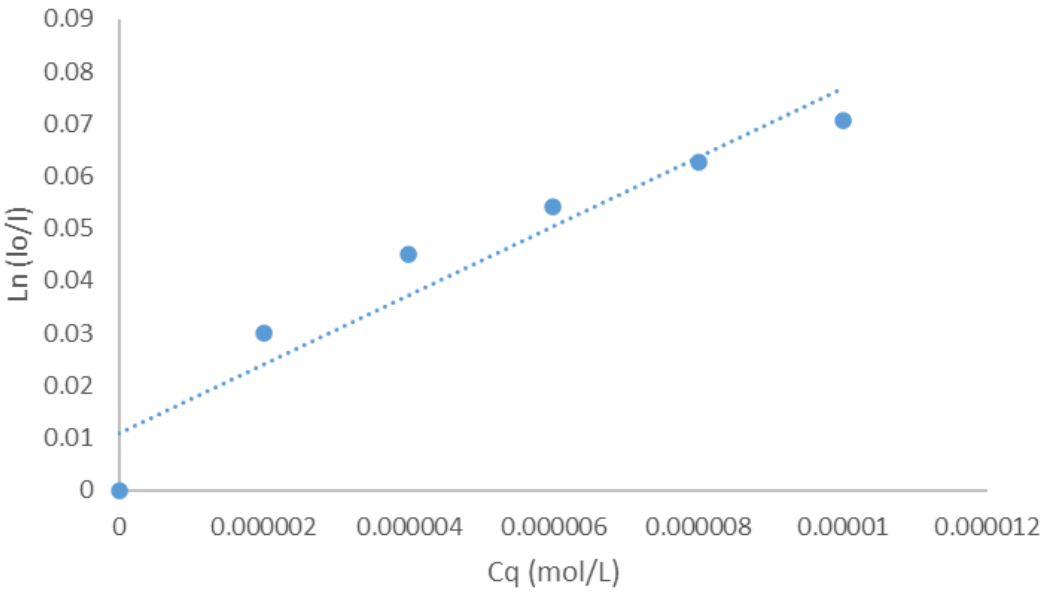

Figure 137. ln (I_0/I) of pyrene as a function of concentration of the quencher, benzophenone, in P(Bz_HF_20) aqueous solution at 25 ºC

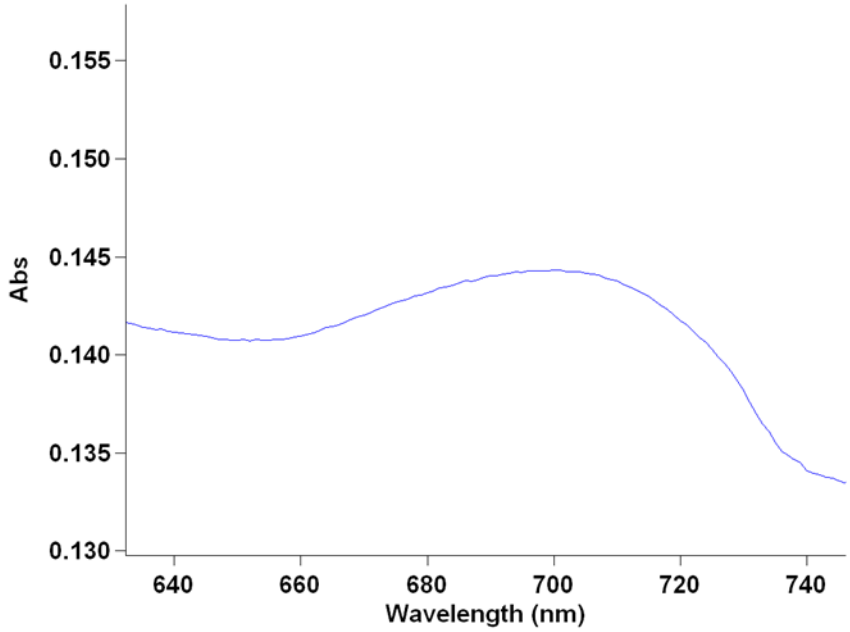

Figure 138. Absorption spectra of C3-loaded P(Bz_HF_5) in water

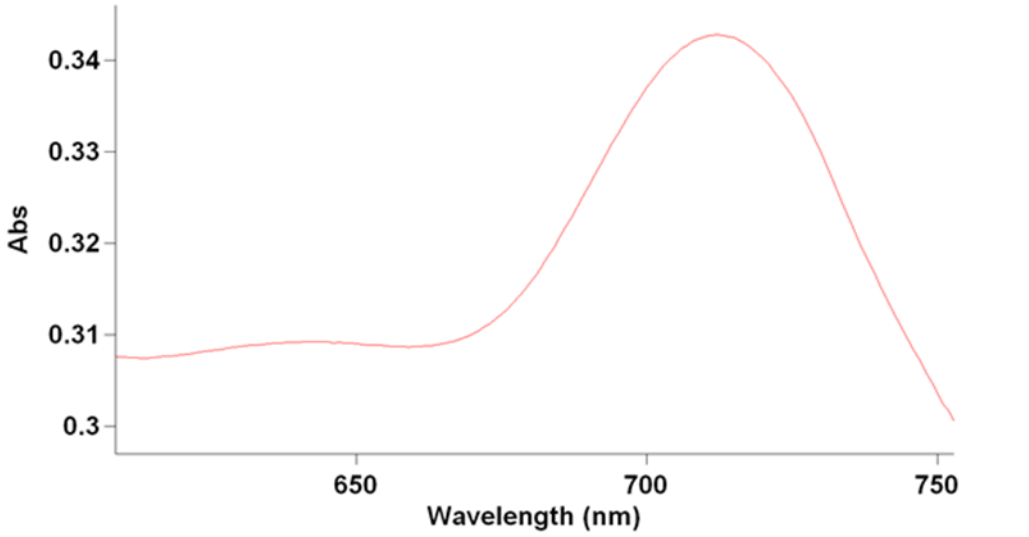

Figure 139. Absorption spectra of C3-loaded P(Bz_HF_10) in water

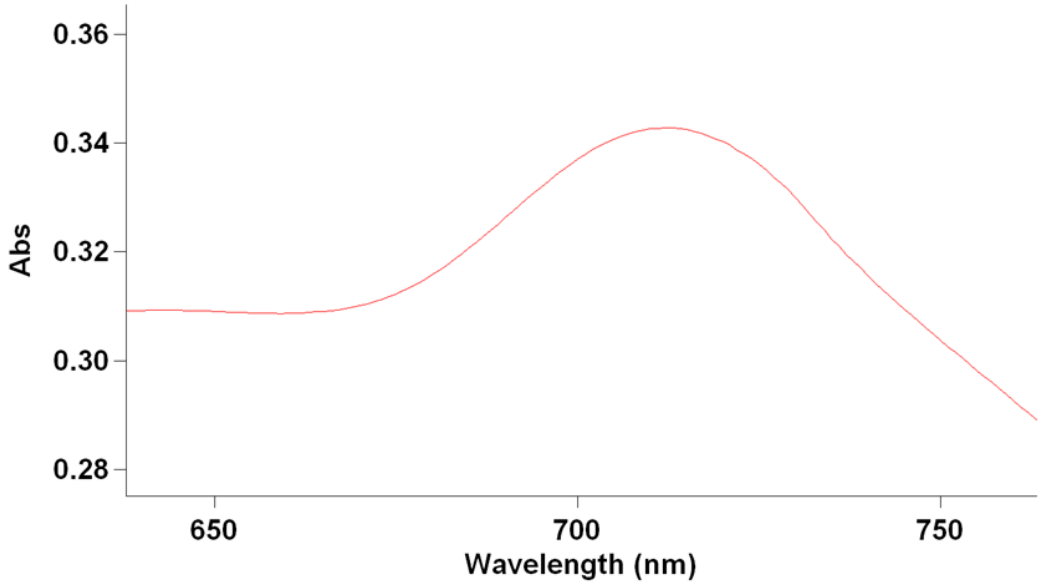

Figure 140. Absorption spectra of C3-loaded P(Bz_HF_20) in water

SIGNAL TO NOISE RATIO (SNR)

C/ (mg/mL)	SNR
0.5	13.04
2	22.41
4	119.7
6	159.03
8	254.35
10	277.21

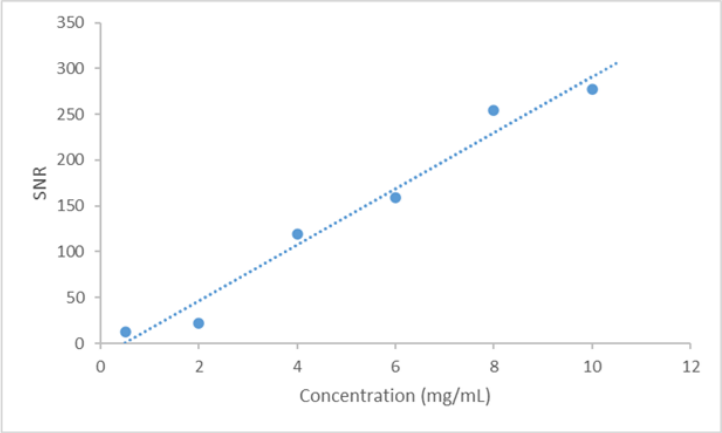

Figure 141. SNR of P(Bz_HF_5)

C/ (mg/mL)	SNR
0.5	51.71
2	83.68
4	158.84
6	396.69
8	425.78
10	592.54

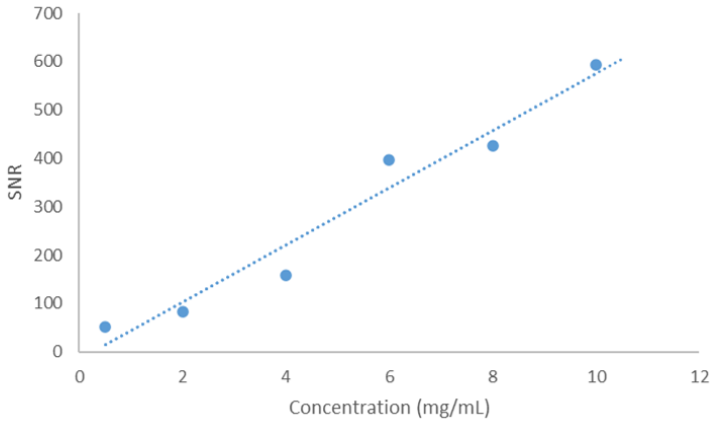

Figure 142. SNR of P(Bz_HF_10)

C/ (mg/mL)	SNR
0.5	59.96
2	97.33
4	430.57
6	591.23
8	592.54
10	725.31

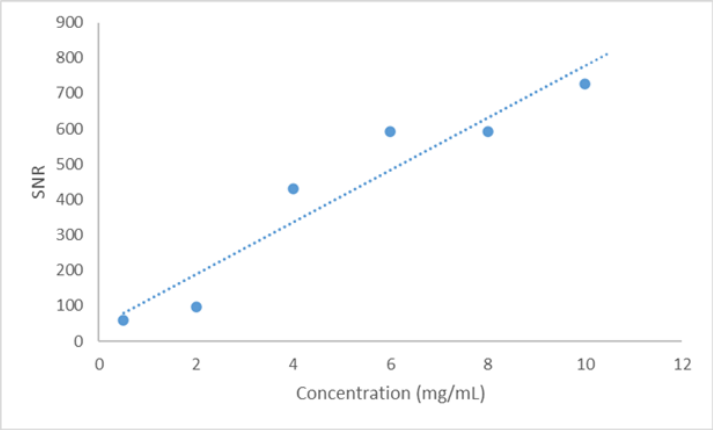

Figure 143. SNR of P(Bz_HF_20)

APPENDIX D: JOURNAL PERMISSION

1.Journal permission for figure 1 in Chapter I

ELSEVIER LICENSE
TERMS AND CONDITIONS

Mar 13, 2022

This Agreement between Mahesh Loku Yaddehige ("You") and Elsevier ("Elsevier") consists of your license details and the terms and conditions provided by Elsevier and Copyright Clearance Center.

License Number	5267180098293
License date	Mar 13, 2022
Licensed Content Publisher	Elsevier
Licensed Content Publication	European Journal of Pharmaceutical Sciences
Licensed Content Title	An emerging class of amphiphilic dendrimers for pharmaceutical and biomedical applications: Janus amphiphilic dendrimers
Licensed Content Author	Dhiraj R. Sikwal,Rahul S. Kalhapure,Thirumala Govender
Licensed Content Date	Jan 15, 2017
Licensed Content Volume	97
Licensed Content Issue	n/a
Licensed Content Pages	22
Start Page	113
End Page	134

Type of Use	reuse in a thesis/dissertation
Portion	figures/tables/illustrations
Number of figures/tables/illustrations	1
Format	both print and electronic
Are you the author of this Elsevier article?	No
Will you be translating?	No
Title	Structural and Surface Properties of Polyamidoamine (PAMAM) – Fatty Acid-based Nanoaggregates Derived from Self-assembling Janus Dendrimers
Institution name	University of Mississippi
Expected presentation date	Mar 2022
Portions	Fig. 2. (b) Structural homology of JDs to a tree.
Requestor Location	Mahesh Loku Yaddehige 478, Coulter hall Department of Chemistry and Biochemistry OXFORD, MS 38655 United States Attn: Mahesh Loku Yaddehige
Publisher Tax ID	98-0397604
Total	0.00 USD
Terms and Conditions	

2.Journal permission for figure 3 in Chapter I

Creative Commons License Deed

Attribution-NonCommercial 4.0 International (CC BY-NC 4.0)

This is a human-readable summary of (and not a substitute for) the license.

You are free to:

Share — copy and redistribute the material in any medium or format

Adapt — remix, transform, and build upon the material

The licensor cannot revoke these freedoms as long as you follow the license terms.

Under the following terms:

Attribution — You must give appropriate credit, provide a link to the license, and indicate if changes were made. You may do so in any reasonable manner, but not in any way that suggests the licensor endorses you or your use.

NonCommercial — You may not use the material for commercial purposes.

No additional restrictions — You may not apply legal terms or technological measures that legally restrict others from doing anything the license permits.

Notices:

You do not have to comply with the license for elements of the material in the public domain or where your use is permitted by an applicable exception or limitation.

No warranties are given. The license may not give you all of the permissions necessary for your intended use. For example, other rights such as publicity, privacy, or moral rights may limit how you use the material.

3.Journal permission for Chapter II

JOHN WILEY AND SONS LICENSE
TERMS AND CONDITIONS

Jan 16, 2022

This Agreement between Mahesh Loku Yaddehige ("You") and John Wiley and Sons ("John Wiley and Sons") consists of your license details and the terms and conditions provided by John Wiley and Sons and Copyright Clearance Center.

License Number	5230870138005
License date	Jan 16, 2022
Licensed Content Publisher	John Wiley and Sons
Licensed Content Publication	ChemNanoMat
Licensed Content Title	Structural and Surface Properties of Polyamidoamine (PAMAM) – Fatty Acid-based Nanoaggregates Derived from Self-assembling Janus Dendrimers
Licensed Content Author	Davita L. Watkins, Mahavir B. Chougule, Daniel G. Abebe, et al
Licensed Content Date	Nov 5, 2020
Licensed Content Volume	6
Licensed Content Issue	12

Licensed Content Pages	10
Type of use	Dissertation/Thesis
Requestor type	Author of this Wiley article
Format	Print and electronic
Portion	Full article
Will you be translating?	No
Title	Structural and Surface Properties of Polyamidoamine (PAMAM) – Fatty Acid-based Nanoaggregates Derived from Self-assembling Janus Dendrimers
Institution name	University of Mississippi
Expected presentation date	Mar 2022
Requestor Location	Mahesh Loku Yaddehige 478, Coulter hall Department of Chemistry and Biochemistry OXFORD, MS 38655 United States Attn: Mahesh Loku Yaddehige
Publisher Tax ID	EU826007151
Total	0.00 USD

4.Journal permission for figure 12 in chapter III

CCC Marketplace™

This is a License Agreement between Mahesh Loku Yaddehige ("User") and Copyright Clearance Center, Inc. ("CCC") on behalf of the Rightsholder identified in the order details below. The license consists of the order details, the CCC Terms and Conditions below, and any Rightsholder Terms and Conditions which are included below.

All payments must be made in full to CCC in accordance with the CCC Terms and Conditions below.

Order Date	17-Jan-2022	Type of Use	Republish in a thesis/dissertation
Order License ID	1178981-1		
ISSN	1759-9962	Publisher	Royal Society of Chemistry
		Portion	Image/photo/illustration

LICENSED CONTENT

Publication Title	Polymer chemistry	Publication Type	e-Journal
Article Title	Polymerization-Induced Self-Assembly (PISA) – control over the morphology of nanoparticles for drug delivery applications	Start Page	350
		End Page	355
		Issue	2
		Volume	5
		URL	http://www.rsc.org/Publishing/Journals/PY/Index.asp
Author/Editor	Royal Society of Chemistry (Great Britain)		
Date	12/31/2009		
Language	English		
Country	United Kingdom of Great Britain and Northern Ireland		
Rightsholder	Royal Society of Chemistry		

REQUEST DETAILS

Portion Type	Image/photo/illustration	Distribution	United States and Canada
Number of images / photos / illustrations	1	Translation	Original language of publication
Format (select all that apply)	Print, Electronic	Copies for the disabled?	No
		Minor editing privileges?	No
Who will republish the content?	Academic institution	Incidental promotional use?	No
Duration of Use	Life of current edition	Currency	USD
Lifetime Unit Quantity	Up to 499		
Rights Requested	Main product		

NEW WORK DETAILS

Title	Thesis	Institution name	University of Mississippi
Instructor name	Davita Watkins	Expected presentation date	2022-05-05

VITA

MAHESH LOKU YADDEHIGE

Department of Chemistry & Biochemistry

University of Mississippi

University, MS 38677

Lmdesilv@go.olemiss.edu, lymahesh@gmail.com

EDUCATION

University of Mississippi: Department of Chemistry, University, MS, 2017-2022

Advisor: Prof. Davita L. Watkins; Degree: Chemistry, Ph.D.

University of Peradeniya: Department of Chemistry, Peradeniya, Sri Lanka, 2009-2014

Advisors: Prof. Chamara Jayasundara; Degree: B.S. Chemistry

PUBLICATIONS

Hamadani, M. C.; Chandrasiri, I.; Yaddehige, M. L.; Dasanayake, S. G.; Owolabi, I.; Flynt, A.; Watkins, D. L.; Tanner, L. E.; Improved Nanoformulation of Linear-Dendrimer Block-co-

Polymer Materials for Red Blood Cell Hitchhiking with Ionic Liquids. Nanoscale, 2022.

Chandrasiri, I.; Yaddehige, M. L.; Li, B.; Sun, Y.; Meador, W.; Dorris, A.; Zia, M.; Hammer, N. I.; Flynt, A.; Delcamp, J. H.; Davis, E.; Lippert, A.; Watkins, D. L.; Core Cross-linked PCL-PAMAM Linear Dendritic Block Copolymers (LDBC) for Theranostic Nanomedicine. ACS Applied Polymer Materials, 2021, https://doi.org/10.1021/acsapm.1c01131.

Ndaleh, D.; Smith, C.; Yaddehige M.L.; Shaik, A.K.; Watkins, D. L.: Hammer, N. I.; Delcamp, J. H.; Shortwave Infrared Absorptive and Emissive Pentamethine-Bridged Indolizine Cyanine Dyes. The Journal of Organic Chemistry, 2021, https://doi.org/10.1021/acs.joc.1c01908

Ranathunge, T. A.; Yaddehige, M. L.; Varma, H. J.; Smith, C.; Nguyen, J.; Owolabi, I.; Kolodziejczyk, W.; Hammer, N. I.; Hill, G.; Flynt, A.; Watkins, D. L.; Heteroacene-based amphiphile as a molecular scaffold for bioimaging probes. Frontiers in Chemistry, 2021. https://doi:10.3389/fchem.2021.729125.

Yaddehige, M. L.; Chandrasiri, I.; Barker, A.; Kotha, A. K.; Dal Williams, J. S.; Simms, B.; Kucheryavy, P.; Abebe, D. G.; Chougule, M. B.; Watkins, D. L. Structural and Surface Properties of Polyamidoamine (PAMAM) – Fatty Acid-based Nanoaggregates Derived from Self-assembling Janus Dendrimers. ChemNanoMat, 2020, 6 (12), 1833–1842. https://doi.org/10.1002/cnma.202000498.

Chandrasiri, I.; Abebe, D. G.; Yaddehige, M. L.; Williams, J. S. D.; Zia, M. F.; Dorris, A.; Barker, A.; Simms, B. L.; Parker, A.; Vinjamuri, B. P.; Le, N.; Gayton, J. N.; Chougule, M. B.; Hammer, N. I.; Flynt, A.; Delcamp, J. H.; Watkins, D. L. Self-Assembling PCL–PAMAM Linear Dendritic Block Copolymers (LDBCs) for Bioimaging and Phototherapeutic

Applications. ACS Applied Bio Materials, 2020, 3 (9), 5664–5677. https://doi.org/10.1021/acsabm.0c00432.

Chandrasiri, I.; Abebe, D. G.; Gupta, S.; Williams, J. S. D.; Rieger, W. D.; Simms, B. L.; Yaddehige, M. L.; Noh, Y.; Payne, M. E.; Fortenberry, A. W.; Smith, A. E.; Ilavsky, J.; Grayson, S. M.; Schneider, G. J.; Watkins, D. L. Synthesis and Characterization of Polylactide-PAMAM "Janus-type" Linear-dendritic Hybrids. Journal of Polymer Science Part A: Polym. Chem. 2019, 57 (13), 1448–1459. https://doi.org/10.1002/pola.29409.

SELECTED PRESENTATIONS

Yaddehige, M. L.; Watkins, D. L. "Multifunctional fluorine-19 magnetic resonance imaging (^{19}F MRI) nanoparticles as theranostic agents", Polymer Colloids, San Diego, CA, February 22, 2022. (Oral presentation)

Yaddehige, M. L.; Watkins, D. L. "Multifunctional fluorine-19 magnetic resonance imaging (^{19}F MRI) nanoparticles as theranostic agents", Nanomedicine and Immunoengineering Rising Stars Symposium, Oxford, MS, October 14, 2020. (Oral presentation)

Ranathunge, T. A.; Yaddehige, M. L.; Zia, M. F.; Varma, H. J.; Flynt, A.; Watkins, D. L. "Self-assembly of amphiphilic fluorescent nanoparticles for bioimaging", 95th Colloid and Surface Science symposium (CSSS), Virtual Meeting, June 14, 2021. (Oral presentation)

Yaddehige, M. L.; Watkins, D. L. "Cationic, Anionic and Neutral Functionalized Polyamidoamine (PAMAM) – Fatty Acid Amphiphilic Janus Dendrimers for Therapeutic

Applications", Mississippi Academy of Sciences (MAS) 84th Annual Meeting, Biloxi, MS, February 20, 2020. (Oral presentation)

Yaddehige, M. L.; Jones, M. C.; Morgan, S. E.; Watkins, D. L. "Synthesis of glycopolymer-modified Janus dendrimers via ROP, RAFT, and thiol-ene click chemistry", CEMOs 2019 Annual Meeting, Jackson Avenue Center, University of Mississippi, University, MS, November 13, 2019. (Poster presentation)

Yaddehige, M. L.; Chandrasiri, I.; Watkins, D. L. "Cationic, Anionic and Neutral Functionalized Polyamidoamine (PAMAM)-Fatty Acid Amphiphilic Janus Dendrimers for Therapeutic Applications", Applied Polymer Technology Extension Consortium Annual Meeting, Baton Rouge, LA, November 2, 2019. (Poster presentation)

Chandrasiri, I.; Yaddehige, M. L.; Watkins, D. L. "PAMAM-PCL/PLA Linear Dendritic Block Copolymers: Enhanced Drug Loading Efficiencies and Practical Approaches Towards Theranostic Nanomedicine", Applied Polymer Technology Extension Consortium Annual Meeting, Baton Rouge, LA, November 2, 2019. (Oral presentation)

Chandrasiri, I.; Yaddehige, M. L.; Watkins, D. L. "Synthesis and characterization of "Janus-type" linear-dendritic block copolymers (LDBCs) for therapeutic applications," 255th ACS National Meeting & Exposition, New Orleans, LA, May 18-22, 2018. (Oral presentation)

PROFESSIONAL TRAINING

Light scattering techniques at light scattering university, Wyatt Technology, Santa Barbara, CA, March 2019. Description: Practical and the theoretical aspects of light scattering, DLS, SLS and GPC data analyze using ASTRA

Cryo-transmission electron microscopy (cryo-TEM) at NUANCE Center, Northwestern University, Evanston, IL, June 2019. Description: Sample (TEM and cryo-TEM grid) preparation, negative staining and hands of experience on utilization of JEOL 1230 TEM with Dr. Reiner Bleher

University of Southern Mississippi (USM) X-ray scattering workshop, University of Southern Mississippi, Hattiesburg, MS, July 2020. Description: Hands-on training on utilization of major neutron and X-ray facilities, application of scattering methods to a variety of polymeric specimen with Dr. Xiaodan Gu

Interdisciplinary research in nanoscience and applied nanotechnology, Minnesota Nano Center, University of Minnesota, Minneapolis, MN, October 2021. Description: Dynamic light scattering techniques, Nanoparticle tracking analyzer and Confocal microscopy training with Dr. James Marti

Cryo-TEM at CharFac, University of Minnesota, Minneapolis, MN, November 2021. Description: Grid preparation, Staining, Glow discharge techniques and Imaging techniques with Dr. Wei Zhang